

**MICROMACHINED SEMI-CIRCULAR CANALS: BIO-INSPIRED
APPROACHES FOR ROTATIONAL
INERTIAL SENSING**

A Dissertation
Presented to
The Academic Faculty

by

Hommoood Alrowais

In Partial Fulfillment
of the Requirements for the Degree
Doctor of Philosophy in the
Electrical and Computer Engineering

Georgia Institute of Technology
December 2018

COPYRIGHT © 2018 BY HOMMOOD ALROWAIS

**MICROMACHINED SEMI-CIRCULAR CANALS: BIO-INSPIRED
APPROACHES FOR ROTATIONAL
INERTIAL SENSING**

Approved by:

Dr. Oliver Brand, Advisor
School of Electrical and Computer
Engineering
Georgia Institute of Technology

Dr. Farrokh Ayazi
School of Electrical and Computer
Engineering
Georgia Institute of Technology

Dr. Muhannad Bakir
School of Electrical and Computer
Engineering
Georgia Institute of Technology

Dr. Peter Hesketh
School of Mechanical Engineering
Georgia Institute of Technology

Dr. Fatih Sarioglu
School of Electrical and Computer
Engineering
Georgia Institute of Technology

Date Approved: July 23, 2018

To the amazing women in my life,

ACKNOWLEDGEMENTS

I would to love to acknowledge and appreciate my teachers, my parents, my family and friends who supported me through this journey. In particular, my advisor, Dr. Oliver Brand, who serves as a continuous role model. I want to thank my committee members, my lab mates throughout the years (Jin-Jyh, Chris, Spyros, Patrick, Choongsoon, Mingu, and the rest of the iSenSys lab members new and old), the IEN support staff with Purnima Sharma in particular. This last-minute written acknowledgement is a reminder to me that no matter I always submit in a caffeine-fueled rushed fashion, but that I am forever grateful for those who supported but are not explicitly mentioned in this paragraph.

TABLE OF CONTENTS

ACKNOWLEDGEMENTS	iv
LIST OF TABLES	viii
LIST OF FIGURES	ix
SUMMARY	xvi
CHAPTER 1. Introduction	1
1.1 Motivation	2
1.1.1 Vestibular Disorders and Current Therapies	2
1.1.2 Vestibular Prostheses	4
1.2 Background	9
1.2.1 Miniaturized Inertial Sensors	9
1.2.2 Gyroscopes	10
1.2.3 Angular Accelerometers	13
1.2.4 Fluid Mass-based Angular Accelerometers	15
1.2.5 Bio-inspired Sensors and Devices	15
1.2.6 State-of-the-Art in Vestibular Prosthesis-Specific Rotation Sensors	20
1.3 Research Objective	21
1.4 Thesis Outline	22
CHAPTER 2. INSPIRATION: SEMICIRCULAR CANALS	24
2.1 Background	24
2.1.1 Historical Background	24
2.2 Mammalian Vestibular System	25
2.2.1 Morphology	25
2.2.2 Labyrinth	26
2.2.3 Labyrinth Fluids	26
2.2.4 Ampulla and Cupula	27
2.2.5 Hair Cells	28
2.2.6 Operating Principle	31
2.3 Hydrodynamic Model of the SCC	31
2.4 Analysis of Semicircular Canals (SCC)	34
2.4.1 Evolution of Semicircular Canals	34
2.4.2 Geometric Design of the SCC	35
2.4.3 Dimension and Properties of the SCC	36
2.4.4 Allometric Analysis of the SCC	37
2.5 Human SCC Performance	38
2.5.1 Dynamic Range and Limit of Detection	39
2.5.2 Cupula and Hair Cell Performance	39
2.5.3 Afferent Signal Dynamic Range and Sensitivity	40
2.5.4 Frequency Range	40
2.6 Evaluation of the SCC as Rotational Sensing Platform	41

2.6.1	Features of the SCC	41
2.6.2	Challenges with the SCC	44
2.6.3	Unknowns	45
2.7	Conclusion	46
CHAPTER 3.	MICROMACHINED SEMICIRCULAR CANALS	47
3.1	Platform Introduction	47
3.1.1	Previous Attempts	47
3.1.2	Biomimicry vs. Bioinspiration	47
3.2	Design Considerations	50
3.2.1	Form and Geometric Consideration	50
3.2.2	Material Consideration	51
3.2.3	Transduction Mechanisms	52
3.2.4	Proposed Designs	53
3.3	Semicircular Canal Analysis	54
3.3.1	Assumptions	55
3.3.2	Forces	55
3.3.3	Analytical model	58
3.3.4	Sensitivity	59
3.3.5	System Linearity	60
3.3.6	Frequency	61
3.4	Simulation	64
3.4.1	Assumptions	65
3.4.2	Acceleration-induced Flow Profile	65
3.4.3	Rotational Sensitivity	66
3.4.4	Linear Acceleration Sensitivity	67
3.4.5	Effect of Wall Stiffness	68
3.4.6	Frequency Response	69
3.4.7	Geometric Parametric Study	71
3.5	Conclusion	75
CHAPTER 4.	THERMAL ANGULAR ACCELEROMETER	77
4.1	Proposed Device and Working Principle	77
4.1.1	Concept	78
4.1.2	Working principle	78
4.1.3	Inertial frames of reference	81
4.1.4	Desired and interfering input signals	83
4.1.5	Suppressing and rejecting interfering signals	83
4.2	Sensor Analysis	84
4.2.1	Forces	84
4.2.2	Non-dimensional analysis	86
4.2.3	Analytical model	88
4.2.4	Sensitivity	89
4.2.5	Linearity	92
4.2.6	Frequency	93
4.3	Finite Element Modeling of Sensor	95
4.3.1	Sensitivity and Cross-Sensitivity	98

4.3.2	Frequency	99
4.4	Design and Fabrication	103
4.4.1	Sensor Design	103
4.4.2	Sensor Fabrication	105
4.4.3	Wafer-level Packaging and Fabrication	107
4.5	Thermal Characterization	111
4.6	Mechanical Characterization	113
4.6.1	Sensitivity/Cross-Axis Sensitivity	115
4.6.2	Frequency Response	117
4.6.3	Plugged Behavior	118
4.6.4	Noise and temperature stability	119
4.7	Conclusion	121
CHAPTER 5.	MAGNETIC BIOMIMETIC ANGULAR ACCELEROMETER	123
5.1	Concept	123
5.1.1	Bioinspired Magnetic Cilia	126
5.2	Magnetic μSCC Design	129
5.2.1	Sensor Design Considerations	130
5.2.2	Working Principle	130
5.2.3	Magnetic Hair Cell Design	131
5.2.4	TMR sensor design	133
5.3	Numerical Simulations	137
5.3.1	Magnetic Simulation	137
5.3.2	Fluid Structure Interaction Simulation	146
5.4	Fabrication	151
5.4.1	Hair cell fabrication	151
5.4.2	Magnetic sensor fabrication	152
5.4.3	Packaging	154
5.5	Magnetic characterization	155
5.5.1	Magnetic sensor characterization	155
5.5.2	Commercial Magnetic Sensor Characterization	159
5.5.3	Magnetic Material Characterization	160
5.5.4	Discussion	161
5.6	Preliminary Testing Results	161
5.6.1	Electronic analog front end	161
5.6.2	Magnetic Mechanical Characterization – Hair cell displacement	163
5.7	Conclusions	168
CHAPTER 6.	CONCLUSIONS AND FUTURE WORK	170
6.1	Research Contributions	171
6.2	Future Work	172
REFERENCES		175

LIST OF TABLES

Table 1.1 - Comparison of state-of-the-art single-axis solid and fluidic gyroscope	12
Table 1.2 - Comparison of state-of-the-art micromachined angular accelerometer performance.	14
Table 1.3 - Comparison of state-of-the-art bio-inspired angular accelerometer performance.	18
Table 1.4 - Comparison of different potential transduction mechanisms for flow sensing	20
Table 3.1- Design comparison of state-of-the-art bio-inspired angular accelerometers...	48
Table 3.2. Geometric and material properties used for laminar flow simulation	65
Table 3.3. Parametric design of closed loops with different shape functions m	74
Table 4.1. Material properties for non-isothermal laminar flow simulations.	96
Table 4.2- Summary of device performance.....	122

LIST OF FIGURES

Figure 1.1 - General schematic of operation for a generic vestibular prosthesis, adopted from [38].	5
Figure 1.2 - Three different embodiments of vestibular prostheses , from left to right are adopted from [35], [36], [39].	6
Figure 1.3 - Diagram of thermal linear accelerometer by MEMSIC [73], and a thermal fluidic gyroscope working principle by [74].	12
Figure 2.1. Sketch of the human labyrinth as depicted by Gray in 1918 in Anatomy of the Human Body [149].	24
Figure 2.2. A diagram of the human inner ear. A close up of the labyrinth highlights both the bony and the membranous labyrinths, adapted from [151].	25
Figure 2.3. (a) A simplified diagram of the semicircular canal with the ampulla highlighted. (b) A close up of the ampulla showcasing the gelatinous cupula with the embedded sensory hair cells connected to the vestibular nerve, adapted from [151].	27
Figure 2.4. (a) Scanning electron microscopy image of a bundle of sensory hair cells by Leonardo Andrade and Bechara Kachar, NIDCD/NIH. (b) Illustration of one type of sensory hair cell's structure, adapted from [151].	29
Figure 2.5. Firing rate of the hair cells based on head motion and head rotation direction, adapted from [151].	30
Figure 2.6. (a) Firing rate of the hair cells as a function of angular velocity in a fly, (b) membrane potential as a function of angular velocity in a fly, as opposed to spike rate, adapted from [161].	30
Figure 2.7. Hydrodynamics of the SCC: Forces acting on semicircular canal under steady-state equilibrium, adapted from [62], [169].	32
Figure 2.8. Geometric depiction of a segmented model labyrinth using toolbox elements from [175].	35
Figure 2.9. MicroCT-scanned right semicircular duct system of a human specimen, with colors marking the parts required as separate STL surface files. SDa, SDp and SDl indicate the anterior, posterior and lateral semicircular ducts, respectively, from [174].	36
Figure 2.10. (a) Effect of animal mass on the major R and minor d radii of the semicircular canals; (b) Comparison between two animals: (a) Size as a function of mass from [111], [182], [183]; (b) Effect of agility on size of the semicircular canal from [188].	38
Figure 3.1 – Different device concepts: (a) Simple circular torus; (b) Helical torus (m=10); (c) Star torus (m=5); Simple elliptical torus (a=2b).	51
Figure 3.2. Proposed design concepts: (a) Simple torus with vertical membrane; (b) Simple torus with horizontal membrane; (c) Simple torus with vertical membrane and ampulla; (d) Simple torus without a membrane.	53
Figure 3.3. Forces and coordinate systems applied to microtorus under rotation: (a) Two dominant forces acting on torus under z-rotation; (b) Three coordinate systems used (i) Cartesian $(\hat{x}, \hat{y}, \hat{z})$ or $(\hat{i}, \hat{j}, \hat{k})$; (ii) Cylindrical system $(\hat{r}, \hat{\theta}, \hat{z})$; (iii) Toroidal system $(\hat{\rho}, \hat{\theta}, \hat{\phi})$; (c) Notation system used for μ SCC as adapted from [211].	58

Figure 3.3.4. Equivalent circuit models: (a) Electrical equivalent model; (b) Mechanical circuit model.	63
Figure 3.5. Parabolic laminar flow induced by a clockwise rotational angular acceleration of 100 rad/s^2 applied to the microtorus, yielding a counter-clockwise body force applied to the fluid with respect to the torus walls. Arrows indicate the magnitude and relative direction of fluid flow in the channel. The arrows for a parabola with zero velocity at the wall and the maximum velocity in the center of the channel.	65
Figure 3.6. Simulation results of maximum axial fluid velocity in the channel center as a response to an applied angular acceleration for (a) a complete microtorus and (b) a horseshoe-type blocked torus.....	66
Figure 3.7. Simulated maximum tangential fluid velocity as a response to applied linear acceleration: (a) maximum tangential fluid velocity as a function of applied linear acceleration in x, y, and z direction; (b) maximum tangential fluid velocity as a function of equivalent angular acceleration.	68
Figure 3.8. The effect of wall stiffness on rotational acceleration of 10 rad/s^2 and linear acceleration of 27.5 mm/s^2 (based on a minor radius of 2.75 mm and rotational acceleration of 10 rad/s^2), assuming a wall thickness of $\sim 20 \text{ }\mu\text{m}$ and the parameters in table 3.2.....	69
Figure 3.9. Simulated time response of maximum fluid velocity as a function of rotational acceleration: (a) Step response output as maximum axial flow velocity as a function of time; (b) Harmonic response output as maximum axial flow velocity as a function of normalized time over the period showing three periods for frequencies from 1 mHz to 25 Hz	70
Figure 3.10. Normalized bode plot of harmonic frequency response in figure 3.9b normalized to the 1 mHz response. Of the maximum axial velocity, the (a) magnitude (b) phase at the peak of the period for each frequency is plotted as a function of frequency.	71
Figure 3.11. (a) Parametric study of the effect of the minor radius on maximum axial velocity for a constant angular rotational acceleration of 100 rad/s^2 . (b) Parametric study of effect of minor radius on the extracted time constant for the same angular rotational acceleration applied as in in figure 3.9a.....	72
Figure 3.12. Effect of curvature factor n on the maximum axial velocity as a function of rotational angular acceleration input of 100 rad/s^2	73
Figure 3.13. The maximum and average axial velocity to angular rotational acceleration of 37 rad/s^2 as a function of shape factor m (shown in table 3.3.) The maximum is based on the volume of the structure and the average takes the average of the velocity of the entirety of the fluid.....	75
Figure 4.1. 3D-rendered model of proposed thermal angular acceleration sensor. The sensor consists of aluminum resistors and interconnects on a glass die with a bonded PDMS channel layer. A cross-section of the PDMS layer is displayed to reveal the semi-hemispherical channel over the resistors which is filled with a fluid.	77
Figure 4.2. Optical image of fabricated angular accelerometer with microtorus radius $R = 2.75 \text{ mm}$	78
Figure 4.3. Thermal angular acceleration sensor schematic with heaters (black) and thermal sensors response in red (increase in temperature) and blue (decrease in temperature) arranged along a torus experiencing (a) counter-clockwise structure rotation	

with maximal response from Wheatstone bridge; or (b) upwards linear acceleration with minimal response from Wheatstone bridge.	80
Fig. 4.4: Acceleration direction is dependent on the inertial frame of reference chosen.	82
Figure 4.5. Finite element method simulation of biomimetic angular accelerometer: (a) Simplified model with straight cylindrical channel and periodic boundary conditions for temperature and pressure at the end of the channel; (b) Full 3D model of the half-torus structure including glass substrate and PDMS cover.....	95
Figure 4.6. (a) Simulated temperature differential profile ($\Delta T = T(1000 \text{ deg/s}^2) - T(0 \text{ deg/s}^2)$) along the circumference of the microtorus for an anticlockwise angular acceleration to the structure of $1,000 \text{ deg/s}^2$. The applied body force is in the clockwise direction (corresponding to a counter-clockwise structure rotation). The scaled height of the profile correlates to ΔT in addition to the color coding. (b) Simulated temperature differential profile for different angular accelerations as a function of the distance from the heater center line.	97
Figure 4.7. Simulated temperature difference between the two temperature sensors as a function of the applied angular acceleration around the desired \hat{z} -axis and interfering \hat{x} and \hat{y} -axis for a bioinspired angular accelerometer with dimensions given in Table 4.1: (a) full microtorus structure; (b) horseshoe-shaped microtorus with 10° gap. The schematics show the rotation axis with respect to microtorus and heater locations (yellow).....	98
Figure 4.8. (a) Simulated normalized response of the angular accelerometer to an angular acceleration step input from 0 to $1,000 \text{ deg/s}^2$: (i) inertial response; (ii) thermal response; (iii) heater response. (b) The simulated effect of the distance of the temperature sensor from the heater on the thermal response of the angular accelerometer subject to the same angular acceleration step input from 0 to $1,000 \text{ deg/s}^2$	99
Figure 4.9. Simulated (a) sensitivity and (b) bandwidth of the sensor as function of the fluid used: silicone oil (5 cSt) or air.	101
Figure 4.10. Simulated (a) sensitivity and (b) the bandwidth of the sensor as function of the fluid used (Silicone Oil or Air) and the release of the structure.	102
Figure 4.11. (a) 3D-rendered model of bioinspired rotation sensor. The sensor consists of aluminum resistors for Joule heating and temperature sensing on a glass chip with a bonded PDMS channel layer. The PDMS layer is cut to show the semi-hemispherical channel cross sections of the torus over the resistors. The relevant dimension labels are marked on the structure. (b) Zoom-in on heater and temperature sensing resistors.	104
Figure 4.12. (a) Fabrication process of latest generation (capped device); (b) Optical image of fabricated angular accelerometer with microtorus radius $R = 2.75 \text{ mm}$	106
Figure 4.13. Contact angle between silicone oil and (a) glass (17°) and (b) oleophobic thin film (70°).	108
Figure 4.14. Wafer-level fabrication process of the thermal rotational accelerometer. .	109
Figure 4.15. Bubble-free liquid encapsulation process: silicone oil wetting on glass (a) without and (b) with patterned oleophobic thin film. (c) size scalability of the parylene-on-oil encapsulation process. The major radii are 3mm, 2.5mm, 2mm, and 1.5mm. The inner radius in all cases is 0.5 mm.	110
Figure 4.16. Optical image of encapsulated bio-inspired angular accelerometer with microtorus radius $R=2.85 \text{ mm}$. (b) 3D confocal laser microscope image of a channel with	

width of 1mm and height of 100m; the device was spray-coated with paint to make it opaque for the laser light.	111
Figure 4.17. Thermal characterization of aluminum heating resistors: (a) Electrical resistance as a function of temperature; (b) Average temperature rise as a function of heating power.	112
Figure 4.18. Thermal IR image of temperature elevation of approx. 10°C (based on calibrated image) of the aluminum thin-film heaters on glass substrate due to Joule heating with 10 mW applied power.	112
Figure 4.19. (a) Interfacing circuitry (amplification and filtering) for the sensor with the block diagram of the Wheatstone bridge circuitry overlaid over the sensor physical layout. The amplified and filtered output voltage of the Wheatstone bridge is output to an oscilloscope and connected to a lock-in amplifier; (b) a sample oscilloscope screenshot of the output of the circuit in yellow and a reference gyroscope shown in blue is shown for a 0.5 Hz sinusoidal angular acceleration with a peak angular acceleration of 1250 deg/s ² . The observed 90° phase shift is indicative of the commercial gyroscope output being proportional to the applied angular rate, while the biomimetic rotation sensor generates a signal proportional to the angular acceleration.	114
Figure 4.20. (a) Measured sensor output voltage as a function of the applied angular acceleration for rotations around three axes. (b) Measured sensor output voltage as a function of the applied angular acceleration around \hat{z} -axis and linear accelerations along the \hat{x} and \hat{y} -axis. The measurements were taken at a frequency of $f = 1$ Hz with a power of 20 mW applied to the heater. Linear accelerations are converted into effective angular accelerations using the microtorus major radius $R = 2.75\text{mm}$	116
Figure 4.21. Measured sensor output voltage at a frequency of $f = 1$ Hz as a function of the applied angular acceleration around \hat{z} -axis when the device is centered on the experimental setup and placed 2 cm away from the center.	117
Figure 4.22. Normalized sensor sensitivity to angular accelerations applied around the z -axis as a function of frequency, with crosses showing experimental results under harmonic excitation, squares showing simulated results under harmonic excitation and circles the transfer function obtained from the simulated response of the sensor to a step input.	118
Figure 4.23. Measured sensor output voltage as a function of the applied angular acceleration around \hat{z} -axis and linear accelerations along the \hat{x} and \hat{y} -axis for a sensor with horseshoe-shaped microtorus with a 10° gap. The measurements were taken at a frequency of $f = 1$ Hz with a power of 20 mW applied to the heater.	119
Figure 4.24. Amplified and low-pass filtered (1,000 Hz cut-off frequency) sensor (orange) and reference gyroscope (blue) signal for an applied square-wave angular acceleration of 1,250 deg/s ² at 0.5 Hz. The extracted sensor sensitivity is 320 $\mu\text{V}/\text{deg/s}^2$ with a noise level of approx. ± 10 mV, resulting in an estimated limit of detection of 30 deg/s ²	121
Figure 5.1 (top) (a) Distribution of the lateral line on the scales of fish. (b) Localization of the superficial neuromasts exposed to freestream flow and the canal neuromasts within small channels. (c) Zoomed-in illustration of the superficial neuromasts (SN). (d) Zoomed-in illustration of the canal neuromasts (CN). Image adapted from [259], [260]. (bottom) Concept of a magnetic hair cell, where the flexible permanent magnet mimics	

the hair cells, while the magnetic sensor mimics mechanoreceptors; adapted from [141].	
.....	124
Figure 5.2. (top) Schematic diagram of the magnetic probe stimulating a single hair bundle with magnetic nano particles attached. (bottom) Frequency spectrum response of bundle motions, entrained at 10,000 Hz. The inset shows the tracked bundle displacement. Image adapted from [134].	125
Figure 5.3. Different magnetic sensing technologies as adapted from [274], including (a) Hall effect, (b) anisotropic magnetoresistance (AMR), (c) giant magnetoresistance (GMR) or giant magnetoimpedance (GMI), and (d) tunneling magnetoresistance (TMR).	127
Figure 5.4a Magnetic sensor noise levels, adapted from [277] highlighted in dashed green line is typical lab noise levels. The noise level of our device at 1 Hz is marked with an x (bottom). Environmental noise levels are orders of magnitude higher than those of the TMR sensors. [279]. Environmental noise levels are orders of magnitude higher than those of the TMR sensors. [279].	128
Figure 5.5. 3D rendering of proposed design with fluid-filled half-torus of major radius R , and minor radius r , flexible magnetic pillar with height H and pillar radius r_p and magnetic sensor(s). The insert shows details of the magnetic hair cell.	129
Figure 5.6. (a) Working principle of sensing the fluid flow using flexible magnetic elastomer pillars: the viscous drag from the laminar fluid flow (arrows) deflects the magnetized flexible pillars causing an asymmetry in the magnetic flux density that can be sensed by strategically-placed magnetic sensors with two different hair cell configurations: upright vs. chandelier down; (b) Wheatstone half-bridge configuration.	131
Figure 5.7. Optical images of fabricated magnetic hair cell bundle: (a) a human hair is shown side-by-side with the magnetic hair cell for reference; (b) A ruler with a 1 mm spacing between two marks is shown with the magnetic hair cells for reference.	132
Figure 5.8. Three different potential cross-sections of the fabricated magnetic hair cells from left to right: rectangular, circular, crescent-shaped.	133
Figure 5.9. Design examples for Wheatstone bridge including four tunneling magnetoresistance sensors with respect to fluid channel and hair cell structure (circle). A clockwise fluid flow is applied causing a flexible magnetic pillar (circle) in the center to deflect. The deflection causes a shift in the magnetic field, thus the resistors will increase (green arrow) or decrease accordingly. The magnitude of change is indicated by the size of the arrow.	134
Figure 5.10. Different TMR-based Wheatstone bridge designs with (a) resistor distance from the hair cell increasing from left to right; and (b) number of resistors increasing from left to right.	136
Figure 5.11. 3D rendering of the magnetic finite element physics simulation. The screen capture details a naively-tilted hair cell by 5 degrees. The z-axis magnetized hair cell is suspended at the top of the with a 20 μm gap between the bottom of the hair cell and the sensors below it. The red arrows highlight the magnetic field lines, while the contour lines are iso-flux density, with the color legend showcasing the magnitude of the magnetic flux density on the surface of the magnet in mT.	139
Figure 5.12. 2D cross section of the center along the plane passing through line A-A' showcasing the pillar and the with the linear array of magnetic sensor locations. The contour lines show lines of equal magnetic flux density magnitude from 2-40 mT in	

increments of 2 mT; (a) zoom-in on the tip of the hair cell experiencing no deflection; (b) zoom-in on the tip of the hair cell experiencing 20 μm deflection at the tip with a silhouette of the pillar under no deflection; (c) an exaggerated illustration of the of the prescribed displacement of the hair cell, with the magnetization axis illustrated in the bottom left. The grid is in μm . The parametric equations describing the dashed line is used to extrude a circle into the desired hair cell shape.....	140
Figure 5.13. Differential signal of magnitude flux density magnitude along line A-A' for three different deflection values (5, 10, and 20 μm) relative to the no deflection case. .	141
Figure 5.14. Magnetic flux density magnitude in the sensitive x-direction as a function of z-axis magnetized cilia deflection for two symmetrically located sensors 50 μm away from the center of the centered hair cell, and the difference between the two signals. ..	142
Figure 5.15 The effect of misalignment along line A-A' on the differential magnetic flux density magnitude in the sensitive x-direction as a function of deflection for two symmetrically located sensors 50 μm away from the centered hair cell.	143
Figure 5.16 Differential signal of magnitude flux density magnitude along line A-A' for five symmetrical paired sensors 25, 50, 75, 100 and 125 μm away from the centered hair cell for: (a) z-axis magnetization; (b) x-axis magnetization.	144
Figure 5.17 Differential signal of magnitude flux density magnitude along line A-A' for five symmetrical paired sensors 25, 50, 75, 100 and 125 μm away from (left) an upright for z-axis magnetized centered hair cell (right) a z-axis magnetized centered chandelier hair cell as a function of deflection.	145
Figure 5.18. (left) 3D model used to characterize hair cell deflection as a function of flow velocity. In the channel, parabolic flow is induced with a maximum velocity of 2 $\mu\text{m/s}$; (inset) cross sectional view of the proposed hair cell design. Dimensions of hair cell are documented in table 5.2.	146
Figure 5.19. Maximum hair cell deflection as a function of flow velocity for a hair cell with dimensions according to table 5.2.....	148
Figure 5.20. Deflection of hair cell as a function of applied angular acceleration around the z-axis (red) and linear accelerations along the x-axis (grey) and the y-axis (blue). The applied linear accelerations are translated into effective angular accelerations using the major radius $R=2.75\text{mm}$	149
Figure 5.21. Transient FSI model: (a) Normalized transient step response of hair cell deflection and flow velocity for two different minor radius tori with the same size hair cell as table 5.2 (b) Magnitude-normalized frequency response of the maximum hair cell deflection to an angular acceleration of 100 deg/s^2 for two different minor radius tori with the same size hair cell as table 5.2.	150
Figure 5.22. Hair cell from CAD design file to fabricated device (a) Draw in CAD; (b)3D Print with Nanoscribe then conformally coat with 10 μm Parylene C; (c)Cast PDMS and peel off reverse mold, then conformally coat reverse mold with 10 μm Parylene C; (d) Cast PDMS with magnetic powder mixture and peel off. The pillars can be magnetized using an electromagnet during or post curing.	152
Figure 5.23. Fabrication Process of magnetic TMR sensor device. (black) silicon substrate (light blue) thermal silicon dioxide (yellow) metal (multi-color) magnetic stack (pink) spacer.....	152
Figure 5.24. Block diagram of the experimental setup and interface circuitry of the sensor.	154

Figure 5.25. Magnetic probe station with a controllable magnetic in the lab of Dr. Kosel's lab at King Abdullah University of Science and Technology (KAUST).	155
Figure 5.26. TMR Magnetic Field Sensitivity: Resistance response of the TMR sensor array with an external magnetic field applied to the X (parallel to easy axis) and Y (perpendicular to easy axis) directions.	156
Figure 5.27. In-house TMR resistance drift over time (a) over 24-hour period (3) zoom-in on 3-hour period. (c) Different device showing improved stability over 20 hours with and without a DC magnetic bias after deposition process improvement. Note the higher resistance. Data collected by Altynay Kaidarova at KAUST.	157
Figure 5.28. In-house TMR resistance stability as a function of current (a) resistance fluctuation; (b) standard deviation (SD) and standard error (SE) of measured resistance (c) Allan Deviation as a function of averaging time with slopes of each regime indicated. Data collected by Altynay Kaidarova at KAUST.	158
Figure 5.29. Commercial TMR2901 signal output as a function of the applied magnetic field in the sensitive direction with a +3V bridge bias.	159
Figure 5.30. Magnetic moment as a function of applied field for a magnetic elastomeric hair cell collected using a vibrating sample magnetometer. The hair cell volume used is $6.3 \cdot 10^{-10} \text{ m}^3$, thus the magnetization is 62.4 kA/m, which is about half the assumption used in our initial simulations.	160
Figure 5.31. Analog front end used to control the large common-mode interference from the Earth's magnetic field, and other large sources of magnetic interference. The top Wheatstone bridge is used as a reference sensor. The bottom Wheatstone bridge is used as sensor with a hair cell manipulated in its vicinity as shown in the small inset. (inset) Arm of a linear positioning stage with a magnetic hair cell attached to the tip and placed above the magnetic sensor.	162
Figure 5.32. Hair cell displacement sensitivity characterization for commercial TMR magnetic sensor with a z-axis magnetized hair cell suspended above it following the possible paths indicated by the color lines overlaying the top view of the magnetic sensor package. The upwards direction indicated by the black arrow is the sensitive direction for the magnetic sensor.	163
Figure 5.33. Sensor signals (green and black) and differential signal (red) stemming from manual rotation of the test setup at approx. 0.8 Hz, demonstrating the rejection of the common-mode signal in the differential setup.	165
Figure 5.34. Sensor signals and differential signal stemming from vibration of the test setup, demonstrating the rejection of signal drifts in the differential signal and the detection of hair cell movement by the TMR aligned with the hair cell.	166
Figure 5.35. Sensor signals and differential signal stemming from manual rotation of the test setup and vibration of the hair cell, again demonstrating the rejection of the common-mode signal in the differential setup: (a) Experimental setup (b) common-mode signal rejection (c) zoom-in (d) control experiment without the hair cell.	167
Figure 5.36. Energy transduction in bioinspired magnetic rotation sensor, and their respective sources within the system.	169

SUMMARY

The human vestibular system maintains visual acuity and stabilizes posture and gait. Failure in the vestibular system can lead to debilitating symptoms of vertigo, disequilibrium, and imbalance. Some patients suffering from vestibular dysfunction in both inner ears (bilateral), there is currently no effective therapy. For individuals suffering from bilateral vestibular dysfunction an emerging option may be a vestibular prosthesis. A significant obstacle hindering progress of vestibular prostheses is the power consumed by angular rotation sensors (gyroscopes). Commercial gyroscopes are actively driven thus consume power continuously. In contrast, the mammalian vestibular system uses the motion of the body to power the sensor. This passive approach paired with a low power transduction mechanism could be a sensing solution for vestibular implants. Nature has developed efficient and simple sensors, actuators and mechanisms that allow for high performance with limited resources. These advantages inspired engineers and designers to base their designs on these natural structures. In this work, a micromachined sensor platform inspired by the semicircular canal in mammalian vestibular systems is developed using two transduction mechanisms (thermal and magnetic). The platform demonstrates two orders of magnitude suppression of cross-axis angular accelerations and inherent insensitivity of the sensor to linear accelerations from its geometrical constraints. The thermal design validates and verifies the potential of the toroidal platform as a rotational inertial sensing system with a resolution around 30 deg/s^2 and a dynamic range of $2,000 \text{ deg/s}^2$.

CHAPTER 1. INTRODUCTION

Humans possess incredible sensory systems that take input stimuli from their surrounding environments. These well-developed sensory systems are not limited to the traditional five senses: touch, smell, sight, hearing, and taste. Other sensory inputs combine to create a “sixth sense.” These include proprioception –the ability to sense the relative position and forces acting on parts of the body–, and the sense of balance. All these sensory systems process stimuli by transducing the input energies into a series of electrical spikes. The information is sent along the nervous systems to the appropriate regions of the brain to further process the information.

Diseases, trauma as well as environmental and genetic factors can lead to complete sensory loss. These debilitating conditions and disorders come as a result of loss of the sensory organ’s ability to process the necessary incoming stimuli. Currently in the United States, 94% of older adults suffer from at least one form of sensory loss or impairment (blindness, deafness, balance-loss, or others) [1]. Fortunately, mammalian brains are neuroplastic, i.e. have the ability of lasting change to the brain throughout the entirety of the person’s life [2]. This amazing ability helped neurosurgeons restore hearing to thousands of deaf people using cochlear implants in the 1980s [3]. Cochlear implants send electrical pulses encoding microphone signals to the auditory nerve. The success of cochlear implants has led to other attempts to restore lost senses. Recently, visual implants have been approved by the Food and Drug Administration (FDA) in the United States to restore limited vision to those with retinitis pigmentosa [4]. Over the past two decades,

attempts have been made to create vestibular implants for patients with bilateral balance loss. The following section will motivate the work in this thesis in more detail.

1.1 Motivation

1.1.1 Vestibular Disorders and Current Therapies

The human vestibular system maintains visual acuity and stabilizes posture and gait. Failure in the vestibular system can lead to debilitating symptoms of vertigo, disequilibrium, and imbalance [5]. A clinical survey reported that more than 35% of Americans above the age of 40 have a vestibular dysfunction [6]. Bilateral vestibular deficit considerably impacts the elderly. Above the age of 80, only 50% of a person's vestibular neurons remain [7]. Vestibular dysfunction often leads to falls, the leading cause of fatal and non-fatal injuries for persons age > 65 years [8]. One survey reports that in 31% of the patients with falls of unknown cause, symptoms of vestibular dysfunction were found [9].

Vestibular disorders can be classified as episodic, chronic, or acute [10]. The most common amongst the episodic is Mènière's Disease. It occurs in about 200 per 100,000 persons in the United States [11]. Chronic cases are progressive in nature and typically bilateral, i.e. in both inner ears. Episodic cases are abrupt and recurring. Patients with acute conditions report severe vertigo and nausea due to permanent damage to the vestibular system. Both chronic and acute conditions can cause deficiency in both inner ears. Loss of balance in both inner ears is called Bilateral Vestibular Deficit (BVD). It is estimated that 500,000 patients suffer from a complete bilateral vestibular deficit (BVD) in Europe and the United States [12]. Bilateral Vestibular Deficit occurs in about 7% of patients experiencing

dizziness [13]. Bilateral dysfunction of the vestibular system may lead to blurred vision, dizziness, an inability to orient oneself correctly, or decreased ability to walk.

One of the most common causes for balance sensory loss is a side-effect of prescription of life-saving antibiotics such as Gentamicin [14]–[16]. The medication kills the sensory hair cells in the inner ears responsible for sensing head motion. Although it is difficult to estimate the impact of ototoxicity on vestibular function, 5-10% of patients treated with Gentamicin report cochlear toxicity [17]. It is estimated that 10-20% of these patients exhibit some degree of vestibular ototoxicity as well [18]. A variety of other causes may lead to bilateral loss of vestibular sensation, including infections such as Meningitis, trauma to the inner ear, bilateral ear surgery, congenital disorders leading to deafness, and disorders of the immune system [13]. Also, vestibular loss can be a side effect of cochlear implantation. Studies estimate that 7% of candidates for cochlear implantation (CI) and 10% of CI recipients exhibit extreme bilateral vestibular dysfunction [19]. There are over 600,000 CI recipients worldwide [20], [21].

Existing solutions to treat vestibular disorders mostly consist of physical therapy. Vestibular rehabilitation therapy can restore function and decrease symptoms for unilateral and minor cases of bilateral vestibular dysfunction. Those who experience severe bilateral dysfunction have limited therapeutic options [12], [22], [23], but other technical therapeutic alternatives are being explored. A potential breakthrough to resolve the underlying cause of vestibular disorders is regenerating the damaged hair cells in the vestibular system in animal models [24], [25] However, there have been no human studies conducted as of early 2018 on human vestibular hair cell regeneration using gene therapy.

Different sensory substitution strategies are being explored by using an external wearable balance system. This includes vibrotactile displays [26]–[28], audio feedback [29] and electrotactile tongue activation [30]–[32]. These solutions tend to improve posture, but cannot emulate vestibular function. Also, they cannot restore the vestibulo-ocular reflex (VOR), which keeps vision from becoming blurry during motion [33]. VOR is a reflex movement that compensates for head motion allowing for stable images on the retina.

The leading therapeutic option for severe bilateral vestibular loss is a vestibular implant or prosthesis. It follows thirty years of cochlear implant success in restoring hearing to deaf patients. The vestibular prosthesis substitutes for unresponsive balance organs in the inner ear [34]–[37]. Although the implant is in early stages of its development, it is showing promising results. In the next section, a description of a vestibular prostheses is given and the challenges facing current state-of-the-art vestibular prostheses are discussed in more detail.

1.1.2 Vestibular Prostheses

Vestibular prostheses (VP) are designed to replace the functions of the peripheral vestibular organs. Using three implantable rotation sensors, patterned electrical stimulation is provided to the vestibular nerve conveying information on the rotation of the head.

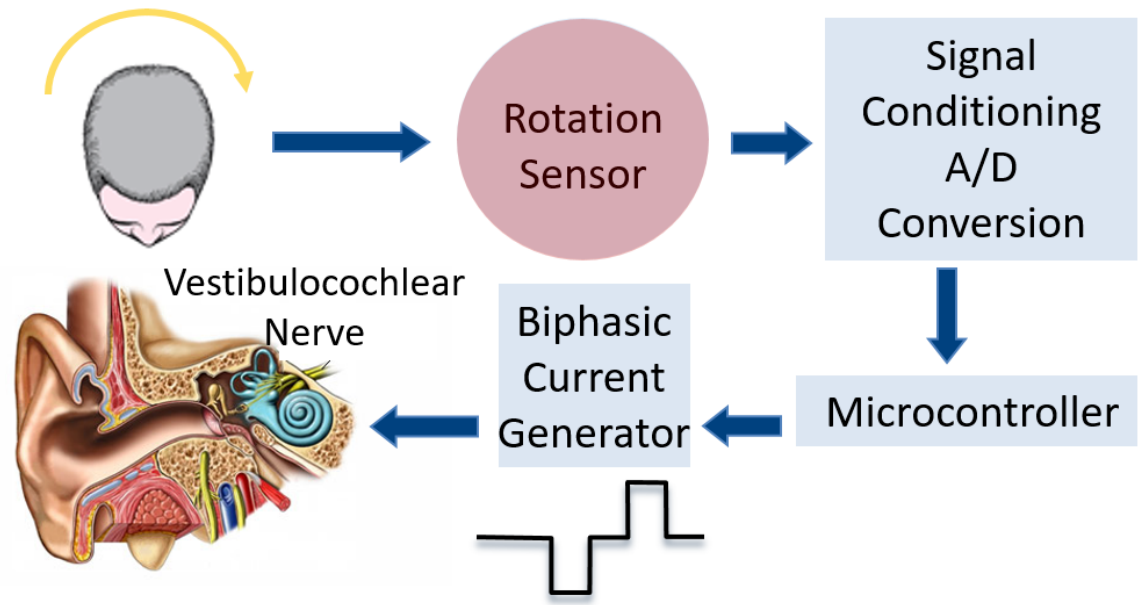
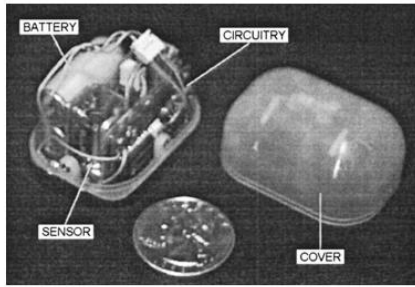


Figure 1.1 - General schematic of operation for a generic vestibular prosthesis, adopted from [38].

The most common version of the VP has external (wearable) and internal (implanted) components. The external components include motion sensors fixed on the patient's head, and a processor converting the signal into a pattern of electrical signals. The internal components consist of electrodes implanted in the vicinity of the vestibular nerve branches. The less common version is a fully implantable VP. Users of the extracorporeal version turn off stimulation during sleep and while taking showers. Current studies have shown that the prostheses can quickly restore clear vision just minutes after turning the stimulation on, or off [12]. This affords the patient the flexibility of choosing when to use stimulation.

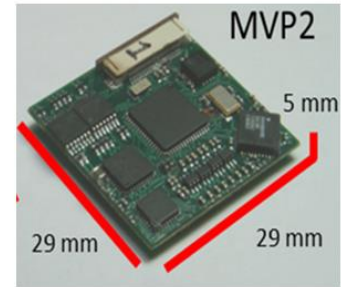
Figure 1.1 describes the basic components and the basic operation of the VP. A comparison between the biological vestibular system and the VP is shown in figure 1.2.



Gong, Merfeld (2000)



Phillips (2010)



Santina (2011)

Figure 1.2 - Three different embodiments of vestibular prostheses , from left to right are adopted from [35], [36], [39].

In the early 1960s, Cohen and Suzuki showed that it was possible to elicit vestibular responses using electrical stimulation of the vestibular apparatus in cats and monkeys [40], [41]. These early attempts lead to the idea of developing a vestibular implant almost 40 years later [36]. Gong and Merfeld [36], [37] demonstrated the first vestibular prosthesis prototype in animal models. The externally head-mounted system only aimed to replace a single axis of rotation on a single side as opposed to a more complex bilateral approach. Angular rotation in the horizontal plane was sensed with a gyroscope. The signal was amplified, filtered, digitized and directed to a microcontroller. The microcontroller sent a signal to the current amplifier that connected to a single implanted electrode. Charge-balanced, biphasic current pulses activated the horizontal vestibular nerve endings. Success was measured by observing the restoration of the vestibulo-ocular reflex. The results were quite promising and illustrated the viability of a unilateral solution in mammals. Della Santina et al. [42] improved upon this work and developed the first 3D vestibular prosthesis prototype using three gyroscopes. The results indicated the ability to restore the vestibulo-ocular reflex for all three axes in rhesus monkeys.

The previous success and regulatory approval of cochlear prostheses by the Food and Drug Administration (FDA) has allowed for the quick adoption of the use of cochlear implants as testbeds for vestibular implants in human clinical trials. This has been achieved by connecting the stimulation electrodes to the vestibular instead of the auditory nerve [21]. The first human experiments demonstrated the feasibility of the solution in one axis [43]. The research and development of a vestibular prosthetic for human use is ongoing [44]–[46]. Progress includes restoring the vestibular-ocular reflex in all three axes [44], thus replicating the success in the rhesus monkey model mentioned earlier [42].

The experiences to date in animals and humans are limited to the restoration of the function the semicircular canals. Limited attempts have been made to restore the otolithic function, which is responsible for sensing linear motion [47], [48]. This could be attributed to the ease of quantifying the vestibulo-ocular reflex. There have been several successful attempts at restoring postural stabilization by electrical and galvanic stimulation [33], [49].

One of the current obstacles facing vestibular prostheses is the size of the implant housing. Similar to cochlear implants, vestibular implants are placed in the mastoid cavity behind the ear and consume a space of 25 x 25 x 10 mm with the thickness being the limiting factor (10 mm). The unilateral vestibular prototype [36] was contained in a 43 x 31 x 25 mm plastic case, and the 3D prototype [42] in a 35 x 35 x 15 mm plastic case. In the first human study, a cochlear implant by Med-EL was used [44]. Its dimensions were 29 x 46 x 6 mm.

Another obstacle for vestibular prostheses is power consumption. The largest portion of the power consumption in the system is due to the required stimulation current for the nerve endings [50]. Based on studying the power requirements of cochlear prostheses, fully implantable solutions have a strict power budget of 1 mW. This low-power requirement assumes 12 hours of operation per day, with the implant using a 5 g ultra-capacitor (energy density of 5 watt-hr/kg), and a 50% efficiency of the power circuit [51]. Current electrical storage (batteries and/or ultra-capacitors) have a lifetime of 500-1000 charge and discharge cycles. For a fully implantable system that would require an outpatient procedure to replace the battery every roughly 1000 charge/discharge cycles [52]. On the other hand, the prosthesis with a behind-the-ear unit has a power budget of 10s of milliwatts [50], [53]. This system does not require an outpatient procedure to replace the battery.

Some researchers have estimated that the natural sensing mechanism of the inner ear in the cochlea requires just 2-14 μW of power [54]. Based on these estimates and the number of haircells in the vestibular system [55], I have estimated the power consumption for the three semicircular canals in one ear to be roughly 10-70 μW .

Future fully implantable vestibular systems would need at least 500-750 μW to fully power its operation [51], [52], [56]. Inertial sensors of vestibular prostheses require a larger power budget than microphones in cochlear implants. The aim is to use approximately 250-500 μW in fully implantable systems for sensing purposes. However, some of the current commercial always-on gyroscopes dissipate about 1600 μW [57], which is more than the total power budget of the fully implantable vestibular prosthesis and roughly 20% of the behind-the-ear solution. On the other hand, state-of-the-art near-

zero-power three-axis accelerometers consume anywhere between 5-25 μ W [58]. Despite the strict power requirement goals for future fully implantable solutions, current researchers have built vestibular prostheses that use sensors that consume orders of magnitude more power. For instance, the uniaxial implant consumed nearly 30 mW per sensor [36], and the 3D device consumed 25 mW in total [42]. In [44], the three axis gyroscope consumed 32.4 mW.

In summary, **while past efforts towards a vestibular prosthesis have validated the ability of the VP to sufficiently activate central mechanisms relying on vestibular function, particularly power consumption requirements limit the possibility of especially fully implantable VP. Thus, the main effort of this research is to mimic the mammalian vestibular system to design low-power angular acceleration sensors.** In the next section, we review currently available solutions for low-power inertial sensing to use in vestibular prostheses.

1.2 Background

1.2.1 Miniaturized Inertial Sensors

Over the past few decades, micromachining has enabled the rapid miniaturization of inertial sensors. This has allowed the explosion of their use in various applications, including automotive, consumer, and medical applications [59]. The current generation of inertial sensors meet the needs of consumer applications, while continuing the push into meeting the needs of industrial, medical, and military applications [60]. In sensing rotation, there are two types of sensors. Gyroscopes are more commonly used and sense angular rate of rotation in deg/s or rad/s. The less widely adopted method senses angular acceleration

directly in deg/s^2 or rad/s^2 . In the following sections, a brief overview of each sensing mechanism is discussed along with its opportunities and drawbacks.

1.2.2 Gyroscopes

1.2.2.1 Solid Mass-based Gyroscopes

The main sensing principle of rotation is utilizing the Coriolis force [59]. The Coriolis force is a fictitious force acting on a moving mass in a rotating system. The most common approach to sensing this force is through a driven vibrating mass [61]. Coriolis force based gyroscopes provide high sensitivity, good power consumption, good cross-axis insensitivity and good stability [59]. The relatively few drawbacks of current state-of-the-art gyroscopes become visible in areas of medical implants and high-shock resistant industrial applications. Medical implants, specifically vestibular prostheses, aim to function continuously for ten years on limited battery power [62]. Commercial gyroscopes have been integrated with vestibular implants [34]. In those implants, gyroscopes proved to consume a third of the power budget [63]. By reducing the sensor's power consumption, the vestibular implants' lifetime could be significantly extended. Another possible drawback of current gyroscopes is the vulnerability of these vibratory mass gyroscopes to microcracks under continuous extended use operation causing fatigue and drift [64]. Also, they are susceptible to failure from high-impact shocks and operation in harsh environments [65]. However, there are recent advancements that provide excellent linear acceleration rejection or shock resistance [66]. In general, solid-state silicon-based gyroscopes must be considered the gold standard for micromachined rotation sensors today in terms of miniaturization, stability, sensitivity, linear acceleration rejection and power

consumption. However, this does not mean that other potential platforms for micromachined inertial rotational sensors should not be investigated, especially if they are based on simple, scalable fabrication processes.

Other approaches include piezoelectric vibrating gyroscopes [67] and surface/bulk acoustic wave gyroscopes [68], which comprise no moving parts. Also, electrostatic [69] and magnetic [70] suspended gyroscopes have been developed. Due to their poor performance compared to vibrating mass gyroscopes, these other approaches are not covered in this overview. Other sensing principles include optical transduction [71], exhibiting excellent sensitivity, and stability performance while suffering from high cost, and poor integration necessary to match the performance of kilometers of optical fibers used in interferometric fiber optic gyroscopes [72]. The micro optical gyroscopes are based on Sagnac effect. Other principles such as the precession principle, or nuclear magnetic resonance are not mature enough to include in the scope of this literature review.

1.2.2.2 Fluidic Mass-based Gyroscopes

To increase robustness for withstanding high shock and harsh environments, fluidic masses were proposed to replace solid masses. This approach removes the vulnerable mass tethers. This approach has been proven successful in sensing linear acceleration using the buoyancy effects and forced convection mechanisms [75] (see figure 1.3). Thermal fluidic mass gyroscopes were proposed in the past two decades, but have not matched the performance of solid mass designs [76]. In sensing rotation with a fluidic mass, an analogous approach to vibrating a solid mass is the jetting of a gas or a liquid to enhance the sensitivity. Jetted steam as a driving mechanism was studied by many groups [77]–[79]. However, these

piezoelectric pump-driven solutions are bulky, power inefficient, and have poor cross-axis insensitivity. Other methods to drive the fluid such as buoyancy, and thermal expansion report sensing with relatively high-power consumption and are suited for applications in industrial applications [80], [81]

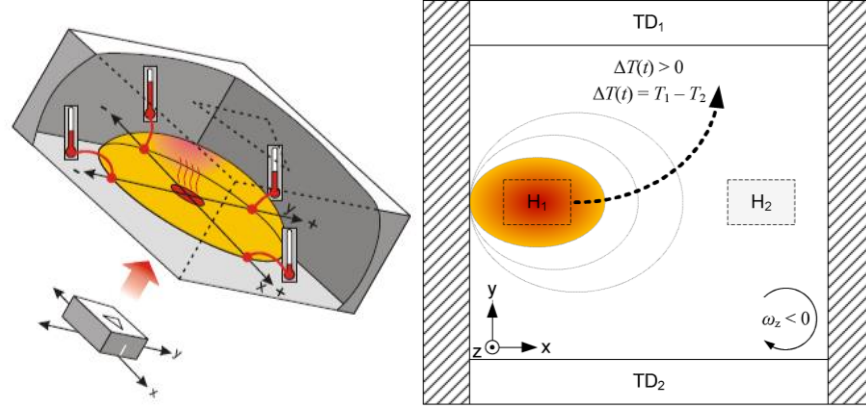


Figure 1.3 - Diagram of thermal linear accelerometer by MEMSIC [73], and a thermal fluidic gyroscope working principle by [74].

. However, both those designs suffer from low sensitivity, and heater-induced signal interference. Finally, Leung utilized bidirectional fluid flow to actively reject the interfering linear acceleration signal [82].

Table 1.1 summarizes state-of-the-art suspended solid mass and fluidic-based gyroscopes.

Table 1.1 - Comparison of state-of-the-art single-axis solid and fluidic gyroscope

Ref.	Technology	Sen. [mV/deg/s]	Freq [Hz]	P. [mW]	Range [rad/s]	Size[mm ²]
[78]	Jetted	0.005	-	300	± 25	324
[83]	Buoyancy	0.02	-	14	± 10	2
[74]	Expansion	1.134	20	20	± 22.5	9
[66]	BAW	0.8	-	-	± 22.5	< 1

1.2.3 Angular Accelerometers

By extending linear acceleration principles to the rotational domain, there lies an opportunity to push the limits of low-power rotational sensing. An alternative to gyroscopes is using angular accelerometers to sense rotational inertial inputs [84]. This potentially could decrease the power consumed by using a non-driven transduction mechanism. In the majority of applications, angular position or angular velocity is the desired output, thus leading to a slow rate of adoption of angular accelerometers [84], because their output needs to be integrated once or twice to obtain angular velocity or angle information, respectively, introducing unwanted errors with each integration [85]. However, their strength comes when the angular acceleration needs to be known directly, including delay-sensitive and real-time applications such as rotating hard disks. Sensing angular acceleration does not need active driving of the structure, as the sensors mass experiences acceleration by the forces applied to the structure. Also, in feedback control applications in industrial settings direct measurement of angular acceleration is advantageous as using angular rate sensors can add noise by differentiation which is noise amplifying [86]. Moreover, applications for angular accelerometers include vehicle and ship stabilization, seismometry, missiles and satellites and stabilizing gyro platforms [87], [88]. However, gyroscopes have widely been adopted for these uses as well.

1.2.3.1 Indirect Solid Mass-based Angular Accelerometers

One method to measure angular acceleration is knowing the distance from the axis of rotation and using linear accelerometers. One example used piezoresistive transduction to measure angular acceleration using multiple linear sensors [89]. The other method is to

combine angular rate measurement and linear acceleration to measure angular acceleration indirectly. This could be done by differentiation with filtering or using Kalman filters as described in [84]. However, these methods are susceptible to noise and inaccuracies.

1.2.3.2 Direct Solid Mass-based Angular Accelerometers

The earliest attempts of sensing angular acceleration directly using microfabricated devices date back to 1995. The first microfabricated capacitive angular accelerometer using a tethered solid mass was presented by Brosnihan et al. [90], with a similar device investigated by O'Brien et al. [91] and Gola [85]. Recently, Jeong [92] presented a capacitive dual-axis design with improved sensitivity and lower power consumption using the HARPSS fabrication process. Others strategically placed piezoresistors on a tethered proof mass to sense angular acceleration using piezoresistive transduction [93]–[95]. Both these transduction mechanisms offer small footprint, low power operation, but the solid masses are still susceptible to shock [65].

Table 1.2 - Comparison of state-of-the-art micromachined angular accelerometer performance.

Ref.	Sen.[$\mu\text{V}/\text{rad}/\text{s}^2$]	Freq [Hz]	P. [mW]	Range[rad/s^2]	Size[mm^2]
[92]	146	5200	0.3	± 4000	1.12
[85]	1000	800	-	± 350	9.5
[91]	6000	250	13	± 200	2.25
[90]	520	500	50	300-3000	0.25

Other approaches to directly measure angular acceleration include using eddy currents [96], optical encoders [97], an amorphous wire [98], and piezoelectric transducers [99],

[100]. Due to their large size or high-power consumption, these methods were not included in this review.

1.2.4 Fluid Mass-based Angular Accelerometers

Similar to fluid-based gyroscopes, researchers attempted to replace the solid mass with a fluid. One common and commercial example is the fluidic rotor angular accelerometer [101], which is incorporated in products by Endevco, Jewel and Columbia. These sensors are common in military, industrial and vehicular applications [102]. They show excellent sensitivity, good dynamic range, decent linearity, and good cross-axis rejection. However, they suffer from large size and high power consumption. The most common fluidic angular accelerometers are toroidal in shape and their design is based on the semicircular canal and are further discussed below. Other fluid based angular accelerometers have been proposed using metallic droplets [103], [104], but have not been implemented.

In the next section, we review bio-inspired rotational and fluid flow sensors to meet our need for a low-power vestibular prosthesis.

1.2.5 Bio-inspired Sensors and Devices

Nature takes advantage of physical effects from the macroscale to the nanoscale [105]. By taking full advantage of these effects, sensory systems of the creatures of the animal kingdom are nearly physics-limited. The visual system is at the one photon level [106]. The auditory system and wind cricket hair cells are nearing thermal noise limitations [107], [108]. For the vestibular system (see chapter 2 for more in depth information on the vestibular system), nature -through natural selection has evolved over thousands of years a

power-efficient, elegant sensor design to sense rotational movement, and inherently reject linear motion [109], [110]. The semicircular canals (SCCs) have been claimed to have reached a near-optimal design [111]. The size of the organ spans only one order of magnitude while the mass of animals spans seven orders of magnitude [5]. Such little variability points in the direction of converging to a local optimal design.

For many years, researchers have studied the elegance and simplicity of nature's sensors. Recent advancements in technologies have allowed scientists to unleash the power of scaling laws to mimic at the micro and nano-scale [105]. This includes the gecko's ability to climb and scale walls [112], the hydrophobicity of lotus leaves [113], and the sub-nanometer sensitivity of haircells [114]. In the following section, bio-inspired design is reviewed as an approach for rotation sensing (based on the passive microtorus platform) and fluid flow sensing (based on haircell-based transducers).

1.2.5.1 Bio-inspired Rotation Sensors

In nature, the fly's haltere structures are shaped like a club and beat opposite to its wings. This driven structure functions as vibratory gyroscope [115]. Researchers have shown that the sensor is not sensitive to low angular rates [116], and, thus, do not meet our vestibular requirements.

Seeking an alternative approach to sense rotation, researchers took inspiration from the semicircular canals (SCC) in the inner ear (refer to chapter 2 for more details on the SCC). Arms et al. [117] was the first to propose using a micromachined pressure sensor to sense the flow in a toroidal channel. Ploechinger [118] proposed to use thermal convection to measure the fluid velocity and correlating it to the angular acceleration, but no device was

implemented for either of those designs. Wolfaardt [119] proposed an improvement on the SCC by changing the torus into a helix to enhance the pressure differential. A macroscale device was tested and a microscale version was proposed with an extensive fabrication process involving bonding dozens of wafers together to form the helix. Moreover, highly-compliant biomimetic capacitive microfabricated electrodes were proposed and simulated and simulated by Bhatti et al. [62], [63], but not tested experimentally.

To use the SCC as an inspiration in designing a rotational sensor, a few obstacles stand in the way of mimicking the performance of the original design. First, the gelatinous membrane inside the SCC has a stiffness of roughly 1-5 Pa [120], [121]. Also, the hair cells measuring the membrane deflection must be embedded in the membrane. Based on current microfabrication techniques and materials, the required aspect ratio for the bio-mimetic membrane would be around 1000:1 to have the same order of magnitude deflections and the same order of magnitude of dynamic performance. Stiffer materials require thinner membranes to emulate or mimic the performance of the soft (1-5 Pa) cupula.

The first to successfully overcome some of these design challenges was Andreou et al. [64] by replacing the vertical membrane with horizontal, suspended piezoresistive cantilevers between two layers of half tori. Such a planar design was independently proposed a few months earlier by Alrowais et al. [122], but not experimentally verified. The reported device boasts low power consumption, but the suspended cantilevers are still susceptible to shock.

Others replaced the membrane with other mechanisms to sense flow. Molecular electric transducers reported good frequency characteristics, high sensitivity, but suffer from large

size and small dynamic range [123]. Recently, a Lorentz force-based magnetic approach to sense fluid rotation in a 3D printed channel was proposed [124]. However, the sensor is limited in the range to above 1500 rad/s², with poor linearity in its operating range and a low cut-off frequency. Another approach extends thermal linear accelerometer principles to rotational ones. The first successful microfabricated thermal bioinspired design was developed by Groenesteijn et al. [125]. The design relied on a complex fabrication process and a lock-in amplifier to sense the output. The authors did not present the frequency behavior or the cross axis-sensitivity of the sensor.

Table 1.3 summarizes the performance of select bio-inspired angular accelerometers.

Table 1.3 - Comparison of state-of-the-art bio-inspired angular accelerometer performance.

Ref.	Sen.[$\mu\text{V}/\text{rad}/\text{s}^2$]	Freq [Hz]	P. [mW]	Range [rad/s ²]	Size[mm ²]
[64]	2500	300	0.3	± 10	36
[123]	30	-	15	875-3500	25
[122]	2.5	-	-	2000-6000	900
[121]	500	50	80	± 450	2500
[124]	1700	<1	20	± 200	64

1.2.5.2 Bio-inspired Flow Sensors

As potential sensors in bio-inspired angular accelerometers, micromachined fluid flow sensors are reviewed in the following. MEMS-based flow sensors are based on thermal principles [126], pressure differential [127], and Coriolis force [128]. Thereby, thermal and Coriolis-based flow sensors present the highest sensitivities. The thermal-based approaches

are widely adopted due to their simplicity, lack of moving parts, high dynamic range, and high sensitivity. However, this approach is power-inefficient [129].

Another approach aims to mimic the design and structure of hair cells and the cupula to sense fluid flow, similar to the semicircular canals. Thereby, the hair cell is exposed to the flow by itself or embedded in a gelatinous membrane mimicking the cupula. Work by Tsukruk et al. [130]–[132] have indicated that embedding the hair cell in a gelatinous membrane can improve sensitivity at low flow by an order of magnitude.

Hair cells are nature's mechano-electrical transducers, consisting of a long pillar/rod that is connected to stress-sensitive sensors at its base. The sensors are responsive to stress caused by the deflection of the long pillars. Originally, the hair cells were thought to open calcium ion channels which turn into electrical signal. However, a recent study has shown that is not the correct hypothesis [133]. Other mechanisms have been proposed but not been proven [134]. The hair cells deflection can occur by a pressure differential across a membrane as in the vestibular system, or physical deflection such as in whiskers, or even work as flow sensors such as in the case of fish or as a microphone in the inner ear [114].

Researchers' fascination with hair cells have led to development of many sensors including but not limited to fluid flow sensors [135], gyroscopes [115], and microphones [136]. The bio-inspired hair-cell-based flow sensors have used thermal [137], piezoresistive [138], [139], capacitive [140], magnetic [141], and optical [142] transduction mechanisms. Piezoresistive and capacitive approaches are the most common. These structures boast high sensitivity and accuracy, due to their high aspect ratio. However, they are unable to sense low-flow conditions, similar to those found in the semicircular canals [114]. Recent

work by Triantafyllou et al. [143] takes advantage of the passive nature of piezoelectric material to achieve near-zero-power transduction. Table 1.4 below compares the different potential transduction mechanisms.

Table 1.4 - Comparison of different potential transduction mechanisms for flow sensing

Transduction mechanism.	Bandwidth	Power	Ease of Fabrication	Noise	Sensitivity
Capacitive	+	+	+	-	+
Thermal	--	-	+	+	++
Magnetic	+	+	-	--	+
Piezoresistive	+	+	-	+	-
Piezoelectric	+	++	+	+	+

Future work needs to push the limit of detection towards the nL/s range as theoretically predicted for some hair cells [144] to meet the threshold of detection in human head rotation.

1.2.6 State-of-the-Art in Vestibular Prosthesis-Specific Rotation Sensors

In this section, rotational inertial sensors that were designed specifically for vestibular prostheses are discussed and analyzed.

The first to design a VP-specific rotation sensor was Shkel [145]. The solution was a vibratory gyroscope. However, it did not prove to be power efficient. After that, Hayden and Challa tried to use differentially coupled linear accelerometers to emulate the gyroscopes [146], [147]. Although the power consumption was reduced, the device did not operate at frequencies below 1Hz, which are necessary for self-guided movement. Bhatti and Toreyin

proposed a bio-inspired sensor based on the semicircular canal [62], [63], but no physical device was produced.

The first viable solution presented was a modified design based on the semicircular canal by Andreou [64], [65]. The solution features an excellent power consumption of $300\mu\text{W}$ per axis. However, no study has been presented on its total frequency response or cross-axis sensitivity. The next VP-specific solution used a thermal principle in a SCC-based toroidal microchannel [125]. The solution seemed promising but was not tested at low rotational accelerations. Also, the solution consumed 15 mW per axis.

Two recent implementations are inching closer to meeting the requirements of the vestibular prosthesis. Jeong presented a dual-axis solid-mass-based angular accelerometer [92]. The solution offers low power operation at $296\text{ }\mu\text{W}$. However, the sensitivity threshold of 0.5 deg/s^2 was not met as the noise of the system was one order of magnitude higher. The other solution by Dellea [148] presented a three-axis piezoresistive gyroscope with power consumption of $980\text{ }\mu\text{W}$, with a noise level of 0.2 deg/s . This solution is a step in the right direction, but requires further study of the cross-axis sensitivity rejection and susceptibility to shock. Most of the dedicated solutions compare well with current low-power three-axis gyroscopes on the market as described earlier which have power consumptions around 1.5 mW .

1.3 Research Objective

The objective of this research is to explore the natural design of the semicircular canals as a platform for rotational inertial sensing. The main application considered here for these sensors is sensory substitution in vestibular prostheses for patients with bilateral vestibular

loss, however other application areas are possible. The objective will be achieved by improved, simple fabrication process, and developing low-power, and shock resistant transduction mechanisms. With mammalian inertial sensors in mind, the sensor's target specifications include a power consumption on the order of 100 μW to 1 mW, a dynamic range of 0-10,000 deg/s^2 , a frequency bandwidth of 20 Hz, low cross-axis sensitivity, fitting well within a human implantation footprint, and a low limit of detection of 1-2 deg/s^2 .

- To meet the goals set forth in the research, the following specific objectives are targeted:
- Developing a simple fluid-filled bio-inspired micro-fabricated platform to enable sensing rotation using different potential transduction mechanisms with a simple analytical and numerical model to describe its behavior.
- Developing a robust, yet power hungry proof-of-concept thermal transduction mechanism to sense rotation based on the bio-inspired platform.
- Integrating a low-power bio-inspired magnetic hair-cell transducer for the proposed sensor.

1.4 Thesis Outline

To address these research objectives, this thesis is outlined in the following manner:

Chapter 2 provides an introduction into the mammalian vestibular system. It covers the morphology and the structure of the semicircular canals in particular. The SCC is analyzed as a sensor and evaluated as a potential platform for an inertial sensing system.

Chapter 3 introduces the proposed micromachined toroidal platform. An analysis of different possible configurations of the micro-toroidal platform is discussed. This is followed by a brief discussion of a lumped-element analytical model of a simplified microtorus structure. The analytical model is validated by a numerical finite-element model of the structure. This numerical model is used for a parametric scaling study of the key geometric and material factors affecting the performance of the structure.

Chapter 4 presents the thermal-based bio-inspired angular accelerometer. This chapter starts off with the working principle of the sensor. An analytical model for its behavior is investigated, followed by numerical multi-physics-based simulations of the device performance. Different generations of fabrication processes and liquid encapsulation methods are explored. The third-generation device is characterized, and the results of the performance are compared to analytical and numerical methods.

Chapter 5 explores a magnetic bio-inspired hair-cell-based scheme to take advantage of the micro-toroidal platform. The structure's working principle and different configurations are evaluated to meet the power and size requirements of the rotation sensor. Basic numerical simulations are conducted to compare the different configurations of the hair cell. This is followed by the fabrication process of the device. Limited characterization of the structure is presented. Inertial experiments conclude the chapter.

Chapter 6 concludes the research and summarizes the main contributions of this work, and outlines future research directions

CHAPTER 2. INSPIRATION: SEMICIRCULAR CANALS

2.1 Background

The chapter will start off with introductory background information on the vestibular system, showcasing the design, theory and hydrodynamic mechanics of the semicircular canals. The chapter will conclude with an analysis and evaluation of the semicircular canal as a rotational inertial platform.

2.1.1 *Historical Background*

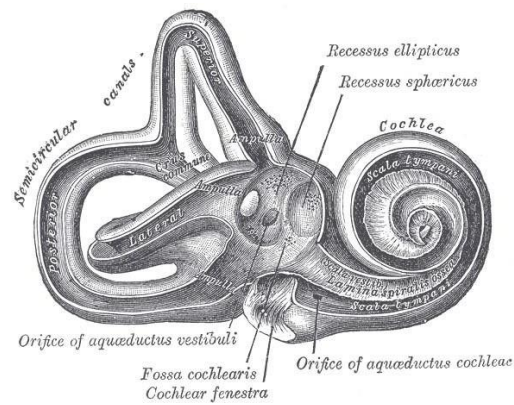


Figure 2.1. Sketch of the human labyrinth as depicted by Gray in 1918 in *Anatomy of the Human Body* [149].

Both Wilson et al. [5] and Kornhuber [150] summarized the history behind the discovery of the vestibular system and understanding its significance. The vestibular nerve was first described by Antonio Scarpa in 1795. In 1824, Pierre Flourens correlated the functions of the vestibular organs back to balance by ablating the parts in animals and observing the corresponding imbalance that follows. This discovery went unnoticed until Friedrich Goltz

in 1870 used both caloric and electrical stimulation to conclude that the inner ear was involved in balance. In the late 1870s, Mach, Brown and Breuer independently deduced the functional significance of the semicircular canals (SCCs) as rotation sensors of the head.

2.2 Mammalian Vestibular System

The vestibular system senses linear and angular accelerations of the head, transducing the mechanical input into a neural signal to be interpreted by the brain. The system is simply concerned with the detection of signals arising from the movements of the head. It does not inform on the state of the external world.

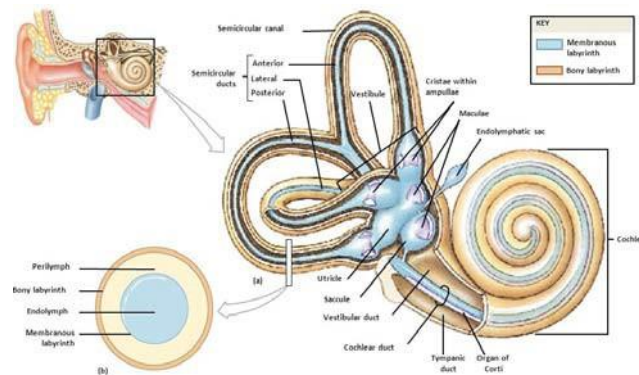


Figure 2.2. A diagram of the human inner ear. A close up of the labyrinth highlights both the bony and the membranous labyrinths, adapted from [151].

2.2.1 Morphology

On both sides of the head, there exists a fluid-filled bony labyrinth in the inner ear, composed of cavities and tubes. An early sketch of the structure is shown in figure 2.1. There is a membranous labyrinth inside the bony one (see figure 2.2). Within this membranous labyrinth, a few sensory organs are located: the cochlea, responsible for

hearing, the semicircular canals, responsible for sensing rotation, and the vestibule which holds the organs responsible for sensing linear acceleration.

2.2.2 Labyrinth

Three interconnected canals lie within one side of the head, mirrored on the other side by another set of three canals [5]. Each semicircular canal is a toroidal soft-tissue tube (membranous labyrinth) filled with a fluid called the endolymph. The tube is of narrow diameter for most of its arc but includes a much-expanded bulbous segment called the ampulla. The ampulla contains the structures responsible for mechanotransduction of rotational motion (the cupula). The narrow section is also called the lumen. The entire vestibular labyrinth is surrounded by perilymphatic fluid within a tightly fitting cartilaginous or bony cavity (bony labyrinth). The membranous labyrinth is suspended by filaments to the bony one. The overall structure of the labyrinth is highlighted in figure 2.2.

Motion between the membranous labyrinth and the bony labyrinth is believed to be negligible [110], and the motion of the semicircular canals is taken to be the same as that of the skull. Thus, it is assumed that the membranous labyrinth follows the bony ducts.

2.2.3 Labyrinth Fluids

The inner ear has two distinct fluids: the endolymph and the perilymph. Under normal circumstances, there is no communication between the perilymph and the endolymph [9]. The two fluids provide an electrochemical gradient that allows the hair cells to transduce the mechanical signal to an electrical one. In recent years, researchers have exploited this

gradient to create an electrochemical battery to power implants [152]. Also, the two-fluid system minimizes the effect of atmospheric pressure modulation [153].

The mechanical properties of the endolymph are very similar to water in terms of viscosity and density. The endolymph's properties allow the narrow SCC to sense angular acceleration [154]. The narrow lumen cross section induces laminar flow in the endolymph allowing for the desired rotational behavior as an integrating angular accelerometer within the normal range of motion of most animals, including mammals, fish, birds, and reptiles. [154]. Researchers have observed that the endolymph does not experience any shear-rate dependent behavior. Thus, it is reasonable to assume that the fluid is Newtonian and incompressible [110], [155].

2.2.4 Ampulla and Cupula

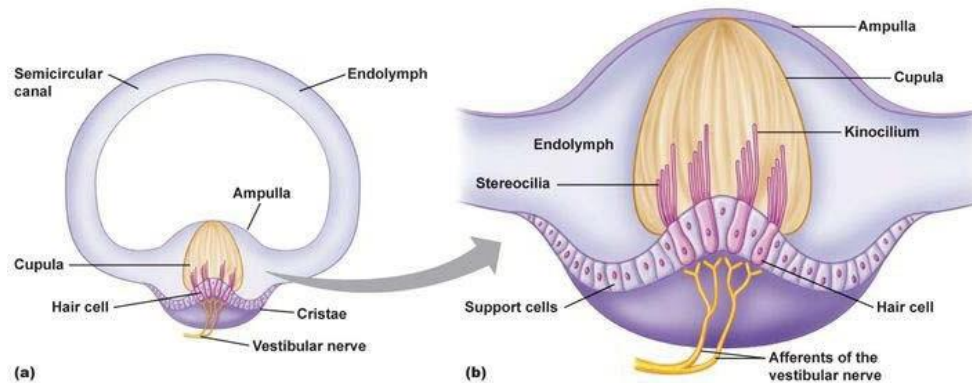


Figure 2.3. (a) A simplified diagram of the semicircular canal with the ampulla highlighted. (b) A close up of the ampulla showcasing the gelatinous cupula with the embedded sensory hair cells connected to the vestibular nerve, adapted from [151].

The cupula is a thick gelatinous membrane structure that occludes and blocks the canal lumen in the ampulla portion of the canal (figure 2.3a). The cupula spans the cross-section of the canal and is attached firmly to the ampulla wall and the crista ampularis at the base of the cupula as shown in figure 2.3. Sensory hair cells are embedded in the gelatinous cupula and are located on the crista ampularis. This ridge of sensory epithelium extends from one side of the ampulla wall in towards the center of the cupula. The deflection of the cupula due to angular head rotation causes the embedded sensory structures to deflect. This deflection correlates with angular motion. The volumetric impedance of the cupula allows for an elastic approximation of its behavior as observed by [156], [157].

2.2.5 Hair Cells

Hair cells are nature's answer to sensing forces [158]. They are located in many organs and serve different purposes and needs translating forces into electrical signals. Nature's mechanotransducers are not selective on their own as experiments have shown [159]. The selectivity is enforced by the geometric constraints that it sets itself within [110].

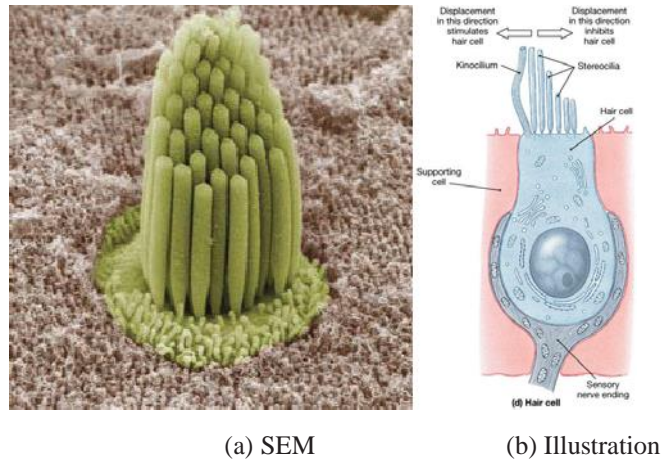


Figure 2.4. (a) Scanning electron microscopy image of a bundle of sensory hair cells by Leonardo Andrade and Bechara Kachar, NIDCD/NIH. (b) Illustration of one type of sensory hair cell's structure, adapted from [151].

Hair cells consist of a bundle of high-aspect ratio structures (stereocilia) that convert mechanical energy into electrical pulses that are sent to the brain. Stereociliary bundles are asymmetrical, with stereocilia graded in height towards the kinocilium as shown in figure 2.4. Deflection of the bundle towards the kinocilium causes the opening of ion channels in the hair cell membrane [108]. The magnitude and direction of the signal is encoded in the frequency of action potential discharge [160].

Within the semicircular canals, hair cells are uniformly oriented on the crista ampularis such that, under normal physiological conditions, deflection of the cupula is excitatory (increasing in frequency) in one direction and inhibitory (decreasing) in the opposite direction (figure 2.5).

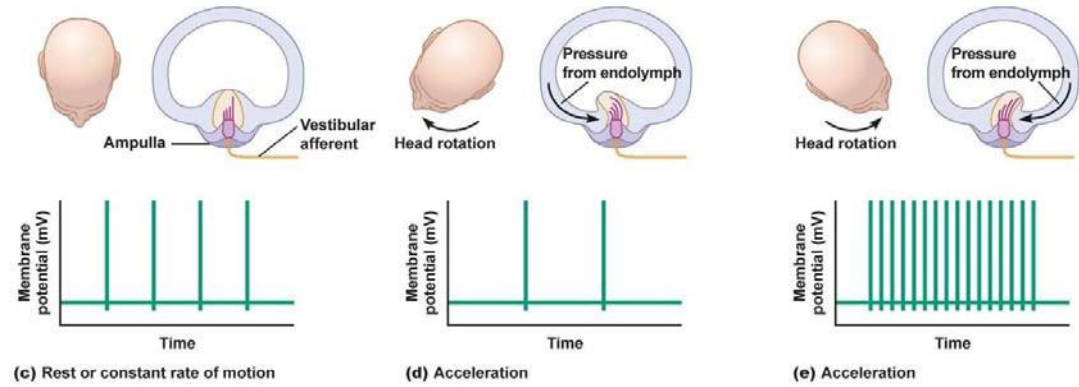


Figure 2.5. Firing rate of the hair cells based on head motion and head rotation direction, adapted from [151].

The resting firing rate for vestibular neurons in mammals ranges from 60-100 spikes/sec, where a spike is a discharge event [159]. Figure 2.6 shows the afferent membrane potential (sensory discharge voltage) and corresponding discharge rate response to a range of angular velocities in a fly [161]. The figure shows that the signal output of the hair cells are unidirectional in response and that both the membrane voltage and the firing rate encodes the angular velocity and sends it to the brain.

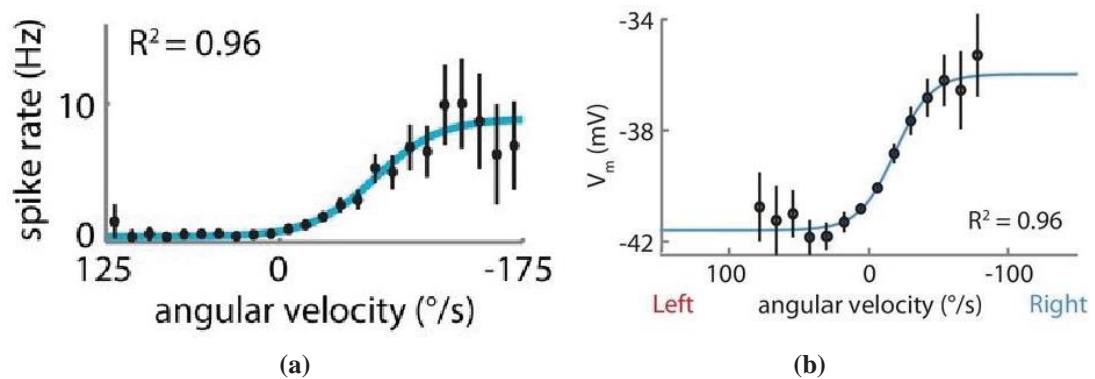


Figure 2.6. (a) Firing rate of the hair cells as a function of angular velocity in a fly, (b) membrane potential as a function of angular velocity in a fly, as opposed to spike rate, adapted from [161].

Measurements of the primary haircells response to head rotation by using electrically probing the neuron have found that the afferent (output) discharge rate, with some exceptions [162], changes nearly linearly with head rotation velocity over the physiologically relevant stimulus frequency range [163].

2.2.6 Operating Principle

The overall physical mechanism behind the SCC is highlighted in figure 2.5. The sensation of angular acceleration by a canal begins with relative motion between the endolymphatic fluid and the canal wall that encloses it. Due to the endolymphatic inertial mass, an angular acceleration in the plane of the canal will tend to cause the fluid to lag the canal walls. This relative movement is resisted by the viscous drag along the canal walls and by the stiffness of the cupula. Because the stereociliary bundles are mechanically coupled to the cupula, deformation of the cupula resulting from angular acceleration of the canal will lead to deflection of the stereocilia. This deflection is translated into a frequency-modulated electrical signal to the vestibular nerve.

An approximate physical analogue of the SCC without a cupula is a fully-filled bubble-free water bottle [164], [165]. If subjected to an angular acceleration, the inertia of the fluid will lag behind and will catch up after a while due to the adhesion of the water to the bottle (friction) and internal cohesion of the fluid (viscosity).

2.3 Hydrodynamic Model of the SCC

The mechanics of the bio-inspired sensor is modeled by the torsion-pendulum model shown in Fig. 2.7. Steinhausen [166], [167] first described the hydrodynamic behavior of

the SCC using a simple torsion-pendulum differential equation that has proven quite well over the years. By measuring and detecting the thresholds of angular accelerations in human subjects, Van Egmond [168] quantitatively evaluated the constants in the Steinhausen model.

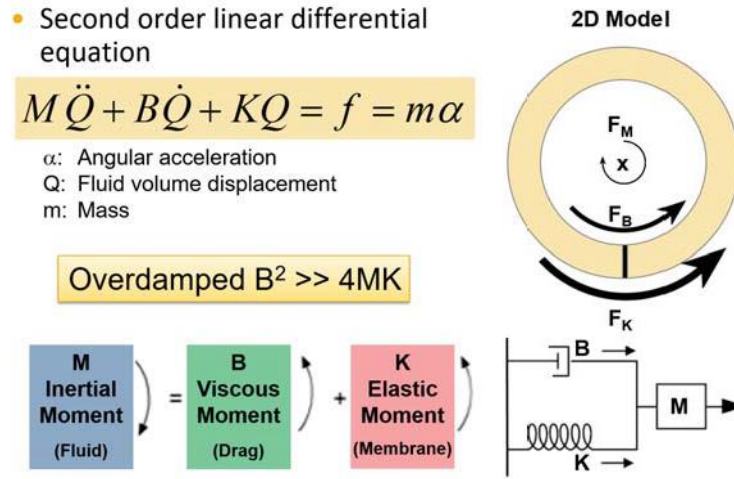


Figure 2.7. Hydrodynamics of the SCC: Forces acting on semicircular canal under steady-state equilibrium, adapted from [62], [169].

Thus, each individual SCC can be modeled as a second-order, highly damped, torsion-pendulum system (figure 2.7). The narrow canal-fluid system mechanically integrates acceleration rendering cupular deflection proportional to angular velocity with zero phase lag over a bandwidth consistent with natural head motion (0.1-10 Hz) [5].

The model describes the relation between the motion of the membrane and the rotation of the head. The inertial forces of the head rotation are balanced by the viscous drag of the fluid in the micro-channel and the elasticity of the membrane. The behavior of the system

is modeled as a second-order, linear, ordinary differential equation of the form modified from [168]:

$$M\ddot{Q} + B\dot{Q} + KQ = f = m\alpha \quad (2.1)$$

where M is the inertial moment, B is the viscous moment, K is the elastic moment, Q is the fluid volume displacement, α is the angular acceleration, and m is the mass.

The system is over-damped which is set when $B^2 \gg 4MK$. This behavior happens due to the small dimensions of the canals and the high viscosity of the fluid, which leads to the viscous moment dominating the behavior. Based on this overdamped system, there are two time constants: the long time constant (τ_1) and the short time constant (τ_2) as shown below [110]:

$$\tau_1 = \frac{B}{K}; \tau_2 = \frac{M}{B} \quad (2.2)$$

In this thesis, we assume that the over-damped torsion-pendulum model is an adequate first approximation of the behavior of the system for sensor design purposes.

In a second order system, solving for $\frac{Q}{\alpha}$, the solution simplifies to

$$\frac{Q}{\alpha} = \frac{m}{\sqrt{(K - M\omega^2)^2 + (B\omega)^2}} \quad (2.3)$$

If we would like to find the volume displacement to angular velocity, we multiply the transfer function above by radial frequency ω , $\frac{Q}{v} = \frac{Q}{\alpha/\omega} = \omega \left(\frac{Q}{\alpha} \right)$. A more in-depth analysis of the torsion-pendulum model is examined in chapter 3.

2.4 Analysis of Semicircular Canals (SCC)

2.4.1 Evolution of Semicircular Canals

The vestibular organs are ancient and were early to develop in the evolutionary timeline, and the gross morphology shows a considerable similarity across vertebrates [110]. The vestibular semicircular canals comprise a well-conserved physiological system in vertebrates, varying little in its fundamental structure and function from species to species [170].

In vertebrates, vestibular organs evolved from simple fluid-filled pits in the skin. These pits contained hair cells sensitive to vibrations arising from external sources or to self-induced animal movements [171]. Later on in the development and evolution, an array of interconnected pits gave rise to the lateral line in fish and the vestibular-cochlea organs in mammals. Although some morphological variation can be found between species, the fundamental physical arrangement and function of the semicircular canals is similar for all vertebrates. In non-mammals, there are two additional organs: the lagena and/or papilla neglecta. These organs affect the response dynamics and the frequency behavior of the vestibular nerve spike rate [172]. Depending on the organ, the firing rate of the vestibular nerve can be correlated to either angular acceleration (as in the papilla neglecta) or angular velocity (as in the cupula). *This insight helps guide our choice as designers in choosing the*

desired output (angular acceleration or angular velocity) based on the correct transduction mechanism.

2.4.2 Geometric Design of the SCC

On a gross anatomical level, the geometry of the SCC is formed to enhance the sensitivity to a particular rotational mechanical stimulus, while rejecting other interfering signals. The elegant structure puts a mechanical restraint on the moving fluid that only allows for flow of the fluid along the circumference of the torus. The biomechanics of the SCC are primarily responsible for the selectivity to angular acceleration in a particular direction. This is predicated on the assumption that the density of the fluid is constant along the circumference and that the torus is rigid [173].

There have been many different attempts to model the SCC geometrically [174], [175]. The most common is a torus with a major radius R , and a minor radius r , even though most SCC are elliptical in shape. Also, the cross section of the lumen is elliptical as well.

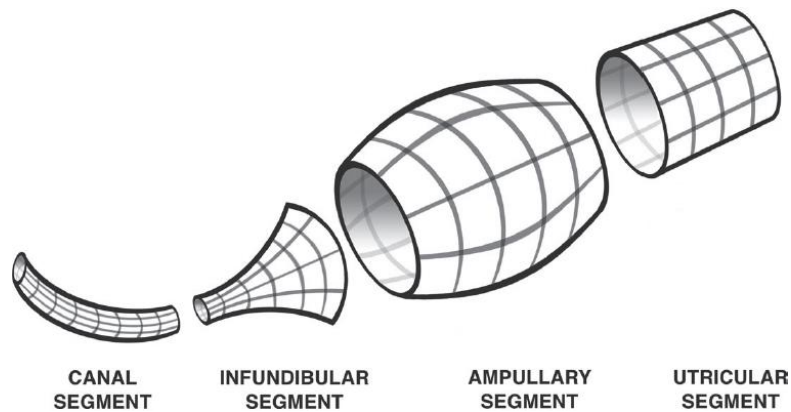


Figure 2.8. Geometric depiction of a segmented model labyrinth using toolbox elements from [175].

Other models include the ampulla as a variable in both function of angle along the circumference [173], [176] and as a multiple of the minor radius [177]. Others have provided toolboxes of common geometric shapes and simplifications to model the generic structure of the SCC [174]. Figure 2.8 shows four examples of geometric shapes used to simplify the modeling of the SCC. Finally, microCT scans of the SCC in humans (figure 2.9) and other animals have helped guide their analyses and simulation [174].

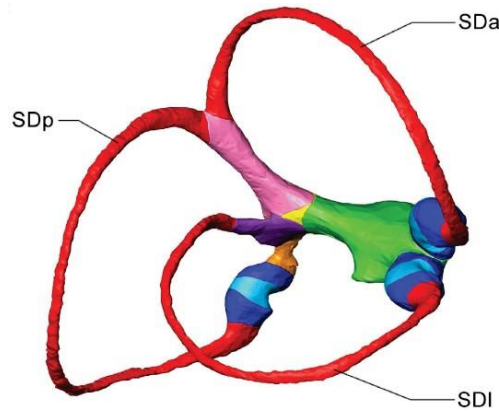


Figure 2.9. MicroCT-scanned right semicircular duct system of a human specimen, with colors marking the parts required as separate STL surface files. SDa, SDp and SDl indicate the anterior, posterior and lateral semicircular ducts, respectively, from [174].

2.4.3 *Dimension and Properties of the SCC*

The canal's nomenclature semicircular comes from the canal's ducts, which are elliptical in shape with a mean minor radius of $150\ \mu\text{m}$ in humans. The three SCCs have major radii of $3.17 \pm 0.21\ \text{mm}$. The lumen of the canal has an elliptic cross section [164]. The utricle's size as a fraction of the circumference of the SCC is about one-half [178]. The ampulla bulges out to about eight times the radius of the lumen [179].

The membranous labyrinth's thickness varies between 15-50 μm [110]. The stiffness of the membranous tissue is orders of magnitude greater than that of the cupula. This leads to believe that the pressure drop in the slender channels will mostly deform the cupula, not leading to the bulging of the ducts [180]. The sensory hair cells extend up to 80 μm into the cupula. The density and viscosity of the endolymph is close to that of water. The density of the cupula is very similar to that of the endolymph.

2.4.4 Allometric Analysis of the SCC

To better understand the effect of shape of the SCC on its performance, we introduce the concept of allometry, which is the study of the relationship between body size to the shape, anatomy, physiology, and behavior of animals. It was first popularized by D'Arcy Thompson in 1917 in his book *On Growth and Form* [181].

Nature's convergence to the torus design to sense angular motion in mammals has spread across a large range of animal sizes from small fish larvae up to whales [154]. Jones and Spells have studied the relationship between the mass, length, and even neck size of the animals to major and minor radii of the SCC [182], as shown in figure 2.10a. Both the minor and major radii increase by only one order of magnitude, while the mass of the animals changes by seven orders of magnitude. This shows a stable and near optimal design as proposed by Squires in [183]. These relationships have been developed to study the growth of species [184], morphological data of fossils of extinct animals [185], and the evolution of humans [186], [187]. Figure 2.10b compares the sensitivity of the SCC in relation to agility between two size-matched species, the *Galago moholi* (blue, agile, leaps bipedally), and *Nycticebus pygmaeus* (yellow, slow, quadruped). This shows that fast

rotations have less variation in sensitivity (tall and narrow distribution for *G. moholi*), whereas animals that rotate slowly have more variation in sensitivity (low and wide distribution for *N. pygmaeus*). *These somewhat contradictory data lead us to study the necessary parameters to optimize the design of a micromachined SCC.*

Jones in [154] speculates that the small cupular deflection and significance of laminar flow dominate as functional features of the semicircular canal. He postulates that this allows the SCC to match the likely range of head movements caused by changes in size, habitat or mode (flight, swimming, or walking) or agility of motion.

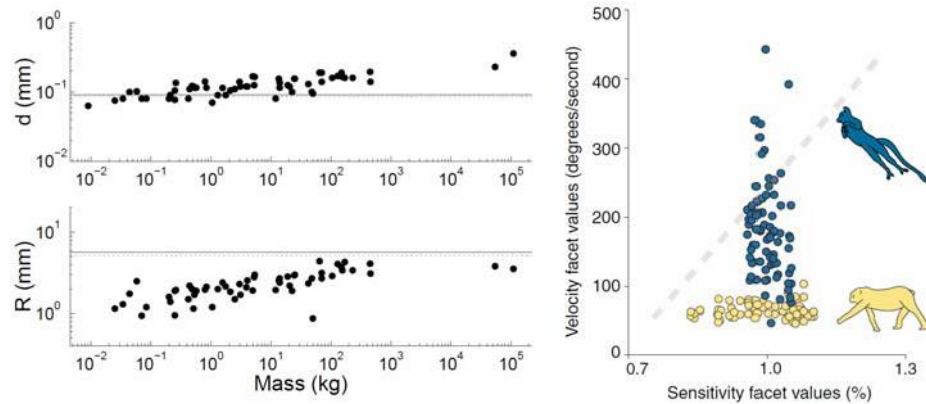


Figure 2.10. (a) Effect of animal mass on the major R and minor d radii of the semicircular canals; (b) Comparison between two animals: (a) Size as a function of mass from [111], [182], [183]; (b) Effect of agility on size of the semicircular canal from [188].

2.5 Human SCC Performance

The vestibular system is an essential part of a biological sensory system that stabilizes gaze via the vestibulo-ocular reflex and controls equilibrium, posture and balance, where a head rotation (input) is transduced into a cupula deflection (output). For simplicity of analysis, the system is assumed to be linear. To study the properties of the linear system, a time-dependent input and output must be chosen. Most researchers either choose angular

acceleration or velocity as their input based on their desired outcomes. However, cupular deflection is difficult to observe, thus other techniques must be used to measure the output of the overall system. Below are two examples of outputs of the system.

The main two quantitative observable outputs of the vestibular systems are the vestibulo-ocular reflex (VOR) and neural recording of the afferents signal of the vestibular nerve [10], [12]. The VOR is measured as the change in eye angle divided by the change in head angle. In either case, researchers are unsure if information processing and adaptation occurs at the hair cell or the cerebellum level or both. This can lead to a misleading characterization of the mechanical transfer function of the SCC system.

2.5.1 Dynamic Range and Limit of Detection

In the normal range of motion, angular velocities up to and larger than $400^\circ/\text{s}$ are experienced, while sustained angular accelerations are no greater than $30^\circ/\text{s}^2$ [177]. Peak head motions can seldom lead to angular velocity steps larger than $600^\circ/\text{s}$ [177], and $10,000^\circ/\text{s}^2$ for angular accelerations [110]. Extreme movements involved in ballet and skate dancing can cause rotation of $720^\circ/\text{s}$ and $2,000^\circ/\text{s}$ respectively [5]. The canals' threshold for angular accelerations is somewhere between $0.035^\circ/\text{s}^2$ and $4^\circ/\text{s}^2$ [177], with an angular velocity threshold between $0.4^\circ/\text{s}$ and $2^\circ/\text{s}$ [164].

2.5.2 Cupula and Hair Cell Performance

The volumetric displacement of the endolymph is on the order of 0-100 pL for normal range of motion [177]. Cupular pressure differentials have been analyzed and simulated to

be in the 0-5 mPa range [120], [121], [157], [177], [180]. The smallest observed pressure differential was calculated to be 0.01 mPa based on both caloric [189]–[191] and inertial stimulations [177]. The cupula roughly deflects between 1-100 nm per $0.1 \text{ }^\circ/\text{s}^2$ [177]. That is 3-5 orders of magnitude smaller than the size of the hair cells. The largest expected deflections should be in the 3-5 μm range [177]. *To put these numbers into perspective, the pressure differentials are on the same order of magnitude as the ones induced by sound waves, but at much lower frequencies.*

2.5.3 Afferent Signal Dynamic Range and Sensitivity

The vestibular afferent signals have a dynamic range of 0-400 spikes/s [9]. The afferent sensitivity to angular acceleration is 0.8-4 spikes/s per $^\circ/\text{s}^2$ [162], [192], [193].

2.5.4 Frequency Range

In humans, the typical frequency range for head rotations due to walking, jogging, or even vigorous headshaking is from 0.05 to 16 Hz [42]. Foundational studies by Goldberg and Fernandez revealed that the angular acceleration of the SCC is effectively coded as velocity by the neurons innervating the SCCs for intermediate frequencies ranging from 0.05-5Hz [162], [192], [193]. A high pass behavior of the canals is exhibited for lower frequencies with a cutoff frequency between 5-50 mHz [194]. The low pass cutoff frequency is around 10-20 Hz [173].

2.6 Evaluation of the SCC as Rotational Sensing Platform

In order to evaluate the SCC as a potential framework for a new micromachined inertial sensor, we need to evaluate it as a sensor. The next section covers the features, challenges and some of the unknowns when it comes to using the SCC as sensors.

2.6.1 Features of the SCC

2.6.1.1 Choice of Sensor Output

Based on previous analysis highlighted in section 2.2.7, as well as the frequency of operation and transduction mechanisms used, the toroidal platform can be used to sense angular acceleration (low frequencies), angular velocity (mid band), and angular position (high frequencies) when correlated to cupular *deflection*. However, if one transduces cupular *velocity* into the desired signal, the sensor will measure angular jerk (low frequencies), angular acceleration (mid band), and angular velocity (high frequencies). If we remove the cupula entirely, the angular velocity of the fluid is directly related to the angular acceleration of the structure. This can be concluded from [171], [172]. If we assume there is no spring force, the KQ term goes to zero, and due to the small channels the viscous term $B\dot{Q}$ dominates the inertial term $M\ddot{Q}$. From the remaining terms, \dot{Q} is just the fluid velocity in the channel. The remaining linear equation shows that the fluid velocity is linearly correlated to the angular velocity. To clarify this, we go back to the second-order differential equation described earlier:

$$\overbrace{M\ddot{Q}}^{\cong 0} + B\dot{Q} + \overbrace{KQ}^{=0} = m\alpha$$

$$B \frac{d\widehat{v_\theta}}{dt} = m\alpha$$

This opens up the opportunity to use multiple sensing mechanisms to sense different rotational motion signals concurrently.

2.6.1.2 Complimentary Pair

SCCs in one ear work complementarily with those in the other ear forming a "push-pull" pair of SCCs [164]. This way, the common mode rejection ratio of the sensory information increases. The resulting difference signal is more linear, and has a gain of at least two.

2.6.1.3 Power Consumption

The fluid motion inside the SCC is powered by the motion of the head, thus the sensing principle is passive in that regard. However, the transduction of the mechanical signal, e.g. cupula deformation, to electrical impulses is not passive, but a very efficient active process. No current estimate has been made to our knowledge of the power consumption of the hair cells in the SCC. However, based on educated estimations from the power consumption of the hair cells in the *auditory* system from Sarpeshkar in his book *Ultra Low Power electronics* [54], we can make a similar educated guess for the power consumption of the *vestibular* system. Using three assumptions of 125mV resting potential [54], the number of haircells in the vestibular system is 134,000 [108] and the power consumption estimate

of each hair cell ranging from 200-500pA/cell [195], [196] (25-67 μ A total current), the expected power consumption would be in the range of 1-10 μ W.

2.6.1.4 Cross-Axis and Linear Acceleration Rejection

The three canals lie in roughly orthogonal planes relative to each other, each canal sensing angular acceleration approximately in its plane of orientation. The angular component of head motion is thereby further decomposed into three directional components. Thus, rotation about the main direction of one canal results in minimal responses in the other two canals. As discussed earlier, the geometric constraint of the toroidal channel limits sensitivity to linear acceleration. This comes out of two assumptions: constant density across the circumference [173], and a rigid channel [155], [173].

2.6.1.5 Motion-matched Frequency Transfer Function

The SCC as a platform is adaptable by varying geometric (i.e. minor and major radii) and material constraints (i.e. choice of fluid) to match the frequency and range of motion of the desired application. This can be deduced by seeing that the sensitivity and the transfer function of the semicircular canals is highly correlated to the size of the animal as described in [154], [183]. Adults, larger animals – generally slower – will have larger SCCs, while children and smaller – and more nimble – animals will have smaller lumens.

2.6.1.6 Relative Tolerance and Insensitivity to Design Variations

The SCC dimensions can vary up to 10% in a human population [178], [183].

Despite this large variation, the structure shows tolerance on the performance of the SCC as a rotation sensor.

2.6.2 *Challenges with the SCC*

2.6.2.1 Sensitivity to Linear Acceleration

A rigid canal is insensitive to linear accelerations as long as the fluid density is uniform across the circumference of the torus [197]. However, the SCC could still be susceptible to linear acceleration as discussed in the following. Steer in 1967 proposed that the reason SCCs are vulnerable to linear accelerations is due to the uneven and elastic walls, where linear acceleration cause a peristaltic pump-like pressure differential that is sensed by the cupula [155]. The thin walls of the ducts are deflected due to the inertia of the fluid causing a restriction that leads to a pressure differential across the cupula. The SCC is susceptible to linear accelerations by surgically plugging or blocking the canal [173], [198]. Researchers were able to successfully eliminate the response of the sensor to angular acceleration by plugging the canal. Moreover, if a density difference is induced in the fluid, the linear acceleration dependency will be pronounced, especially to the time-varying orientation of gravity [199]. Even a small density difference (roughly 0.1 kg/m^3) would be sufficient to induce a response from interfering linear signals [189]–[191], [199]. This small difference can be easily achieved by raising the temperature in one part of the endolymph by roughly 0.3°C .

The latter can be easily observed in caloric testing of human subjects [164]. Cold or hot water is injected into the ear canal. The temperature gradient created in the endolymph causes a pressure differential across the cupula, thus inducing an interfering signal. Also, this is the

experience of most people after drinking alcohol [5]; the alcohol diffuses into the cupula reducing its density compared to the endolymph. The opposite ocular nystagmus is observed when heavy water is injected instead.

2.6.3 *Unknowns*

2.6.3.1 Drift

Little is known about the drift behavior of the SCC at zero input or the baseline drift of the afferent nerve potentials in the SCC over an extended period of time.

2.6.3.2 Noise

No known experimental studies have been conducted on the noise performance of the SCC in mammals. The $(1/f)$ -noise is dominant in the range of normal motion for vestibular evoked response electrical recordings measured from the skin [200], and direct measurement of cochlear and saccular hair bundle potentials the noise varies inversely with frequency [201], [202]. Also, low-frequency mechanical stimuli affecting the deflection of the SCC hair cells has favored larger hair cells that overcome Brownian motion noise [203].

2.6.3.3 Linearity

The SCC is expected to behave linearly as long as the flow in the lumen is laminar [159]. The transition to turbulent flow is expected to be above the normal range of inertial input of the SCC. Other sources of non-linearity include large deflection of the cupula and nonlinear firing or saturation of the hair cells.

2.6.3.4 Hysteresis

The systems shows negligible to no hysteresis [204]. One potential source of hysteresis is if the cupula was modeled as a viscoelastic material and experienced an extreme inertial input.

2.6.3.5 Reliability

Based on humans, the vestibular system's mean time to failure is on the order of decades. However, it is operated in a controlled temperature environment.

2.7 Conclusion

Based on literature review and survey of the SCC, its performance and its drawbacks, it seems prudent to explore the SCC as potential inspiration for a rotational inertial platform based on micro-machining techniques. A well-designed micromachined SCC would be (1) completely or mostly passive; powered by motion and requiring little to no power for transduction; (2) the closed-loop torus platform could be used to sense either angular velocity or angular acceleration based on the chosen transduction mechanism; (3) the sensor is complimentary to current state of the art gyroscope in potentially providing sensory integration (angular velocity and acceleration); (4) the platform has a robust and proven track record and has been utilized by most species to sense rotations; and (5) the platform can take advantage of current engineering design and optimization, robust micromachining techniques and a wide variety of materials not available to animals.

CHAPTER 3. MICROMACHINED SEMICIRCULAR CANALS

3.1 Platform Introduction

The many advantages of the simple microtorus structure encourage us to investigate it as a platform for rotational inertial sensing, as described in section 2.5. The simple elegant design inherently rejects linear acceleration and only accepts rotational movement within the plane of the torus. This section will describe the rationale and design considerations behind the proposed bioinspired angular motion platform of the microtorus. These design considerations are validated by analytical and numerical models based on the semicircular canal.

3.1.1 *Previous Attempts*

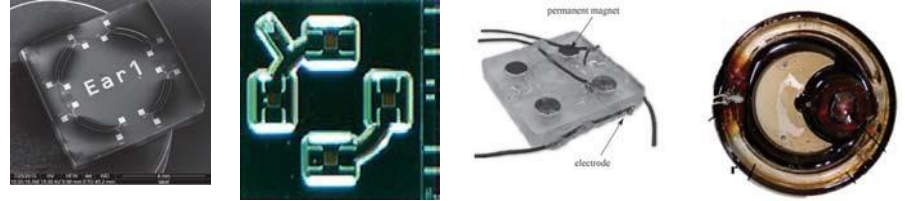
The approach of using a fluid-filled microtorus for rotation sensing has been proposed previously, as is different described in section 1.2.4.1. The different design features of previous attempts are summarized in table 3.1. In section 3.1.2, we discuss the design philosophy differences between biomimicry and bioinspiration using the examples in table 3.1.

3.1.2 *Biomimicry vs. Bioinspiration*

Engineers and designers have looked to nature to improve and design better solutions for human problems. Biomimicry is the pure replication of nature's designs. For example, the design of nano-textured hydrophobic surfaces is designed to replicate the structure of shark skin [105]. In contrast, bioinspiration distills the best design elements and insights from nature and combines them with other engineered designs for greater improvements in performance. Bioinspiration can take advantage of multiple species-specific design

elements to improve upon natural performances. One example is the nose design of high-speed bullet trains in Japan based on the beaks of three different birds used to reduce drag and noise pollution [205].

Table 3.1- Design comparison of state-of-the-art bio-inspired angular accelerometers.



First Author	Groenesteijn	Andreou	Van Tiem	Fu
Year	2014	2014	2015	2017
Ref.	[125]	[64]	[124]	[206]
Transduction	Thermal	Piezoresistive	Magnetic	Chemical
R	2.25 mm	1.75 mm	15 mm	30 mm
r	20 μ m	0.375 mm	0.4x3 mm	2.5 mm
n=R/r	112.5	4.6	5-37.5	12
Channel Shape	Circular	Circular	Rectangular	Circular
Sensing	Fluid velocity	Fluid velocity	Fluid velocity	Pressure diff.
Features		Horizontal	3D printed	
Cupula	X	X	X	✓
Hair Cell	X	✓	X	X
Ampulla	X	✓	X	X
Utricle	X	X	X	✓

The analysis in this chapter will consider whether biomimicry or bioinspiration are the best route to base the design of the proposed inertial sensor. To do so, we must understand the essential design elements of the SCCs.

3.1.2.1 Microtorus (Closed-loop Shape)

The closed-loop design feature is *a necessity* to ensure the signal separation. The closed-loop promotes the signal stemming from rotational movement in the plane of the torus while blocking signals from linear motion. Other factors to consider here are the general shape of the torus (circle, ellipse, or an arbitrarily-shaped loop) and the cross section (circle, square, ellipse). All the micromachined SCCs included in table 3.1 have a closed-loop in some form.

3.1.2.2 Cupula (Spring or Piston)

The cupula impacts both the frequency and sensitivity performance of the semicircular canals [120]. However, the cupula is *not necessary* to sense rotation. Other species use lateral lines [207] or papilla neglecta [172] that do not include a soft membrane. The design requirements for a structure with a cupula, as discussed earlier in section 1.2.4.1, make it difficult to fabricate using current techniques and materials. Only Fu et al. [206] included a cupula-like structure in their design.

3.1.2.3 Hair Cells (Transducer)

The embedded hair cells transduce a pressure differential across the cupula into an electrical signal. Hair cells are *not necessary* because there are other methods to convert mechanical energy into electrical signals. However, Andreou [64] used hair cell-like piezoresistive strain sensors integrated into a horizontally suspended cantilever.

3.1.2.4 Ampulla (Channel Enlargement)

It has been thought that the ampulla is a mechanical amplifier of the pressure differential across the membrane in a way that a larger membrane is easier to deflect. While *not necessary*, a channel enlargement should be considered if a pressure differential approach is considered. Andreou [64] integrated a channel enlargement near the transducer.

3.1.2.5 Utricle (Fluid Storage)

Some researchers proposed that the utricle provides fluidic storage for the SCC [123]. Others theorized that the utricle provides non-linear turbulent behavior that can enhance the sensitivity of the structure [208]. The utricle is *not a necessary* structure for the proposed device. Fu et al. [206] incorporated an utricle-like fluid cavity in their sensor.

3.2 Design Considerations

It is important to consider the range of design choices that are available to adjust and tweak in order to optimize performance in both biomimicry and bioinspiration. To realize the design features discussed in section 3.1.2, a designer can modify geometry, materials, and transduction mechanisms.

3.2.1 *Form and Geometric Consideration*

The most basic form an SCC-analogue can take is a simple circular torus with a minor radius r and a major radius R . The simple torus can be with or without an occluding membrane of thickness t , and could have an expanded ampulla of radius b . However, the μ SCC is not restricted to the circular shape. We can adjust both the cross section of the

channel and the overall shape of the closed-loop channel. Figure 3.1 provides examples of various closed-loop shapes.

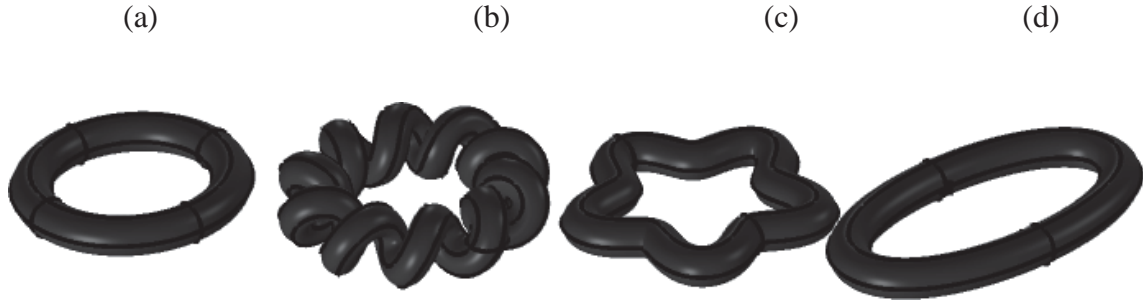


Figure 3.1 – Different device concepts: (a) Simple circular torus; (b) Helical torus ($m=10$); (c) Star torus ($m=5$); Simple elliptical torus ($a=2b$).

Another factor to consider is the orientation of the membrane. In the mammalian SCC, the cupula is oriented vertically (normal to the plane of the torus). But for microfabrication purposes, it might be easier to design a horizontal occluding membrane (in the plane of the torus). This will be further explored in section 3.2.4. In nature, the closed-loop is a non-planar saddle-like structure [209]. Considering this research, there is a choice between fabricating a simpler planar structure or mimicking the non-planar design of the SCC. While a non-planar structure is an option, this research will mainly focus on planar toroids.

3.2.2 Material Consideration

The materials selected for the fluid, the channel and the membrane of the sensor need to be considered. For the fluid, density ρ and dynamic viscosity μ are integral to the behavior of the system. Moreover, the fluid must have a low-vapor pressure to prevent the fluid from evaporating over time. The stiffness of both the channel E_{ch} and the membrane E_m must also be considered. Other important material properties will be discussed based on the

transduction mechanism chosen, such as thermal, mechanical or magnetic properties. In section 3.3, we will analyze how these variables affect the performance of the system.

3.2.3 Transduction Mechanisms

Overall, the transduction mechanism chosen needs to have the following characteristics: passive or low-power consumption, wide-enough bandwidth, linear signal transduction, as well as transducing the desired input signal. One needs to consider the desired input signal (angular velocity or angular acceleration of the fluid) to choose the proper transduction mechanism for converting the mechanical inertial energy of the fluid to an electrical signal. For a membrane-based design, the deflection of the membrane will correlate with angular velocity. However, the fluid velocity will correlate with angular acceleration in the case of a non-membrane-based design. Thus, two different types of transducers need to be considered depending on the actual design: pressure/force sensors (deflection) or flow meters (fluid velocity).

For pressure sensors –especially flexible ones–, a wide range of transduction mechanisms exist, with capacitive, piezoelectric and piezoresistive transducers dominating [210]. They offer high sensitivity and low-power sensing. Most promising of these for the application in mind are piezoelectric filaments that offer passive transduction, high sensitivity and linearity [143]. For flow sensing, thermal caloric sensing offers the highest sensitivity mechanism especially in low flow sensing [129]. Other options include mechanical and acoustic principles, but none match the sensitivity of the thermal sensors. However, thermal sensors suffer from lower bandwidth and higher power consumption.

3.2.4 Proposed Designs

After reviewing the multitude of design considerations in the sections above, designs with features and geometries were selected that are simple to analyse, implement, and reflect the natural form of the SCC. Below are the potential microtorus designs:

1. Simple torus with membrane (Design 1)

- (a) Vertical membrane (1a)
- (b) Horizontal membrane (1b)
- (c) Horizontal membrane with ampulla (1c)

2. Simple torus without a membrane (Design 2)

For simplicity, the analysis of the initial platform will consider a channel with circular cross-section only. Based on previous analysis by Alrowais et al. and Töreyn et al. [63], [122] and further discussed in Appendix A1, the membrane-based designs (designs 1a-c) are promising but do not have the simplicity of the non-membrane design (design 2).

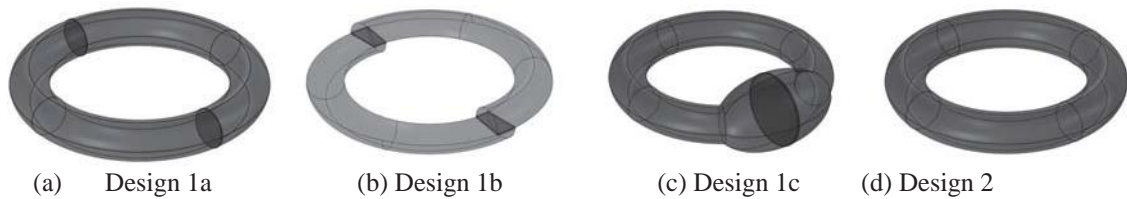


Figure 3.2. Proposed design concepts: (a) Simple torus with vertical membrane; (b) Simple torus with horizontal membrane; (c) Simple torus with vertical membrane and ampulla; (d) Simple torus without a membrane.

3.3 Semicircular Canal Analysis

An analytical model of the system can build a first-order understanding of the system. Based on the model, the sensor parameters can be tailored according to need. This section will focus on the analysis of the simple circular torus with a circular cross-section without a membrane (design 2). Thereby, the analytical model largely follows derivations found in [110], [211]. For an analysis of the behavior of the membrane-based designs (design 1a-c), please refer to Appendix A1.

Nomenclature

r, R	Minor, and major radius of torus
κ	Curvature factor or ratio of minor to major radii of torus r/R
n	Inverse curvature factor or ratio of major to minor radii of torus R/r
ω	Angular frequency where $\omega = 2\pi f$
$\theta, \dot{\theta}, \ddot{\theta}$	Angular displacement, velocity and acceleration of channel
$\phi, \dot{\phi}, \ddot{\phi}$	Angular displacement, velocity and acceleration of fluid
$\delta, \dot{\delta}, \ddot{\delta}$	Rel. ang. displacement, velocity and acceleration of fluid to channel
ρ	Density
μ, ν	Dynamic viscosity and kinematic viscosity
a, a_T, α	Linear, tangential and angular acceleration
Re	Reynold's number
Dn	Dean's number
$\hat{x}, \hat{y}, \hat{z}$ or $\hat{i}, \hat{j}, \hat{k}$	Cartesian coordinate components
$\hat{r}, \hat{\theta}, \hat{z}$	Cylindrical coordinate components
$\hat{\rho}, \hat{\theta}, \hat{\phi}$	Toroidal coordinate components
$v_{\hat{\theta}}, v_{\hat{r}}$	Axial, and radial flow velocity

3.3.1 Assumptions

Assumptions are made to find an analytical model for the microtorus: (1) all parameters are assumed to be temperature independent; (2) the channel is considered to have a circular cross section; (3) the fluid is assumed to be incompressible, with a laminar flow and no slip boundary condition inside the torus; (4) low frequency oscillations are assumed to yield a quasi-steady-state solution for the velocity flow profile; (5) viscous heat dissipation is ignored at the target velocities and accelerations; (6) entrance effects are considered negligible since $L_{ent} \gg 1$ with $L_{ent} = 0.1rRe$; and (7) small curvature $\kappa \ll 1$ is considered, where $\kappa = r/R$, or $n = R/r$ where $n > 1$.

3.3.2 Forces

In this section, the forces acting on the fluid-filled microtorus are summarized. Thereby, the three coordinate systems highlighted in figure 3.3 are considered: the Cartesian coordinate system with axes $\langle \hat{x}, \hat{y}, \hat{z} \rangle$ or $\langle \hat{i}, \hat{j}, \hat{k} \rangle$, the cylindrical coordinate system with axes $\langle \hat{r}, \hat{\theta}, \hat{z} \rangle$, and the toroidal coordinate system with axes $\langle \hat{\rho}, \hat{\theta}, \hat{\phi} \rangle$. Upon applied angular acceleration around the z-axis, the two dominant forces acting on the fluid-filled microtorus (in the rotating coordinate system) are the Euler force F_e and the drag force F_d (see figure 3.3). The Euler force F_e is the tangential force, i.e. in the angular ($\hat{\theta}$) direction, that is felt in response to the applied angular acceleration. For a given angular acceleration α , the Euler force F_e experienced by a mass m , as well as the associated Euler or tangential acceleration a_T , increase with increasing distance R from the rotation axis:

$$F_{e_i} = \rho(R_j\ddot{\phi}_k - R_k\ddot{\phi}_j) \quad (3.1)a$$

$$\text{If rotating around } \hat{z} \text{ or } \hat{k}, \quad F_e = -ma_T = -m\ddot{\phi}R = -m\alpha R \quad (3.1)b$$

$$F_a = \rho a_i \quad (3.2)$$

$$F_{\theta_i} = 2\rho(v_j\dot{\theta}_k - v_k\dot{\theta}_j) \quad (3.3)$$

$$F_{c_i} = \rho R_i(\dot{\theta}_j^2 - \dot{\theta}_k^2) \quad (3.4)$$

The minus sign in equation (3.1)b stems from the fact that in the rotating coordinate system the mass lags behind the actual rotation because of its inertia, i.e. experience a fictitious force F_e . This force is best understood when considering riding on a merry-go-round: as the ride starts, we are experiencing a force against the ride direction (the Euler force), while we experience a force in ride direction when the ride stops. Counteracting the Euler force is the drag force F_d stemming from the viscosity of the fluid and the non-slip boundary conditions along the microtorus walls. This drag force is proportional to the fluid velocity with respect to the walls. As the example of the merry-go-round shows we must consider different reference systems: (i) the rotating reference system of the person riding on the merry-go-round and (ii) the stationary reference system of a person next to the merry-go-round. The person on the merry-go-round experiences forces and movements with respect to the movement of the rotating platform itself. Translated to the fluid-filled microtorus, this is the relative movement of the fluid with respect to the channel walls, characterized by $\delta, \dot{\delta}, \ddot{\delta}$, the relative angular displacement, velocity, and acceleration of the fluid with respect to the channel walls. On the other hand, the person next to the merry go round sees the movement of the rotating platform and that of the person sitting on it. Translated to the

fluid-filled microtorus, this corresponds to the angular displacement, velocity and acceleration of the microtorus walls, $\theta, \dot{\theta}, \ddot{\theta}$, as well as the angular displacement, velocity and acceleration of the fluid, $\phi, \dot{\phi}, \ddot{\phi}$. Since the sensors rotate with the microtorus, the relative movement between fluid and microtorus walls is most important for the system design and defined by $\delta = \theta - \phi$; this is analogue to the observer riding on the merry-go-round and observing the forces acting on a body as illustrated in figure 3.3c.

Equation (3.2)-(3.5) summarizes the acting body forces. Thereby, a body force is expressed in units of force per volume [Nm^{-3}]. Equation (3.2) represents the Euler force discussed above. There are interfering signals that obfuscate the intended rotational signal. Equation (3.3) is the linear inertial force F_a , which is density ρ times linear acceleration a_i . Other interfering forces include the centrifugal force F_c (equation (3.4)) and the Coriolis force F_θ (equation (3.5)) in the radial (\hat{r}) direction. These two radial interfering signals can be neglected, based on an order of magnitude calculation of equations (3.4) and (3.5). According to [212], the forces are too small to create secondary radial flow based on our design parameter space.

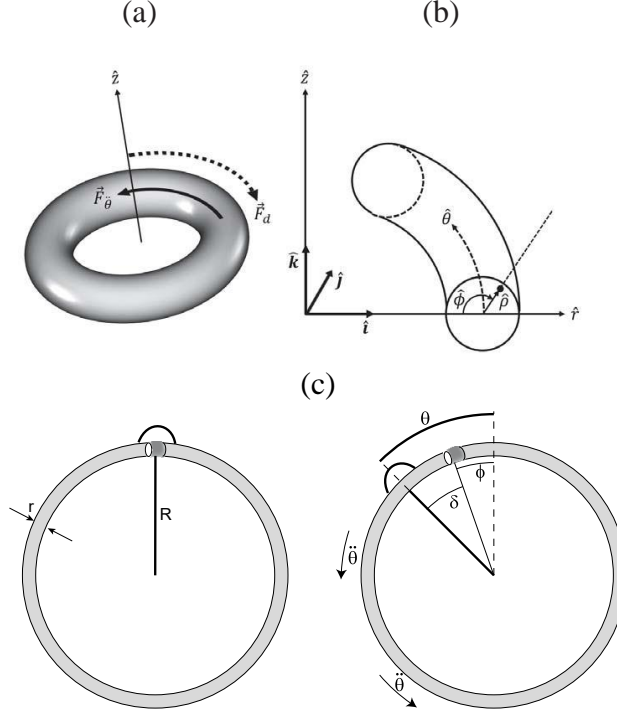


Figure 3.3. Forces and coordinate systems applied to microtorus under rotation: (a) Two dominant forces acting on torus under z-rotation; (b) Three coordinate systems used (i) Cartesian $(\hat{x}, \hat{y}, \hat{z})$ or $(\hat{i}, \hat{j}, \hat{k})$; (ii) Cylindrical system $(\hat{r}, \hat{\theta}, \hat{z})$; (iii) Toroidal system $(\hat{\rho}, \hat{\theta}, \hat{\phi})$; (c) Notation system used for μ SCC as adapted from [211].

3.3.3 Analytical model

Using Newton's laws, we balance the forces acting on the system as shown in figure 3.3. In steady state, the viscous drag of the fluid in the microchannel cancels the Euler force. According to [110], the laminar mass flow is governed by the steady-state Navier-Stokes equations for incompressible flow. The continuity and momentum equations are

$$\vec{\nabla} \cdot \vec{v} = 0 \quad (3.5)$$

$$\rho \left(\frac{\partial \vec{v}}{\partial t} + (\vec{v} \cdot \vec{\nabla}) \vec{v} \right) = \vec{F}_b + \mu \nabla^2 \vec{v} \quad (3.6)$$

where α_v is the velocity vector, μ the dynamic viscosity, ρ the density, and \vec{F}_b are the body forces acting on the fluid. Due to the toroidal shape of the device, cylindrical coordinates $(\hat{r}, \hat{\theta}, \hat{z})$ are used. Assuming an axially symmetric velocity flow i.e. the velocity solution is constant in the angular $\hat{\theta}$ direction, we can simplify the equations as:

$$\rho \frac{\partial \vec{v}_\theta}{\partial t} - \mu \left[\frac{\partial^2 \vec{v}_\theta}{\partial r^2} + \frac{1}{r} \frac{\partial \vec{v}_\theta}{\partial r} \right] = \sum \hat{F}_b \quad (3.7)$$

where v_θ is the fluid velocity in the polar/axial direction.

3.3.4 Sensitivity

According to [213], the steady state solution to (3.7) for the maximum velocity (at the center of the channel where $r=0$) is

$$v_\theta = \frac{\rho R r^2}{4\mu} \ddot{\theta} \quad (3.8)$$

We define the sensitivity as the ratio of the fluid velocity to angular acceleration as

$$S_{\frac{v}{\ddot{\theta}}} = \frac{\rho R r^2}{4\mu} \quad (3.9)$$

Thus, due to laminar flow in the microchannels, the fluid velocity is strictly proportional to inertial forces, and linearly correlates to angular acceleration. To achieve high sensitivity, we should have large minor and major radii and use a fluid with high density and low viscosity.

3.3.5 System Linearity

In order to estimate the dynamic range of the sensor, we must study the limits of the sensor's linearity. There are two causes of potential non-linearity in the flow of the fluid. The first is the transition from laminar to turbulent flow. The other is when the secondary forces (centrifugal and Coriolis forces) are approximately the same order of magnitude as the Euler rotational forces. The interfering forces could lead to secondary flows in the radial direction depending on the magnitude of the angular velocity and the frequency of rotation.

Turbulence transition nonlinearity

Turbulent flow in the toroid is dependent on the curvature factor κ and the Reynolds number Re . According to [214], the transition to turbulent flow is higher in toroids than in straight pipes. Critical Reynolds number values range from 2000–5000 depending on κ values between 0.05–0.3. To find the critical angular accelerations, we chose the conservative lower bound of $Re_{cr} < 2000$. The critical angular acceleration at which turbulent flow may impact the sensor result can be found from the definition of Re (equation (3.10) and equation (3.8)), and is given in equation (3.11).

$$Re = \frac{\rho v_{\theta} r}{\mu} \quad (3.10)$$

$$\ddot{\theta}_{cr} = \frac{\mu^2 Re_{cr}}{\rho^2 r^3 R} \quad (3.11)$$

An order of magnitude calculation is performed based on the proposed values ($\rho \sim 10^3$ kg/m³, $\mu \sim 1$ mPa·s, $r \sim 100$ μ m, $R \sim 1$ mm), resulting in a critical angular acceleration on the order of 10^6 rad/s². This value is roughly three orders of magnitude higher than even

extreme rotational accelerations experienced by humans on a daily basis. Based on this we can assert that this non-linearity does not limit our desired dynamic range.

Secondary Flow Nonlinearity

According to [111], the secondary forces are more substantial when the angular fluid velocity $v_{\dot{\theta}}$ is equal to the radial fluid velocity $v_{\dot{r}}$. Based on the balancing forces of equations (3.1) - (3.3) [111], and assuming only one axis of rotation around vector \hat{k} , the ratio of the angular to radial velocities is shown below:

$$\frac{v_{\dot{r}}}{v_{\dot{\theta}}} = \frac{\rho \dot{\theta} r^2}{4\mu} = \frac{rRe}{4R} \quad (3.12)$$

If we set the ratio of the radial to angular velocities to one and assume a curvature factor of $\kappa = 0.1r$, this leads to a critical Reynolds number Re_{cr} of roughly 40. With a minor radius r of 100 μm , an angular acceleration α of $4 \cdot 10^6 \text{ rad/s}^2$ is required to reach this critical velocity. However, if we increase r by an order of magnitude to 1 mm, the critical angular acceleration α_{cr} drops to 400 rad/s^2 . This validates Muller's [111] intuitive calculation that for the SCC, the secondary flows do not play a crucial role especially in the lumen for minor radii smaller than 2 mm. Additional simulation and modeling results investigating secondary-flow velocities can be found in Appendix A2.

3.3.6 Frequency

To model the frequency behavior of the sensor, the fluid-filled microtorus is considered to be a lumped element with an inertial force and a drag force. Calculating the transfer function of this lumped element model will describe the frequency behavior of the system.

The first step is the transduction of the input rotational acceleration to the fluid velocity inside the microchannel. One method is to consider the balance of forces acting in the system. The inertial forces and viscous forces acting on the liquid balance the inertial force acting on the torus. Based on this condition, the forces acting on the system can be modeled as [110], [169], [171], [211].:

$$m\ddot{\phi} = b\dot{\delta} \quad (3.13)$$

$$m\ddot{\theta} - m\ddot{\delta} = b\dot{\delta} \quad (3.14)$$

$$m\ddot{\theta} = m\alpha = m\ddot{\delta} + b\dot{\delta} \quad (3.15)$$

where α is the angular acceleration of the torus, $\ddot{\delta}$ is the relative acceleration between the head and the fluid, $\ddot{\theta}$ is the channel acceleration, $\ddot{\phi}$ is the fluid acceleration, m is the mass of the fluid and b is the viscous drag coefficient. Applying the Laplace transform on equation (3.15) and solving for the desired transfer function results in:

$$\frac{\dot{\delta}}{\alpha}(s) = \frac{1}{s + b/m} \quad (3.16)$$

When applying a unit step of angular acceleration to equation (3.16) and finding the inverse Laplace transformation, the time-domain response of the maximum fluid velocity is:

$$\ddot{\delta}(t) = S_v \left[1 - e^{-\frac{b}{m}t} \right] \quad (3.17)$$

To find the constants m and b , we calculate the mass of the fluid in the torus for m , and use the laminar flow viscous drag in a cylindrical channel to calculate b as shown below:

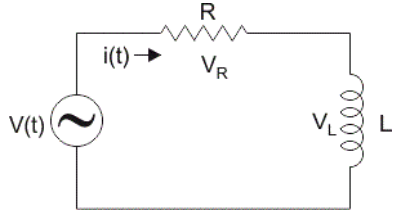
$$m = 2\rho\pi^2 r^2 R \quad (3.18)$$

$$b = 16\mu\pi^2 R \quad (3.19)$$

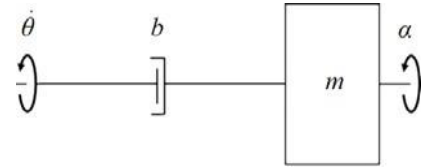
An equivalent electrical circuit in the form of an LR series circuit (figure 3.4) with the inductance being the inertance of the fluid (equation (3.21)) and the resistance being the hydraulic resistance for laminar flow in a circular channel [215] (equation (3.21)) can be used to model the system.

$$L_{fluid} = \frac{\rho L}{A} = \frac{\rho(2\pi R)}{(\pi r^2)} = \frac{2\rho R}{r^2} \quad (3.20)$$

$$R_{channel} = \frac{8\mu L}{\pi r^4} = \frac{8\mu(2\pi R)}{\pi r^4} = \frac{16\mu R}{r^4} \quad (3.21)$$



(a) Lumped element model



(b) LR-series equivalent series

Figure 3.3.4. Equivalent circuit models: (a) Electrical equivalent model; (b) Mechanical circuit model.

Based on either of the electrical or mechanical equivalent models, the viscous time constant of the system $\tau_{viscous}$ and the corner frequency $f_{viscous}$ can be determined as:

$$\tau_{viscous} = \frac{m}{b} = \frac{L_{fluid}}{R_{fluid}} = \frac{\rho r^2}{8\mu} \quad (3.22)$$

$$f_{viscous} = \frac{4\mu}{\pi\rho r^2} \quad (3.23)$$

This is equivalent to the short time constant found in the mammalian semicircular canal.

3.4 Simulation

A finite element analysis of the sensor was performed using COMSOL Multiphysics Software 5.3a (COMSOL). The isothermal laminar flow module was used. A body force of material density multiplied by the acceleration (in units of force per volume) was applied to the fluid to simulate the applied angular acceleration. Applying the body force assumes a stationary observer attached to the wall of the channel. This is the “inverse” problem to accelerating the torus walls, with the fluid lagging behind. As discussed before, this corresponds to the Euler force experienced by the fluid mass when observed from the rotating coordinate system. In the case of the 3D model, two methods were used to apply this body force: the first was by mapping forces in cylindrical coordinates to Cartesian coordinates; the second was by creating a toroidal coordinate system as shown in figure 3.3 earlier. Both methods yielded similar results. The mesh was refined until the solution converged. No slip boundary conditions were applied to the walls. Geometrical and material properties used for the simulation are summarized in Table 3.2. These dimensions and material properties were chosen based on the range of dimensions of the human semicircular canals [204] and using silicone oil as a the fluid due to its favorable properties (low viscosity and low vapor pressure). The numerical calculations will be validated later on in chapter 4 with experiment results.

Table 3.2. Geometric and material properties used for laminar flow simulation

Symbol	Quantity	Value	Units
R	Major radius	2.75	mm
r	Minor radius	500	μm
ρ_f	Fluid density	990	kg/m^3
μ	Dynamic viscosity	5	$mPa \cdot s$

3.4.1 Assumptions

The fluid was assumed to be incompressible and the flow laminar. The laminar flow assumption is due to the low Reynolds number ($Re < 1$) for the applied accelerations.

3.4.2 Acceleration-induced Flow Profile

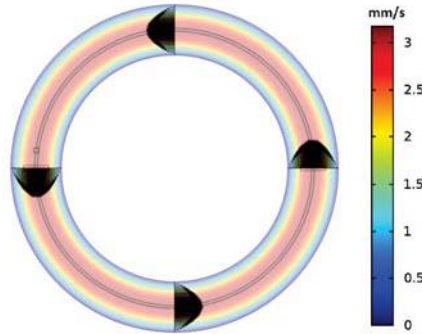


Figure 3.5. Parabolic laminar flow induced by a clockwise rotational angular acceleration of 100 rad/s^2 applied to the microtorus, yielding a counter-clockwise body force applied to the fluid with respect to the torus walls. Arrows indicate the magnitude and relative direction of fluid flow in the channel. The arrows for a parabola with zero velocity at the wall and the maximum velocity in the center of the channel.

As an example, figure 3.5 shows the magnitude of the simulated velocity flow field (with respect to the channel walls) in case of applying a clockwise angular acceleration of 100 rad/s^2 to the microtorus walls. As discussed before, clockwise angular acceleration results in a counterclockwise Euler force, which is applied to the fluid via a body force. The

resulting parabolic flow profile characteristic for laminar around the torus is visible with a maximum velocity in the center of the microfluidic channel.

3.4.3 Rotational Sensitivity

Figure 3.6a shows the simulated maximum tangential velocity component in the center of the circular channel for microtorus with the dimensions given in table 3.2 as a function of the applied angular acceleration for rotations around the \hat{z} -axis.

To highlight the importance of the torus structure in promoting signals stemming from an in-plane rotation around the \hat{z} -axis, figure 3.6b shows the same velocity component as a function of the applied angular acceleration for a horseshoe-shaped microtorus (an incomplete torus with a 10-degree break) with otherwise same dimensions. Clearly, the blocked torus sensitivity to rotations around the \hat{z} -axis is reduced by at least a factor of 40 compared to the unblocked torus, highlighting the importance of a closed torus.

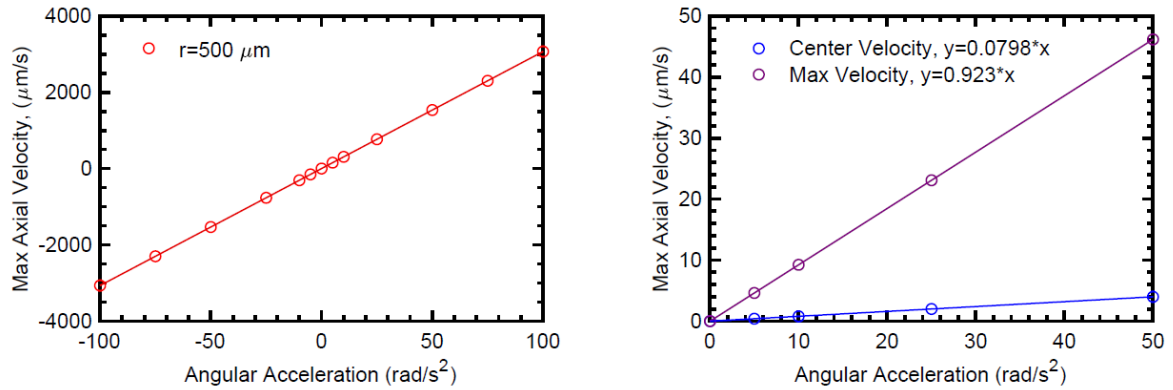


Figure 3.6. Simulation results of maximum axial fluid velocity in the channel center as a response to an applied angular acceleration for (a) a complete microtorus and (b) a horseshoe-type blocked torus.

3.4.4 Linear Acceleration Sensitivity

Figure 3.7a shows the simulated maximum tangential velocity as a function of applied linear accelerations in the $\hat{x}, \hat{y}, \hat{z}$ -directions for a microtorus with the dimensions given in table 3.2. As shown in equation (3.1), the tangential acceleration displacing the fluid with respect to the torus walls is equal to the applied angular acceleration times the major radius R . Thus, to compare the microtorus response to angular and linear accelerations, the linear acceleration can be transformed into an apparent angular acceleration by dividing it by the major radius R . The results are shown in figure 3.7b, which showcases thirteen orders of magnitude cross-axis rejection, which is roughly -260 dB. Thus, as expected, the sensor geometry almost completely blocks the signals stemming from the in-plane linear accelerations.

An angular acceleration of 1 rad/s^2 applied around the \hat{z} -axis introduces a maximum tangential flow velocity of $30.7 \text{ }\mu\text{m/s}$ in the channel (figure 3.6a). To achieve the same flow velocity due to a linear acceleration in \hat{x} and \hat{y} directions, this acceleration would have to be $5 \cdot 10^8 \text{ m/s}^2$ according to figure 3.7a. This again highlights to excellent linear acceleration rejection by the fluid-filled microtorus.

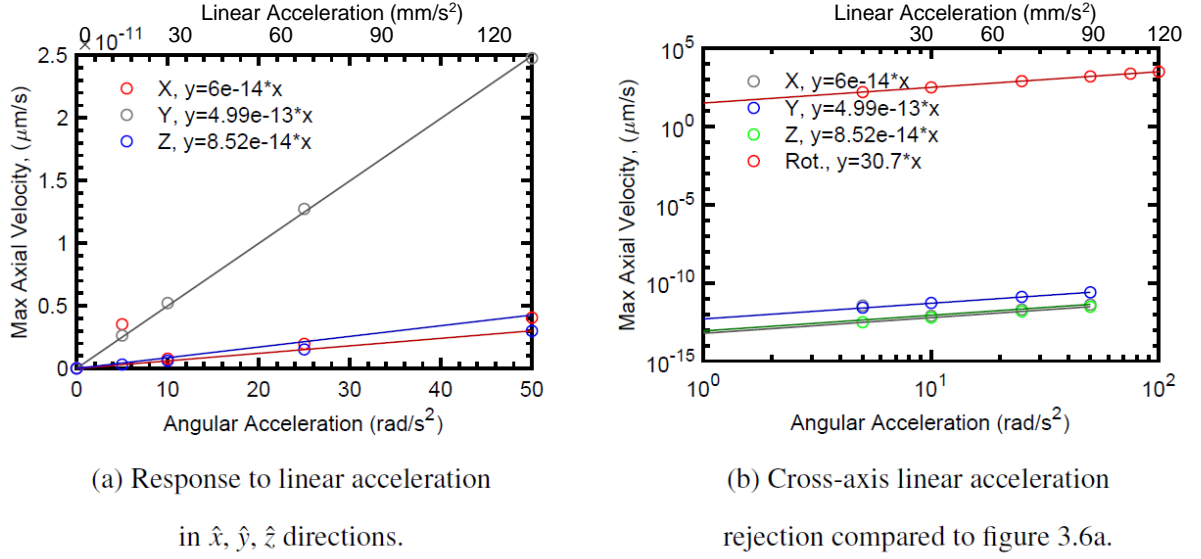


Figure 3.7. Simulated maximum tangential fluid velocity as a response to applied linear acceleration: (a) maximum tangential fluid velocity as a function of applied linear acceleration in x, y, and z direction; (b) maximum tangential fluid velocity as a function of equivalent angular acceleration.

3.4.5 Effect of Wall Stiffness

A fluid-structural interaction module was used to study the effect of the wall stiffness on the behavior of the microtorus. Figure 3.8a shows the simulated magnitude of the tangential flow velocity for a microtorus with the dimensions given in table 3.2 as a function of the Young's modulus of the torus wall for a constant angular acceleration of 10 rad/s^2 applied around the \hat{z} -axis. Clearly, the wall stiffness has no effect on the rotational sensitivity in the range of Young's moduli studied. Figure 3.8b, however, highlights that the sensitivity to linear acceleration increases with reduction in wall stiffness. In this case, a linear acceleration of 27.5 mm/s^2 was applied in \hat{x} -direction. In both case, the torus wall thickness was assumed to be $\sim 20 \text{ }\mu\text{m}$. However, the geometric constraint continues to reject the linear acceleration. The micromachined torus might be more sensitive to linear

acceleration as the walls become thinner, but this does not affect our design as we do not assume thin walls.

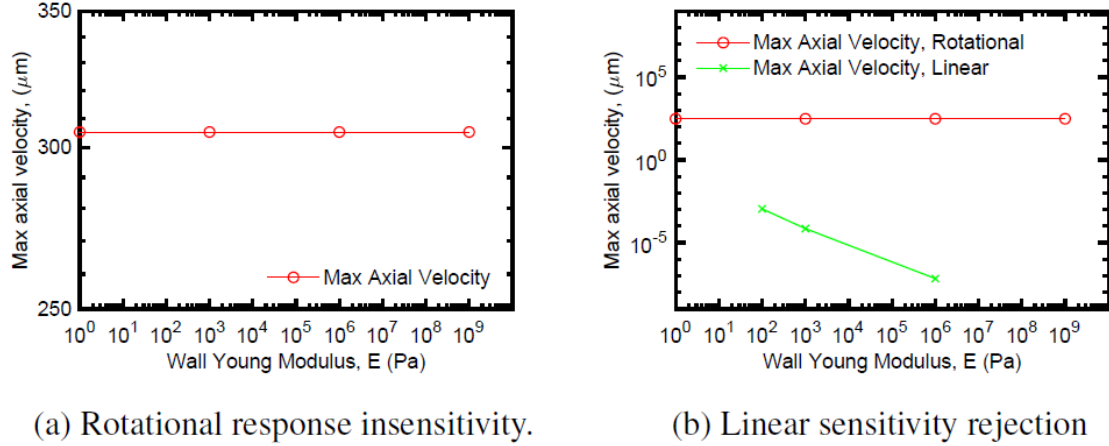


Figure 3.8. The effect of wall stiffness on rotational acceleration of 10 rad/s^2 and linear acceleration of 27.5 mm/s^2 (based on a minor radius of 2.75 mm and rotational acceleration of 10 rad/s^2), assuming a wall thickness of $\sim 20 \text{ } \mu\text{m}$ and the parameters in table 3.2.

3.4.6 Frequency Response

Two approaches were used in studying the frequency behavior of the device. In the first approach, an angular acceleration step input much shorter than the mechanical time constant of the system was applied and the mechanical response was simulated. The second approach applied harmonic rotational oscillations to the device at different frequencies. The time step for the harmonic simulation was 1/50th of the time period and the simulation was run for at least three periods after it reached harmonic steady state. According to [216], oscillating flow in a laminar flow regime can be simulated numerically with high accuracy. This gives initial confidence to the accuracy of our simulated harmonic model.

Figure 3.9a summarizes the sensor response to an angular acceleration step input from 0 to 100 rad/s^2 for micro-torii with different minor radii r . Plotted is the maximum tangential flow velocity in the channel center as a function of the time from the step input. Two results can be extracted from this simulation: first, the microtorus sensitivity to angular accelerations, as defined in equation (3.8), indeed increases with r^2 ; this can be seen by the increase of the steady-state flow velocity with r . Secondly, the characteristic time constant of this mechanical system increases with the square of minor radius r as well, as is highlighted by the slope of the transients in figure 3.9.

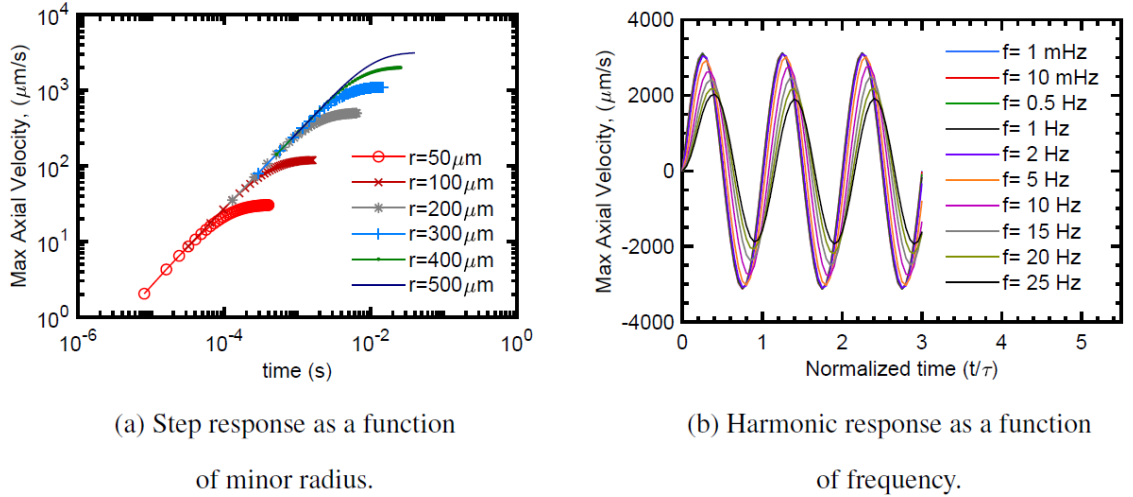


Figure 3.9. Simulated time response of maximum fluid velocity as a function of rotational acceleration: (a) Step response output as maximum axial flow velocity as a function of time; (b) Harmonic response output as maximum axial flow velocity as a function of normalized time over the period showing three periods for frequencies from 1 mHz to 25 Hz..

Figure 3.9b showcases simulated harmonic time responses of the maximum tangential flow velocity a function of the normalized time due to a 100 rad/s^2 angular acceleration sinusoidal input with frequencies from 1 mHz to 25 Hz. The normalized time is thereby the time divided by the oscillation period $T = f^{-1}$. It can be clearly seen that, as the

frequency increases, there is a phase delay and a decrease in tangential flow velocity amplitude.

The low-pass frequency domain behavior of the fluid-filled microtorus subject to applied angular acceleration, as extracted from the amplitude and phase behavior of the harmonic response in figure 3.9b is shown in figure 3.10. The simulated cut-off frequency is 20 Hz, which is very close to the value of 25.7 Hz calculated from the analytical model presented in section 3.3.8.

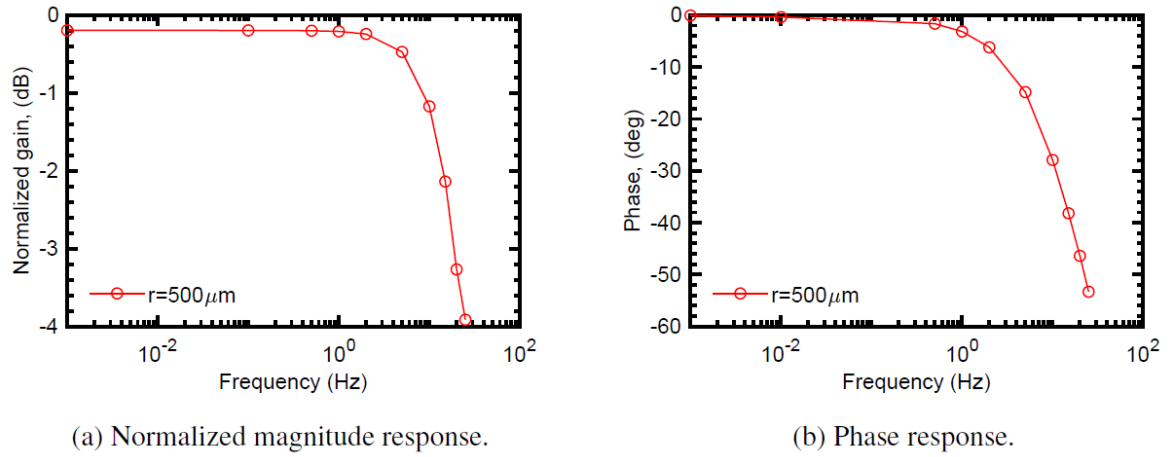


Figure 3.10. Normalized bode plot of harmonic frequency response in figure 3.9b normalized to the 1 mHz response. Of the maximum axial velocity, the (a) magnitude (b) phase at the peak of the period for each frequency is plotted as a function of frequency.

3.4.7 Geometric Parametric Study

The COMSOL model allow to study the effect of geometrical parameters and material properties on the fundamental behavior of the fluid-filled microtorus. As an example, figure 3.11a shows the effect of the minor radius on the maximum tangential flow velocity for an applied angular acceleration of 100 rad/s^2 around the \hat{z} -axis for the microtorus dimensions and material properties given in table 3.2. The results show a quadratic

relationship (i.e., a slope of 2 in the log-log plot) between the minor radius r and the maximum tangential flow velocity $v_{\hat{\theta}}$ as expected from equation (3.8). Figure 3.11b shows the extracted viscous time constant τ and the sensitivity as a function of the minor radius r

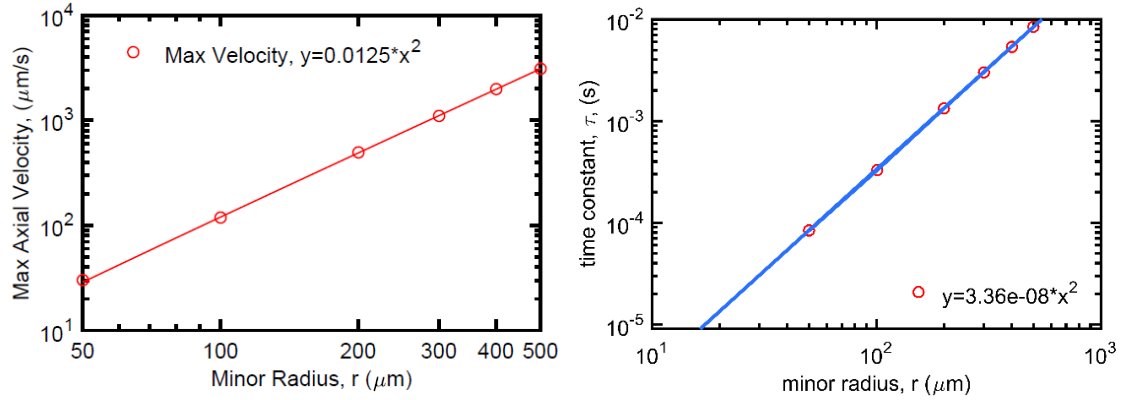
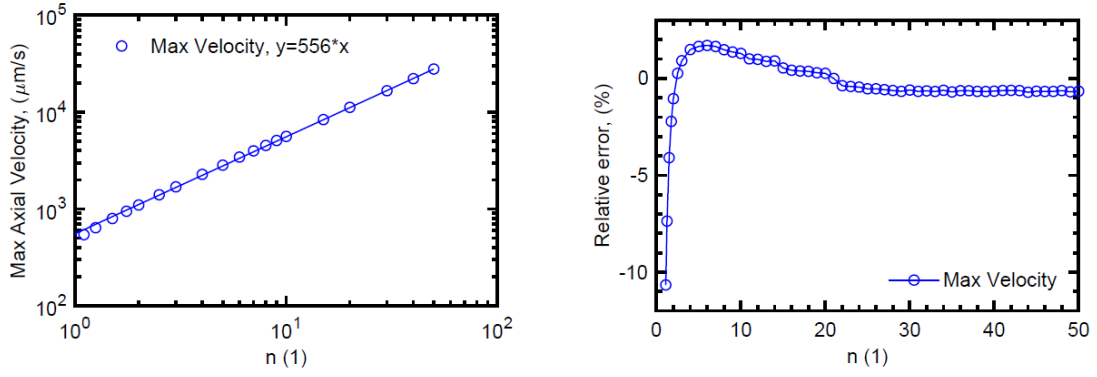


Figure 3.11. (a) Parametric study of the effect of the minor radius on maximum axial velocity for a constant angular rotational acceleration of 100 rad/s^2 . (b) Parametric study of effect of minor radius on the extracted time constant for the same angular rotational acceleration applied as in in figure 3.9a.

Figure 3.12a shows the effect of the curvature factor n , i.e. the ratio of the major to minor radius, on the maximum tangential flow velocity for an angular acceleration of 100 rad/s^2 around the \hat{z} -axis and a constant minor radius r being $500 \mu\text{m}$. The results show a linear relationship between the curvature factor n and the maximum tangential flow velocity $v_{\hat{\theta}}$ as expected from equation (3.8). However, as discussed in section 3.3, the analytical model deviates from the simulated results for $n < 10$ as indicated by the increase in relative error in figure 3.12b as $n \rightarrow 1$.



(a) Response as a function of curvature factor n . (b) Relative error of simulation result compared to the analytical solution.

Figure 3.12. Effect of curvature factor n on the maximum axial velocity as a function of rotational angular acceleration input of 100 rad/s^2 .

COMSOL simulations allow to investigate more complex torus geometries as well. Table 3.3 shows the effect of a shape function m on the general shape of a closed-loop torus. The shape function m dictates the frequency of oscillation of the minor radius as a function of the relative position along the circumference. The modulation functions are a parametric function of the parameter s , where $0 \leq s \leq 2\pi$. It modulates the x and y dimensions of the torus using as follows:

$$x = (3000\mu\text{m} + 1000\mu\text{m} \cdot \sin(m \cdot s)) \cdot \cos(s) \quad (3.24)$$

$$y = (3000\mu\text{m} + 1000\mu\text{m} \cdot \sin(m \cdot s)) \cdot \sin(s) \quad (3.25)$$

It can be seen that $m = 0$ is the standard simple circular torus. As m increases, the shape morphs into an elliptical torus with an asymmetric channel width.

Table 3.3. Parametric design of closed loops with different shape functions m .

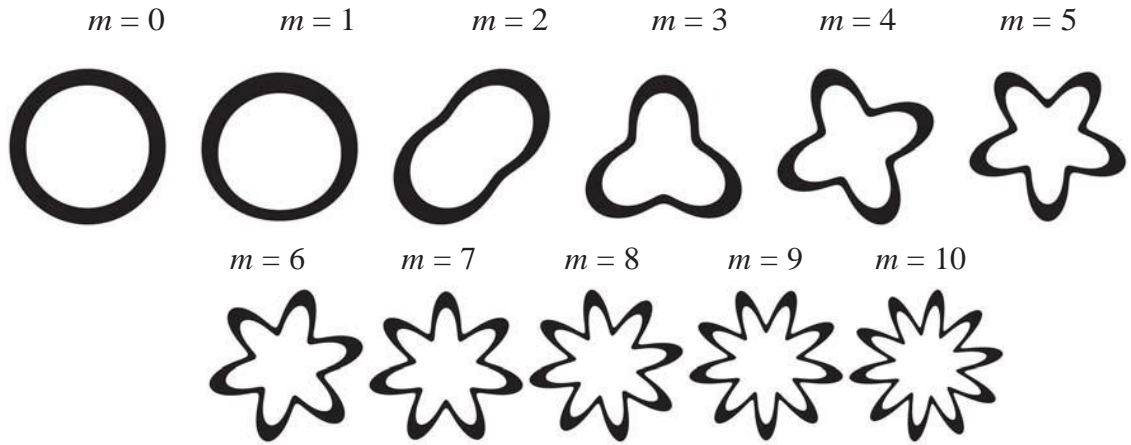


Figure 3.13 shows the steady-state maximum and average tangential flow velocity for a constant angular acceleration of $\sim 37 \text{ rad/s}^2$ as a function of the shape factor m . The average tangential fluid velocity decreases monotonically with m , similar in behavior to a low-pass filter. However, the maximum tangential fluid velocity increases for the cases of $m = 1, 2$ compared to the base case of $m = 0$, and then monotonically decreases afterward. Interestingly, the optimal case where $m = 1$ is most similar in shape to the mammalian semicircular canals.

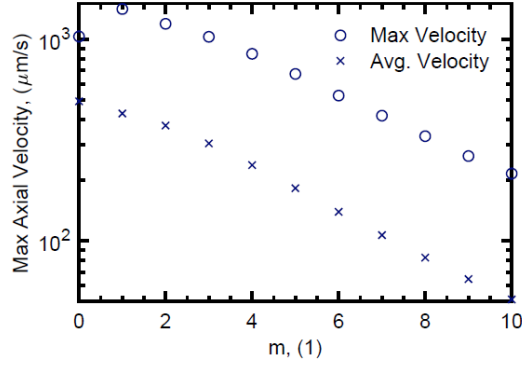


Figure 3.13. The maximum and average axial velocity to angular rotational acceleration of 37 rad/s^2 as a function of shape factor m (shown in table 3.3.) The maximum is based on the volume of the structure and the average takes the average of the velocity of the entirety of the fluid.

3.5 Conclusion

The main factors that dominate the fluid-filled microtorus' response to angular accelerations are the fluid material properties, density and dynamic viscosity, and the minor and major radii of the channel. Based on the sensitivity relationship (equation (3.9)) and the viscous corner frequency (equation (3.23)), it is evident that an increase in sensitivity typically leads to a decrease in bandwidth. The gain-bandwidth product is found by taking the products of equations (3.9) and (3.23). This product scales linearly with the factor R/π or in the form $(n \cdot r)/\pi$ or $r/(\kappa \cdot \pi)$. Thus, it is prudent to maximize the minor radius r and the curvature factor n while keeping the dimensions of the structure within the design constraints. An interesting solution to improve the sensitivity is to modulate the minor radius r as a function of the position along circumference as seen in figure 3.13.

Clearly, the bioinspired microfluidic platform is still in its infancy. Silicon-based micromachined rotation sensors are currently superior in terms of power consumption, sensitivity, robustness and overall performance. However, the simplicity and passive nature of the microfluidic platform motivates the research in this thesis to explore the limits

of a bioinspired microfluidic angular accelerometer with an as simple as possible and scalable fabrication process.

CHAPTER 4. THERMAL ANGULAR ACCELEROMETER

In this chapter, we introduce the thermal transduction mechanisms for the proposed angular acceleration sensor. The chapter will begin by describing the working principle, as well as the analysis and design of the thermally-transduced angular acceleration sensor based on a microtorus. Furthermore, the fabrication and characterization of the thermal sensor will be presented. Finally, the results of the mechanical testing will be revealed and analyzed.

4.1 Proposed Device and Working Principle

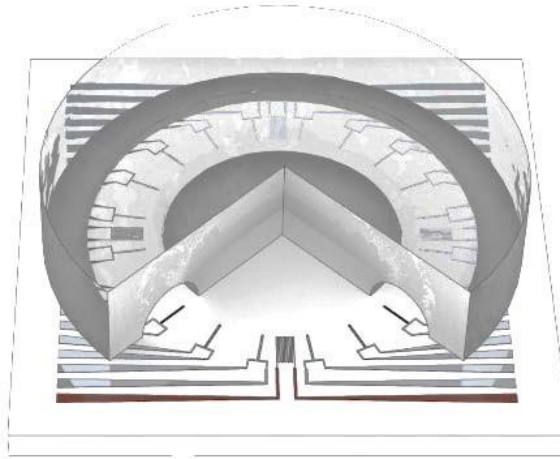


Figure 4.1. 3D-rendered model of proposed thermal angular acceleration sensor. The sensor consists of aluminum resistors and interconnects on a glass die with a bonded PDMS channel layer. A cross-section of the PDMS layer is displayed to reveal the semi-hemispherical channel over the resistors which is filled with a fluid.

In chapter 2, the natural system of the semicircular canals was introduced which converts the inertial mechanical energy to a chemical energy that is then converted to electrical pulses. In this chapter, we propose a bio-inspired angular acceleration sensor based on a microtorus similar to the semicircular canals but employing a thermal-to-electrical transduction mechanism (see device schematic in figure 4.1, an optical image of a fabricated

angular accelerometer with a major radius of 2.75 mm in figure 4.2, and its working principle in figure 4.3).

4.1.1 Concept

The device can be characterized as a microfluidic calorimetric thermal flow sensor with a geometric constraint on the fluid flow. In the calorimetric low-flow linear regime of thermal flow sensors, the measured temperature differential is strictly proportional to the fluid velocity until a threshold velocity [129]. In micromachined thermal linear accelerometers, the inertial forces accelerating the fluid will correlate to the fluid velocity [217]. By adding the microtorus geometry, the fluid velocity linearly correlates to angular acceleration.

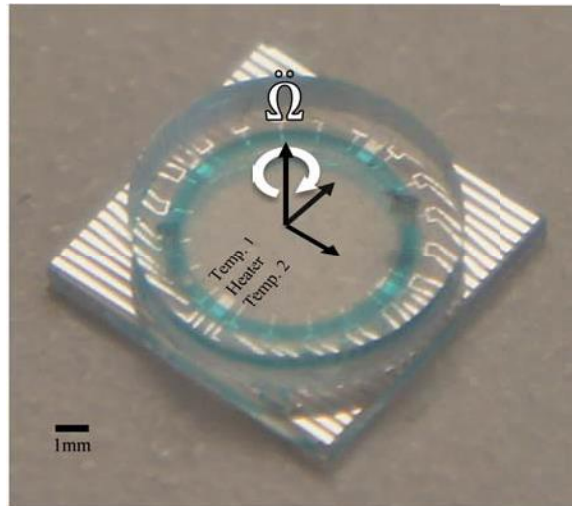


Figure 4.2. Optical image of fabricated angular accelerometer with microtorus radius $R = 2.75$ mm.

4.1.2 Working principle

The working principle of the device is highlighted in figure 4.3 and further elaborated in the simulation section in figure 4.7. The device requires a symmetric thermal gradient to operate. To create the thermal gradient, energy is introduced to the system by applying an

electric potential across a thin film resistor, which causes joule heating. The power injected by the heater into the fluid remains constant with small flow velocities [218]. The heating element induces a symmetric temperature profile in the fluid along the microtorus channel. An inertial force will cause the fluidic mass to accelerate relative to the walls with a parabolic velocity profile inside the microchannel due to laminar flow. The flow disturbs the symmetrical temperature profile around the heater causing a temperature gradient. In the case of creeping flow ($Re \ll 1$), the velocity profile has a fixed shape function multiplied by the magnitude of the mean velocity [219], [220]. The increase in the temperature downstream (in the direction of fluid flow or the red resistors R1 and R4 in figure 4.3a) will equal the decrease upstream (away from fluid flow or the blue resistors R2 and R3 in figure 4.3a) up to a threshold velocity [221]. This temperature asymmetry is detected by temperature-sensitive resistors due to the temperature coefficient of resistance. The minimum number of heaters and temperature sensors to operate the device with interfering signal rejection is two heaters and four temperature sensors. However, additional thermal sensors can be placed along the circumference for redundancy and further signal processing.

Figure 4.3 depicts the response of the system to a counter-clockwise angular acceleration and linear acceleration. The heaters are depicted in black. The showcased device is operating using two heaters located at 3 o'clock and 9 o'clock marks. The temperature-sensitive resistors R₁, R₂, R₃ and R₄ are connected in a Wheatstone bridge as shown in the circuit schematics. Upon anti-clockwise angular acceleration of the structure (black arrow) and a resulting clockwise rotation of the fluid (green arrow) with respect to the structure due to fluid inertia (figure 4.3a), the red thermal sensors (R₁ and R₄) will experience an

increase in temperature, while the blue ones (R_2 and R_3) see a decrease in temperature; thus, the Wheatstone bridge will experience maximal output if connected as shown in the circuit diagram. However, upon in-plane upwards linear acceleration of the structure, the Wheatstone bridge will experience no output due to the symmetric change in resistance in both legs of the bridge (figure 4.3b).

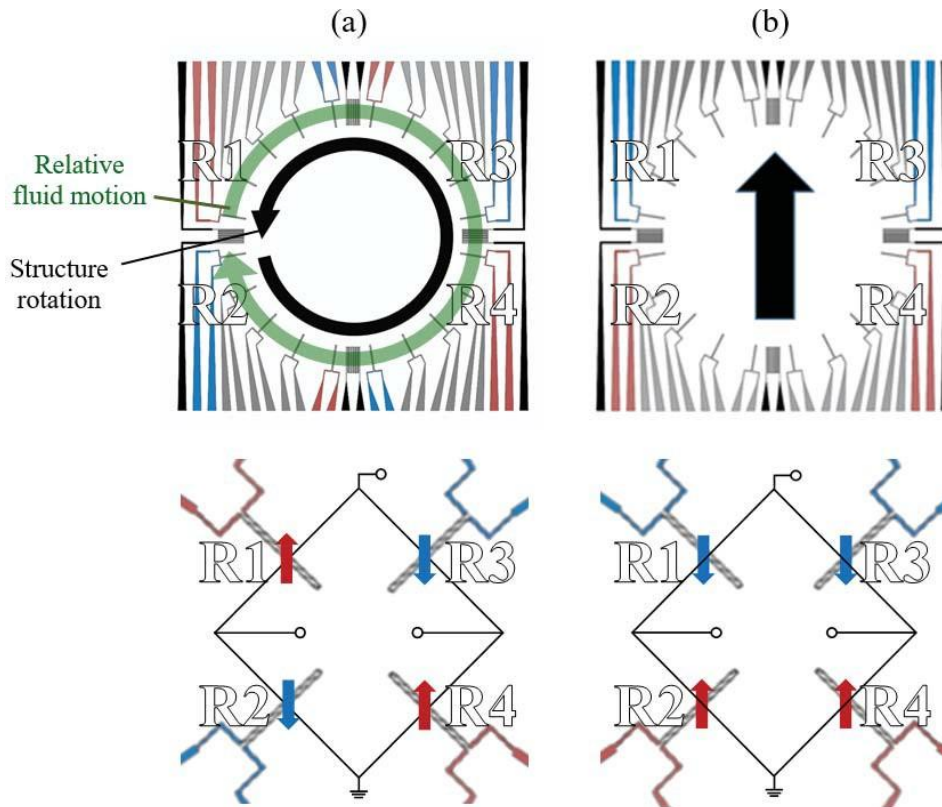


Figure 4.3. Thermal angular acceleration sensor schematic with heaters (black) and thermal sensors response in red (increase in temperature) and blue (decrease in temperature) arranged along a torus experiencing (a) counter-clockwise structure rotation with maximal response from Wheatstone bridge; or (b) upwards linear acceleration with minimal response from Wheatstone bridge.

4.1.3 Inertial frames of reference

In the thermal linear accelerometer literature, consistency in properly setting up the inertial frames of reference is lacking. In general, there are two different inertial reference frames used; these two systems are shown in figure 4.4 below.

The first frame is a fixed inertial reference frame I , which is located outside of the structure. The second frame is an accelerating reference frame attached to the walls of the structure as shown in frame B . Depending on the point of reference of the inertial frame, the *relative direction* of the acceleration of the fluid will flip. Upon the initial anticlockwise acceleration $\{\vec{\alpha}\}^I$ of the microtorus wall in frame reference I , **the fluid will lag the channel walls due to the inertia of the fluid. This is supported by the following papers from the literature regarding semicircular canals** [109], [110], [120], [121]. It is important to note that the relative motion of the fluid is anticlockwise to the observer in frame I .

To better understand the dynamics of the system, accelerating frame reference B is chosen as the reference frame in this work. In frame B , the observer is attached to the microtorus walls and, thus, accelerating anticlockwise at the same rate as the structure. In the microfluidic angular accelerometer, the resistive temperature sensors act as “observer” and they indeed rotate with the structure. In this frame of reference, acceleration of the fluid relative to the wall and thus observer $\{\vec{\alpha}\}^B$ is clockwise, i.e. having the opposite sign of the acceleration of the structure in the previous frame, but the same magnitude.

Thermal μ SCC (Fixed Inertial Frame) Thermal μ SCC(Accelerating Inertial Frame)
(Co-rotating frames)

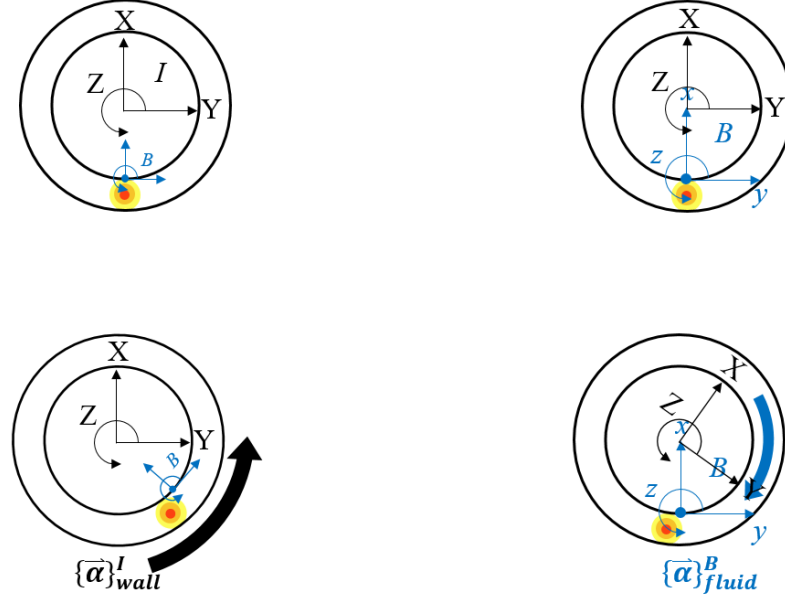


Fig. 4.4: Acceleration direction is dependent on the inertial frame of reference chosen.

$$\left| \{ \vec{\alpha} \}^I \right| = \left| \{ \vec{\alpha} \}^B \right| \quad (4.1)$$

In frame reference B , the walls of the channel are not accelerating relative to the observer as they are fixed relative to the rotating observer. Going forward the authors will continue to use the accelerating reference frame B to explain the working principle of the device. This accelerating inertial frame of reference is more relevant as designers care about *the relative motion of the fluid with respect to the fixed heater and temperature sensor attached to the rotating structure*. In the literature of thermal linear accelerometers, some authors assume an accelerating inertial reference frame as shown in the following example papers [222], [223]. However, a recent review paper of thermal linear accelerometers [224]

shows a fixed inertial frame. Both descriptions point to the same physical phenomenon, but from two different viewing frames.

Based on this explanation, our proposed device works as localized linear accelerometer as described in the literature. There are several forces contributing to the output of the thermal device. The viscous drag and inertial Euler forces affect the device as discussed in section 3.3. Another force is caused by the buoyancy effect due to density variations in the heated fluid. The buoyancy force will be sensed when any acceleration acts on a density gradient, even changes as small as 0.1 kg/m^3 (roughly 0.01% or 100 ppm change in water for instance) [189]–[191], [199].

4.1.4 Desired and interfering input signals

The viscous drag inhibits the signal by adding friction to the fluid flow. The rotational inertial force is the signal of interest. The buoyancy is an interfering signal that will have to be distinguished from the desired signal of rotational input. To resolve self-interference caused by heating the fluid, a few methods are discussed in the next section.

4.1.5 Suppressing and rejecting interfering signals

All non-desired buoyancy and inertial forces will need to be suppressed and rejected. The fluid-filled torus should inherently suppress any inertial signal other than the in-plane rotation [155], [170], [197]. This is based on the assumption that the fluid has *constant density across the circumference* of the torus [189]. This assumption is *not true* in our thermal-based design due to the active heating element causing a density gradient.

Besides the inherent mechanical filter function of the torus promoting signals from in-plane rotations, other techniques can be used to suppress signals from interfering accelerations. One possible technique uses strategically placed sensors along the channel. Under different accelerations, a unique signature of signals will be outputted. This technique is further explained in [225].

Another technique uses two heaters and four resistors connected in a full Wheatstone bridge. If connected properly, this arrangement can suppress any common-mode signal, while amplifying the desired (differential) signal. This is illustrated in figure 4.3. In rotation, the Wheatstone bridge will be at its maximal change. When under linear acceleration, both legs of the bridge experience the same change. The output of the bridge should be zero. Thus, the sensor is immune to linear acceleration and only measures angular accelerations, even in the presence of buoyancy forces. In the interfacing circuitry, adding an instrumentation amplifier can further suppress common mode signals.

4.2 Sensor Analysis

The section introduces an analytical model of the sensing system, which helps build a first order understanding of the system, and guide the design of the sensor parameters according to need.

4.2.1 Forces

Equations (4.1)-(4.5) define the body forces acting on the system. Thereby, the body forces are expressed in units of force per volume [Nm^{-3}], which is equivalent to the density ρ times the linear acceleration a_i . In the reference frame rotating with the inertial sensor (as

described earlier as reference frame B), there are three Cartesian unit vectors $\langle \hat{i}, \hat{j}, \hat{k} \rangle$. These unit vectors when used as a subscript show the main direction for linear motion, and axis of rotation for rotational motion. When the subscript is dropped for rotational motion in this thesis, z or k-axis rotation is assumed. In this reference frame, the (fictitious) Euler force F_e causes a tangential acceleration along the circumference of rotation. The tangential acceleration relates to the applied angular acceleration though $\alpha = a_T / R$, where α , a_T , and R are the angular acceleration, tangential acceleration, and major radius of the torus, respectively. The linear inertial force F_a is density ρ times the acceleration a .

$$F_{e_i} = \rho(R_j \ddot{\phi}_k - R_k \ddot{\phi}_j); \quad (4.2)a$$

$$\text{If rotating around } \hat{z} \text{ or } \hat{k}, F_e = -ma_T = -m\ddot{\phi}R = -m\alpha R \quad (4.2)b$$

$$F_a = \rho a_i \quad (4.3)$$

$$F_{\theta_i} = 2\rho(v_j \dot{\theta}_k - v_k \dot{\theta}_j) \quad (4.4)$$

$$F_{c_i} = \rho R_i (\dot{\theta}_j^2 - \dot{\theta}_k^2) \quad (4.5)$$

$$F_b = \rho a \beta \Delta T \quad (4.6)$$

The centrifugal force F_c (equation (4.5)) and Coriolis force F_Ω (equation (4.4)) in the radial direction can be neglected, based on an order of magnitude calculation. According to [111], the forces are too small to create secondary radial flow based on our design parameter space.

Finally, the work done by pressure gradients will be simplified into a body force (the buoyancy force F_b ; equation (4.6)) using the Boussinesq approximation [226]. The

approximation is based on low temperature variations ($\beta \cdot \Delta T \ll 1$), where β is the coefficient of thermal expansion and ΔT is the heater temperature rise compared to the ambient.

4.2.2 Non-dimensional analysis

Non-dimensional parameters based on the Buckingham Pi theorem [227] need to be defined to help analyze the system. By extending the linear thermal accelerometer analysis to rotational accelerometers based Bahari et al. [228], we arrive at the following non-dimensional parameters in equations (4.6) - (4.12). The Reynolds number Re relates the inertial forces to the viscous forces. The dean number De indicates the effect of curvature on the velocity flow. If $De < 1$, as shown in section 3.3, the microtorus will have the same friction factor and velocity profile as a straight [229]. It is expected that the Dean number will not exceed one because to do so would require an extremely high velocity.

$$Re = \frac{\rho v r}{\mu} \quad (4.7)$$

$$\kappa = \frac{r}{R} \quad (4.8)$$

$$De = \kappa^{0.5} Re \quad (4.9)$$

$$Gr_{rot} = \frac{\rho^2 \ddot{\phi} R r^3 \beta \Delta T}{\mu^2} \quad (4.10)$$

$$Pr = \frac{c \mu}{k} \quad (4.11)$$

$$Ra_{rot} = Gr_{rot} Pr = \frac{c\rho^2\ddot{\phi}Rr^3\beta\Delta T}{k\mu} \quad (4.12)$$

$$\delta T = Ra_{rot}\Delta Tf(d, r, R) \quad (4.13)$$

The Prandtl Number Pr is the ratio of the momentum diffusivity to the thermal diffusivity. A $Pr > 1$ means that momentum transfers better than heat, which is desirable. The rotational Grashof number $Gr_{\dot{\Omega}}$ relates the buoyancy forces to the viscous forces. $Gr_{\dot{\Omega}}$ is based on the fluid thermal properties and the system parameters. The rotational Rayleigh number $Ra_{\dot{\Omega}}$ is the Gr_{rot} multiplied by Pr number. The expected sensitivity for the device δT (temperature difference between two detectors) will correlate with rotational Rayleigh number, ΔT , and $f(d, r, R)$ is a function of the channel shape and distance between the heater and the temperature sensor d [228]. Also according to [228], if a system's Rayleigh number is lower than a critical value, the heat transfer by the contained fluid is mainly conductive. According to Wu [230], only a small percentage of the heat transfer is due to convection if the Rayleigh number is smaller than 100. Based on values in table 4.1, the expected rotational Rayleigh number is 0.0125 for a thermal rotational accelerometer filled with silicone oil and rotated at 1 rad/s² angular acceleration with a major radius of 2.75 mm and a minor radius of 500 μm . Therefore, heat transfer is concluded to be primarily conductive. However, it is the heat transfer by convection due to the fluid flow induced by an applied angular acceleration that creates the differential temperature detected by the two temperature sensors. To address the effect of gravity, when experiencing a 1 g linear acceleration, the Rayleigh number is 45, which is still below the 100 threshold mentioned above.

4.2.3 Analytical model

To find an analytical model for the sensor, assumptions must be made to simplify the model:

(1) All parameters are assumed constant with temperature; (2) The channel has a circular cross section; (3) The fluid is assumed to be an incompressible fluid, with laminar flow and no slip boundary conditions inside the microtorus, and assuming that low frequency oscillations yields a quasi-steady-state solution for velocity flow profile; (4) Small curvature $\kappa \ll 1$, where $\kappa = r/R$ is assumed; (5) We assume that the metals, the die and the channel walls are heat sinks to calculate the temperature profile of the flow in the channel; moreover, heat transfer by radiation is ignored. Based on thermal low flow sensors, heat transfer is dominated by conduction. However, the output signal is caused by natural convection [228]. For simplicity, these assumptions are used in our model.

Using Newton's first law, we balance the forces acting on the system as shown in figure 3.3a. The viscous drag of the fluid in the microchannel cancels out the buoyancy and inertial forces. According to [231], the non-isothermal laminar mass flow is governed by the steady-state Navier-Stokes equations for incompressible flow. The continuity, momentum and energy equations are

$$\vec{\nabla} \cdot \vec{v} = 0 \quad (4.14)$$

$$\frac{\partial \vec{v}}{\partial t} + \rho(\vec{v} \cdot \vec{\nabla})\vec{v} = F + \rho\beta(T - T_0) + \mu\nabla^2 \vec{v} \quad (4.15)$$

$$\frac{\partial T}{\partial t} + (\vec{v} \cdot \vec{\nabla})T = \alpha\nabla^2 T \quad (4.16)$$

where \vec{v} is fluid velocity (with respect to the channel walls), μ is dynamic viscosity and ρ is density, T is temperature and T_c is temperature outside of the device, F_b are the body forces acting on the fluid, and α_{fluid} is thermal diffusivity.

Due to the toroidal shape of the device, we will use cylindrical coordinates. The viscous heat dissipation term is ignored for the expected velocities [231]. Due to the Boussinesq approximation assumption, we set the heat source term to zero [232]. Assuming an axially symmetric velocity flow solution, we can simplify the equations to:

$$\frac{\partial \vec{v}_\theta}{\partial t} = \sum F_i + \rho\beta(T - T_0) + \mu \left[\frac{\partial^2 \vec{v}_\theta}{\partial r^2} + \frac{1}{r} \frac{\partial \vec{v}_\theta}{\partial r} \right] \quad (4.17)$$

$$\frac{\partial T}{\partial t} + \frac{\vec{v}_\theta}{r} \frac{\partial T}{\partial \theta} = \alpha \left[\frac{1}{r^2} \frac{\partial^2 T}{\partial \theta^2} \right] \quad (4.18)$$

where v_θ is the fluid velocity in the axial direction.

4.2.4 Sensitivity

According to [124], [213], the steady state solution to (4.16) is

$$v_\theta = \frac{\rho R r^2}{4\mu} \dot{\Omega} \quad (4.19)$$

We define the sensitivity of the fluid velocity to angular acceleration as

$$S_{\frac{v}{\dot{\Omega}}} = \frac{\rho R r^2}{4\mu} \quad (4.20)$$

The relationship between the fluid velocity and temperature profile depends on the fluid's thermal and inertial parameters, the geometry of the channel, the initial conditions, and the configuration of the temperature sensors and heaters. Based on quasi-steady state differential equation for temperature in one dimension for laminar calorimetric flow sensors [218], the temperature difference induced by the heater compared to the ambient temperature is

$$\Delta T = \frac{P}{k \left(\frac{r}{d} w_H + \pi r^2 (\lambda_1 - \lambda_2) \right)} \quad (4.21)$$

$$\lambda_{1,2} = \frac{1}{2\alpha_{fluid}} \left[v \pm \sqrt{v^2 + \frac{4(\alpha_{fluid})^2}{r^2}} \right] \quad (4.22)$$

where P is the power dissipated by the heater, w_H is the heater width, and $\lambda_{1,2}$ are the eigenvalues to the differential equation in [218]. Also, the difference in temperature between the upstream and downstream detectors δT can be calculated using

$$\delta T = \Delta T \left(e^{\lambda_2(d-w_H)} - e^{\lambda_1(-d+w_H)} \right) \quad (4.23)$$

If we plug in (4.20) in (4.22), and take its derivative with respect to velocity, assuming

$w_H \rightarrow 0$, we can define the sensitivity of δT to fluid velocity as

$$S_{\frac{\delta T}{v}} \sim \frac{d}{r} \frac{P}{\alpha_{fluid} k} f(r, R, d) \quad (4.24)$$

where $f(r,R,d)$ is a function of the minor and minor radii and the distance between the temperature sensors and the heater [228], [233]. It is highly dependent on geometry of the channel. To convert the change in temperature δT into a measurable voltage, we take advantage of the temperature coefficient of resistance of metals. The change in resistance is expressed as

$$R_T = R_0 + \alpha_{TCR} R_0 \delta T \quad (4.25)$$

$$\Delta R = \alpha_{TCR} R_0 \delta T \quad (4.26)$$

R_0 is the initial resistance under no flow and no heating condition, ΔR is the change in resistance due to heating and/or flow, and α_{TCR} is the temperature coefficient of resistance. We assume that α_{TCR} is constant across the output temperature.

The change in temperature relates to the output voltage according to the full Wheatstone bridge equation (4.26). The change in resistance ΔR for each resistor is assumed to be approximately the same for simplification purposes

$$V_G = AV_0 \left[\frac{R + \Delta R}{R + \Delta R + R - \Delta R} - \frac{R - \Delta R}{R + \Delta R + R - \Delta R} \right] \quad (4.27)$$

$$V_G = AV_0 \frac{\Delta R}{R} \quad (4.28)$$

V_G is the bridge voltage. A is the electronic gain. V_0 is the applied voltage. If we plug (4.25) into (4.27), we arrive to

$$V_G = \alpha_{TCR} \delta T A V_0 \quad (4.29)$$

The sensitivity of the sensor is defined as the change in voltage output divided by change in the angular acceleration

$$S_{\frac{V_G}{\Omega}} = \alpha_{TCR} A V_0 S_{\frac{\delta T}{v}} S_{\frac{v}{\Omega}} \quad (4.30)$$

We plug in the sensitivities into (4.29) and assume that $d \sim r$ to simplify the equation.

$$S_{\frac{V_G}{\Omega}} \approx \alpha_{TCR} A V_0 \frac{\rho P R r^2}{\mu \alpha_{fluid} k} g(r, R, d) \quad (4.31)$$

Based on **Error! Reference source not found.**, we can choose the materials for improved sensitivity. This includes metals of high temperature coefficient of resistance, fluids with higher Pr number, higher density, with low viscosity. Other design choices are operating the device at higher power levels, and most important of all increasing the minor radius r (assuming that $R=n r$), as the sensitivity of the sensor is proportional to r^3 . Based on this analysis, the minor radius is the critical dimension to control in designing the sensor. However, increasing r is limited by its effect on the frequency behavior (see section 4.2.6).

4.2.5 Linearity

In order to estimate the dynamic range of the sensor, we must study the limits of its linearity [234]. The velocity boundary layer thickness δ is the distance at which the velocity reaches free stream velocity. The thermal boundary layer thickness δ_{th} is the distance at which the thermal gradient ceases to exist [235]. The two are related by the Prandtl number $\delta_{th} = Pr^{-1/3} \delta$ [215]. In most liquids, $Pr > 1$. Thus, the thermal layer is smaller than the velocity layer. According to [215], calorimetric flow sensors operate in the linear regime when the velocity boundary layer thickness $\delta \gg d$. Also, forced convection starts

dominating the heat transfer when $\delta_{th} \sim d$. Generally, conduction dominates within the thermal boundary layer.

As the flow velocity increases, the dominant heat lost mechanism becomes forced convection at a critical velocity. This will be the critical velocity where convective cooling of the heater starts and the temperature difference between the temperature sensors becomes nonlinear. This partially explains the potential output saturation at high acceleration because any increase in temperature due to acceleration is offset by convective cooling of the heater from the high fluid velocity. This non-linearity can also be attributed to the dependence of fluid's properties on temperature and inertia [236]. According to [218], the turn over velocity or the critical saturation velocity is

$$v_{to} = \frac{2\alpha_{fluid}}{r} \quad (4.32)$$

By plugging (4.32) into (4.18), we arrive at a rough estimate of the dynamic range of

$$\dot{\Omega}_{to} = \frac{8\mu\alpha_{fluid}}{\rho R r^3} \quad (4.33)$$

4.2.6 Frequency

To model the frequency behavior of the sensor, three transfer functions are considered: (1) the viscous transfer function from the applied angular acceleration to the fluid velocity (discussed in section 3.3.8), (2) the transfer function from the fluid velocity to fluid temperature profile and (3) the transfer function from the heater temperature to the fluid temperature profile. The heater rise time is not considered, as we assume the heater is at the desired temperature.

The latter two transfer functions can be modeled as an RC circuits [236], [237]. The difference between the two time constants is their *characteristic length*. One is based on the distance between the heater and the temperature sensor. The other on the radius of the channel. The characteristic time constants and cut-off frequencies are given by

$$\tau_{th1} = R_{th1}C_{th1} \cong \frac{r^2}{\pi^2\alpha} \quad (4.34)$$

$$f_{th1} \cong \frac{\pi\alpha}{2r^2} \quad (4.35)$$

$$\tau_{th2} = R_{th2}C_{th2} \cong \frac{d^2}{\pi^2\alpha} \quad (4.36)$$

$$f_{th2} \cong \frac{\pi\alpha}{2d^2} \quad (4.37)$$

where τ_{th1} and f_{th1} correspond to the transfer function from the fluid velocity to fluid temperature profile and τ_{th2} and f_{th2} to the transfer function from the heater temperature to the fluid temperature profile. Since in our designs $d \approx r$, both time constants are similar.

For velocity profile with high Prandtl numbers, the velocity field develops relatively quickly and it is the development of the temperature differential that determines the response time. This leads to the last two time constants dominating the transfer function of the sensor. The expected frequency response would be a second order transfer function of real poles. It has been shown that laminar flow observes a consistent frequency behavior until a critical velocity [238]. This means that the main property of the fluid that impacts the device's performance is the fluid thermal diffusivity [222] affecting both the frequency

response and the sensitivity of the device. Less diffusive fluids such as liquids will have higher sensitivity, but smaller bandwidth. Any increase in sensitivity is offset by a reduction in bandwidth. The resulting low bandwidth can be overcome by operating the device in a closed loop configuration with a PID controller [239]. Another solution is characterizing the device transfer function and adding a compensating transfer function to the output to increase the bandwidth, as used by commercial thermal linear accelerometers [240].

4.3 Finite Element Modeling of Sensor

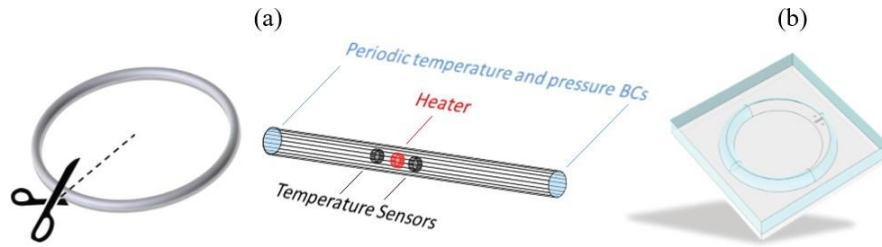


Figure 4.5. Finite element method simulation of biomimetic angular accelerometer: (a) Simplified model with straight cylindrical channel and periodic boundary conditions for temperature and pressure at the end of the channel; (b) Full 3D model of the half-torus structure including glass substrate and PDMS cover.

A finite element analysis of the sensor was performed using COMSOL Multiphysics Software 5.3a (Burlington, MA). The non-isothermal laminar flow module was used. The fluid was assumed to be incompressible and the flow laminar. The effect of viscous dissipation and the work done by pressure changes were considered. The simulation process started with a simplified linear channel with symmetric boundary conditions for heat and pressure, as shown in Figure 4.5. This was followed by a 3D simulation of the full structure. The simplified model was used to optimize the design of the structure due to its fast simulation times. The complete packaged 3D model was used to plot the figures in this

section. The geometric parameters used were $R=2.75$ mm, $r=300$ μm , $d=350$ μm . The material properties used unless noted otherwise are presented in table 4.1. It should be noted that the effect of gravity is not included in the simulations presented in section 4.3. This is motivated by the fact that gravity in the $-\hat{z}$ -direction had a negligible effect on the results. Other orientations with respect to gravity are not presented.

Table 4.1. Material properties for non-isothermal laminar flow simulations.

Symbol	Quantity	Glass	Al	PDMS	Silicone Oil	Units
ρ	Density	2210	2700	970	930	kg/m^3
k	Thermal conductivity	1.14	238	0.16	0.1	$\text{W}/(\text{m} \cdot \text{K})$
c	Heat capacity	730	900	1460	1400	$\text{J}/(\text{kg} \cdot \text{K})$
μ	Dynamic viscosity	–	–	–	5	$\text{mPa} \cdot \text{s}$
β	Coefficient of vol. exp.	–	–	–	0.001	$1/\text{K}$

As an example, Fig. 4.6a shows the simulated temperature differential, i.e. the temperature difference between a fluid-filled microtorus with applied and zero angular acceleration, along the torus with two heaters on opposite sides in case of applying a clockwise angular acceleration of $1,000 \text{ deg}/\text{s}^2$. The resulting temperature asymmetry around the heater is clearly visible with a maximum temperature difference between up and downstream temperature sensor location of approx. 75 mK. The temperature profile is shown in Fig. 4.6b for different applied angular accelerations and highlights the importance of an optimal location for the temperature sensor to maximize sensitivity. Just near the heater, thermal conduction dominates and the temperature difference would be too small. When the sensors are too far away from the heater, the effect of convection decreases and the heater is not felt. Thus, there is an optimal location or region for the sensor. This location is dependent on the amplitude of the acceleration. As the input acceleration increases, the maximum

temperature differential occurs further away from the heater. For the frequencies and magnitudes of interest, an optimal region is highlighted in red and comes out to be between 150-300 μm from the heater in Fig. 4.6b.

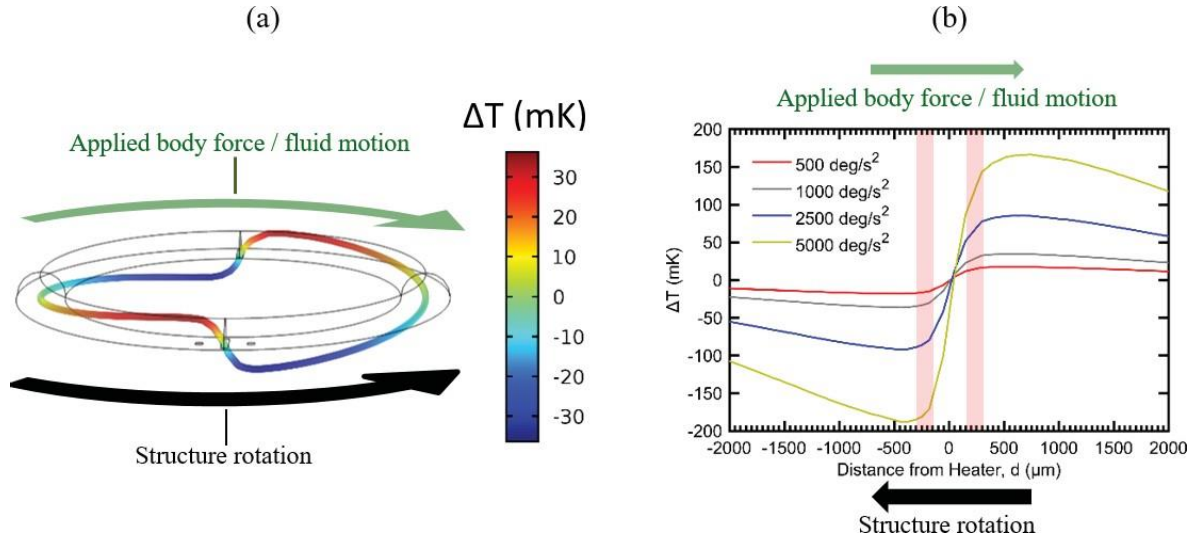


Figure 4.6. (a) Simulated temperature differential profile ($\Delta T = T(1000 \text{ deg/s}^2) - T(0 \text{ deg/s}^2)$) along the circumference of the microtorus for an anticlockwise angular acceleration to the structure of 1,000 deg/s^2 . The applied body force is in the clockwise direction (corresponding to a counter-clockwise structure rotation). The scaled height of the profile correlates to ΔT in addition to the color coding. (b) Simulated temperature differential profile for different angular accelerations as a function of the distance from the heater center line.

A body force of the density times the acceleration was applied to the fluid to simulate the applied angular acceleration. A point of constant pressure was set to the reference pressure of 0 Pa on the circumference of the torus. A constant power was applied to the heating resistor, which was modeled as a boundary between the glass and the silicone oil. The outside boundaries were set to room temperature. The temperature detectors were modeled as boundaries as well. The mesh was refined until the solution converged. The device is simulated under the assumption that the heater has reached steady-state. To simulate the temperature sensed by the temperature detectors, the temperature was averaged over the sensor's area. Two methods were used to apply the body force. The first method mapped

cylindrical coordinates to Cartesian. The second is by creating a toroidal coordinate system. Both methods had similar results.

4.3.1 Sensitivity and Cross-Sensitivity

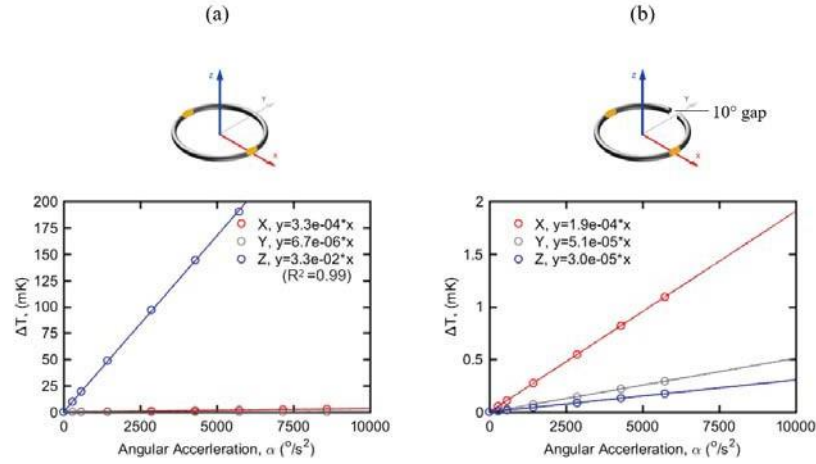


Figure 4.7. Simulated temperature difference between the two temperature sensors as a function of the applied angular acceleration around the desired \hat{z} -axis and interfering \hat{x} and \hat{y} -axis for a bioinspired angular accelerometer with dimensions given in Table 4.1: (a) full microtorus structure; (b) horseshoe-shaped microtorus with 10° gap. The schematics show the rotation axis with respect to microtorus and heater locations (yellow).

Fig. 4.7a shows the simulated temperature difference between the two temperature sensors for an angular accelerometer with the dimensions given in Table 4.1 as a function of the applied angular acceleration for rotations around the \hat{x} , \hat{y} , and \hat{z} -axis. The distance between the heater and the detectors is $250 \mu\text{m}$ in the simulations, unless specified otherwise. To highlight the importance of the torus structure, Fig. 4.8b shows the simulated temperature difference between the temperature sensors as a function of the applied angular acceleration for a horseshoe-shaped microtorus (an incomplete torus with a 10-degree break) with otherwise same dimensions. As expected, the sensor geometry promotes signals stemming from the in-plane rotation around the \hat{z} -axis with a sensitivity of 33

$\mu K / (^\circ / s^2)$, while signals from rotations around the \hat{x} and \hat{y} -axis are suppressed by at least two orders of magnitude. Also, clearly seen from comparing the blocked case to the unblocked case, the sensor sensitivity to rotations around the \hat{z} -axis is reduced by two orders of magnitude while the cross-sensitivities to angular accelerations around the \hat{x} and \hat{y} -axis remain largely unchanged.

4.3.2 Frequency

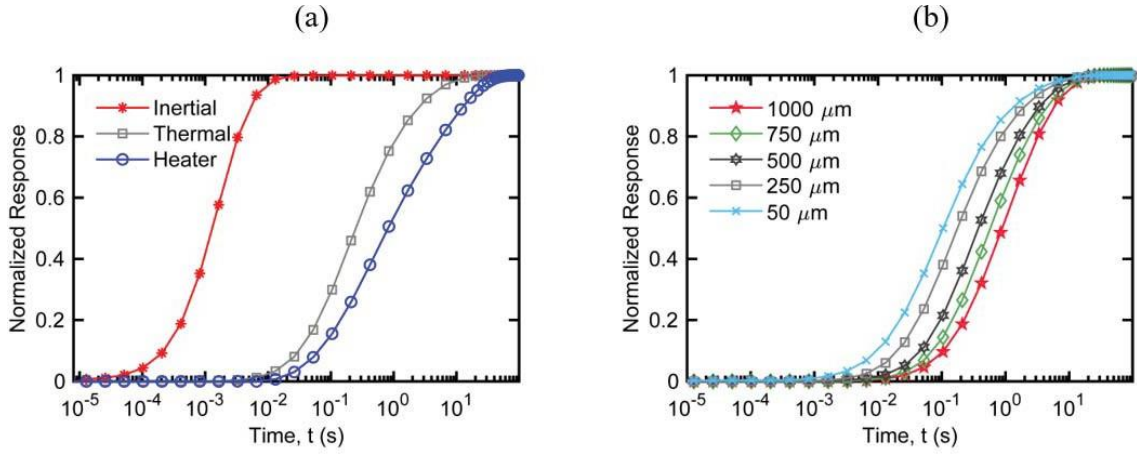


Figure 4.8. (a) Simulated normalized response of the angular accelerometer to an angular acceleration step input from 0 to 1,000 deg/s^2 : (i) inertial response; (ii) thermal response; (iii) heater response. (b) The simulated effect of the distance of the temperature sensor from the heater on the thermal response of the angular accelerometer subject to the same angular acceleration step input from 0 to 1,000 deg/s^2 .

Two approaches were used in studying the frequency behavior of the device: In the first approach highlighted in figure 4.8 (and later on in figure 4.22), an angular acceleration step input much shorter than the mechanical time constant of the system was applied and the mechanical response was simulated with both the heater on and off. The second approach applied harmonic rotational oscillations to the device at different frequencies. The harmonic oscillation results are highlighted in section 4.6.2 and Figure 4.22. The coupled-physics time-dependent simulation uses the steady-state temperature elevation of the heater

under no flow as an initial condition. The time step for the harmonic simulation was 1/50th of the time period and the simulation was run for at least 5 periods after it reaches harmonic steady state. According to [216], oscillating flow in a laminar flow regime can be simulated numerically with high accuracy. This gives confidence to the accuracy of our simulated harmonic model.

Fig. 4.8 summarizes the sensor response to an angular acceleration step input from 0 to 1,000 deg/s². Thereby, the normalized inertial and thermal responses are compared. The normalized *inertial* response to the 1,000 deg/s² step input is defined as the ratio of the maximum flow velocity of the fluid in the center of the torus at time t to the steady state maximum flow velocity. This step response shows the purely mechanical behavior of the system with a characteristic time constant of 2 ms (taken at 63.2% of the steady state value), corresponding to a cut-off frequency of 80 Hz. On the other hand, the normalized *thermal* response to the 1,000 deg/s² step input considers the thermal effects as well and is defined as the ratio of the temperature differential between the two temperature detectors at time t to their steady-state temperature differential. The resulting thermal time constant is 440 ms, corresponding to a 0.4 Hz cut-off frequency, which is off by a factor of two if you compare to the analytical model τ_{th} . This could be attributed due to the different geometric shape (circle vs. semicircle). The critical dimensions r and d are close in value; thus they could be affecting the expected value. Thus, the thermal transduction scheme slows the sensor response by approximately two orders of magnitude. For comparison, Fig. 4.8a also shows the normalized heater response (as defined above) to a step input of applied power to the heater under a constant angular acceleration of 1,000 deg/s². The resulting characteristic time constant is 1750 ms. A way to improve the bandwidth of the thermal

system is by moving the temperature sensors closer to the heater (see also equation (4.37) and (4.38)). This would result in a faster transient behavior as shown in Fig. 4.8b, but at the expense of sensor sensitivity (see also equation (4.24)). The thermal time constant of the system for temperature sensors that are $50\text{ }\mu\text{m}$ from the heater is 200 ms. The time constant increases to 1600 ms when the distance between the heater and the detector increases to $1000\text{ }\mu\text{m}$.

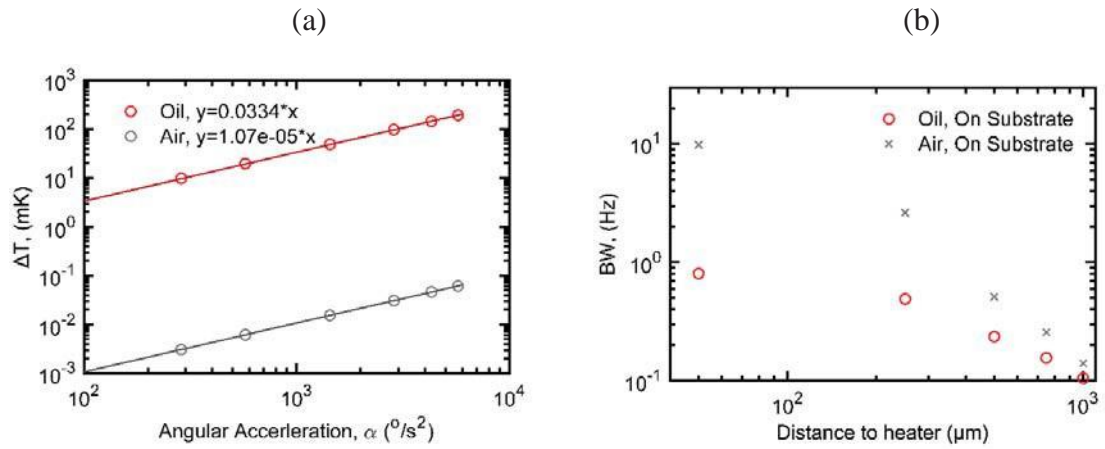


Figure 4.9. Simulated (a) sensitivity and (b) bandwidth of the sensor as function of the fluid used: silicone oil (5 cSt) or air.

In addition, the use of less viscous fluids was considered. Water (1 cSt) and lower viscosity silicone oil (0.55 cSt) could be used to improve the sensor bandwidth. However, these fluids have lower vapor pressures and experience evaporation out of the polymeric microtorus. Thus, we chose the silicone oil (5 cSt) with the lowest viscosity that had little to no vapor pressure. Figure 4.9 compares the simulated sensitivity and bandwidth of the thermal angular acceleration sensor for the cases of using either silicone oil (5 cSt) or air as fluid. The sensor sensitivity of the device drops by roughly three orders of magnitude when switching to air. The gain in bandwidth is heavily dependent on the distance between the heater and the temperature sensors. At best, the simulation indicates a one order of

magnitude increased bandwidth for smaller distances. With temperature sensors being further away from the heater, the bandwidth becomes independent of the fluid used. It is believed that thermal losses to the substrate rather than thermal transport through the fluid are responsible for this fact.

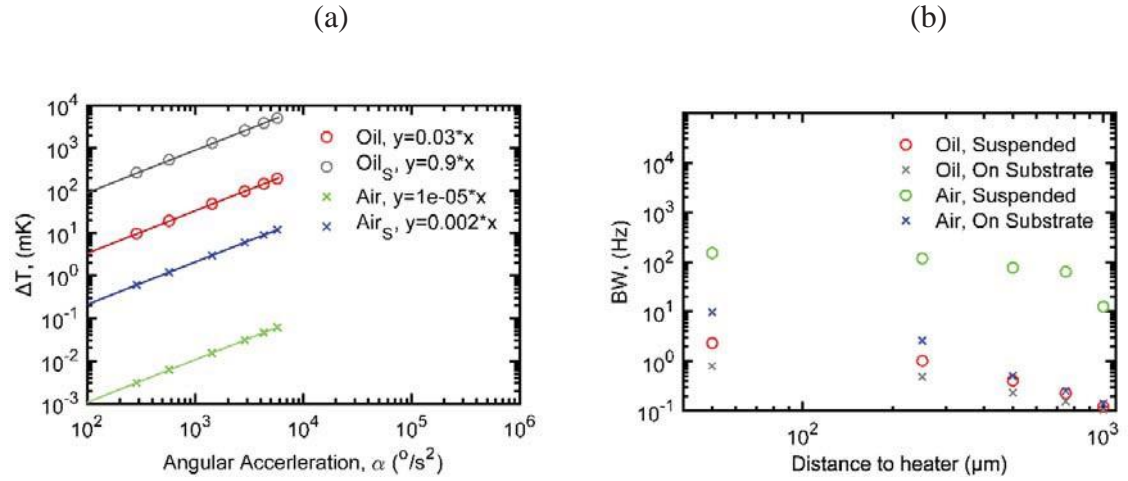


Figure 4.10. Simulated (a) sensitivity and (b) the bandwidth of the sensor as function of the fluid used (Silicone Oil or Air) and the release of the structure.

To this end, the effect of thermally decoupling the heaters and sensors from the substrate on the sensor sensitivity and bandwidth was simulated (Figure 4.10). Thereby, a thermally decoupled structure was simulated by drawing a rectangular boundary for the heater “suspended without tethers” in the middle of the channel. The impact of thermally decoupling the heaters and temperature sensors from the substrate by e.g. micromachining is significant: using the 5 cSt silicone oil as fluid could lead to a 30x sensitivity improvement over the unreleased structure; in case of air, the released structure sensitivity increased by at least two orders of magnitude over the unreleased structure. As seen in figure 4.10b, the release of the heaters and temperature sensors furthermore increases the bandwidth of the device using the silicone oil as a fluid by a factor of 2 at best. The

bandwidth approaches that of the unreleased structure if the temperature sensors are located further away from the heater. The use of air improves the bandwidth by an order of magnitude if the temperature sensors are located close to the heater, and even by the more than two orders of magnitude for detectors located farther away from the heater. Thus, thermal decoupling of the temperature sensors and heaters from the substrate should be considered; however, would complicate the fabrication process and was not evaluated experimentally.

4.4 Design and Fabrication

Two main iterations of the thermal μ -SCC were designed and fabricated: one uncapped and the other capped and fluid-filled. The uncapped design will not be discussed. See the following for more details [122], [241]. The fabrication process for the capped devices is described below:

4.4.1 Sensor Design

The latest-generation sensor design comprises two or more linear thermal accelerometers that are placed along the circumference of a microfabricated torus to detect the tangential acceleration induced by an applied angular acceleration along the torus as illustrated in figure 4.11.

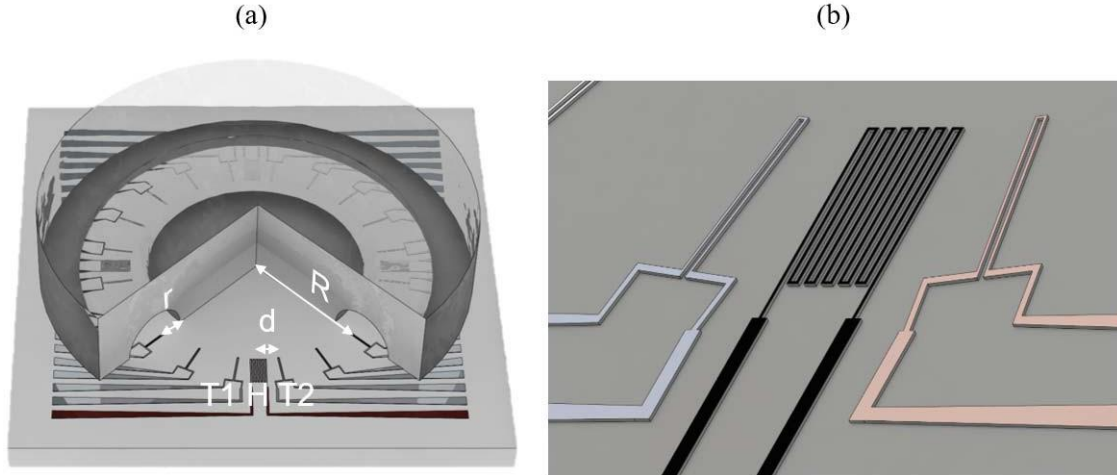


Figure 4.11. (a) 3D-rendered model of bioinspired rotation sensor. The sensor consists of aluminum resistors for Joule heating and temperature sensing on a glass chip with a bonded PDMS channel layer. The PDMS layer is cut to show the semi-hemispherical channel cross sections of the torus over the resistors. The relevant dimension labels are marked on the structure. (b) Zoom-in on heater and temperature sensing resistors.

Each linear thermal accelerometer comprises a central heating resistor and two symmetrically placed resistive temperature sensors. Each meandering heater structure with a heater width of $8\ \mu\text{m}$ covers an area of length and width of $750\ \mu\text{m}$ and $390\ \mu\text{m}$, respectively, while the temperature sensors are $750\ \mu\text{m}$ long and $45\ \mu\text{m}$ wide as shown in 4.11b. The minimum number of heaters and temperature sensors to operate the device with interfering signal rejection is two heaters and four temperature sensors. However, additional thermal sensors can be placed along the circumference for redundancy and further signal processing. To simplify the fabrication and packaging process, a half-torus cut along the plane of rotation was used as the microfluidic channel with minor and major radii of r and R , respectively. The heaters and the temperature sensors cross the channel perpendicular to the flow. Each temperature sensor is placed a distance d away from the heater, where d is roughly the length of the minor radius [215]. To further simplify fabrication, heaters and temperature sensors are not suspended within the channel, but are

fabricated on a glass substrate. The glass substrate minimizes the conductive heat losses to the substrate and maximize heat transfer to the fluid. Lin et al. presented such a non-floating convective thermal angular accelerometer [242]. The fluid chosen for the sensor is a silicone oil (Sigma Aldrich), because of its low-vapor pressure (less than 1 μ Torr), relatively high thermal conductivity (0.1 W/m K), and low viscosity (5 cSt) to allow faster fluid flow. Aluminum was chosen as the resistor material for its high temperature coefficient of resistance (3900 ppm/K). An aluminum alloy with 3% copper was used in the final structure to minimize the effect of electromigration [243], [244]. A dielectric layer of SiO₂ can be added to insulate the resistors from electrically conductive liquids.

4.4.2 Sensor Fabrication

The fabrication highlighted in figure 4.12 starts by depositing 125 nm of aluminum via sputtering on a glass wafer. The aluminum resistors and connections are patterned and etched using reactive ion etching (PlasmaTherm ICP). Next, the PDMS torus is formed. To this end, an inverse aluminum mold for casting the microfluidic channel is built using CNC milling (HAAS) as described in [245]. A 1/64" square tungsten mill bit was used to create the semicircular channels. The mill was spun at 25 kRPM. The milling instructions were created using SolidWorks 2016 HSMWorks. PDMS (Sylgard 184, 10:1 ratio) is cast on the aluminum mold. After crosslinking the PDMS in an oven at 70 °C for one hour, two sub-300 μ m inlet holes are punctured into the microfluidic channel using a Harris puncture tool.

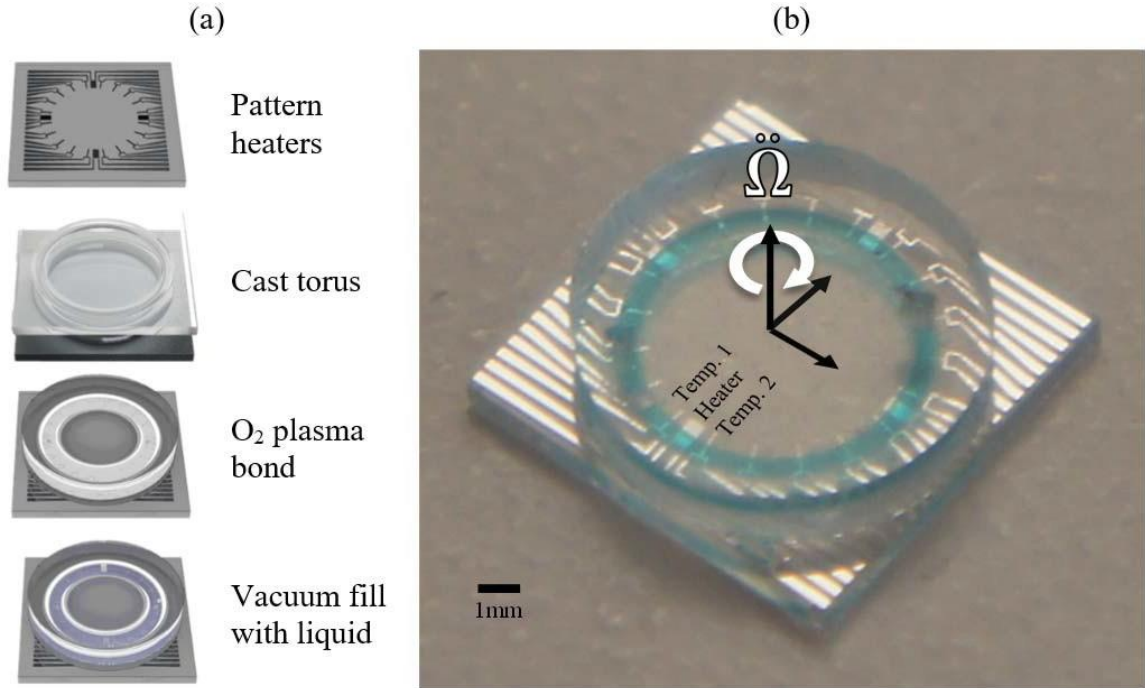


Figure 4.12. (a) Fabrication process of latest generation (capped device); (b) Optical image of fabricated angular accelerometer with microtorus radius $R = 2.75\text{mm}$

The PDMS cover and glass substrate are exposed to an oxygen plasma for one minute (< 200 mTorr, 18 W), then bonded.

The finished devices were wire bonded to a 28-pin ceramic package (Spectrum Semiconductor Materials) to ease electrical connection to the interfacing circuitry. The circular fluid channel is filled with silicon oil using a vacuum process [246]. By submerging the device and package into a fluid under vacuum, the air inside the torus evacuates and is replaced with the surrounding fluid. Optionally, the fluid-filled packaged device is afterwards covered with UV-curable epoxy EPO-TEK OG116 (Epoxy Technologies) and exposed to a broadband UV light source for thirty minutes.

4.4.3 *Wafer-level Packaging and Fabrication*

In this section, the possibility of wafer-level liquid encapsulation is investigated to move the fluid filling of the microtorus from a slow device-level process to a wafer-level process. Traditional post-fabrication techniques for filling microfluidic channels include submerged vacuum filling [247] and fluid injection with inlet/outlet sealing post injection [125]. These methods suffer from bubble formation and slow filling times [246]. On the other hand, in-process fluid encapsulation [248] is promising for drug delivery, force sensors and tunable microlenses.

Solid-on-liquid-encapsulation for microsystems can be achieved by a variety of methods. The most common method involves the condensation of a vapor as solid onto a low-vapor pressure liquid [248]. While most thin-film deposition techniques allow for solid materials to be deposited on liquids, internal stresses in the thin film material may cause wrinkling and potentially film delamination [249]. However, deposited parylene (poly(pxylylene)) thin films do not exhibit internal stresses regardless of thickness [249]. Thus, parylene-encapsulated liquids have been used for a number of transducers and actuators, including microlenses [250], pressure sensors [251], and force sensors [252]. In addition, the encapsulated liquid has been used as a sacrificial layer to create free standing membranes [253], and fluidic channels [254].

Compared to [241] and the fabrication process described in the previous chapter, the revised fabrication process described here retains its simplicity while allowing for batch fabrication and bubble-free filling of the microfluidic channels. The fabrication process takes advantage of the low vapor pressure of silicone oil and the ability to selectively bead the

oil by patterning an oleophobic thin film. The process departs from most other liquid encapsulation schemes in using a lower viscosity oil to allow for fluid flow. In particular, a silicone oil normally used as a lubricating oil for vacuum pumps has been chosen (ISO 54, Lubricating Specialties Company, USA).

The silicone oil preferentially wets the oleophilic glass substrate while repelling from regions covered by an oleophobic film (Green Onions Supply Screen Protector). Contact angle measurements (Figure 4.13) yield a contact angle of 17° for the silicone oil on glass, while a much larger contact angle of 70° was measured on the oleophobic film. This contrast enables the patterning of the liquid in the desired geometry.

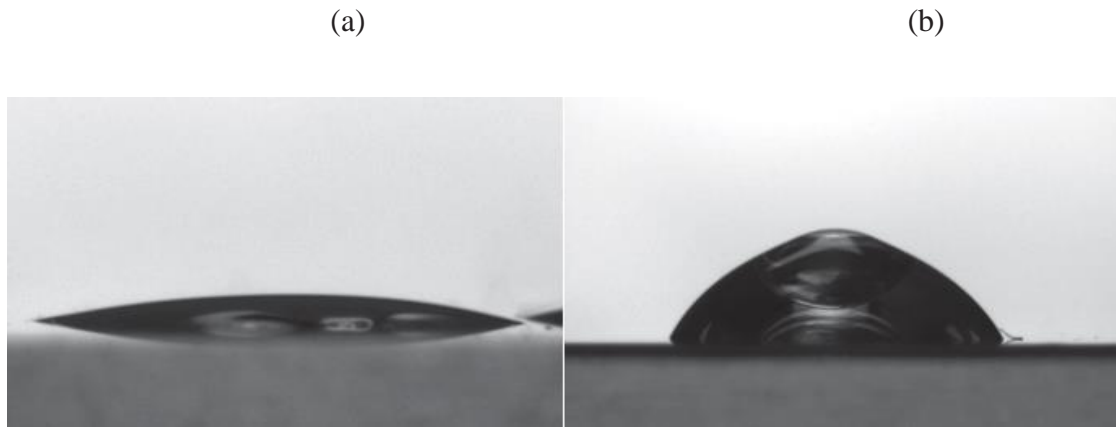


Figure 4.13. Contact angle between silicone oil and (a) glass (17°) and (b) oleophobic thin film (70°).

The fabrication and packaging process is highlighted in Figure 4.14. As before, the fabrication process starts with the deposition and patterning of 125nm aluminum to form the resistors of the thermal transducers (Figure 4.14i). The encapsulation process starts with laser-patterning the oleophobic dry thin film on the glass substrate (Figure 4.14ii).

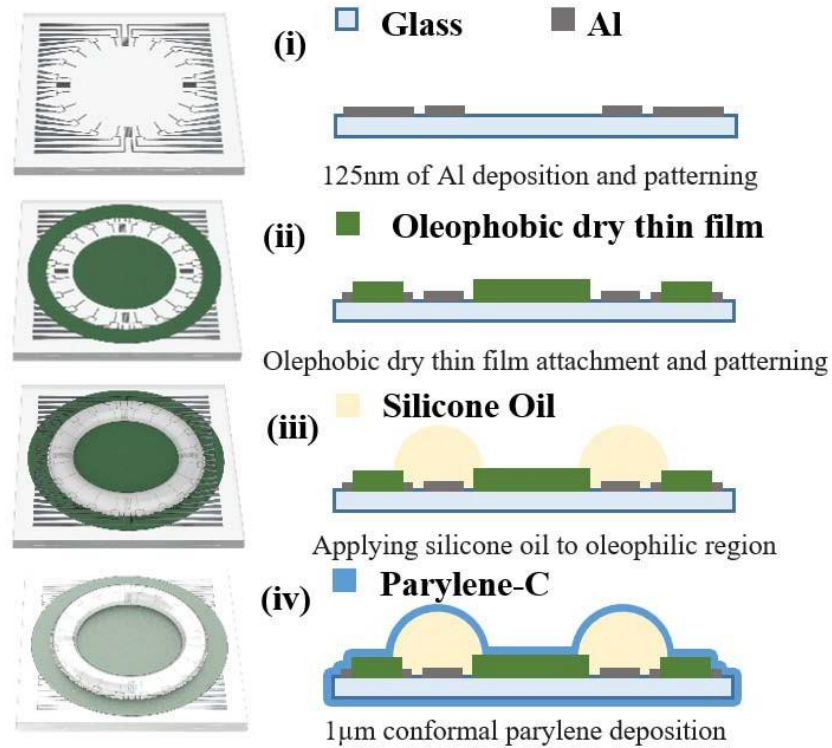


Figure 4.14. Wafer-level fabrication process of the thermal rotational accelerometer.

The film pattern allows to dispense not only shape-controlled droplets, but even more complex microfluidic structures, such as half-tori, of low-vapor-pressure ($\sim 1 \mu\text{Torr}$) silicone oil (Figure 4.14iii). This is followed by a conformal coating with $1 \mu\text{m}$ of Parylene C (Figure 4.14iv), enabling rapid bubble-free, wafer-level encapsulation. Figure 4.15 compares silicon oil patterns on a glass substrate with and without the oleophobic film and demonstrates the size-scalability of the patterned microtorus structures. The process can be made more scalable by offering parallel dispensing of the liquid using an array of nozzles and actuated using a robotic arm. The CVD coating of parylene is inherently a batch fabrication process.

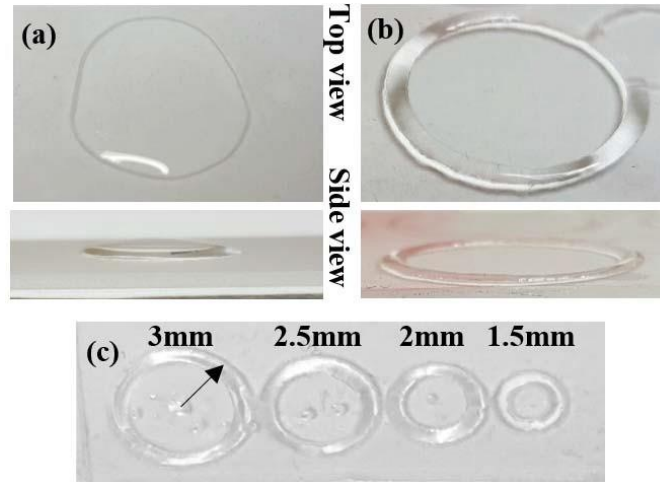


Figure 4.15. Bubble-free liquid encapsulation process: silicone oil wetting on glass (a) without and (b) with patterned oleophobic thin film. (c) size scalability of the parylene-on-oil encapsulation process. The major radii are 3mm, 2.5mm, 2mm, and 1.5mm. The inner radius in all cases is 0.5 mm.

An optical image of a fabricated sensor with a microtorus radius of $R = 2.85\text{mm}$ is shown in Figure 4.16a. Figure 4.16b depicts a confocal laser microscope image of the channel encapsulated channel area. The fluid forms an oval shaped cross section with a 5:1 aspect ratio. Due to the transparency of the fluid and the encapsulating parylene film, the device was sprayed with paint to allow the confocal microscope to focus.

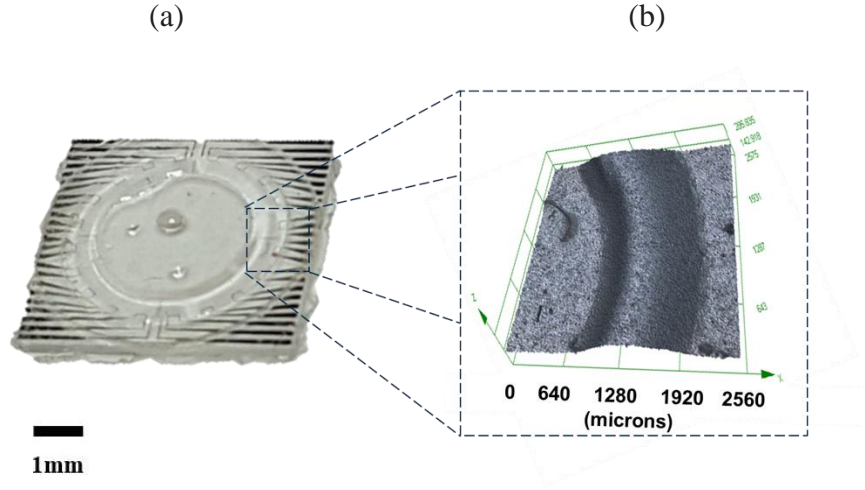


Figure 4.16. Optical image of encapsulated bio-inspired angular accelerometer with microtorus radius $R=2.85\text{mm}$. (b) 3D confocal laser microscope image of a channel with width of 1mm and height of 100μm; the device was spray-coated with paint to make it opaque for the laser light.

4.5 Thermal Characterization

A packaged angular accelerometer with the dimensions given in Table 4.1 was placed in an environmental chamber (ENVEC, Japan) at temperatures from 20 to 90 °C to characterize the temperature coefficient of the thin film aluminum resistors. Figure 4.21a shows the electrical resistance of a typical heater as a function of temperature. The effective thin film temperature coefficient of resistance (TCR) is 2100 ppm/K, which is lower than the bulk TCR of 3900 ppm/K reported for aluminum in the literature [244]. Besides the use of an Al-1%Cu alloy, the discrepancy could be attributed to the thickness of the resistors and the thermal coefficient mismatch between the substrate and the resistors as discussed in [244]. The average temperature elevations of the resistors due to Joule heating from the applied power are extracted based on the measured TCR (see figure 4.17b).

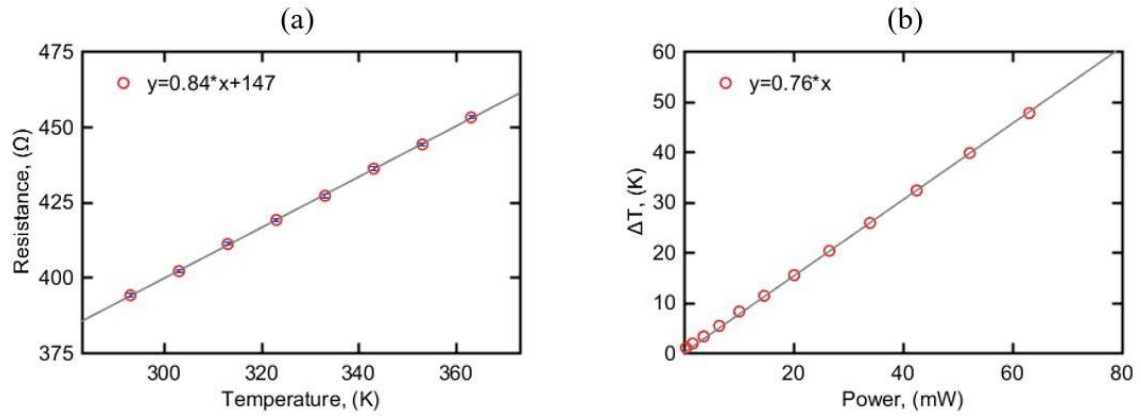


Figure 4.17. Thermal characterization of aluminum heating resistors: (a) Electrical resistance as a function of temperature; (b) Average temperature rise as a function of heating power.

Figure 4.18 is a thermal IR image of the on-substrate heater, which had a thermal efficiency of $\sim 0.7^\circ\text{C}/\text{mW}$. This highlights the thermal loss to the glass substrate of the simpler second design.

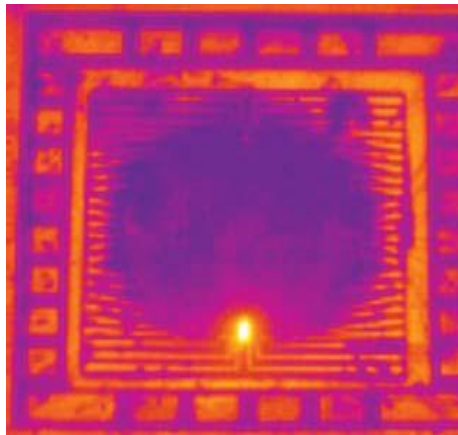


Figure 4.18. Thermal IR image of temperature elevation of approx. 10°C (based on calibrated image) of the aluminum thin-film heaters on glass substrate due to Joule heating with 10 mW applied power.

4.6 Mechanical Characterization

Rotational motion is achieved by mounting the sensors on a rotary stage driven by a stepper motor (SureStep 23079), which was controlled using an analog input from a function generator (Tektronix AFG3022B). For the chosen stepper motor, the angular rate linearly correlates to the applied voltage. The maximum frequency used with the stepper motor was 5 Hz; higher applied frequencies caused instabilities in the rotation setup. An additional setup provides linear acceleration (Rockwell Automation MPAS-A6066B). The sensor output was measured as shown in figure 4.19. The temperature sensors R_1 , R_2 , R_3 and R_4 are arranged in a Wheatstone bridge as shown and connected to an instrumentation amplifier (TI INA551). Gain and offset were adjusted to achieve high output voltages without clipping. The amplified signal is passed through a passive 1,000 Hz low-pass filter to eliminate high-frequency noise. In this work, the instrumentation amplifier gain was set at 5,000. The applied bridge voltage was 1 V. The heater power was set to 20mW, corresponding to an average temperature increase of approx. 15 °C. The amplified bridge output voltage is displayed on an oscilloscope (Tektronix TDS2022C) for direct viewing. A sample image capture of the oscilloscope is shown in Figure 4.24b for a sinusoidal 0.5 Hz rotation at a maximum angular acceleration of 1250 deg/s². The output of a reference gyroscope (Murata ENC-03R) is shown in blue and the tested sensor output is in yellow. In addition, the amplified and filtered sensor output is connected to a lock-in amplifier (Stanford Research Systems 830) for recording the signal amplitude via a DAQ board (NI PCI-6251). The instruments are computer-controlled via GPIB connections. The interface circuitry is powered by two D cell batteries (9.6V), reducing the number of connections to

the test set up. A slip ring (Adafruit Industries) was used to connect the rotary stage to the experimental set up.

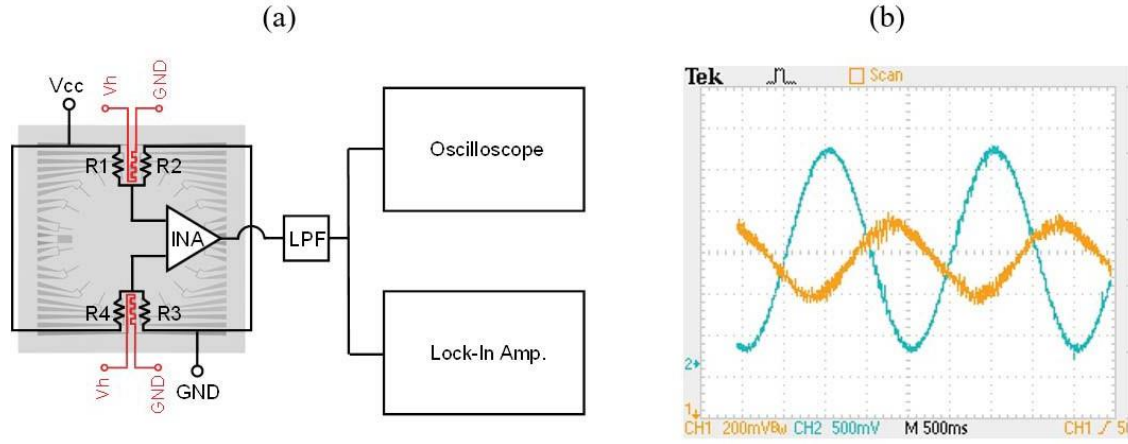


Figure 4.19. (a) Interfacing circuitry (amplification and filtering) for the sensor with the block diagram of the Wheatstone bridge circuitry overlaid over the sensor physical layout. The amplified and filtered output voltage of the Wheatstone bridge is output to an oscilloscope and connected to a lock-in amplifier; (b) a sample oscilloscope screenshot of the output of the circuit in yellow and a reference gyroscope shown in blue is shown for a 0.5 Hz sinusoidal angular acceleration with a peak angular acceleration of 1250 deg/s². The observed 90° phase shift is indicative of the commercial gyroscope output being proportional to the applied angular rate, while the biomimetic rotation sensor generates a signal proportional to the angular acceleration.

The device is tested under harmonic motion excitation at 0.5 Hz. Thus, the angular position

θ will be $\theta = A \cdot \cos(\omega t)$, with being $\omega = 2\pi f$. The velocity will be

$$v = \frac{d\theta}{dt} = \dot{\theta} = -\omega \cdot A \cdot \sin(\omega t) = -\omega \cdot A \cdot \cos(\omega t - \frac{\pi}{2})$$

The acceleration will be $a(t) = -\omega^2 \cdot A \cdot \cos(\omega t)$. The output from the angular accelerometer (orange) should be 90° out of phase with the angular velocity output (blue) from the commercial gyroscope. The observed 90° phase shift is indicative of the commercial gyroscope output being proportional to the applied angular rate, while the biomimetic rotation sensor generates a signal proportional to the angular acceleration. This gives us

confidence that the proposed biomimetic device operates as an angular accelerometer, not as an angular velocity/rate sensor. This is validated by the paper from [64] which also showcases a 90° phase shift to the commercial gyroscope.

4.6.1 Sensitivity/Cross-Axis Sensitivity

Figure 4.20a shows the measured output voltage of the device to applied angular accelerations around three axes. The tested sensor has a sensitivity of $124 \mu\text{V}_{rms}/(\text{deg}/\text{s}^2)$ for angular accelerations up to $2,000 \text{ deg}/\text{s}^2$ at 1 Hz applied in the plane of the microtorus. The measured devices cross-axis sensitivity to angular accelerations around the other two axes is more than an order of magnitude (25-fold) smaller than for the in-plane rotation around the \hat{z} -axis. This is consistent with the simulation results (Figure 4.7a). Using the measured TCR of the temperature sensors and the circuitry of the Wheatstone bridge, the simulated temperature difference in Figure 4.7a can be translated into an effective voltage signal to compare with experimental results in Figure 4.25a.

This transduction coefficient is calculated to be $10.5 \text{ mV}/\text{mK}$. Compared to the simulation result in figure 4.7a of $33 \mu\text{K}/(\text{deg}/\text{s}^2)$, the experimental result in Figure 4.20a is about a factor of ~ 3 smaller. Because of lack of proper material property characterization in terms of thermal properties of the silicone oil used, both in terms of absolute value and temperature dependence, one must be careful to compare experimental and simulation absolute values. Moreover, the temperature sensors average the temperature over their entire length, while the simulation averages the temperature only inside channel. This leads to expected lower experimental values compared to the simulated data. Figure 4.20b shows the cross-axis sensitivities to linear accelerations in \hat{x} and \hat{y} -directions. Thereby, the applied

linear accelerations are converted into equivalent angular accelerations, to allow for comparison with the angular acceleration sensitivity on equal footing. To do this, the applied linear accelerations were converted to angular accelerations by dividing them by the major radius of the microtorus. Considering equivalent angular accelerations, the measured linear acceleration sensitivity is about -50 dB compared to the sensitivity of the in-plane angular acceleration, highlighting the suppression of linear acceleration signals even in the case of the thermal sensing principle by using four temperature sensors (and two heaters) properly connected in a Wheatstone bridge (see Fig. 4.19).

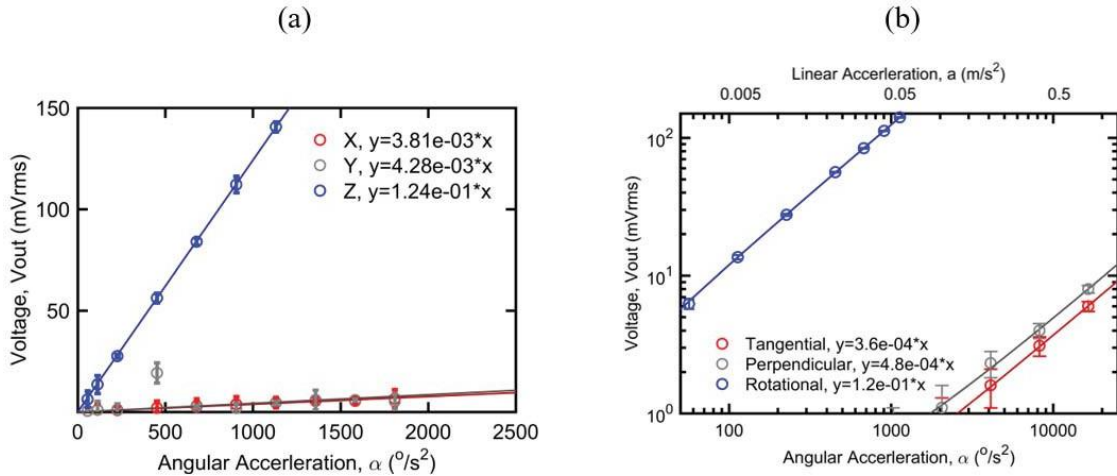


Figure 4.20. (a) Measured sensor output voltage as a function of the applied angular acceleration for rotations around three axes. (b) Measured sensor output voltage as a function of the applied angular acceleration around \hat{z} -axis and linear accelerations along the \hat{x} and \hat{y} -axis. The measurements were taken at a frequency of $f = 1$ Hz with a power of 20 mW applied to the heater. Linear accelerations are converted into effective angular accelerations using the microtorus major radius $R = 2.75$ mm.

The rejection of linear acceleration signals in case of a complete microtorus structure can also be demonstrated by mounting the sensor off-center on the rotation stage. Figure 4.21 compares the performance of the device, i.e. the output voltage as a function of the applied in-plane (\hat{z} -axis) angular acceleration, for the case of mounting the sensor in the center of the rotation stage and 2 cm off axis, which adds tangential and centrifugal accelerations

acting on the sensor. The measured on-axis rotational sensitivity of the sensor for 1 Hz rotation is $124 \mu\text{V}/(\text{deg}/\text{s}^2)$, while the measured off-axis rotational sensitivity is $127 \mu\text{V}/(\text{deg}/\text{s}^2)$, indicating again a good rejection of linear acceleration signals.

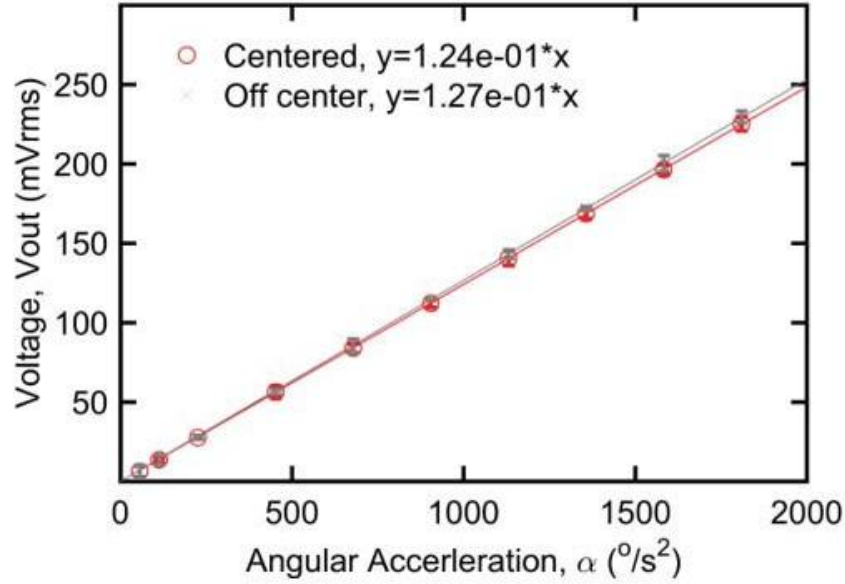


Figure 4.21. Measured sensor output voltage at a frequency of $f = 1$ Hz as a function of the applied angular acceleration around \hat{z} -axis when the device is centered on the experimental setup and placed 2 cm away from the center.

4.6.2 Frequency Response

The measured normalized frequency response of the packaged sensor is shown in figure 4.22, along with the simulated behavior using harmonic excitation at different frequencies up to 5 Hz and based on the analysis of the simulated step response. Thereby, the frequency response was calculated from the thermal step response using the system identification toolbox in MATLAB (MathWorks). The biomimetic thermal sensor has a second-order transfer function with corner frequencies at ~ 0.16 Hz and ~ 1 Hz. The frequency behavior of the measured output under harmonic angular acceleration oscillation compares well to

the simulated harmonic output and the fitted transfer function of the step response, as discussed in section 4.4.

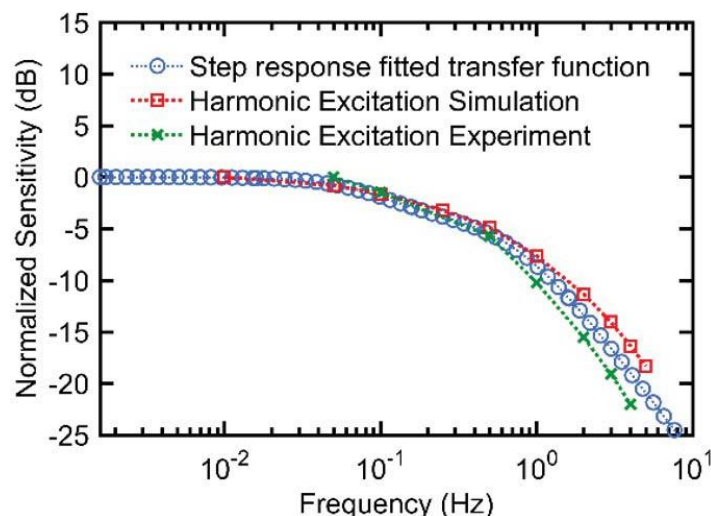


Figure 4.22. Normalized sensor sensitivity to angular accelerations applied around the z-axis as a function of frequency, with crosses showing experimental results under harmonic excitation, squares showing simulated results under harmonic excitation and circles the transfer function obtained from the simulated response of the sensor to a step input.

4.6.3 Plugged Behavior

To understand and observe the sensor behavior more fully, a plugged torus was also fabricated. This helps isolate all the different forces acting on the system. The complete torus will be sensitive to both inertial and buoyancy force for angular acceleration and linear acceleration perpendicular to the sensor. In contrast, the plugged one will only sense buoyancy forces [37], [155], [198].

Figure 4.23 shows the effect of plugging the device. A horseshoe-shaped (an incomplete torus with a 10-degree break) channel with the same major and minor radii was bonded and tested under the same conditions as the unplugged device (figure 4.20b). By blocking the path of the fluid in the torus, the sensitivity of the sensor to in-plane angular

accelerations around the \hat{z} -axis is as expected reduced, with the measured rotational sensitivity in the plugged sensor being only $9 \mu\text{V}/(\text{deg}/\text{s}^2)$, compared to $124 \text{ V}/(\text{deg}/\text{s}^2)$ in the unplugged torus. At the same time, the sensitivity to linear accelerations is increased. The measured tangential linear sensitivity increased to $2400 \text{ nV}/(\text{deg}/\text{s}^2)$ from $360 \text{ nV}/(\text{deg}/\text{s}^2)$ in the unplugged case. As well, the perpendicular direction experiences an increase from $480 \text{ nV}/(\text{deg}/\text{s}^2)$ to $720 \text{ nV}/(\text{deg}/\text{s}^2)$. This illustrates the effect of the unplugged torus as a geometric constraint in promoting the rotational acceleration and rejecting the linear accelerations.

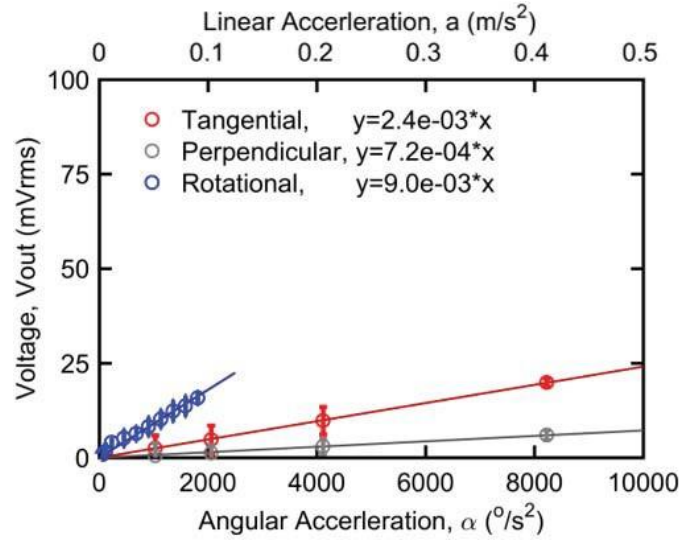


Figure 4.23. Measured sensor output voltage as a function of the applied angular acceleration around \hat{z} -axis and linear accelerations along the \hat{x} and \hat{y} -axis for a sensor with horseshoe-shaped microtorus with a 10° gap. The measurements were taken at a frequency of $f = 1 \text{ Hz}$ with a power of 20 mW applied to the heater.

4.6.4 Noise and temperature stability

While a detailed noise analysis and optimization is subject to future work, the current limit of detection can be estimated from signals recorded using the oscilloscope (see setup Figure 4.16). As an example, Figure 4.24 shows the amplified and low-pass filtered sensor

response to a $1,250 \text{ deg/s}^2$ square-wave signal applied at 0.5 Hz. With an extracted sensitivity of approx. $320 \mu\text{V/deg/s}^2$, the observed noise level of $\pm 10 \text{ mV}$ translates to an estimated limit of detection around 30 deg/s^2 . This can likely be further improved by limiting the bandwidth of the low-pass filter (currently 1,000 Hz). For comparison, the noise seen from the lock-in amplifier (see error bars in Figure 4.20b) is only of the order of $\pm 0.5 \text{ mV}$, which would correspond to a limit of detection of roughly 5 deg/s^2 .

However, this does not take into consideration the long-term stability and drift experienced by the sensor. The main two possible sources of drift are the heaters and temperature sensors experiencing electromigration due to Joule heating, and the other is the leaking of fluid out of the device due to improper sealing. The first is addressed by using an aluminum-copper alloy that minimizes electromigration as described in section 4.4.1. A proper hermetic seal using the parylene-on-oil process addresses the second issue. The initial fabrication process suffered from loss of fluid due to both evaporation and improper sealing during fabrication. The long-term drift experienced by the sensor can be addressed in practical terms by recalibrating the sensors to a known value to reestablish a proper baseline. According to [224], self-test circuit for continuous checking of the integrity of the heater, detector and associated circuitry of the accelerometer can also be made available to increase the device reliability as shown in [255]–[257].



Figure 4.24. Amplified and low-pass filtered (1,000 Hz cut-off frequency) sensor (orange) and reference gyroscope (blue) signal for an applied square-wave angular acceleration of $1,250 \text{ deg/s}^2$ at 0.5 Hz. The extracted sensor sensitivity is $320 \text{ } \mu\text{V/deg/s}^2$ with a noise level of approx. $\pm 10 \text{ mV}$, resulting in an estimated limit of detection of 30 deg/s^2 .

4.7 Conclusion

Table 4.2 summarizes the device sensitivity and cross-axis sensitivities. Thereby, notation S_{ij} is used to describe the sensitivities, where i is applied axis of rotation, and j is the measured axis of rotation. For linear accelerations, the notation is S_{Gk} , where k is linear acceleration axis.

The demonstrated bioinspired angular accelerometer mimics the semicircular canals of the mammalian vestibular system, but uses a thermal transduction mechanism to allow for a simple two-mask fabrication. Multiple thermal flow sensors, properly designed along the fluid-filled microtorus and connected in a Wheatstone bridge, suppress interfering signals from cross-axis angular accelerations and linear accelerations even in the presence of buoyancy effects.

Table 4.2- Summary of device performance

Sensitivity	Units	This work
S_{ZZ}	$\mu\text{V}/\text{deg}/\text{s}^2$	124
S_{XZ}	$\mu\text{V}/\text{deg}/\text{s}^2$	3.8
S_{YZ}	$\mu\text{V}/\text{deg}/\text{s}^2$	4.3
S_{GX}	$\text{mV}/\text{m}/\text{s}^2$	7.5
S_{GY}	$\text{mV}/\text{m}/\text{s}^2$	10
S_{GX}/S_{ZZ}	dB	-50.7
S_{GY}/S_{ZZ}	dB	-48.2

The device improves on the cross-axis insensitivity of thermal inertial sensors. However, it still lags other sensors in bandwidth and power consumption. These issues can be addressed based on techniques used for current commercial linear thermal acceleration sensors. The device's power consumption can be improved by pulse-operating the device or thermally insulating the heater and temperature sensors using micromachining techniques. The low bandwidth caused by the use of the fluid [231] can be overcome by thermally insulating the heater and temperature sensors using micromachining or operating the device in a closed loop configuration with a PID controller [239]. The required micromachining steps would however complicate the fabrication process. Another solution is characterizing the device transfer function and adding a compensating transfer function to the output to increase the bandwidth, as used by commercial thermal linear accelerometers [258]. It is believed that the incomplete encapsulation of the closed channel due to the inlet holes leads to non-optimal cross-axis rejection. The device's actual dynamic range was only tested up to $2,000 \text{ deg}/\text{s}^2$ due to test setup limitations and is likely considerably higher. Further characterization of the zero-rate drift and the noise level need to be performed to accurately determine the limit of detection of the current sensor.

CHAPTER 5. MAGNETIC BIOMIMETIC ANGULAR ACCELEROMETER

In this chapter, we introduce the *magnetic* transduction mechanism for the proposed angular acceleration sensor. The chapter will begin by describing the working principle as well as the design and simulation of the magnetic hair cell-based sensor. Furthermore, the fabrication and characterization of the magnetic inertial sensor will be presented. Finally, preliminary results of the mechanical testing will be shown and analyzed.

5.1 Concept

As discussed in section 4.7 on thermal transduction, the main limiting factors of the bioinspired thermal angular accelerometer were the slow response time and thus limited bandwidth, and the high power needed to create the needed temperature gradient. In section 3.2.3, we discussed different options for power efficient and responsive mechanisms. An alternative approach is the use of a permanent magnet, which intrinsically produces a gradient in the magnetic field (rather than a temperature gradient). Exploring this intrinsic magnetic field gradient for sensing eliminates the need to *actively* power the structure to establish a temperature gradient. Thus, a small flexible permanent magnet in conjunction with a power-efficient magnetic sensor may overcome the power challenges faced by the thermally transduced device. Another benefit of a magnetically-transduced sensor is its fast response, which ensures that the sensor will only be limited by the mechanical response of the torus.

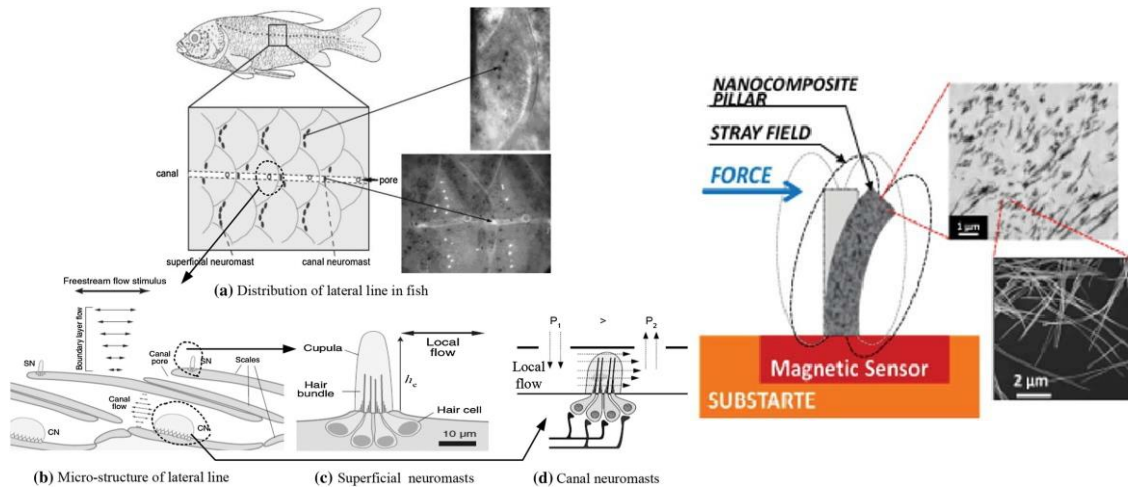


Figure 5.1 (top) (a) Distribution of the lateral line on the scales of fish. (b) Localization of the superficial neuromasts exposed to freestream flow and the canal neuromasts within small channels. (c) Zoomed-in illustration of the superficial neuromasts (SN). (d) Zoomed-in illustration of the canal neuromasts (CN). Image adapted from [259], [260]. (bottom) Concept of a magnetic hair cell, where the flexible permanent magnet mimics the hair cells, while the magnetic sensor mimics mechanoreceptors; adapted from [141].

In [141], our collaborators at KAUST proposed bioinspired flow sensors using flexible magnetic pillars produced using magnetic nanowires embedded into PDMS micro-pillars. The design is inspired by lateral flow lines in fish that detect fluid flow while in motion [207]. Based on the biophysical model of the lateral flow lines summarized by Shizhe et al. [260], the local free-stream acceleration is correlated to the hair cell deflection of the canal neuromasts. The inspiration and the idea of the flow sensor is shown in figure 5.1.

Moreover, a recent *in vitro* study of live *auditory* frog hair cells used magnetic nanoparticles, attached to hair cell cultures using antibodies, to probe the hair cell movement by a magnetic sensor while actuating using an external magnetic field [261]. An illustration of the setup is shown in figure 5.2. This study demonstrates the ability to detect small deflections (on the order of nanometers) of magnetically-activated hair cells using a

nearby magnetic probe and encouraged the development of the bioinspired magnetic hair-cell readout in this work.

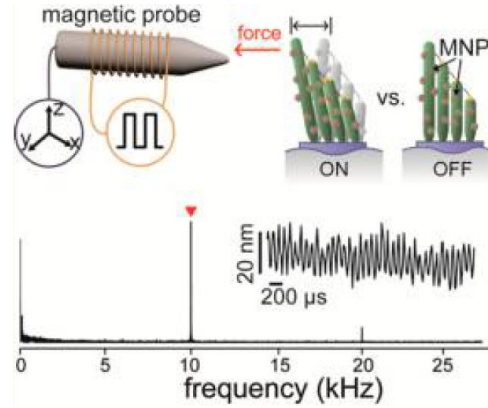


Figure 5.2. (top) Schematic diagram of the magnetic probe stimulating a single hair bundle with magnetic nano particles attached. (bottom) Frequency spectrum response of bundle motions, entrained at 10,000 Hz. The inset shows the tracked bundle displacement. Image adapted from [134].

By adding a geometric toroidal closed-loop constraint, we can convert the flow sensor into an inertial rotation sensor. This concept was originally demonstrated by Andò et al. on the macroscale by integrating a ferrofluid in a toroidal channel with electro-active polymers as the mechanical transducers [262]. Thus, to realize this concept on the micro-scale, we combine two design elements: the microfluidic closed-loop torus and the mechanical hair cells. The microfluidic closed loop torus was analyzed extensively in section 3.3. In the following subsection, we discuss previous attempts to create magnetic artificial cilia.

5.1.1 *Bioinspired Magnetic Cilia*

As described in section 1.2.4.2 and 2.2.5, hair cells are nature's mechano-electrical transducers. The hair cell is a biological sensor consisting of a long pillar/rod that is connected to stress-sensitive sensors at its base. The sensors are responsive to stress caused by the deflection of the long pillars.

Recently, magnetic micromachined hair cells have been developed for a variety of possible applications including actuation of cell cultures [263], force sensors [264], microfluidic pumping [265], [266] and sensing fluid flow in microfluidic devices [141]. To create these artificial magnetic hair cells, a high-aspect ratio flexible magnet is placed in close proximity to an array of magnetic sensors. The first successful implementation of this principle was to demonstrate sound transduction for an artificial cochlea by McGary et al. [267]. Evans et al. [268] created soft polymer-based artificial hair cells by mixing PDMS with a ferrofluid, but demonstrated magnetic actuation only. Others [269], [270] continued to use these polymeric magnetic hair cells for actuation of fluid flow, until Hein et al. initially proposed the use of magnetic nanowires on giant magnetoresistive (GMR) sensors as flow sensors [271].

The microfabricated flexible magnets are the first part of this sensing system and are typically magnetic composites, where a soft elastic material such poly-dimethylsiloxane (PDMS) is mixed with a ferrofluid or magnetic powder, such as nickel iron cobalt alloys including those made by [272], [273]. The second part of this flow sensing system is the magnetic sensing element. There are many varieties of magnetic to electric transduction mechanisms that have been introduced over the years. These different underlying

transduction mechanisms, including Hall effect, the anisotropic magnetoresistance (AMR), giant magnetoresistance (GMR) or giant magnetoimpedance (GMI) and tunneling magnetoresistance, are presented in figure 5.3.

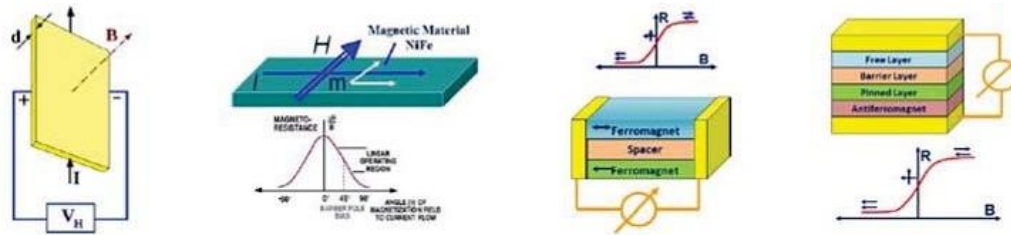


Figure 5.3. Different magnetic sensing technologies as adapted from [274], including (a) Hall effect, (b) anisotropic magnetoresistance (AMR), (c) giant magnetoresistance (GMR) or giant magnetoimpedance (GMI), and (d) tunneling magnetoresistance (TMR).

Hall effect magnetic sensors transduce an applied magnetic field into an electrical voltage across an electrical conductor. Due to its limited sensitivity, the output signal is sometimes amplified using a magnetic flux concentrator. Hall effect sensors have relatively large power consumption requirements (on the order of 5-20 mW) [274], despite current low-power hall effect sensors [275] that are still noisier than the alternatives. Magnetoresistance (or impedance) is a material property where the electrical resistance (or impedance) is a function of the applied external magnetic field caused by a variety of effects. AMR depends on the angle between the electrical current and the applied magnetic field. AMR offers a slight improvement in power consumption, two-orders of magnitude higher sensitivity than the Hall effect, but smaller dynamic range [274]. GMR improves on the sensitivity by less than an order of magnitude, with a similar dynamic range as AMR [274].

A multi-layer TMR sensor is a good candidate to sense the change in the magnetic gradient due to fluid flow. The three main layers in a TMR element are, from bottom to top: a pinned ferromagnetic layer, the tunnel barrier layer, and a free ferromagnetic layer [276]. The

tunneling resistance of TMR sensors is sensitive to external magnetic fields. TMR offers good temperature stability, the highest sensitivity and best power performance [277], [278]. However, the fabrication process for TMRs is typically more complicated. In addition to fabrication complexities, there are some limitations that need to be overcome with using a magneto-electric transduction effect to sense fluid flow. The first is the stability of the magnetic properties of the flexible hair cell submerged in a fluid over an extended period of time. Finally, TMR offer an excellent noise performance as shown in figure 5.4, with only the larger in size fluxgate sensors having a better noise performance. However, based on figure 5.4b, we might need to shield our devices as the laboratory environment will overwhelm the TMR sensor and we will not reach the sensors limit.

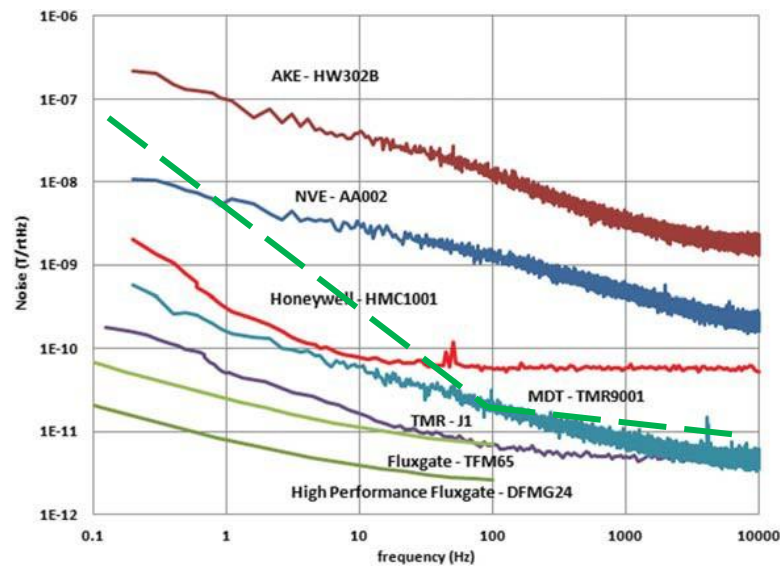


Figure 5.4a Magnetic sensor noise levels, adapted from [277] highlighted in dashed green line is typical lab noise levels. The noise level of our device at 1 Hz is marked with an x (bottom). Environmental noise levels are orders of magnitude higher than those of the TMR sensors. [279]. Environmental noise levels are orders of magnitude higher than those of the TMR sensors. [279].

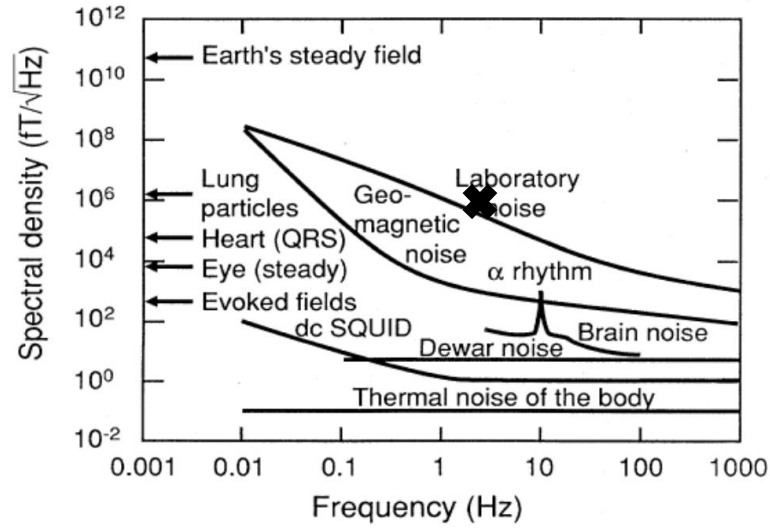


Figure 5.4b (continued) Environmental noise levels are orders of magnitude higher than those of the TMR sensors. [279].

5.2 Magnetic μ SCC Design

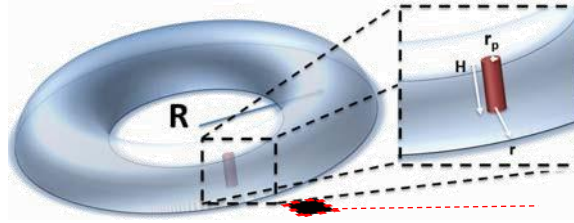


Figure 5.5. 3D rendering of proposed design with fluid-filled half-torus of major radius R , and minor radius r , flexible magnetic pillar with height H and pillar radius r_p and magnetic sensor(s). The insert shows details of the magnetic hair cell.

The design of the magnetic μ SCC consists of three components (see figure 5.5): The first is the microfluidic microtorus. The semi-hemispherical channel will be similar to the channel presented in section 4.4; it is easy to fabricate and meets the required geometric constraint. The second component is the magnetic hair cell. The hair cell is responsible for passively generating a symmetric magnetic field distribution across the magnetic sensors, the last component of the system. The magnetic field distribution will be disturbed when the hair cell is deflected by the drag force of the fluid flow induced by an applied angular

acceleration. The magnetic sensing elements complete the system, where proper and strategic care and planning are needed for placing the sensing elements relative to the hair cell(s).

5.2.1 Sensor Design Considerations

There are a few sensor design requirements that need proper evaluation, and will guide the design of the system. The power requirements for the bio-inspired magnetic sensors are to consume less than 1 mW. Based on that, TMR sensors are chosen and consume on the order of 10-100 μ W [274]. The tradeoff between power consumption and signal stability needs to be evaluated. The TMR magnetic sensor's stability comes at the cost of higher power consumption [141]. In addition, the sensor's bandwidth should only be limited by the mechanical response of the torus, with that being on the order of 20 Hz. Also, magnetic sensors are susceptible to all magnetic fields including the Earth's magnetic field or magnetic fields generated by electronic equipment. Such fields can be orders of magnitude larger than the intended signal stemming from the flexible permanent magnet. Thus, in order to sense the small output signals, proper sensor design must suppress signals from such interfering magnetic field sources. These requirements and limitations are taken into consideration as we discuss the working principle of the proposed magnetic μ SCC sensor in the next section.

5.2.2 Working Principle

The basic working principle of the magnetic cilia is that the drag-force deflection of the magnetized hair cell causes an asymmetry in the magnetic field distribution around the hair cell, which is sensed by at least two magnetic sensors embedded below it. In case of

magnetoresistance sensors, the change in the magnetic field causes a change in the resistance of the element. The main goal is to create a large magnetic field *gradient* which upon deflection can be locally sensed by the magnetic sensor. Thus, a large magnetic field is not necessary as long as there is a large magnetic gradient. A large magnetic field can cause a DC bias of the magnetic sensors, thus moving them into a less sensitive or even an undesirable saturated region of operation. As shown in figure 5.6, there are two proposed structures: one with the magnetic pillar fixed to the bottom of the channel (upright design), and the other with the pillar fixed to the ceiling of the channel (chandelier design). The magnetoresistors are arranged in a Wheatstone bridge configuration to eliminate common-mode signals and amplify the desired differential signal as shown in figure 5.6b. In both cases, the magnetic sensors are embedded in the bottom substrate.

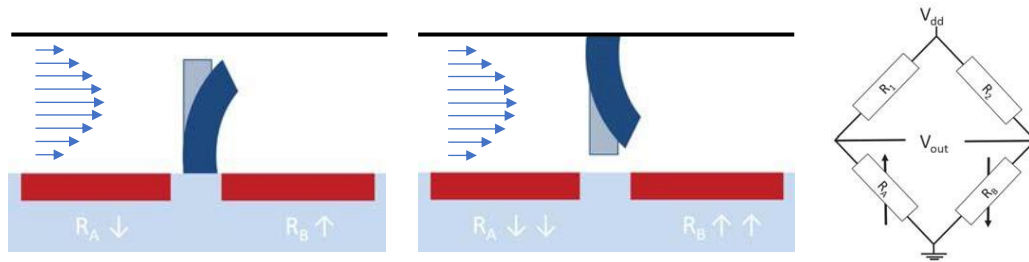


Figure 5.6. (a) Working principle of sensing the fluid flow using flexible magnetic elastomer pillars: the viscous drag from the laminar fluid flow (arrows) deflects the magnetized flexible pillars causing an asymmetry in the magnetic flux density that can be sensed by strategically-placed magnetic sensors with two different hair cell configurations: upright vs. chandelier down; (b) Wheatstone half-bridge configuration.

5.2.3 Magnetic Hair Cell Design

An example of fabricated magnetic hairs cell or cilia structures is presented in figure 5.7. The shown structure mimics the natural staggered bundle of cilia [159], but the designer can shape the cilia or cilia array and, thus, the resulting magnetic field distribution to suit

their needs. The high aspect ratio structure allows for reduced stiffness to increase the sensitivity of the device. Moreover, the structure is tapered at the base for fabrication stability and adhesion robustness.

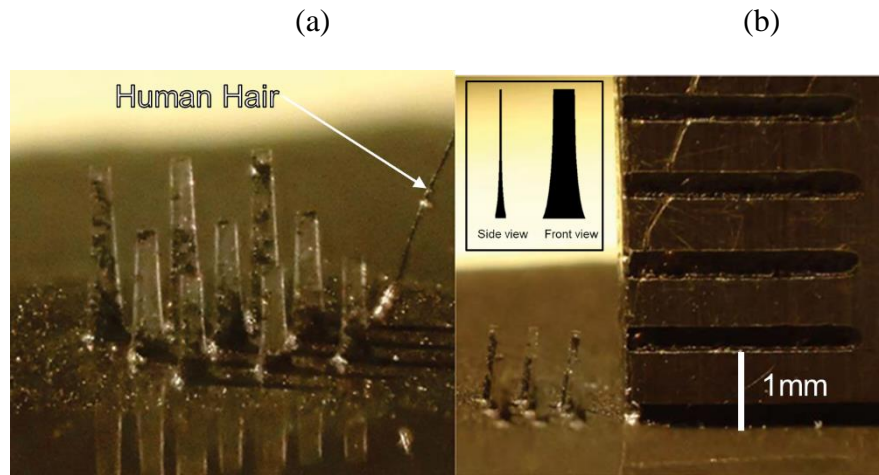


Figure 5.7. Optical images of fabricated magnetic hair cell bundle: (a) a human hair is shown side-by-side with the magnetic hair cell for reference; (b) A ruler with a 1 mm spacing between two marks is shown with the magnetic hair cells for reference.

The cross-sectional shape of the hair cells is a design parameter and its impact will be investigated using numerical modeling in section 5.3.2. A flat rectangular beam is likely to be the best candidate for flow coupling and reduced stiffness. A circular or a crescent shaped hair are other potential options and are presented in figure 5.8. The asymmetrical shape of the crescent structure might be useful to counteract any magnetic non-linearity, and could mimic the asymmetric response of hair cells in nature [38].

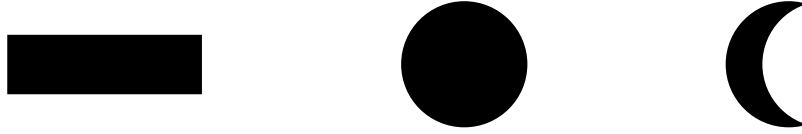


Figure 5.8. Three different potential cross-sections of the fabricated magnetic hair cells from left to right: rectangular, circular, crescent-shaped.

Another design consideration is the magnetic material and the resulting material properties of the hair cells. The base elastomeric material chosen for the micropillar is PDMS, since this is also the material used for building the semicircular microtorus. It is specifically chosen for its low Young's modulus value, making the pillars highly elastic and easy to bend even at small flow velocities. The magnetic material chosen for this work is a nickel-iron-based magnetic powder. The magnetic material concentration relative to the elastomer material will affect both the stiffness and the magnetization strength retained by the hair cell. More magnetic material will make the hair cell stiffer, but will also increase the magnetic field *so a tradeoff between the two needs to be considered.*

Finally, the distribution of the magnetic materials within the hair cell itself is a design parameter. Two potential arrangements are a uniform distribution of the magnetic powder throughout the elastomer or a concentration at the tip.

5.2.4 TMR sensor design

The tunneling resistor geometric structure, configuration and layout are of utmost importance to ensure high sensitivity, stability, no hysteresis, low noise levels, cross signal and common-mode rejection. Additional design criteria are the placement and orientation of the sensors relative to the channel, each other and the hair cells, the number of

magnetoresistor elements and the spacing between elements. The shape and area of each resistor element is important for noise and stability performance [280]. Two different approaches to meet these requirements include either a commercially available TMR Wheatstone bridge based on linear magnetic sensors as discussed in section 5.5.2 or a customized in-house TMR Wheatstone bridge sensor.

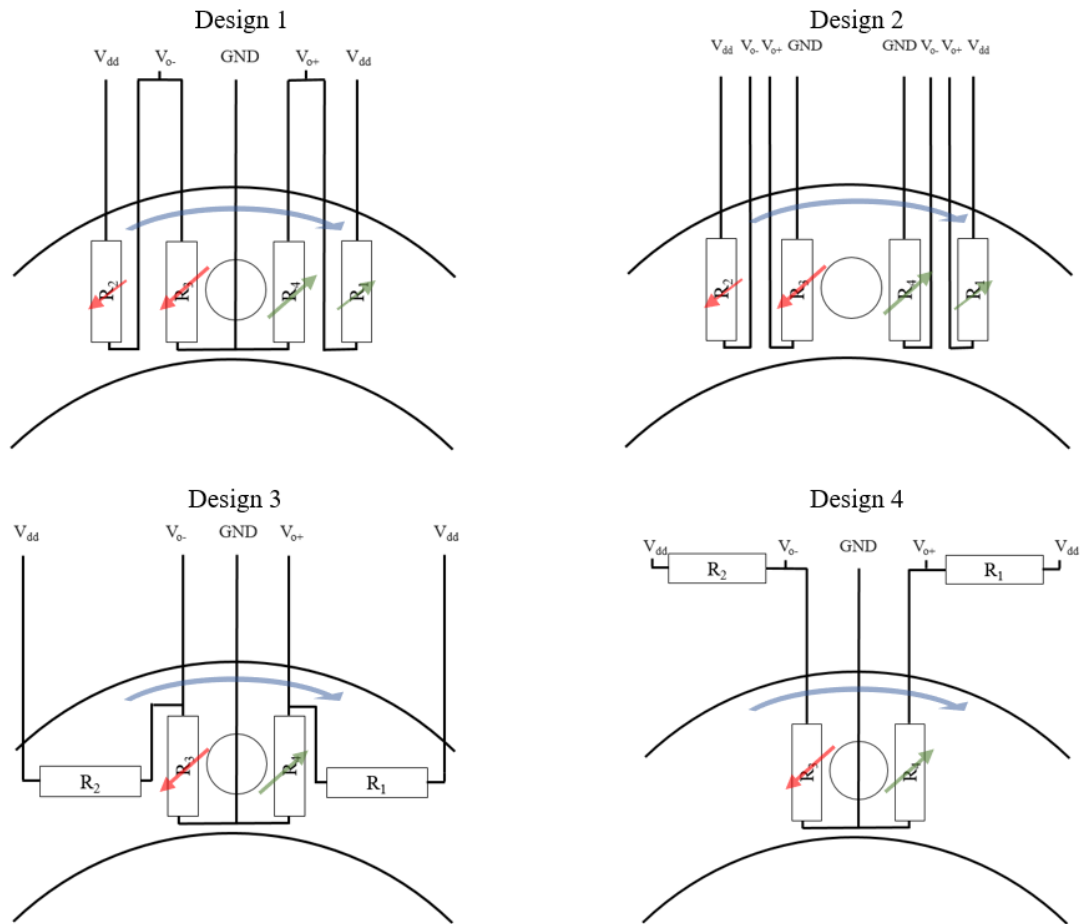
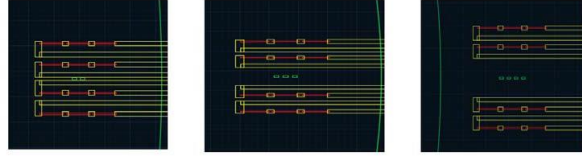


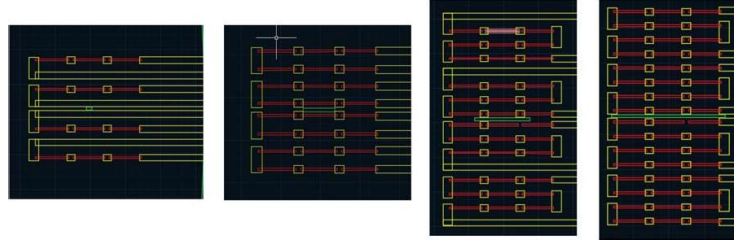
Figure 5.9. Design examples for Wheatstone bridge including four tunneling magnetoresistance sensors with respect to fluid channel and hair cell structure (circle). A clockwise fluid flow is applied causing a flexible magnetic pillar (circle) in the center to deflect. The deflection causes a shift in the magnetic field, thus the resistors will increase (green arrow) or decrease accordingly. The magnitude of change is indicated by the size of the arrow.

To better explain the different configurations shown in figure 5.9, a clockwise fluid flow is applied inside the channel. The fluid flow will deflect a flexible magnetic pillar in the center of the channel to the right. The resistors are placed symmetrical to the magnetic pillar and are designed to sense the magnetic field component perpendicular to their length direction based on the magnetization step. The change in magnetic field experienced by each resistor will be dependent on the location and orientation of the resistors. Maximum magnetic sensitivity is assumed when the resistors are perpendicular to the flow, while minimal when parallel to it.

Based on those assumption, design 1 places all four resistors inside the channel oriented perpendicular to the channel. R_1 and R_4 are on one side of the hair cell while R_2 and R_3 are on the opposite side. R_1 and R_4 increase with R_4 experiencing more resistance change, while R_2 and R_3 decrease, with R_3 decreasing more in magnitude. Based on the interconnections shown in design, the Wheatstone bridge will experience non-maximal change. Another configuration is shown in design 2 that gives more flexibility to the designer. By proper connections as shown in design 2 via wirebonding, a full Wheatstone bridge configuration achieving largest output voltage change for the applied fluid flow is achieved. Two more factors to consider are placement of the resistors inside or outside the channel and the orientation of the resistors. In designs 1–3, all resistors are placed within the channel, experiencing the same flow and temperature. Design 4 puts the reference resistors R_1 and R_2 outside the channel and further away from the hair cells influence. In designs 3 and 4, R_1 and R_2 are rotated by 90 degrees to minimize their sensitivity to the external magnetic field from the pillar. These configurations are half-Wheatstone bridge designs.



(a)



(b)

Figure 5.10. Different TMR-based Wheatstone bridge designs with (a) resistor distance from the hair cell increasing from left to right; and (b) number of resistors increasing from left to right.

Another way to control the sensitivity and behavior of the system is controlling the distance between the location of the hair cell and the magnetoresistors as well as the number of elements per resistor as shown in figure 5.10. It is hard to predict the effect of the distance between the resistors and the pillars, due to the effect of misalignment during the fabrication process. Simulation results in section 5.3.1 will consider this issue. On the number of elements per resistor, more elements increase the resistance while allowing for high bias voltages, thus increasing the sensitivity of the device. Also, more elements will lead to spatial averaging of the signal and reduce any high-frequency magnetic noise.

5.3 Numerical Simulations

Numerical simulations were performed using COMSOL to get a basic understanding of the device operation and the sensitivity to be expected. The response of the angular acceleration sensor is dependent on the design and placement of the flexible magnetic cilia and the TMR sensors, where the deflection of the cilia changes the magnetic field sensed by the magnetic sensors. The following simulations have been performed: 1. A basic study of the magnetic field distribution as a function of the shape and magnetization of the magnetic cilia, as well its location with respect to the magnetic sensors; and 2. a fluidic-structural interaction simulation of the flexible magnetized pillars to get an idea of the cilia deflection to be expected. After those two components are verified, the simulations are coupled to predict the expected magnetic field magnitude change at the sensor locations due to a given rotational input. As will be seen, the response of the magnetic angular acceleration sensor is highly dependent on the artificial cilia characteristics (both mechanical and magnetic), and to a lesser extent, on the TMR sensor's behavior.

5.3.1 Magnetic Simulation

The simulation of the magnetic field generated by the cilia was performed using COMSOL 5.3a using the *Magnetic Fields, No Currents* module. The simulations are used to (1) evaluate the effects of magnetization direction, (2) study the effects of the alignment and placement of the hair cell relative to the sensors, (3) compare the performance of different configurations (chandelier vs. upright), and (4) calculate a nominal value for expected change in magnetic flux density per 100 nm of deflection. This information will guide the design of the magnetic μ SCC.

An initial 2D simulation was used for basic intuition validation. However, the results and figures in this section are based on 3D simulations. Table 5.1 summarizes the material properties and the dimensions used in these magnetic simulations.

Table 5.1. Geometric and material properties used for fluid structure interaction simulations.

Symbol	Quantity	Value	Units
r	Celia Radius	45	μm
h	Celia Height	450	μm
g	Gap	20	μm
w	Element width	3	μm
l	Element height	50	μm
M	Magnetization	140	kA/m

The assumptions are that the pillar is uniformly and isotropically magnetized in a single direction. A magnetization domain condition was applied to the hair cell based on the values found in [141], [264], [281]. The remanent magnetic moment calculation from the vibrating sample magnetometer yields values on the order of 1-10 $\mu A \cdot m^2$ or memu. To apply the magnitude of the magnetization domain condition M to the hair cell, the magnetic moment is divided by the volume of the hair cell ($2.86 \cdot 10^{-12} m^3$). The initial direction of the magnetization was parallel to the long axis of the hair cell (z-axis). The hair cell is set up in the upside-down configuration (chandelier), with a gap of 20 μm .

In figure 5.11, the distributed magnetic field lines (shown only around the south pole) of a z-axis magnetized pillar suspended over a linear array of magnetic sensor is presented. The

sensors placed along the line A-A' in figure 5.11 are symmetrically placed with distances of 25, 50, 75, 100 and 125 μm away from the centered hair cell. To reduce the effects of meshing, the magnetic flux density inside a domain of volume $50 \times 3 \times 10 \mu\text{m}$ (representing a hypothetical sensor) is averaged to calculate the desired magnetic flux density.

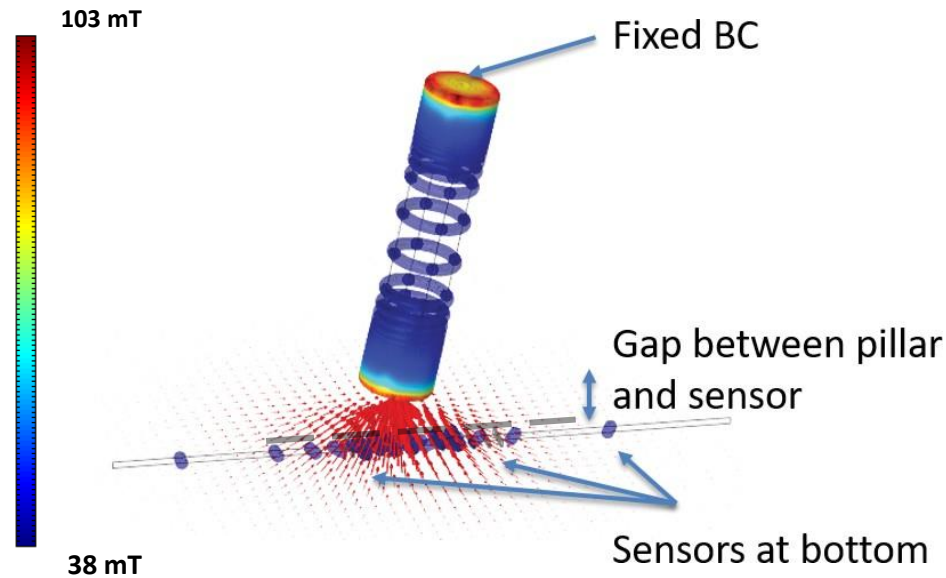


Figure 5.11. 3D rendering of the magnetic finite element physics simulation. The screen capture details a naively-tilted hair cell by 5 degrees. The z-axis magnetized hair cell is suspended at the top of the with a $20 \mu\text{m}$ gap between the bottom of the hair cell and the sensors below it. The red arrows highlight the magnetic field lines, while the contour lines are iso-flux density, with the color legend showcasing the magnitude of the magnetic flux density on the surface of the magnet in mT.

It can be noticed that the magnetic field lines are concentrated -as expected- near the base of the pillar. It is expected that the high gradient near the tip of the magnet can be exploited to achieve higher sensor sensitivities for the chandelier design.

To model the change in magnetic flux density as a function of hair cell deflection, a simplistic parametric model of the beam's x-axis deflection to relevant fluid flow magnitudes was applied to the geometry of the cylinder as a prescribed displacement. The cylinder was extruded from the fixed circle along a parametric line with parameter s between 0 and 1.

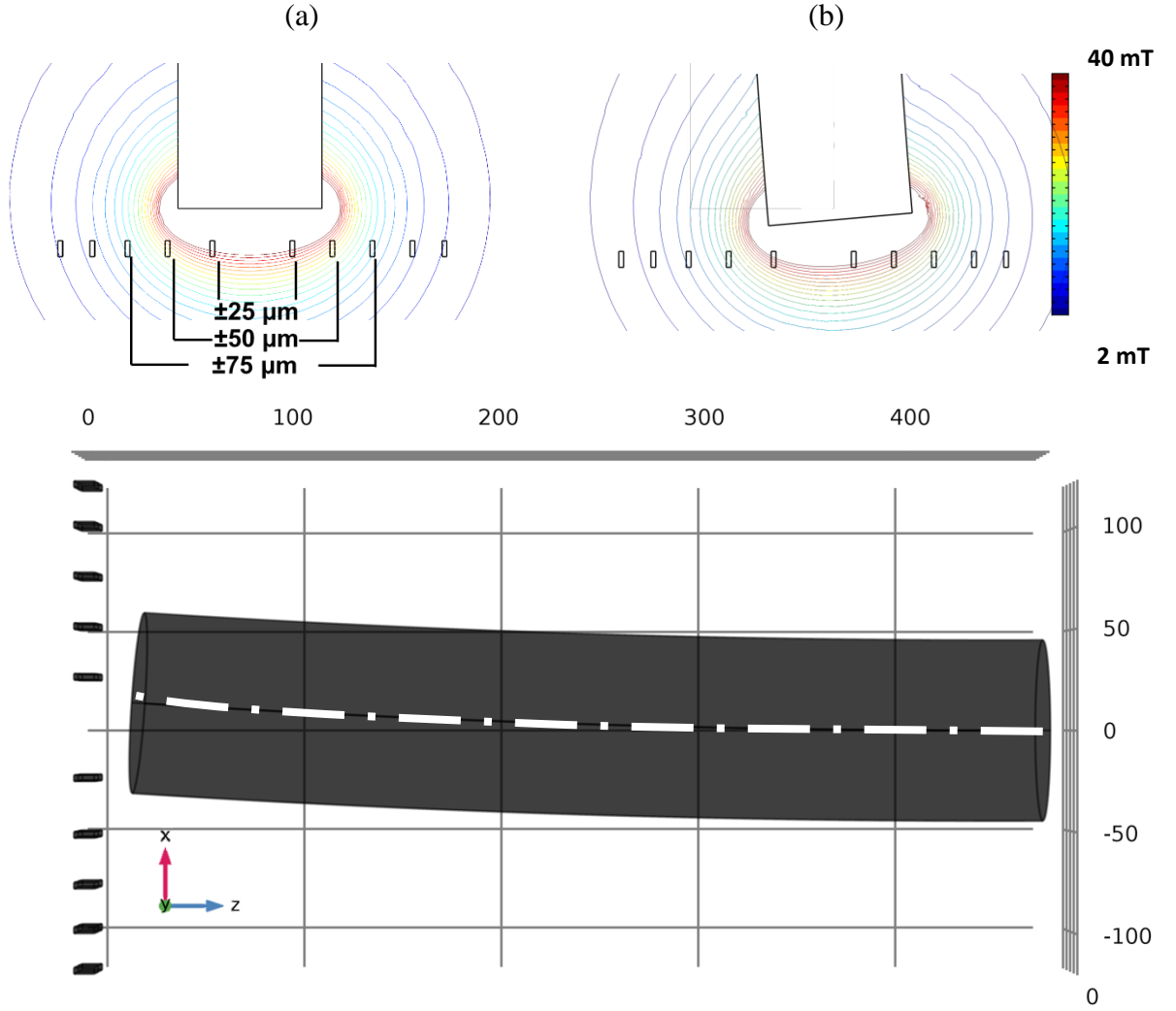


Figure 5.12. 2D cross section of the center along the plane passing through line A-A' showcasing the pillar and the with the linear array of magnetic sensor locations. The contour lines show lines of equal magnetic flux density magnitude from 2-40 mT in increments of 2 mT; (a) zoom-in on the tip of the hair cell experiencing no deflection; (b) zoom-in on the tip of the hair cell experiencing 20 μm deflection at the tip with a silhouette of the pillar under no deflection; (c) an exaggerated illustration of the of the prescribed displacement of the hair cell, with the magnetization axis illustrated in the bottom left. The grid is in μm . The parametric equations describing the dashed line is used to extrude a circle into the desired hair cell shape.

The expression for this set of parametric equations for the line for dimensions $\langle x, y, z \rangle$ are

$$x = a \cdot s^2; y = 0; z = 450 \cdot s \text{ with } a \text{ as the maximum deflection in } \mu\text{m} \text{ experienced at the}$$

bottom of a suspended hair cell, while keeping the magnetization magnitude and direction constant.

Figure 5.12 shows the effect of the deflection of the pillar on the magnetic field lines. A deflection at the tip of the flexible permanent magnet results in a variation in the magnetic flux density magnitude sensed just below it. It can be observed that the contour lines shift to the right about $20\text{ }\mu\text{m}$ as well (the same amount as the deflection). The magnetic flux density difference observed along line A-A' (see figure 5.13) can point towards an optimal location for the magnetic sensor relative to the hair cells. A distance of roughly $50\text{-}75\text{ }\mu\text{m}$ away from the center (i.e. just on the edge of the hair cells initial location considering the hair cell radius of $45\text{ }\mu\text{m}$) provides the maximum change.

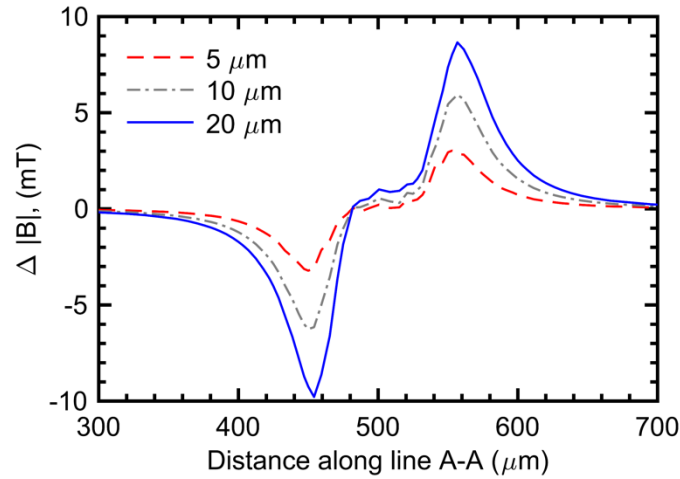


Figure 5.13. Differential signal of magnitude flux density magnitude along line A-A' for three different deflection values (5, 10, and $20\text{ }\mu\text{m}$) relative to the no deflection case.

Figure 5.14 shows the magnetic flux density magnitude in the sensitive x-direction as a function of deflection for two symmetrically located sensors $25\text{ }\mu\text{m}$ away from the edge of the centered hair cell, and the difference between the two signals. It can be seen that each sensor is experiencing a DC bias of roughly 16 mT . However, the difference signal under no deflection is near zero, highlighting the benefit of the differential setup.

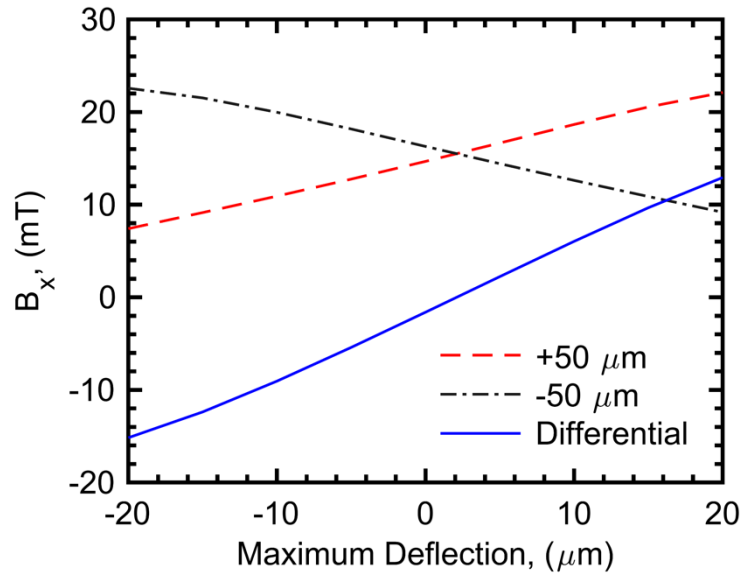


Figure 5.14. Magnetic flux density magnitude in the sensitive x-direction as a function of z-axis magnetized cilia deflection for two symmetrically located sensors 50 μm away from the center of the centered hair cell, and the difference between the two signals.

Proper alignment is crucial for the sensor's performance. Figure 5.15 shows the differential signal of magnitude flux density magnitude as a function of cilia deflection for four different alignments of the hair cell. Thereby, the sensors are shifted along the line A-A' to the right. It can be observed that with a 50 μm shift the sensor's output behavior inverts and has a 35 mT bias under no deflection. The output becomes nonlinear and asymmetric with a 100 μm shift. Under a 150 μm shift, the DC bias goes down to 5mT with a lower sensitivity than the centered case and similar in sensitivity to the 50 μm case. The linearity and the sensitivity are thus highly dependent on location. This shows that proper TMR sensor placement and alignment are key for optimizing the performance of the proposed device.

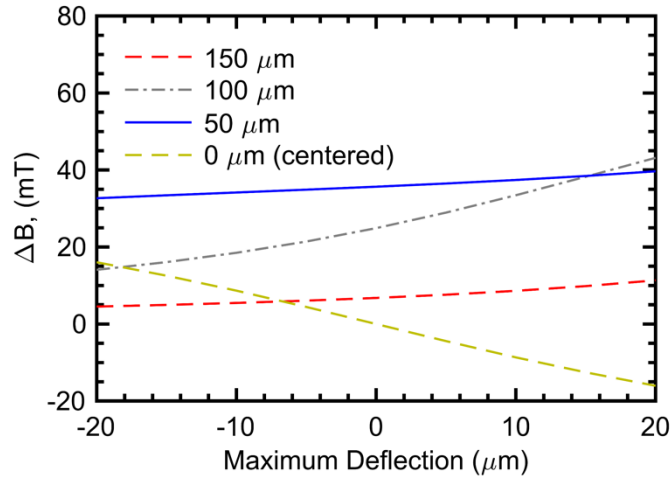


Figure 5.15 The effect of misalignment along line A-A' on the differential magnetic flux density magnitude in the sensitive x-direction as a function of deflection for two symmetrically located sensors 50 μm away from the centered hair cell.

The effect of the angle of the magnetization is presented in figure 5.16 as the differential signal of magnitude flux density magnitude along line A-A' for five symmetrical paired sensors 25, 50, 75, 100 and 125 μm away from the centered hair cell. The maximum sensitivity is for the 50 μm sensor pair for z-axis magnetization, while the maximum is sensed by the 75 μm pair for the x-axis magnetization. However, the 25 μm pair shows non-linearities for both magnetizations. Based on a factor of roughly two in the best-case sensitivity improvement in z-axis over the x-axis best-case sensitivity, it seems overall that marginally better to magnetize the hair cell along its long axis.

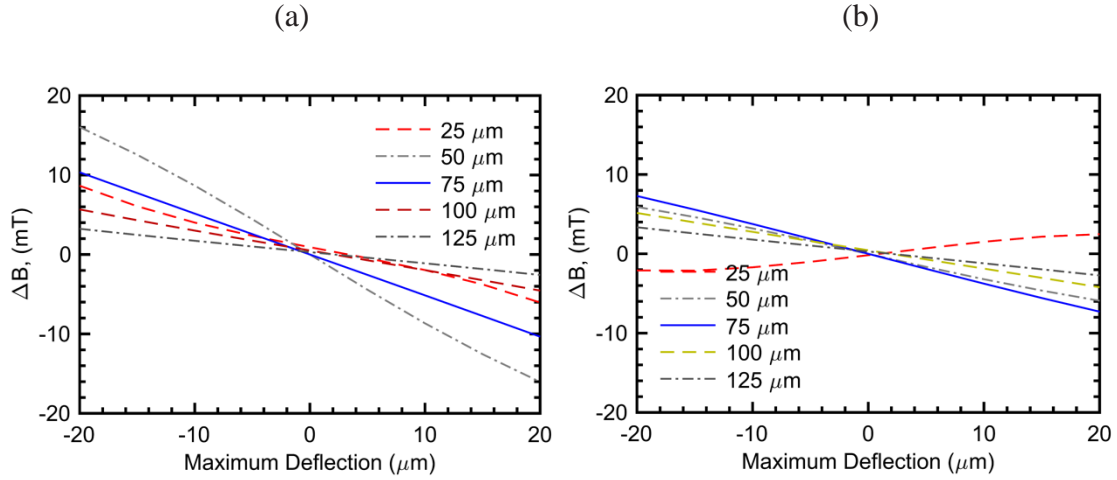


Figure 5.16 Differential signal of magnitude flux density magnitude along line A-A' for five symmetrical paired sensors 25, 50, 75, 100 and 125 μm away from the centered hair cell for: (a) z-axis magnetization; (b) x-axis magnetization.

Another factor to consider is the configuration of the sensor (see figure 5.6). The results of this section up to this point were from the chandelier configuration. Figure 5.17 shows results for the upright design, again for the case of five symmetric sensor locations. As can be observed the sensitivity to deflection is low, and highly sensitive to sensor location. The chandelier design offers a more attractive option/configuration for our differential sensing purposes.

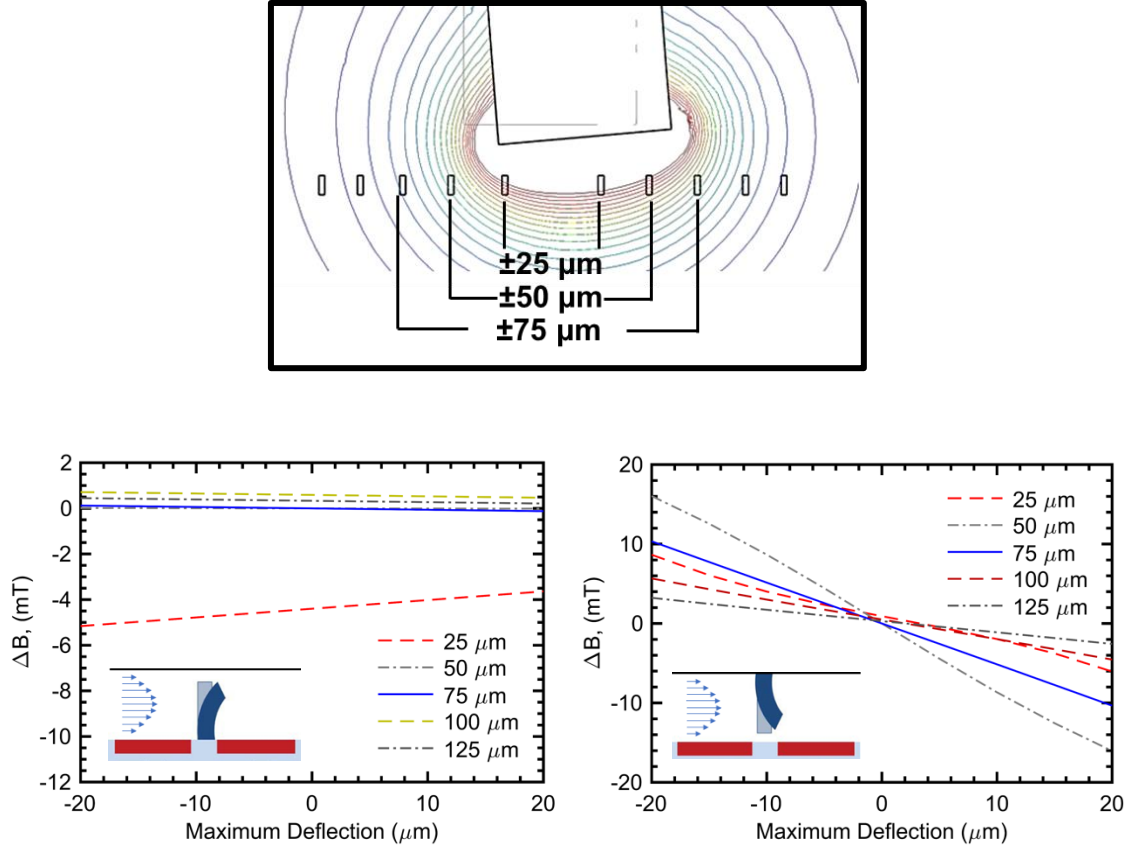


Figure 5.17 Differential signal of magnitude flux density magnitude along line A-A' for five symmetrical paired sensors 25, 50, 75, 100 and 125 μm away from (left) an upright for z-axis magnetized centered hair cell (right) a z-axis magnetized centered chandelier hair cell as a function of deflection.

Conclusions

This section on magnetic simulation was documented and used to guide the design choices of the sensor. The chandelier design can increase the sensitivity substantially, and is more location tolerant than the upright design. The edges of the hair cells show a strong magnetic field gradient that can potentially be exploited. The direction of magnetization does not have as much of an effect as was expected. However, as magnetic sensor alignment with respect to the hair cell will be extremely crucial in optimizing the magnitude response of the sensor.

5.3.2 Fluid Structure Interaction Simulation

To quantitatively model and understand the deflection of the bioinspired cilia due to fluid flow, a numerical fluid structure interaction multiphysics finite element model was created using COMSOL 5.3a. The simulations are used to (1) evaluate the stiffness of the proposed hair cells and compare them to their natural counterparts, (2) calculate a nominal value for expected hair cell deflection per 1 mm/s fluid flow, (3) evaluate the sensitivity of the hair cell deflection to 1 deg/s² induced in-plane rotation, and (4) understand the transient behavior of the hair cell. This information will be used to optimize the design of the magnetic μ SCC.

5.3.2.1 Basic Fluid Flow Modeling

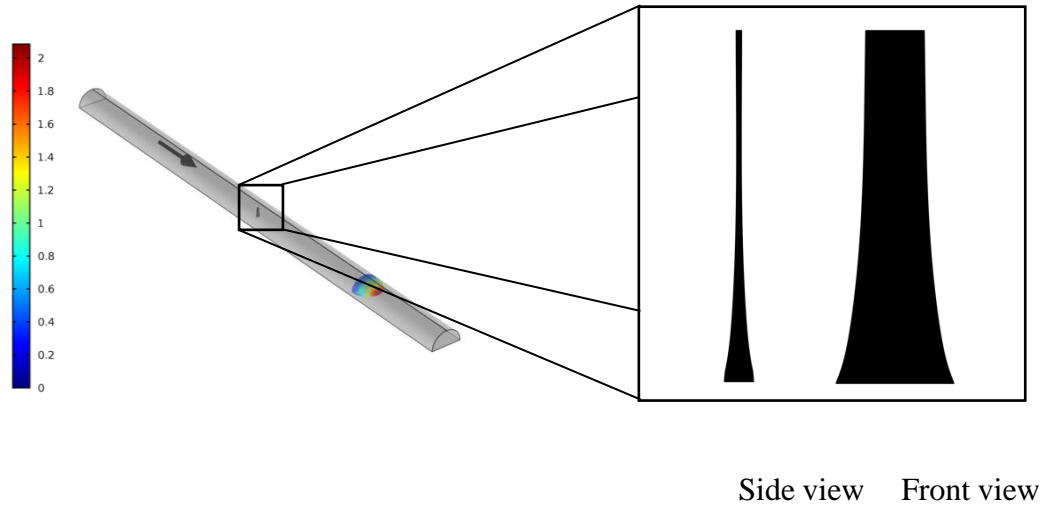


Figure 5.18. (left) 3D model used to characterize hair cell deflection as a function of flow velocity. In the channel, parabolic flow is induced with a maximum velocity of 2 $\mu\text{m/s}$; (inset) cross sectional view of the proposed hair cell design. Dimensions of hair cell are documented in table 5.2.

The first model is presented in figure 5.18. A straight semi-hemispherical channel with radius r and length L with an embedded hair cell were used to calculate the effective

stiffness of the hair cell and its response to laminar fluid flow. A cross section of the proposed hair cell is presented in figure 5.18a. The hair cell and channel dimensions and material properties used are summarized in table 5.1. The fluid structure interaction (FSI) module was used in the linear elastic regime which is expected to be the region of operation. A fixed constraint was applied to the base of the cilia. A periodic flow boundary condition was applied to both ends of the channel to simulate the model of a torus.

Table 5.2. Geometric and material properties used for fluid structure interaction simulations.

Symbol	Quantity	Value	Units
L	Length	$2.75 \cdot 2\pi$	mm
r	Minor radius	500	μm
ρ_f	Fluid density	990	kg/m^3
μ	Dynamic viscosity	5	$mPa \cdot s$
E_{hc}	Young's modulus of hair cell	750	kPa
ρ_{hc}	Hair cell material density	1000	kg/m^3
h	Hair cell height	300	μm
t_{top}	Hair cell thickness	5	μm
t_{bottom}	Hair cell thickness	25	μm
w_{top}	Hair cell width at top	50	μm
w_{bottom}	Hair cell width at bottom	100	μm

Initial simulations were conducted to characterize the deflection of the hair cell to fluid flow inside a linear semi-hemispherical channel as shown in figure 5.19. Within the fluid flow range of interest (0-50 $\mu m/s$), the deflection of the hair cell is linear and is 5 μm for 50 $\mu m/s$ average flow rate. Based on these initial simulation results, the hair cells have maximum deflections on the order of 100 nm/($\mu m/s$) flow velocity depending on the material properties and design of the hair cells. This means the angle of deflection will be

small and the operation is in the linear regime. These deflections are on the same order of magnitude as the cupula displacement in mammals as described in [157], [282]. A boundary load was applied to the top of the hair cell of 1 nN and the resultant maximum deflection was 5.65 μm , thus the calculated stiffness is 180 $\mu\text{N/m}$. That is ~ 3 orders of magnitude large than natural vestibular hair cells (44 nN/m) [203].

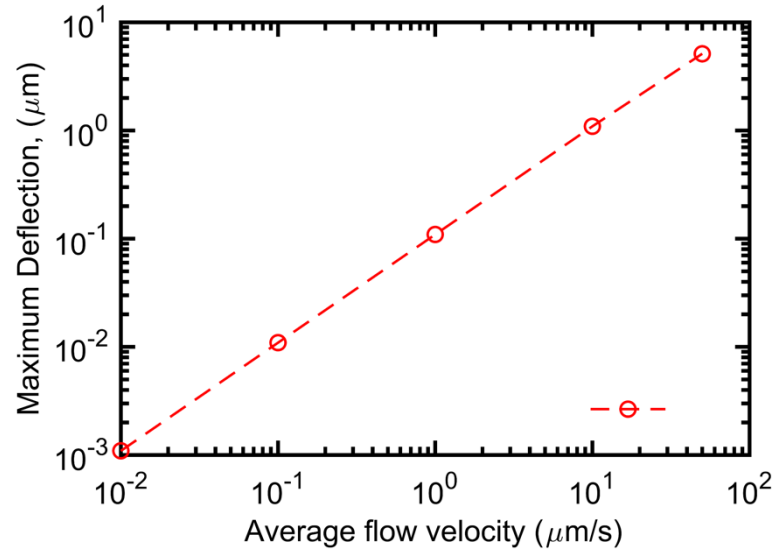


Figure 5.19. Maximum hair cell deflection as a function of flow velocity for a hair cell with dimensions according to table 5.2.

5.3.2.2 Inertial Fluid Flow Modeling

After the fluid flow characterization, a 3D model was constructed using a semi-hemispherical torus as the microfluidic channel. It modeled the pillar's deflection induced by the range of angular and linear accelerations of interest (0-1000 deg/s^2). The hair cell with dimensions in table 5.2 was situated in a semi-torus ($R=2.75 \text{ mm}$; $r=500\mu\text{m}$). The rest of the properties are the same. Flow was induced using body force domain conditions similar to previous simulation sections. The sensitivities to z-axis rotational acceleration as well as to x,y-axis

linear accelerations are shown in figure 5.20 with an inset showing an illustration of the torus. Similar to section 4.3.3, the applied linear accelerations were converted into apparent angular accelerations using the major torus radius R .

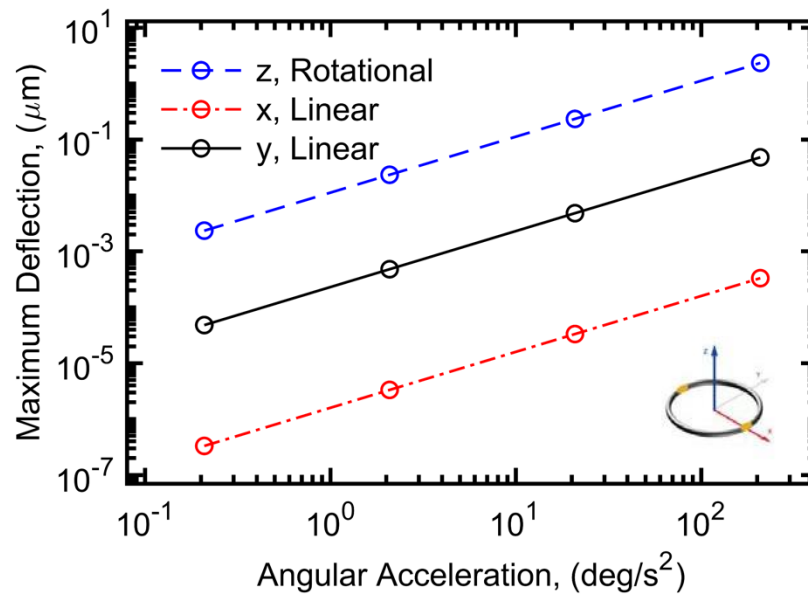


Figure 5.20. Deflection of hair cell as a function of applied angular acceleration around the z-axis (red) and linear accelerations along the x-axis (grey) and the y-axis (blue). The applied linear accelerations are translated into effective angular accelerations using the major radius $R=2.75\text{mm}$.

The pillar deflection shows high sensitivity to in-plane angular acceleration with a simulated sensitivity of $0.01 \mu\text{m}/(^{\circ}/\text{s}^2)$, but almost no sensitivity to x-axis in-plane linear acceleration (four orders of magnitude smaller than the rotational sensitivity using equivalent acceleration). However, the y-axis in-plane acceleration was two orders of magnitude smaller to the rotational equivalent sensitivity only. This increased sensitivity could be attributed to the density differential between the fluid and the hair cell.

5.3.2.3 Transient Fluid Flow Modeling

Using the torus model from the previous section, a transient response to a step input of angular acceleration is shown in figure 5.21a. The normalized responses with respect to the maximum velocity in the channel and the maximum displacement are plotted. It can be seen that the hair cell time response is slightly faster than the normalized velocity response for both tori in the beginning. The velocity in the larger channel torus, however, passes the normalized displacement at the 20 ms mark. This is a non-intuitive.

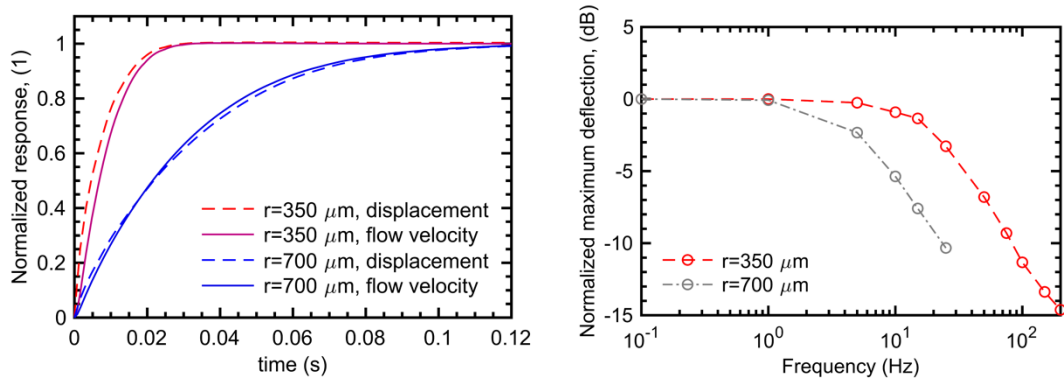


Figure 5.21. Transient FSI model: (a) Normalized transient step response of hair cell deflection and flow velocity for two different minor radius tori with the same size hair cell as table 5.2 (b) Magnitude-normalized frequency response of the maximum hair cell deflection to an angular acceleration of 100 deg/s^2 for two different minor radius tori with the same size hair cell as table 5.2.

A normalized bode plot of the deflection of hair cells with two tori with radii of $350 \mu\text{m}$ and $700 \mu\text{m}$ is shown in figure 5.21b. The transient and frequency simulations show that the dynamic response of the device is not limited by the frequency response of the pillar, but the mechanical frequency response of the fluid in the microchannel. Overall, cut-off frequencies in the range of 10-50 Hz are thus achievable using this magnetically sensed design.

5.4 Fabrication

Fabricating the magnetic μ SCC involves fabricating the magnetic hair cell structures, fabricating the magnetic sensing element, assembling the two parts and packaging the system.

5.4.1 Hair cell fabrication

Polydimethylsiloxane (PDMS) (Sylgard 184 Silicone Elastomer, Dow Corning Corporation) is prepared by mixing the pre-polymer and the curing agent in a 10:1 weight ratio. The magnetic powder (MQP-16-7-20068-070, Magnequench) is mixed in with PDMS in a 10-50% weight ratio. A mold was created using two-photon polymerization lithography by the Nanoscribe Photonic Professional GT tool (Nanoscribe GmbH, Germany) at King Abdullah University of Science and Technology's cleanroom. Next, a reverse mold was created by Moussi and Kosel [283] by encircling the 3D printed part with a 3D printed frame (using the Nanonscibe) to cast the PDMS. After casting, the reverse PDMS is cured in a 90 °C environmental chamber for an hour, PDMS is gently pulled out. The reverse mold is coated with 10 μ m of Parylene C (SCS Labcoater 2, USA) to reduce adhesion. Finally, the reverse mold is filled with PDMS under high vacuum for at least 10 minutes to properly fill the narrow parts of the mold. The mold is cured in an environmental chamber (Envec, Japan) at 65 degrees Celsius for an hour, either subjected to a strong magnetic field from a permanent magnet or the structure is magnetized post casting using an electromagnet (Model 3470, GMW Magnet Systems, USA). The fabrication of the elastomeric magnetic hair cell is shown in figure 5.22.

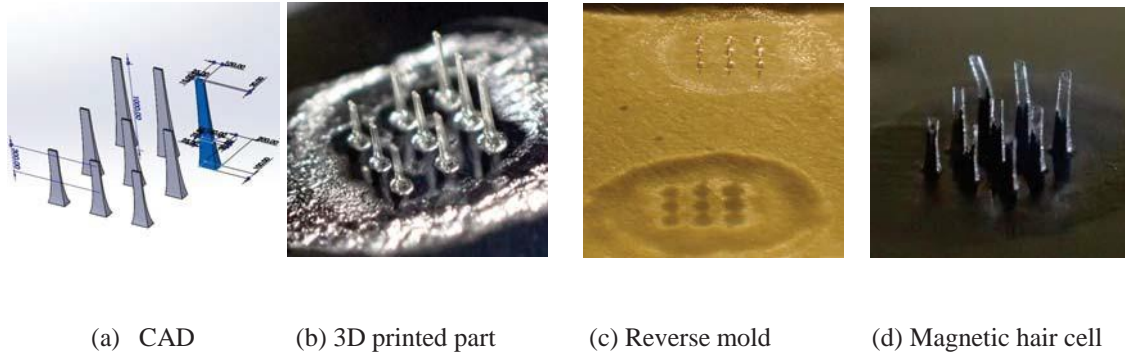


Figure 5.22. Hair cell from CAD design file to fabricated device (a) Draw in CAD; (b) 3D Print with Nanoscribe then conformally coat with 10 μm Parylene C; (c) Cast PDMS and peel off reverse mold, then conformally coat reverse mold with 10 μm Parylene C; (d) Cast PDMS with magnetic powder mixture and peel off. The pillars can be magnetized using an electromagnet during or post curing.

5.4.2 Magnetic sensor fabrication

5.4.2.1 KAUST TMR Sensor

The fabrication process starts with growing thermal oxide on a silicon wafer. This is followed by deposition of a metal contact and the magnetic stack. The metal contact is patterned and a spacer polymer is then added and patterned. The process concludes with a secondary contact to be able to probe the resistance of the magnetic stack.

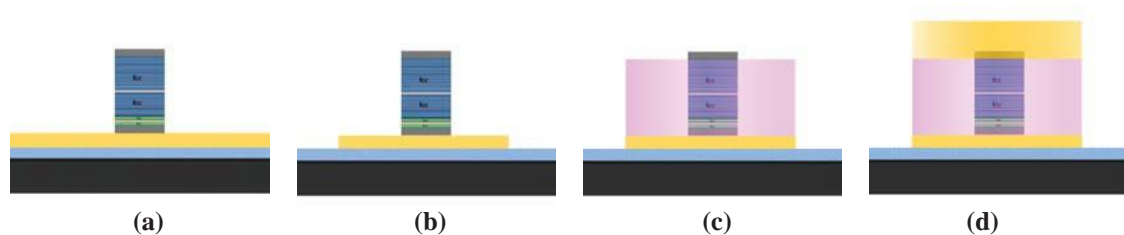


Figure 5.23. Fabrication Process of magnetic TMR sensor device. (black) silicon substrate (light blue) thermal silicon dioxide (yellow) metal (multi-color) magnetic stack (pink) spacer.

Figure 5.23 highlights the process. The magnetic stack is composed of inter-layered thin films deposited by magnetron sputtering under high vacuum (Singulus Rotaris tool) onto silicon substrates. The final magnetic tunnel junction configuration for each layer was (in nm): Si / SiO₂ / Ta (5) / CuN (25) / Ta (5) / CuN (25) / Ta (3) / Pt₃₈Mn₆₂ (20) / Co₇₀Fe₃₀ (2.2) / Ru (0.85) / Co₄₀Fe₄₀B₂₀ (2.4) / MgO (1.6) / Co₄₀Fe₄₀B₂₀ (2.4) / Ta (10) / CuN (30) / Ru (7) / Ta (10).

A 3190 A/m magnetic field was applied to the substrates during the deposition step in order to define the easy axis in the pinned and free layers. The fabrication of the sensors required six lithographic steps, as described in [284]. The magnetic thin-film layers were patterned by direct laser writing on photoresist followed by soft sputter etching. The stacks were covered with a 100 nm layer of Al₂O₃ deposited by sputtering. The contact leads were then defined by lift off.

5.4.2.2 Commercial TMR sensor

An alternative and backup plan to the in-house TMR sensor are commercially available linear tunneling magnetic junction sensors in a full Wheatstone bridge configuration (e.g. TMR2901), which exhibit good linearity, good dynamic range, high sensitivity and low noise levels as shown in figure 5.4 adapted from [277] for a similar device TMR-J1.

5.4.3 Packaging

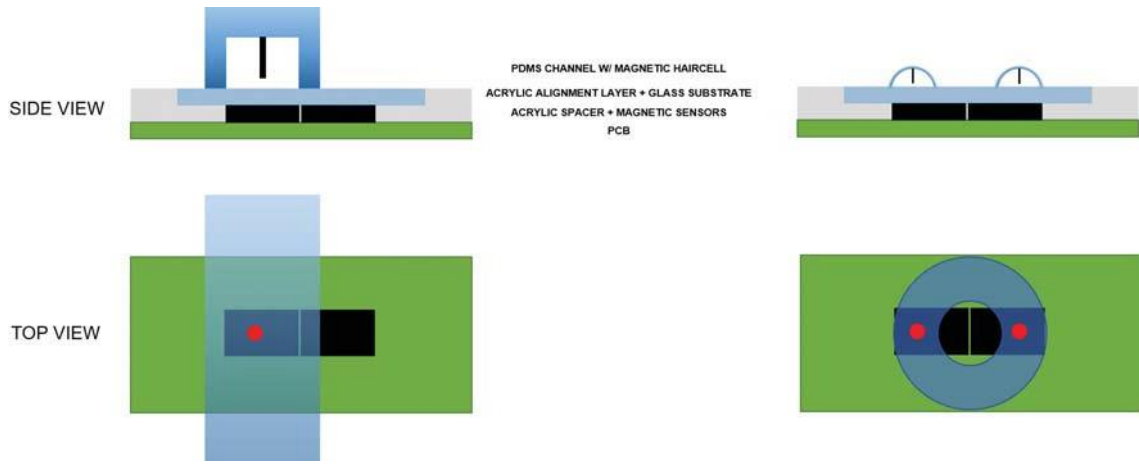


Figure 5.24. Block diagram of the experimental setup and interface circuitry of the sensor.

The device's overall packaging process is described in figure 5.24. Two template structures were created to test (1) the sensor response to the fluid flow and (2) the inertial response using a microfluidic torus. The first step is to create the PDMS channel with an embedded hair cell. The second step is to create a substrate with embedded commercial TMR devices and a more planar surface to allow for bonding with the channel layer. The third step is to align and bond the magnetic substrate to the PDMS channel on top.

5.5 Magnetic characterization

5.5.1 Magnetic sensor characterization

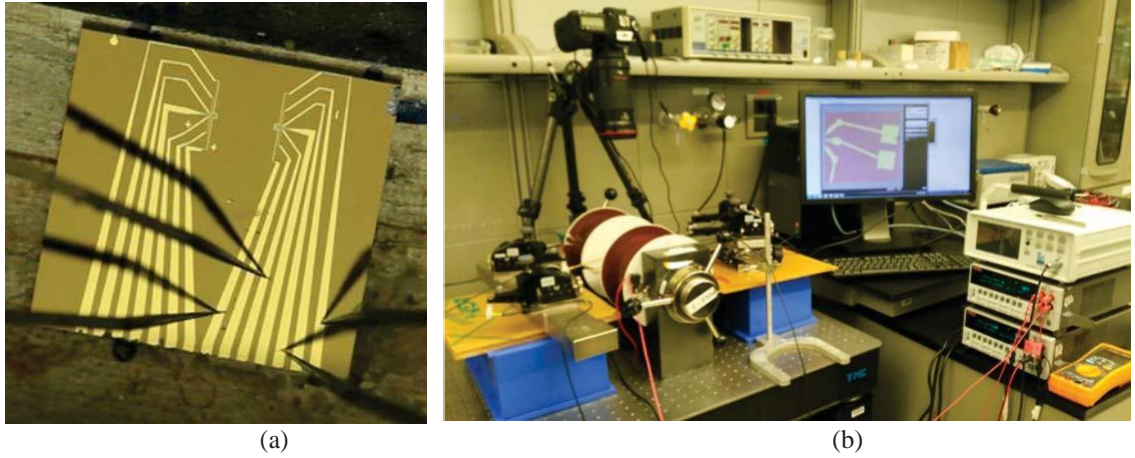


Figure 5.25. Magnetic probe station with a controllable magnetic in the lab of Dr. Kosel's lab at King Abdullah University of Science and Technology (KAUST).

The test setup used to characterize the custom TMR sensors is shown in figure 5.25b. The probe station is combined with an electromagnet. The resistance of the device is measured using a 4-point Kelvin probe configuration to eliminate any lead resistances. A current of 10 mA was applied using a Keithley 2400-C in 4-wire resistance mode and ten consecutive voltage measurements were averaged at each field step. The iron-core Helmholtz coils were driven by a Kepco Bop72-6m Bipolar DC Power Supply / Amplifier (72V 6A 400W) working as amplifier to another Keithley 2400-C in current source mode, while the field was monitored using a F.W. Bell Gaussmeter model 6010. The field was swept with 0.1 Oe steps, and its direction was the same as that of the easy axis of the free layer. The magnetoresistance properties were all measured at room temperature.

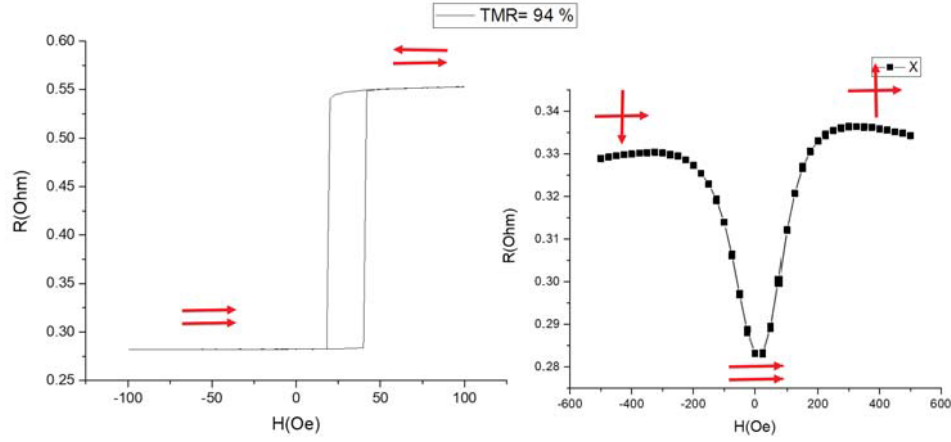


Figure 5.26. TMR Magnetic Field Sensitivity: Resistance response of the TMR sensor array with an external magnetic field applied to the X (parallel to easy axis) and Y (perpendicular to easy axis) directions.

Figure 5.26 highlights the behavior of the magnetic sensor when the magnetic field lines are parallel and perpendicular to the easy axis of the TMR element. The arrows indicate the behavior of the applied magnetic field relative the magnetic layer in the junction. The parallel sensor experiences large abrupt changes with high sensitivity but large hysteresis (behaves more like a switch). The perpendicular one is less sensitive over the same magnetic field range compared to the parallel direction. The cross section of each magnetic junction was elliptical in shape with dimensions $1 \times 1.2 \mu m^2$. The performance of this magnetic junction sensor is characterized by a $\sim 100\%$ TMR ratio as highlighted by the doubling resistance in figure 5.26 (left). The TMR ratio is defined as $(R(H_{+\infty}) - R(H_{-\infty})) / R(H_{-\infty})$, where $R(H_{+\infty})$ is the resistance in the anti-parallel position, and $R(H_{-\infty})$ is the resistance in the parallel position), and the junction has a resistance area product of $0.3 - 0.5 \Omega \cdot \mu m^2$.

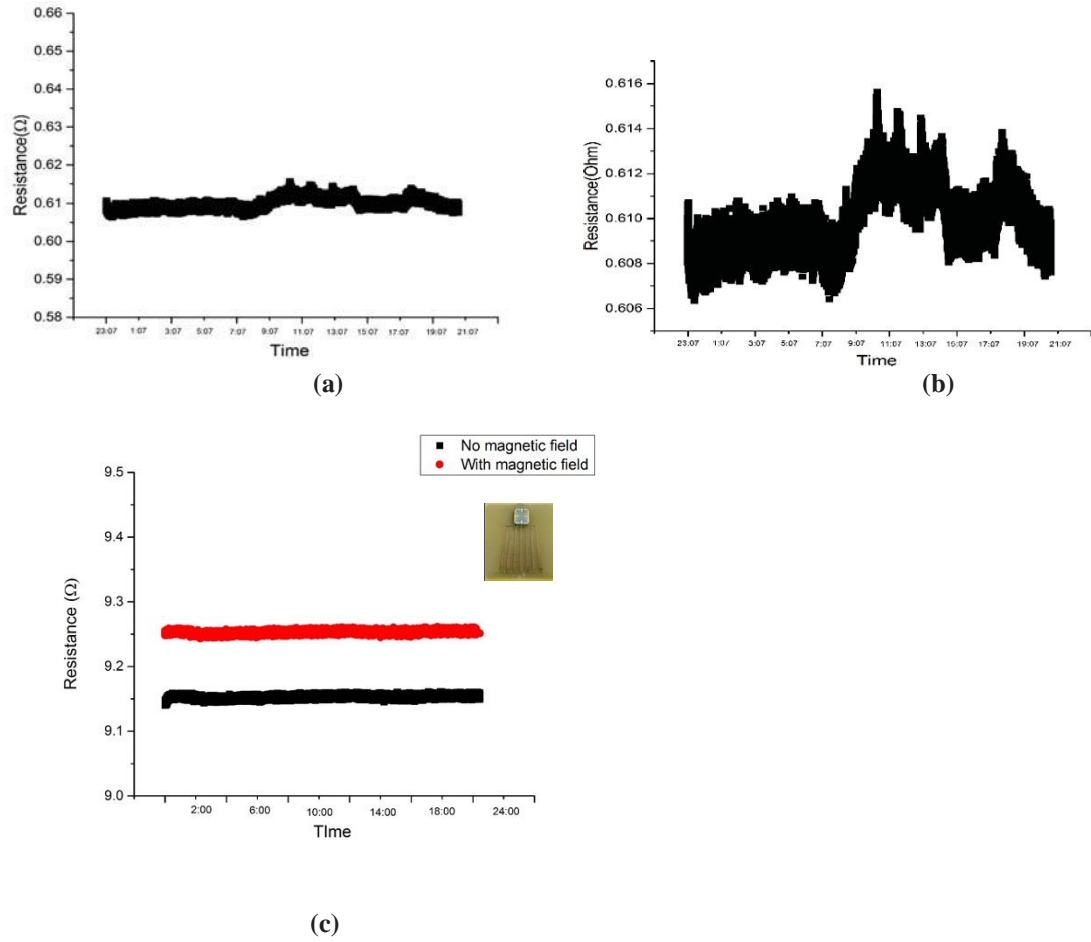


Figure 5.27. In-house TMR resistance drift over time (a) over 24-hour period (3) zoom-in on 3-hour period. (c) Different device showing improved stability over 20 hours with and without a DC magnetic bias after deposition process improvement. Note the higher resistance. Data collected by Altynay Kaidarova at KAUST.

Figure 5.27a shows the measured 4-point resistance over twenty hours and over three hours in figure 5.27b. An improvement to the magnetic deposition step allowed for better stability and higher resistance as observed in figure 5.27c. Also, it has been observed that power consumption can affect the stability of the sensor over time as seen in figure 5.28a. The fluctuations are reduced as observed by the decrease in the standard deviation and standard error in figure 5.29b as the current consumption goes up.

Despite overall general good stability, an Allan variance calculation is evaluated to characterize the drift and stability of the in-house TMR sensor and shown in figure 5.28c. The three slopes observed correlate to the angle of random walk (-0.24 vs. -0.5) and bias instability (+0.125 vs. 0) and the rate ramp (+0.956 vs +1). The characterization highlights the long term drift experienced by the in-house magnetic sensor.

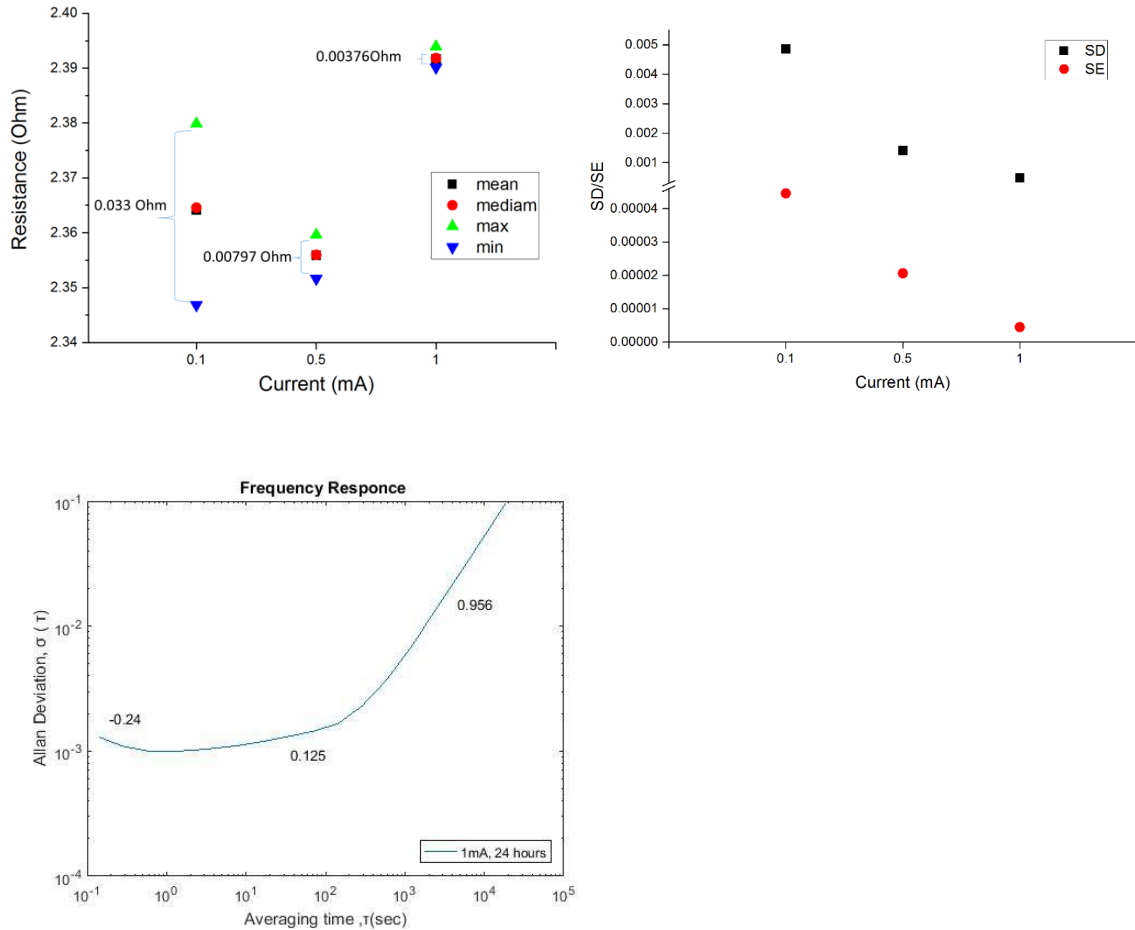


Figure 5.28. In-house TMR resistance stability as a function of current (a) resistance fluctuation; (b) standard deviation (SD) and standard error (SE) of measured resistance (c) Allan Deviation as a function of averaging time with slopes of each regime indicated. Data collected by Altynay Kaidarova at KAUST.

5.5.2 Commercial Magnetic Sensor Characterization

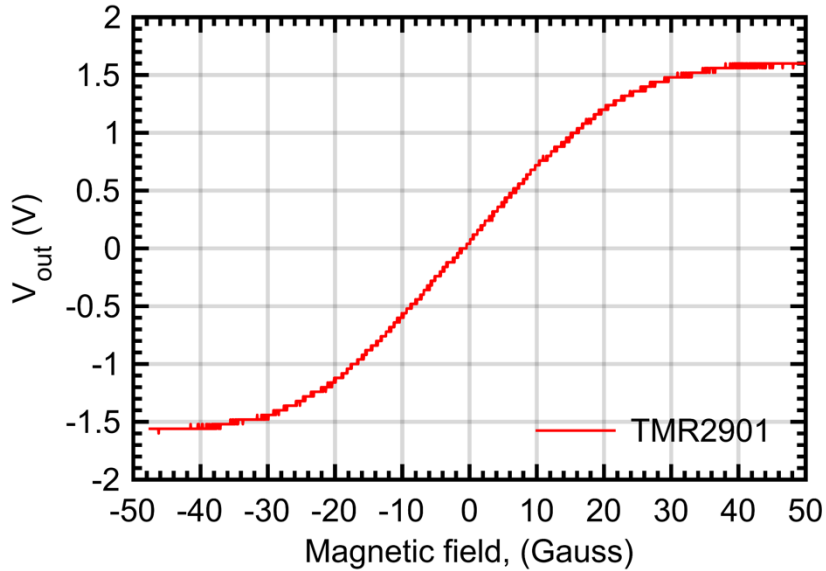


Figure 5.29. Commercial TMR2901 signal output as a function of the applied magnetic field in the sensitive direction with a +3V bridge bias.

The commercial TMR2901 linear magnetic sensor is a Wheatstone bridge TMR-based magnetic sensor. The sensor has a good dynamic range of ± 30 G and a very low hysteresis of 0.1 G. The sensitivity of the commercial magnetic sensor was measured using a setup similar to the one used in section 5.6.1. An electromagnet (Model 3470, GMW Magnet Systems, USA) was controlled by a current source directly (Keithley 2400, USA) and the resulting magnetic field was measured by a magnetic probe (F.W. Bell Gaussmeter model 6010). The data from the probe was collected by F.W. Bell software. The voltage output of the TMR 2901 was acquired by a NI-PCI-6251 DAQ card. (National Instruments, USA). Thereby, a 3V bridge voltage was supplied to the sensor from a voltage source (Keithley 2636 Sourcemeter, USA). The measured sensitivity of 75 mV/G matched the specification of 25 mV/V/G with +3V bridge voltage as shown in figure 5.29.

5.5.3 Magnetic Material Characterization

In order to investigate the magnetic properties of the magnetic hair cell, the material is characterized via vibrating sample magnetometer (VSM, Lakeshore). To this end, the z-axis magnetized hair cell (magnetized along its long axis) is firmly affixed to the sample holder using adhesive tape to prevent any movement. The measurement was conducted by applying a DC magnetic field between 15 kOe and 15 kOe at room temperature. The field is applied, while oscillating the holder at 83 Hz with 1mm amplitude. The measured magnetization curve is shown in figure 5.31.

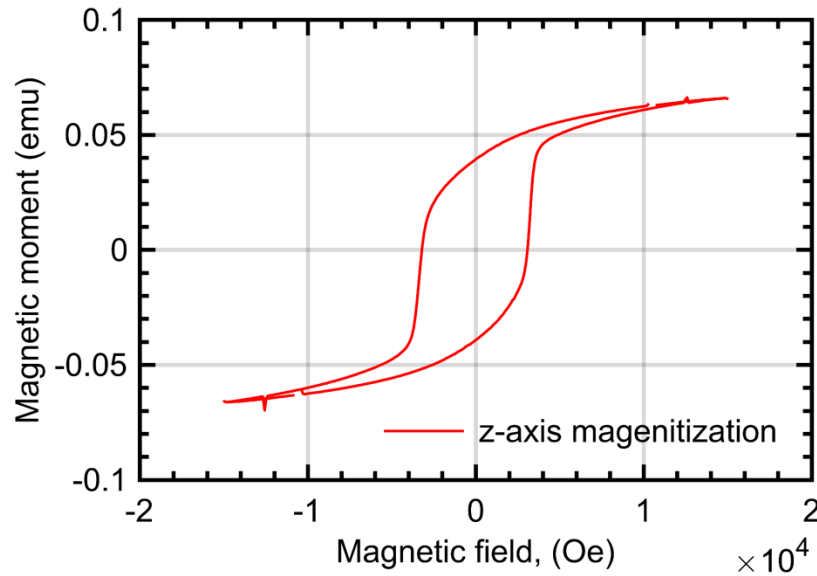


Figure 5.30. Magnetic moment as a function of applied field for a magnetic elastomeric hair cell collected using a vibrating sample magnetometer. The hair cell volume used is $6.3 \cdot 10^{-10} \text{ m}^3$, thus the magnetization is 62.4 kA/m, which is about half the assumption used in our initial simulations.

The resultant curve shows that the remanent magnetization in the axial (long axis) direction is 39.3 memu, with a saturation and saturation magnetization of 66 memu. Using a hair cell volume of $6.3 \cdot 10^{-10} \text{ m}^3$, this results in a relatively high value for the magnetization

of 62.4 kA/m, implying that the magnetization process in a strong magnetic field of 0.8 T followed by elevated temperature curing is effective in creating a strong flexible permanent magnet. The high remanence value shows the permanent magnetic properties of the cilium which are on par with previous magnetic hair cells [264], [281] due to the higher magnetic powder content with a weight ratio of 50%. However, the extra magnetic powder can lead to stiffer hair cells, thus less deflection.

5.5.4 Discussion

Based on the characterizations of the two available magnetic sensors, the in-house sensors were set aside and mechanical testing focused on the use of the commercial linear magnetic sensors for its ease of use, linearity, low offset and common-mode rejection.

5.6 Preliminary Testing Results

5.6.1 Electronic analog front end

As mentioned before, two TMR sensors in close proximity are used in a differential setup to remove common-mode interference signals stemming from the earth's magnetic field or electromagnetic interference signals from electrical equipment, passing cars and passing trains [267]–[271]. The analog front end highlighted in figure 5.31 is critical for processing and addressing any large common mode signal.

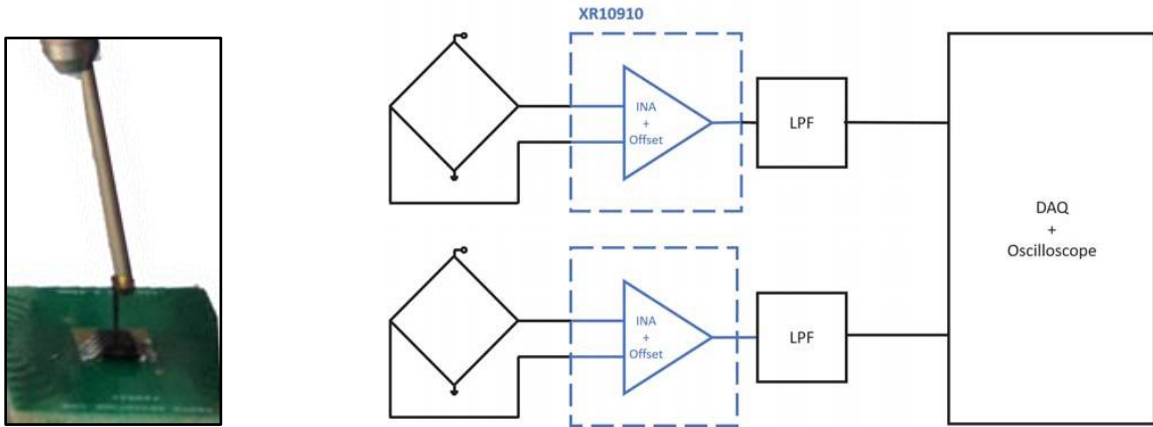


Figure 5.31. Analog front end used to control the large common-mode interference from the Earth’s magnetic field, and other large sources of magnetic interference. The top Wheatstone bridge is used as a reference sensor. The bottom Wheatstone bridge is used as sensor with a hair cell manipulated in its vicinity as shown in the small inset. (inset) Arm of a linear positioning stage with a magnetic hair cell attached to the tip and placed above the magnetic sensor.

The two Wheatstone bridge sensors TMR 2901 (MultiDimension, China) are placed parallel to one another and 3 mm apart to detect any interfering signal on both sensors. One sensor will experience the magnetic fields of the magnetized hair cell and the Earth magnetic field, while the other will only experience the Earth’s magnetic field. The output signals from the Wheatstone bridge sensors are amplified by instrumentation amplifiers (AFE-XR10910) and low-pass filtered. A digital offset is used to center the output in the middle of the output range. The signal is digitized by a PCI6200 (National Instruments, USA) DAQ. The difference of the two signals is the desired signal caused by the deflection of the magnetized hair cell. It should be noted that using custom-designed TMR, one sensor can be placed slightly upstream, the other downstream from the magnetic hair cell, so that one sensor sees an increase in signal while the other sees a decrease. Arranged in a Wheatstone like shown in figure 5.9, the desired differential signal is amplified, while common-mode interference signals are rejected.

5.6.2 Magnetic Mechanical Characterization – Hair cell displacement

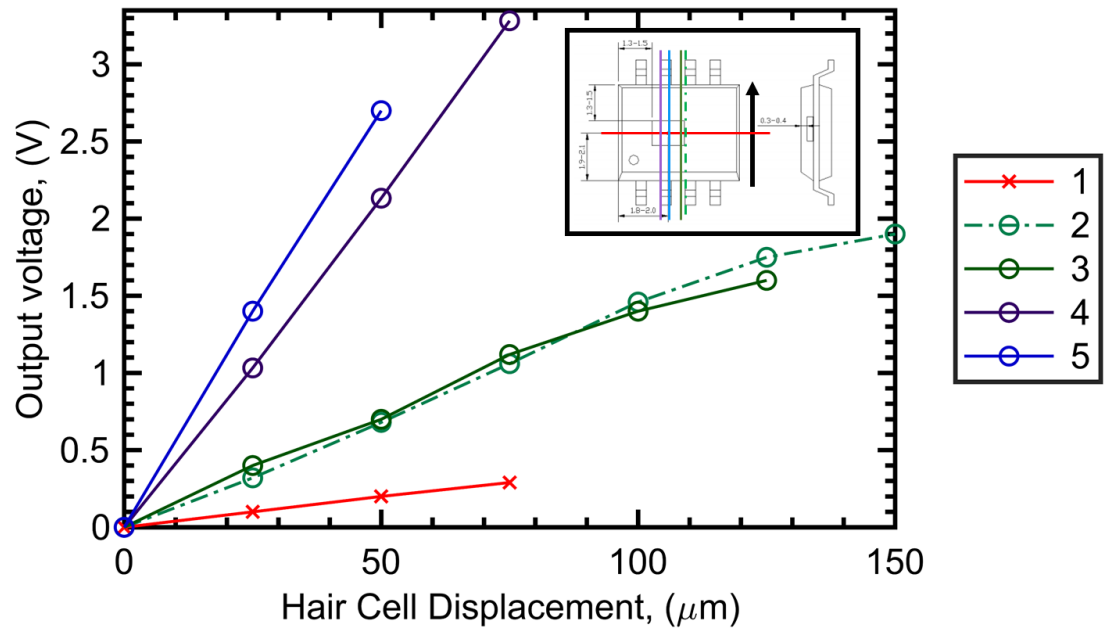


Figure 5.32. Hair cell displacement sensitivity characterization for commercial TMR magnetic sensor with a z-axis magnetized hair cell suspended above it following the possible paths indicated by the color lines overlaying the top view of the magnetic sensor package. The upwards direction indicated by the black arrow is the sensitive direction for the magnetic sensor.

Figure 5.32 shows the output of the TMR Wheatstone bridge magnetic sensor as a function of the hair cell displacement. As indicated in the inset of figure 5.31, the sensor was shifted/displaced 25 microns per step using x-y-z linear positioning stages (Klinger Scientific, USA and Micro Controle, France) with respect to a magnetic hair cell. Different movements of the hair cell with respect to the sensor were performed, as is highlighted in the inset of figure 5.32 by the traces 1-5. Trace 1 in light blue has the hair cell well aligned with the magnetic field sensor and shows the highest sensitivity per 25μm step of roughly 1.4V/25μm, followed by trace 5 (1.1V/25μm). Trace 3 and 4 followed the same path with 0.3-0.4V/25μm, while trace 2 was displacing the hair cell in the in-sensitive direction with 0.1V/25μm. Overall, Figure

5.32 highlights the ability of the TMR sensor to detect movements of the hair cell at least in the micrometer range. It also highlights that proper alignment is crucial to achieve high sensitivity.

To showcase the ability of the system to sense the deflection of the hair cell while rejecting the interfering signals coming from the Earth's magnetic field and other strong magnetic interference sources, experiments with two neighboring TMR sensors as shown in figure 5.31 were carried out. Thereby, one of the magnetic sensors is used as a reference sensor, while the other is aligned to the magnetic micro pillar. The system is exposed to two initial inputs: the first is a manually-applied angular rotation using a rotation stage; the second is a mechanically coupled vibration using a repurposed cell phone vibrator. The vibration source alternates between no vibration and a high-frequency vibration every 500 ms.

In figure 5.33, a ~ 0.8 Hz mechanical rotation is applied to the substrate. As seen in the figure, both sensors are exposed to variations in the Earth's magnetic field due to the rotation. However, the differential signal in red shows the rejection of the oscillating common mode signal.

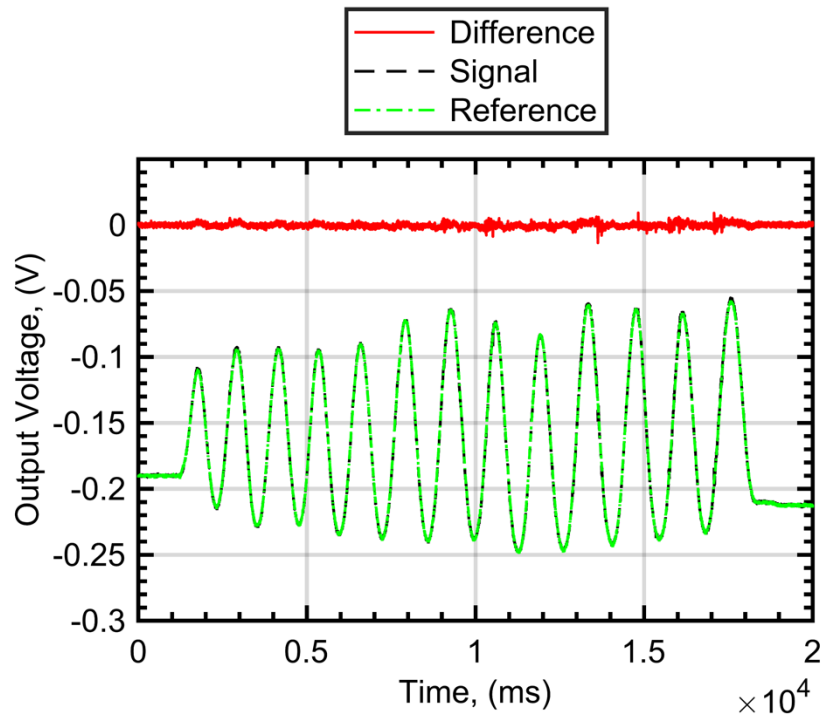


Figure 5.33. Sensor signals (green and black) and differential signal (red) stemming from manual rotation of the test setup at approx. 0.8 Hz, demonstrating the rejection of the common-mode signal in the differential setup.

In a second experiment, a mechanical vibration is applied to the setup by placing the mechanical vibrator on the optical table next to the test setup. The vibrations couple into the substrate and the hair cell begins to deflect. It can be seen from figure 5.34 that the high-frequency vibration is sensed by the magnetic sensor with the magnetic hair cell in close proximity, but not by the reference sensor. The differential signal eliminates any drifts and common mode signals and creates a more stable baseline. This shows the ability of the magnetic sensor to detect the small deflections of the hair cell, but the deflection magnitude has not been quantified.

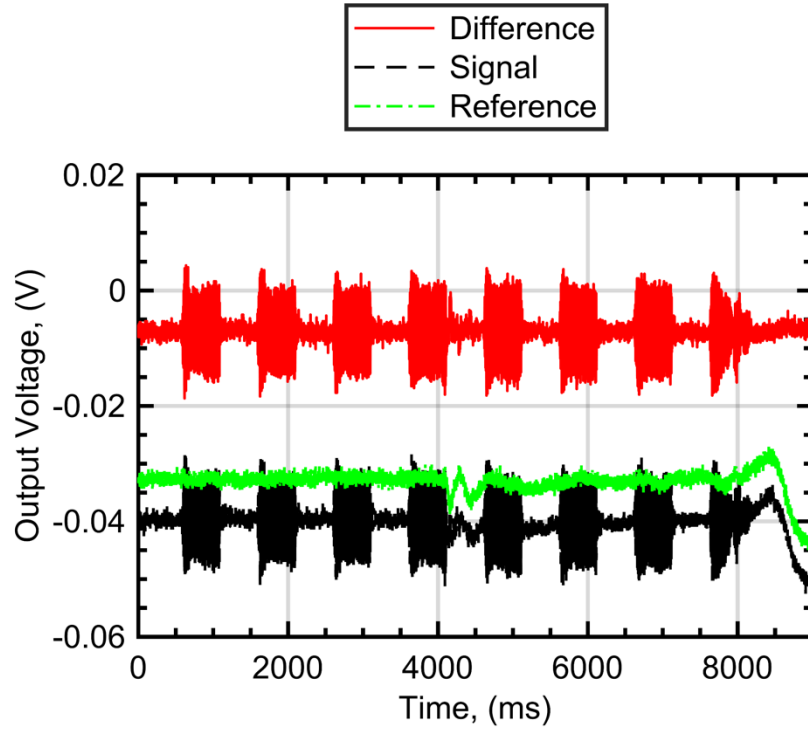


Figure 5.34. Sensor signals and differential signal stemming from vibration of the test setup, demonstrating the rejection of signal drifts in the differential signal and the detection of hair cell movement by the TMR aligned with the hair cell.

Figure 5.35a shows the ability of the system to detect the vibration-induced small deflections of the magnetic hair cell while eliminating the common mode signal due to the rotation of the system in the Earth's magnetic field. As seen figure 5.35a, the differential signal is able to detect the high frequency vibrations accurately, while rejecting most of the common mode signal. By zooming in on the time series in figure 5.35b,c, the magnetic sensor is able to detect the 160 Hz vibrations of the hair cell. This makes us believe that the proposed fluid-based rotational inertial sensor using the magnetic transduction mechanism will be limited in the frequency domain by the transfer function of the fluid, unlike in the case of the thermal transduction where the thermal transduction mechanism itself limits the frequency response.

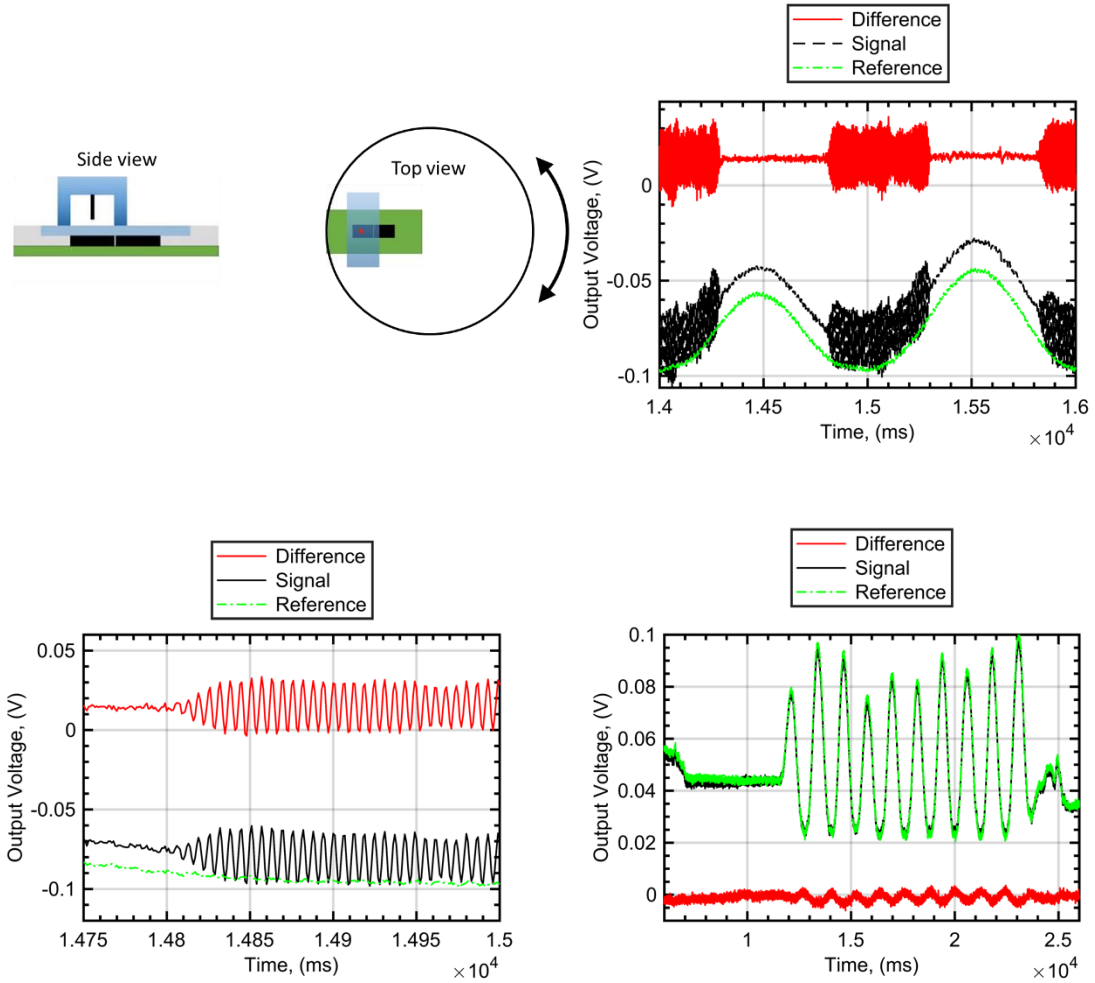


Figure 5.35. Sensor signals and differential signal stemming from manual rotation of the test setup and vibration of the hair cell, again demonstrating the rejection of the common-mode signal in the differential setup: (a) Experimental setup (b) common-mode signal rejection (c) zoom-in (d) control experiment without the hair cell.

To verify that the signal we are detecting on the sensing device is not caused by the magnet inside most consumer vibrators, the same experiment is repeated with the hair cell removed, thus having two reference sensors. Despite the vibrator behaving similar to figure 5.35a, the results shown in figure 5.35d indicate the lack of any sensitivity to the vibrations without a hair cell nearby. This result highlights qualitative common-mode rejection, but also showcases the relative potential sensitivity of the current system to the small vibrations of the flexible micromagnet.

5.7 Conclusions

In this chapter, we presented magnetic transduction as a promising new implementation of the micromachined semicircular platform for rotational inertial sensing. The concept is adapted from bioinspired micromachined magnetic hair cells for flow sensing developed by our collaborators at KAUST. Magnetic elastomeric pillars consisting of an elastomeric polymer with embedded magnetic powder mimic the vestibular hair cells. The hair cells were proposed to be integrated in a closed-loop microfluidic channel on top of an array of sensitive TMR sensors in a Wheatstone bridge configuration to detect the bidirectional deflections in the pillars' stray fields due to inertial fluid flow caused by the rotation of the device. Compared to the thermal approach highlighted in chapter 4, the magnetic transduction allows for higher bandwidth and a much-reduced power consumption.

Based on the proposed concept, preliminary studies and simulations were conducted to test the feasibility of the concept. The multiphysics finite element simulations (based on characterization of magnetic material properties) provided intuition on how best to proceed forward. The idea is to mount the PDMS microtorus with embedded magnetic hair cell on top of a silicon substrate with custom-designed TMR sensors. Because of limited performance of the initially fabricated TMR sensors, a test setup was build using commercial TMR sensor to study the fundamentals of the system, in particular the ability to sense hair cell motion and reject common mode signals stemming from e.g. the Earth's magnetic field. During these experiments it became apparent that proper alignment of the hair cell with respect to the TMR sensor is crucial. While basic concepts of the magnetic

sensing approach could be verified, the detection of angular acceleration was not yet successful, likely because of alignment issues.

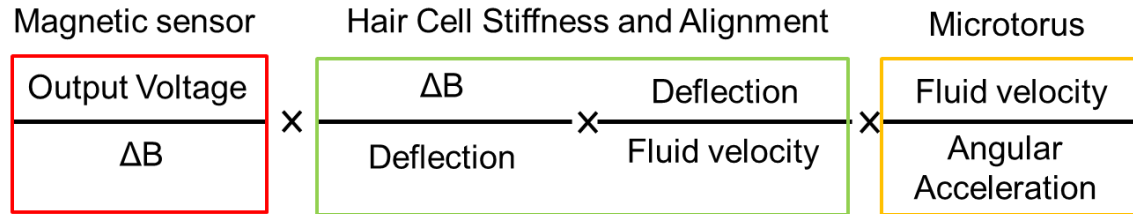


Figure 5.36. Energy transduction in bioinspired magnetic rotation sensor, and their respective sources within the system.

Figure 5.36 highlights three main possible areas of improvements for future generations of the magnetic-based sensor. Despite the current performance of the proposed magnetic sensor, the output could be improved by orders of magnitude by focusing on optimizing the hair cell and the magnetic sensor: (1) significantly reducing the size of the flexible magnet down to the order of sub-100 nm in radius; or by replacing the mechanical hair cell with a ferrofluid droplet suspended as part of a two-phase liquid, thus reducing the stiffness dramatically; (2) solving the alignment problem to take advantage of the extremely high magnetic gradients near the tip of a permanent magnet; and (3) optimizing the sensitivity of the custom TMR sensor, its noise performance, and magnetic isolation and shielding. After optimizing the sensor and its packaging, the sensor needs to be investigated as both a liquid flow sensor, then followed by inertial mechanical measurements to validate this promising, yet experimentally not verified sensor concept.

CHAPTER 6. CONCLUSIONS AND FUTURE WORK

The objective of this thesis has been to explore the mammalian semicircular canal and use it as inspiration for a rotational inertial sensing platform. After the motivation of the research is presented in Chapter 1, a literature survey of the current state-of-the-art in micromachined rotational inertial sensors and bioinspired sensors is provided. Chapter 2 gives a brief background to the mammalian semicircular canal and its operating principle. A summary of the human semicircular canal (SCC) dimensions and metrics is presented as a benchmark to compare the results obtained in this thesis. An evaluation of the potential of the SCC as platform is discussed, summarizing the advantages, challenges, and any unknowns of this approach. Chapter 3 analyzes micromachined semicircular canals and reviews the current state-of-the-art. This is followed by a dissection of the different parts of the SCC from an engineering perspective. Design considerations and issues ranging from materials, transduction mechanism and geometry are evaluated, leading to select basic designs. The remainder of the chapter deals with the analysis of the proposed design as a sensor, and numerical simulations to validate our proposed designs. Subsequently, two different transduction mechanisms are investigated for the platform and presented in the following two chapters. Chapter 4 demonstrates a bioinspired angular accelerometer using thermal transduction including design, analytical and numerical analysis, fabrication and experimental characterization. The chapter validates and verifies the potential of the toroidal platform as a rotational inertial sensing system with a resolution around 30 deg/s^2 and a dynamic range of $2,000 \text{ deg/s}^2$, however with limited bandwidth and relatively large power consumption. To address the shortcomings of the thermally transduced angular

accelerometer in terms of bandwidth and power consumption, Chapter 5 proposes a magnetic transduction mechanism. The chapter presents a thorough numerical analysis a magnetically-transduced angular accelerometer based on a micromachined semicircular canal. This is followed by preliminary experimental results validating the concept and highlighting current technical challenges in terms of component alignment. As of now, the bioinspired angular accelerometer with thermal transduction is clearly more developed than the magnetic approach. However, the microfluidic angular accelerometer with magnetic sensing is very promising if its current shortcomings with respect to component performance and assembly can be addressed.

In the following, the major contributions of this thesis are summarized, as well as suggestions for future and related research.

6.1 Research Contributions

The major contributions of the dissertation are summarized as below.

- Bio-inspired micromachined semicircular canal (μ SCC)
 - First proposal and analysis of a horizontal membrane for a micromachined semicircular canal. The concept was later validated by Andreou et al.
 - In-depth and generalizable analysis of bio-inspired *micromachined* fluidic torus as a platform and technology to enable rotational inertial sensing.
- Thermal μ SCC

- First co-demonstration (same time as University of Twente device) of thermal-based micromachined bio-inspired angular accelerometer.
- First validation of transient behavior of thermal angular accelerometer using a multiphysics numerical simulation.
- Numerical and experimental validation of the inherent ability of the torus to reject linear acceleration (based on plugged torus experiments).
- Development of cross-talk rejection technique for buoyancy-related interference signals based on multiple transducers in a Wheatstone bridge arrangement.
- First demonstration of parylene-on-liquid as a packaging and encapsulation platform for inertial sensors.
- Magnetic μ SCC
 - Development and numerical analysis of a bio-inspired magnetically-transduced angular accelerometer based on magnetic hair cell and TMR magnetic sensors.
 - Fabrication of chandelier-type magnetic cilia embedded into micromachined microtorus structure.

6.2 Future Work

Based on this brief body of work, I believe that the fluid-filled microtorus as a platform has the promise and potential to complement current commercial gyroscope via enabling soft inertial sensors for commercial and medical applications. Thus, many opportunities lie ahead to explore and improve upon the presented contributions. Below are some of the research directions that have been identified:

- **Optimization of magnetic-based μ SCC:** As described in section 5.8, the magnetic transduction mechanism provides several design knobs to tweak to gain orders of magnitude improvement in performance, such as proper scaling down of the magnetic hair cell, or perfecting alignment, placement magnetization direction, sensor configuration can allow very sensitive force sensors. Solving some of the technical challenges regarding active and passive shielding would enable magnetic sensors in many other domains.
- **Transduction mechanisms:** Past the two presented transduction mechanisms (thermal and magnetic), a few other mechanisms that can propel the microtorus widespread adoption. These include piezoelectric transduction based PVDF fibers, two-phase liquid systems whether capacitive or magnetic transduction, or even the triboelectric effect to sense fluid flow inside the microtorus.
- **Geometry exploration:** Another fun and interesting study is the geometric optimization of the microfluidic closed-loop to enable significant improvements in sensitivity and bandwidth. One earlier method proposed was the study and testing of the modulation of torus circumference. Another is the study of the effect of ampullas on the overall performance of the platform. This coupled with the potential for the first coupled or even decoupled demonstration 3-axis sensing using micromachined microtori.
- **Co-sensing of angular velocity and angular acceleration:** Based on results presented in chapter 2, future research of the co-sensing both angular velocity and angular acceleration for a single micromachined loop or from two-concentric loops at the same time.
- **Validation of mammalian SCC operation using μ SCC as platform to test hair cell organelles *ex vivo*:** Micromachined semicircular canals (μ SCC)

could potentially prove most useful when used as platforms for scientists to characterize and grow vestibular organoids as test beds, replacing test animals as the vehicle to study and understand the mammalian vestibular system. Vestibular organoids could one day be the ultimate solution to bilateral vestibular dysfunction cause hair cell loss.

REFERENCES

- [1] C. Correia *et al.*, “Global Sensory Impairment in Older Adults in the United States,” *J. Am. Geriatr. Soc.*, vol. 64, no. 2, pp. 306–313, Feb. 2016.
- [2] J. B. Fallon, D. R. F. Irvine, and R. K. Shepherd, “Cochlear Implants and Brain Plasticity,” *Br. Med. Bull.*, vol. 63, pp. 183–193, 2002.
- [3] E. Hoskison, S. Mitchell, and C. Coulson, “Systematic review: Radiological and histological evidence of cochlear implant insertion trauma in adult patients,” *Cochlear Implants Int.*, vol. 18, no. 4, pp. 192–197, Jul. 2017.
- [4] D. L. Cheng, P. B. Greenberg, and D. A. Borton, “Advances in Retinal Prosthetic Research: A Systematic Review of Engineering and Clinical Characteristics of Current Prosthetic Initiatives,” *Curr. Eye Res.*, vol. 42, no. 3, pp. 334–347, Mar. 2017.
- [5] V. J. Wilson, J. Buttner-Ennever, and K. E. Cullen, *The Vestibular System: A Sixth Sense*. Oxford University Press, 2012.
- [6] Y. Agrawal, J. P. Carey, C. C. Della Santina, M. C. Schubert, and L. B. Minor, “Disorders of Balance and Vestibular Function in US Adults: Data From the National Health and Nutrition Examination Survey, 2001-2004,” *Arch. Intern. Med.*, vol. 169, no. 10, p. 938, May 2009.
- [7] S. D. Rauch, L. Velazquez-Villaseñor, P. S. Dimitri, and S. N. Merchant, “Decreasing Hair Cell Counts in Aging Humans,” *Ann. N. Y. Acad. Sci.*, vol. 942, no. 1, pp. 220–227, Oct. 2001.
- [8] M. C. Hornbrook, V. J. Stevens, D. J. Wingfield, J. F. Hollis, M. R. Greenlick, and M. G. Ory, “Preventing Falls Among Community-Dwelling Older Persons: Results From a Randomized Trial,” *The Gerontologist*, vol. 34, no. 1, pp. 16–23, Feb. 1994.
- [9] S. J. Herdman and R. Clendaniel, *Vestibular Rehabilitation*. F.A. Davis, 2014.
- [10] R. F. Lewis, “Advances in the Diagnosis and Treatment of Vestibular Disorders: Psychophysics and Prosthetics,” *J. Neurosci.*, vol. 35, no. 13, pp. 5089–5096, Apr. 2015.
- [11] Y. Agrawal and L. B. Minor, “Ménière’s Disease and Other Causes of Episodic Vertigo - Oxford Medicine,” in *Oxford Textbook of Vertigo and Imbalance*, Oxford Medicine, 2013.
- [12] J.-P. Guyot, A. Perez Fornos, N. Guinand, R. van de Berg, R. Stokroos, and H. Kingma, “Vestibular assistance systems: promises and challenges,” *J. Neurol.*, vol. 263, pp. 30–35, 2016.
- [13] T. Brandt, M. Dieterich, and M. Strupp, “Bilateral Vestibular Failure: Causes and Courses - Oxford Medicine,” in *Oxford Textbook of Vertigo and Imbalance*, Oxford Medicine, 2013.
- [14] M. B. Gillespie and L. B. Minor, “Prognosis in Bilateral Vestibular Hypofunction,” *The Laryngoscope*, vol. 109, no. 1, pp. 35–41, Jan. 1999.

- [15] W. M. Grünbauer, M. Dieterich, and T. Brandt, "Bilateral vestibular failure impairs visual motion perception even with the head still," *NeuroReport*, vol. 9, no. 8, p. 1807, Jun. 1998.
- [16] L. B. Minor, "Gentamicin-induced bilateral vestibular hypofunction," *JAMA*, vol. 279, no. 7, pp. 541–544, Feb. 1998.
- [17] O. W. Guthrie, "Aminoglycoside induced ototoxicity," *Toxicology*, vol. 249, no. 2, pp. 91–96, Jul. 2008.
- [18] C. Wall III, D. M. Merfeld, S. D. Rauch, and F. O. Black, "Vestibular prostheses: The engineering and biomedical issues," *J. Vestib. Res.*, vol. 12, no. 2,3, pp. 95–113, Jan. 2002.
- [19] G. Licameli, G. Zhou, and M. A. Kenna, "Disturbance of vestibular function attributable to cochlear implantation in children," *The Laryngoscope*, vol. 119, no. 4, pp. 740–745, Apr. 2009.
- [20] G. M. Clark, "The multi-channel cochlear implant: Multi-disciplinary development of electrical stimulation of the cochlea and the resulting clinical benefit," *Hear. Res.*, vol. 322, pp. 4–13, Apr. 2015.
- [21] T. A. K. Nguyen *et al.*, "Characterization of Cochlear, Vestibular and Cochlear-Vestibular Electrically Evoked Compound Action Potentials in Patients with a Vestibulo-Cochlear Implant," *Front. Neurosci.*, vol. 11, Nov. 2017.
- [22] V. C. Zingler *et al.*, "Causative factors and epidemiology of bilateral vestibulopathy in 255 patients," *Ann. Neurol.*, vol. 61, no. 6, pp. 524–532, Jun. 2007.
- [23] N. Guinand *et al.*, "Vestibular Implants: 8 Years of Experience with Electrical Stimulation of the Vestibular Nerve in 11 Patients with Bilateral Vestibular Loss," *ORL*, vol. 77, no. 4, pp. 227–240, 2015.
- [24] X. Du *et al.*, "Regeneration of mammalian cochlear and vestibular hair cells through Hes1/Hes5 modulation with siRNA," *Hear. Res.*, vol. 304, pp. 91–110, Oct. 2013.
- [25] W. Li, D. You, Y. Chen, R. Chai, and H. Li, "Regeneration of hair cells in the mammalian vestibular system," *Front. Med.*, vol. 10, no. 2, pp. 143–151, Jun. 2016.
- [26] B. L. Day, "Galvanic vestibular stimulation: new uses for an old tool," *J. Physiol.*, vol. 517, no. 3, pp. 631–631, Jun. 1999.
- [27] F. Ehtemam, P. A. Forbes, A. C. Schouten, F. C. T. van der Helm, and R. Happee, "Galvanic Vestibular Stimulation Elicits Consistent Head & Neck Motion in Seated Subjects," *IEEE Trans. Biomed. Eng.*, vol. 59, no. 7, pp. 1978–1984, Jul. 2012.
- [28] C. Fujimoto *et al.*, "Noisy galvanic vestibular stimulation induces a sustained improvement in body balance in elderly adults," *Sci. Rep.*, vol. 6, p. 37575, Nov. 2016.
- [29] J. Hegeman, F. Honegger, M. Kupper, and J. H. J. Allum, "The balance control of bilateral peripheral vestibular loss subjects and its improvement with auditory prosthetic feedback," *J. Vestib. Res.*, vol. 15, no. 2, pp. 109–117, Jan. 2005.

- [30] N. Vuillerme and R. Cuisinier, "Sensory Supplementation through Tongue Electrotactile Stimulation to Preserve Head Stabilization in Space in the Absence of Vision," *Invest. Ophthalmol. Vis. Sci.*, vol. 50, no. 1, pp. 476–481, Jan. 2009.
- [31] Y. P. Danilov, M. E. Tyler, and K. A. Kaczmarek, "Vestibular sensory substitution using tongue electrotactile display," in *Human Haptic Perception: Basics and Applications*, Birkhäuser Basel, 2008, pp. 467–480.
- [32] T. Yamanaka, Y. Sawai, T. Murai, T. Nishimura, and T. Kitahara, "Long-term effects of electrotactile sensory substitution therapy on balance disorders," *NeuroReport*, vol. 27, no. 10, p. 744, Jul. 2016.
- [33] L. A. Thompson, C. Haburcakova, and R. F. Lewis, "Vestibular ablation and a semicircular canal prosthesis affect postural stability during head turns," *Exp. Brain Res.*, vol. 234, no. 11, pp. 3245–3257, Nov. 2016.
- [34] B. Chiang, G. Y. Fridman, C. Dai, M. A. Rahman, and C. C. Della Santina, "Design and performance of a multichannel vestibular prosthesis that restores semicircular canal sensation in rhesus monkey," *Ieee Trans. Neural Syst. Rehabil. Eng.*, vol. 19, no. 5, pp. 588–598, Oct. 2011.
- [35] C. Dai, G. Y. Fridman, N. S. Davidovics, B. Chiang, J. H. Ahn, and C. C. Della Santina, "Restoration of 3D vestibular sensation in rhesus monkeys using a multichannel vestibular prosthesis," *Hear. Res.*, vol. 281, no. 1–2, pp. 74–83, Nov. 2011.
- [36] W. Gong and D. M. Merfeld, "Prototype Neural Semicircular Canal Prosthesis using Patterned Electrical Stimulation," *Ann. Biomed. Eng.*, vol. 28, no. 5, pp. 572–581, May 2000.
- [37] W. Gong and D. M. Merfeld, "System design and performance of a unilateral horizontal semicircular canal prosthesis," *IEEE Trans. Biomed. Eng.*, vol. 49, no. 2, pp. 175–181, 2002.
- [38] H. Toreyin, "Design of a Low-Power Interface Circuitry for a Vestibular Prosthesis System," Dissertation, 2014.
- [39] J. O. Phillips, S. M. Bierer, L. Ling, K. Nie, and J. T. Rubinstein, "Real-time communication of head velocity and acceleration for an externally mounted vestibular prosthesis," in *2011 Annual International Conference of the IEEE Engineering in Medicine and Biology Society, EMBC*, 2011, pp. 3537–3541.
- [40] J.-I. Suzuki, K. Goto, K. Tokumasu, and B. Cohen, "Implantation of Electrodes near Individual Vestibular Nerve Branches in Mammals," *Ann. Otol. Rhinol. Laryngol.*, vol. 78, no. 4, pp. 815–826, Aug. 1969.
- [41] B. Cohen, J.-I. Suzuki, and M. B. Bender, "Eye Movements from Semicircular Canal Nerve Stimulation in the Cat," *Ann. Otol. Rhinol. Laryngol.*, vol. 73, no. 1, pp. 153–169, Mar. 1964.
- [42] C. C. D. Santina, A. A. Migliaccio, and A. H. Patel, "A Multichannel Semicircular Canal Neural Prosthesis Using Electrical Stimulation to Restore 3-D Vestibular Sensation," *IEEE Trans. Biomed. Eng.*, vol. 54, no. 6, pp. 1016–1030, Jun. 2007.

- [43] I. Conrad Wall, M. I. Kos, and J.-P. Guyot, "Eye Movements in Response to Electric Stimulation of the Human Posterior Ampullary Nerve," *Ann. Otol. Rhinol. Laryngol.*, vol. 116, no. 5, pp. 369–374, May 2007.
- [44] A. Perez Fornos *et al.*, "Artificial Balance: Restoration of the Vestibulo-Ocular Reflex in Humans with a Prototype Vestibular Neuroprosthesis," *Front. Neurol.*, vol. 5, 2014.
- [45] J. S. Golub *et al.*, "Prosthetic implantation of the human vestibular system," *Otol. Neurotol. Off. Publ. Am. Otol. Soc. Am. Neurotol. Soc. Eur. Acad. Otol. Neurotol.*, vol. 35, no. 1, pp. 136–147, Jan. 2014.
- [46] A. Perez Fornos *et al.*, "The vestibular implant: A probe in orbit around the human balance system," *J. Vestib. Res.*, vol. 27, no. 1, pp. 51–61, Jan. 2017.
- [47] A. R. de Miguel, J. C. F. Gonzalez, and A. R. Macias, "Vestibular Response to Electrical Stimulation of the Otolith Organs. Implications in the Development of A Vestibular Implant for the Improvement of the Sensation of Gravitoinertial Accelerations," *J. Int. Adv. Otol.*, vol. 13, no. 2, pp. 154–161, Aug. 2017.
- [48] M. M. Iversen *et al.*, "Low-intensity ultrasound activates vestibular otolith organs through acoustic radiation force," *J. Acoust. Soc. Am.*, vol. 141, no. 6, pp. 4209–4219, Jun. 2017.
- [49] I. V. Orlov, Y. K. Stolbkov, and V. C. Shuplyakov, "Effects of artificial feedback to the vestibular input on postural instability induced by asymmetric proprioceptive stimulation," *Neurosci. Behav. Physiol.*, vol. 38, no. 2, pp. 195–201, Feb. 2008.
- [50] R. Saba, "Cochlear implant modelling: stimulation and power consumption," phd, University of Southampton, 2012.
- [51] M. Yip, P. Bowers, V. Noel, A. Chandrakasan, and K. M. Stankovic, "Energy-efficient waveform for electrical stimulation of the cochlear nerve," *Sci. Rep.*, vol. 7, no. 1, p. 13582, Oct. 2017.
- [52] M. Yip, R. Jin, H. H. Nakajima, K. M. Stankovic, and A. P. Chandrakasan, "A Fully-Implantable Cochlear Implant SoC with Piezoelectric Middle-Ear Sensor and Arbitrary Waveform Neural Stimulation," *IEEE J. Solid-State Circuits*, vol. 50, no. 1, pp. 214–229, Jan. 2015.
- [53] M. W. (Michael W. Baker, "A low-power cochlear implant system," Thesis, Massachusetts Institute of Technology, 2007.
- [54] R. Sarpeshkar, *Ultra Low Power Bioelectronics: Fundamentals, Biomedical Applications, and Bio-Inspired Systems*. Cambridge University Press, 2010.
- [55] A. J. Hudspeth, "How the ear's works work," *Nature*, vol. 341, no. 6241, pp. 397–404, Oct. 1989.
- [56] J. Georgiou and C. Toumazou, "A 126- μ W cochlear chip for a totally implantable system," *IEEE J. Solid-State Circuits*, vol. 40, no. 2, pp. 430–443, Feb. 2005.
- [57] "ICM-20689 | TDK." [Online]. Available: <https://www.invensense.com/products/motion-tracking/6-axis/icm-20689/>. [Accessed: 12-Jun-2018].

- [58] “MC3672 3-Axis Accelerometer,” *mCube*. [Online]. Available: <http://www.mcubemems.com/product/mc3672-3-axis-accelerometer/>. [Accessed: 12-Jun-2018].
- [59] D. Xia, C. Yu, and L. Kong, “The Development of Micromachined Gyroscope Structure and Circuitry Technology,” *Sensors*, vol. 14, no. 1, pp. 1394–1473, Jan. 2014.
- [60] K. Liu *et al.*, “The development of micro-gyroscope technology,” *J. Micromechanics Microengineering*, vol. 19, no. 11, p. 113001, 2009.
- [61] N. Yazdi, F. Ayazi, and K. Najafi, “Micromachined inertial sensors,” *Proc. IEEE*, vol. 86, no. 8, pp. 1640–1659, 1998.
- [62] P. T. Bhatti and M. A. McClain, “Low-power sensing for vestibular prostheses,” in *2011 Annual International Conference of the IEEE Engineering in Medicine and Biology Society, EMBC*, 2011, pp. 3131–3134.
- [63] H. Toreyin and P. T. Bhatti, “A Finite Element Analysis of a Biomimetic Angular Rotation Sensor for a Vestibular Prosthesis,” in *34th Annual International IEEE EMBS Conference*, 2012.
- [64] C. M. Andreou, Y. Pahitas, and J. Georgiou, “Bio-Inspired Micro-Fluidic Angular-Rate Sensor for Vestibular Prostheses,” *Sensors*, vol. 14, no. 7, pp. 13173–13185, Jul. 2014.
- [65] C. M. Andreou, Y. Pahitas, E. Pilavaki, and J. Georgiou, “Bio-mimetic gyroscopic sensor for vestibular prostheses,” in *2013 IEEE Biomedical Circuits and Systems Conference (BioCAS)*, 2013, pp. 17–20.
- [66] D. E. Serrano *et al.*, “Substrate-decoupled, bulk-acoustic wave gyroscopes: Design and evaluation of next-generation environmentally robust devices,” *Microsyst. Nanoeng.*, vol. 2, p. 16015, Apr. 2016.
- [67] R. Tabrizian, M. Hodjat-Shamami, and F. Ayazi, “High-Frequency AlN-on-Silicon Resonant Square Gyroscopes,” *J. Microelectromechanical Syst.*, vol. 22, no. 5, pp. 1007–1009, Oct. 2013.
- [68] R. C. Woods, H. Kalami, and B. Johnson, “Evaluation of a novel surface acoustic wave gyroscope,” *IEEE Trans. Ultrason. Ferroelectr. Freq. Control*, vol. 49, no. 1, pp. 136–141, Jan. 2002.
- [69] F. T. Han, Y. F. Liu, L. Wang, and G. Y. Ma, “Micromachined electrostatically suspended gyroscope with a spinning ring-shaped rotor,” *J. Micromechanics Microengineering*, vol. 22, no. 10, p. 105032, 2012.
- [70] N.-C. Tsai, W.-M. Huang, and C.-W. Chiang, “Magnetic actuator design for single-axis micro-gyroscopes,” *Microsyst. Technol.*, vol. 15, no. 4, pp. 493–503, Apr. 2009.
- [71] S. Mitatha, C. Sirawattananon, J. Ali, and P. P. Yupapin, “Four Point Probe Micro-Optical Gyroscope With Self Calibration Control,” *IEEE Sens. J.*, vol. 13, no. 7, pp. 2705–2710, Jul. 2013.
- [72] V. M. N. Passaro, A. Cuccovillo, L. Vaiani, M. De Carlo, and C. E. Campanella, “Gyroscope Technology and Applications: A Review in the Industrial Perspective,” *Sensors*, vol. 17, no. 10, p. 2284, Oct. 2017.

- [73] "MEMSIC - Accelerometers." [Online]. Available: <http://www.memsic.com/accelerometers/>. [Accessed: 21-Aug-2018].
- [74] J. Bahari, R. Feng, and A. M. Leung, "Robust MEMS Gyroscope Based on Thermal Principles," *J. Microelectromechanical Syst.*, vol. 23, no. 1, pp. 100–116, Feb. 2014.
- [75] A. M. Leung, J. Jones, E. Czyzewska, J. Chen, and B. Woods, "Micromachined accelerometer based on convection heat transfer," in , *The Eleventh Annual International Workshop on Micro Electro Mechanical Systems, 1998. MEMS 98. Proceedings*, 1998, pp. 627–630.
- [76] H. B. Nguyen, F. Mailly, L. Latorre, and P. Nouet, "Design of a monolithic 3-axis thermal convective accelerometer," in *2013 Symposium on Design, Test, Integration and Packaging of MEMS/MOEMS (DTIP)*, 2013, pp. 1–4.
- [77] Y. Ai, X. Luo, and S. Liu, "Design and Modeling of Micromachined Thermal Convective Gyroscope with Bidirectional Jets," in *8th International Conference on Electronic Packaging Technology, 2007. ICEPT 2007*, 2007, pp. 1–5.
- [78] P. T. Hoa, T. X. Dinh, and V. T. Dau, "Design Study of Multidirectional Jet Flow for a Triple-Axis Fluidic Gyroscope," *IEEE Sens. J.*, vol. 15, no. 7, pp. 4103–4113, Jul. 2015.
- [79] H. Chang, X. Gong, S. Wang, P. Zhou, and W. Yuan, "On Improving the Performance of a Triaxis Vortex Convective Gyroscope Through Suspended Silicon Thermistors," *IEEE Sens. J.*, vol. 15, no. 2, pp. 946–955, Feb. 2015.
- [80] J. Bahari and A. M. Leung, "Micromachined three-axis thermal accelerometer with a single composite heater," *J. Micromechanics Microengineering*, vol. 21, no. 7, p. 075025, Jul. 2011.
- [81] P. Shooshtari, A. Leung, and J. Jones, "Suppression of spurious signals in thermal MEMS gyroscope," in *2012 IEEE Sensors*, 2012, pp. 1–4.
- [82] R. Feng, J. Bahari, J. D. Jones, and A. M. Leung, "MEMS thermal gyroscope with self-compensation of the linear acceleration effect," *Sens. Actuators Phys.*, vol. 203, pp. 413–420, Dec. 2013.
- [83] R. Zhu, H. Ding, Y. Su, and Z. Zhou, "Micromachined gas inertial sensor based on convection heat transfer," *Sens. Actuators Phys.*, vol. 130–131, pp. 68–74, Aug. 2006.
- [84] S. J. Ovaska and S. Valiviita, "Angular acceleration measurement: a review," *IEEE Trans. Instrum. Meas.*, vol. 47, no. 5, pp. 1211–1217, 1998.
- [85] A. Gola *et al.*, "A 2.5-rad/s² resolution digital output MEMS-based rotational accelerometer for HDD applications," *IEEE Trans. Magn.*, vol. 39, no. 2, pp. 915–919, Mar. 2003.
- [86] G. J. O'Brien, "MEMS angular rate and angular acceleration sensors with CMOS switched capacitor signal conditioning," Ph.D., University of Michigan, United States -- Michigan, 2004.
- [87] H. J. Wolfaardt, "Theory of the microfluidic channel angular accelerometer for inertial measurement applications," University of Pretoria, 2005.

- [88] P. Jedlička, J. Buben, and J. Kozák, "Strong-Motion Fluid Rotation Seismograph," *Bull. Seismol. Soc. Am.*, vol. 99, no. 2B, pp. 1443–1448, May 2009.
- [89] N. Furukawa and K. Ohnishi, "A structure of angular acceleration sensor using silicon cantilevered beam with piezoresistors," in , *Proceedings of the 1992 International Conference on Industrial Electronics, Control, Instrumentation, and Automation, 1992. Power Electronics and Motion Control, 1992*, pp. 1524–1529 vol.3.
- [90] T. J. Brosnihan, A. Pisano, and R. T. Howe, "Surface Micromachined Angular Accelerometer with Force Feedback," in *Proceedings of the ASME Dynamic Systems and Control Division*, 1995, vol. 57–2, pp. 941–947.
- [91] G. J. O'Brien, D. J. Monk, and K. Najafi, "Angular accelerometer with dual anchor support," in *TRANSDUCERS, Solid-State Sensors, Actuators and Microsystems, 12th International Conference on, 2003*, 2003, vol. 2, pp. 1371–1374 vol.2.
- [92] Y. Jeong, H. Töreyin, A. Daruwalla, P. Bhatti, and F. Ayazi, "A dual-axis single-proof-mass angular accelerometer for a vestibular prosthesis," in *2016 38th Annual International Conference of the IEEE Engineering in Medicine and Biology Society (EMBC)*, 2016, pp. 4695–4698.
- [93] R. Amarasinghe, D. V. Dao, T. Toriyama, and S. Sugiyama, "A silicon micromachined six-degree of freedom piezoresistive accelerometer," in *Proceedings of IEEE Sensors, 2004*, 2004, pp. 852–855 vol.2.
- [94] E. J. Eklund and A. M. Shkel, "Single-mask fabrication process for linear and angular piezoresistive accelerometers," US7939355 B2, 10-May-2011.
- [95] J. Mizuno, K. Nottmeyer, M. Amemori, Y. Kanai, and T. Kobayashi, "The study of silicon bulk micromachined angular acceleration sensor," *JSAE Rev.*, vol. 21, no. 1, pp. 79–84, Jan. 2000.
- [96] M. T. Restivo and F. G. de Almeida, "The use of eddy currents on the measurement of relative acceleration," *Sens. Actuators Phys.*, vol. 113, no. 2, pp. 181–188, Jul. 2004.
- [97] A. H. Kadhim, T. K. M. Babu, and D. O'Kelly, "Measurement of steady-state and transient load-angle, angular velocity, and acceleration using an optical encoder," *IEEE Trans. Instrum. Meas.*, vol. 41, no. 4, pp. 486–489, Aug. 1992.
- [98] R. Lassow and T. Meydan, "An angular accelerometer using amorphous wire," *IEEE Trans. Magn.*, vol. 31, no. 6, pp. 3179–3181, 1995.
- [99] W. A. Clark, J. A. Geen, and J. Kuang, "Piezoelectric Transducers and Inertial Sensors using Piezoelectric Transducers," US20100058861 A1, 11-Mar-2010.
- [100] R. Marat-Mendes, C. J. Dias, and J. N. Marat-Mendes, "Development of a piezoelectric sensor to measure angular acceleration," in *10th International Symposium on Electrets, 1999. ISE 10. Proceedings, 1999*, pp. 759–762.
- [101] R. D. Evans, "Development and testing of a triaxial angular accelerometer for high-performance aerospace vehicles." 01-Jan-1970.

- [102] G. C. Willems, "A Detailed Evaluation of the Endevco Model 7302 (Trade Name) Angular Accelerometer,," NAVAL BIODYNAMICS LAB NEW ORLEANS LA, NAVAL BIODYNAMICS LAB NEW ORLEANS LA, NBDL-83R009, Aug. 1983.
- [103] K. Yoo, C. Lee, and J. Kim, "A digital accelerometer using a microscale liquid-metal droplet in photosensitive glass channel," in *Solid-State Sensors, Actuators and Microsystems Conference, 2009. TRANSDUCERS 2009. International*, 2009, pp. 676–679.
- [104] H. Zeng, "Bio-Inspired Inertial Sensors for Human Body Motion Measurement," Ohio State, 2012.
- [105] P. B. Bhushan, "Biomimetics," in *Encyclopedia of Nanotechnology*, P. B. Bhushan, Ed. Springer Netherlands, 2012, pp. 290–298.
- [106] F. Rieke and D. A. Baylor, "Single-photon detection by rod cells of the retina," *Rev. Mod. Phys.*, vol. 70, no. 3, pp. 1027–1036, Jul. 1998.
- [107] J. Casas, T. Steinmann, and G. Krijnen, "Why do insects have such a high density of flow-sensing hairs? Insights from the hydromechanics of biomimetic MEMS sensors," *J. R. Soc. Interface*, vol. 7, no. 51, pp. 1487–1495, Oct. 2010.
- [108] A. Hudspeth, "Mechanical amplification of stimuli by hair cells," *Curr. Opin. Neurobiol.*, vol. 7, no. 4, pp. 480–486, Aug. 1997.
- [109] S. Highstein and R. R. Fay, *The Vestibular System*, vol. 19. Springer, 2004.
- [110] R. D. Rabbitt, E. R. Damiano, and J. W. Grant, "Biomechanics of the Semicircular Canals and Otolith Organs," in *The Vestibular System*, S. M. Highstein, R. R. Fay, and A. N. Popper, Eds. Springer New York, 2004, pp. 153–201.
- [111] M. Muller, "Size Limitations in Semicircular Duct Systems," *J. Theor. Biol.*, vol. 198, no. 3, pp. 405–437, Jun. 1999.
- [112] P. B. Bhushan, "Gecko Effect," in *Encyclopedia of Nanotechnology*, P. B. Bhushan, Ed. Springer Netherlands, 2012, pp. 943–951.
- [113] P. B. Bhushan and P. M. Nosonovsky, "Lotus Effect," in *Encyclopedia of Nanotechnology*, P. B. Bhushan, Ed. Springer Netherlands, 2012, pp. 1224–1233.
- [114] J. Tao and X. (Bill) Yu, "Hair flow sensors: from bio-inspiration to biomimicking—a review," *Smart Mater. Struct.*, vol. 21, no. 11, p. 113001, 2012.
- [115] H. Droogendijk, R. A. Brookhuis, M. J. de Boer, R. G. P. Sanders, and G. J. M. Krijnen, "Towards a biomimetic gyroscope inspired by the fly's haltere using microelectromechanical systems technology," *J. R. Soc. Interface*, vol. 11, no. 99, p. 20140573, Oct. 2014.
- [116] H. Droogendijk, M. J. de Boer, R. G. P. Sanders, and G. J. M. Krijnen, "5 - Bio-inspired hair-based inertial sensors," in *Biomimetic Technologies*, T. D. Ngo, Ed. Woodhead Publishing, 2015, pp. 93–119.
- [117] S. W. Arms and C. P. Townsend, "Mems based angular accelerometer," US20030047002 A1, 13-Mar-2003.

- [118] H. Ploechinger, "Sensor for detecting a rotational movement or an angular acceleration," US6722199 B2, 20-Apr-2004.
- [119] H. J. Wolfaardt and P. S. Heyns, "Dynamic Modeling of a Novel Microfluidic Channel Angular Accelerometer," *J. Vib. Control*, vol. 14, no. 4, pp. 451–467, Apr. 2008.
- [120] E. Njeugna, J. L. Eichhorn, C. Kopp, and P. Harlicot, "Mechanics of the cupula: effects of its thickness," *J. Vestib. Res. Equilib. Orientat.*, vol. 2, no. 3, pp. 227–234, 1992.
- [121] P. Selva, C. M. Oman, and H. A. Stone, "Mechanical properties and motion of the cupula of the human semicircular canal," *J. Vestib. Res. Equilib. Orientat.*, vol. 19, no. 3–4, pp. 95–110, 2009.
- [122] H. Alrowais, H. Toreyin, O. Brand, and P. T. Bhatti, "Design and analysis of a biomimetic angular acceleration sensor for a vestibular prosthesis," in *NMC 2013: 10th International Workshop on Nanomechanical Sensing*, 2013.
- [123] S. Cheng, M. Fu, M. Wang, X. Li, M. Xiao, and T. Wang, "Modeling for Fluid Transients in Liquid-Circular Angular Accelerometer," *IEEE Sens. J.*, vol. PP, no. 99, pp. 1–1, 2016.
- [124] J. van Tiem, J. Groenesteijn, R. Sanders, and G. Krijnen, "3D printed bio-inspired angular acceleration sensor," in *2015 IEEE SENSORS*, 2015, pp. 1–4.
- [125] J. Groenesteijn, H. Droogendijk, M. J. de Boer, R. G. P. Sanders, R. J. Wiegerink, and G. J. M. Krijnen, "An angular acceleration sensor inspired by the vestibular system with a fully circular fluid-channel and thermal read-out," in *2014 IEEE 27th International Conference on Micro Electro Mechanical Systems (MEMS)*, 2014, pp. 696–699.
- [126] P. Bruschi and M. Piotto, "Design Issues for Low Power Integrated Thermal Flow Sensors with Ultra-Wide Dynamic Range and Low Insertion Loss," *Micromachines*, vol. 3, no. 2, pp. 295–314, Apr. 2012.
- [127] L. Löfdahl and M. Gad-el-Hak, "MEMS-based pressure and shear stress sensors for turbulent flows," *Meas. Sci. Technol.*, vol. 10, no. 8, p. 665, 1999.
- [128] J. Groenesteijn *et al.*, "Parametric amplification in a micro Coriolis mass flow sensor," *J. Appl. Phys.*, vol. 115, no. 19, p. 194503, May 2014.
- [129] J. T. W. Kuo, L. Yu, and E. Meng, "Micromachined Thermal Flow Sensors—A Review," *Micromachines*, vol. 3, no. 3, pp. 550–573, Jul. 2012.
- [130] M. S. Triantafyllou, G. D. Weymouth, and J. Miao, "Biomimetic Survival Hydrodynamics and Flow Sensing," *Annu. Rev. Fluid Mech.*, vol. 48, no. 1, pp. 1–24, 2016.
- [131] M. E. McConney *et al.*, "Biologically inspired design of hydrogel-capped hair sensors for enhanced underwater flow detection," *Soft Matter*, vol. 5, no. 2, pp. 292–295, 2009.
- [132] M. E. McConney, K. D. Anderson, L. L. Brott, R. R. Naik, and V. V. Tsukruk, "Bioinspired Material Approaches to Sensing," *Adv. Funct. Mater.*, vol. 19, no. 16, pp. 2527–2544, Aug. 2009.

- [133] M. Delling *et al.*, “Primary cilia are not calcium-responsive mechanosensors,” *Nature*, vol. advance online publication, Mar. 2016.
- [134] J.-H. Lee *et al.*, “Magnetic Nanoparticles for Ultrafast Mechanical Control of Inner Ear Hair Cells,” *ACS Nano*, vol. 8, no. 7, pp. 6590–6598, Jul. 2014.
- [135] H. Droogendijk, J. Casas, T. Steinmann, and G. J. M. Krijnen, “Performance assessment of bio-inspired systems: flow sensing MEMS hairs,” *Bioinspir. Biomim.*, vol. 10, no. 1, p. 016001, 2015.
- [136] F. A. Banser, “Micromachined biomimetic optical microphones with improved packaging and power consumption,” Thesis, Georgia Institute of Technology, 2012.
- [137] W. S. Chung, O. Kwon, J. S. Lee, Y. K. Choi, and S. Park, “Local flow speed measurement using tunable ac thermal anemometry,” *J. Mech. Sci. Technol.*, vol. 19, no. 7, pp. 1449–1459, Jul. 2005.
- [138] A. R. Aiyar, C. Song, S. H. Kim, and M. G. Allen, “An All Polymer Air-Flow Sensor Array using a Piezoresistive Composite Elastomer,” in *IEEE 22nd International Conference on Micro Electro Mechanical Systems, 2009. MEMS 2009*, 2009, pp. 447–450.
- [139] N. Chen, C. Tucker, J. M. Engel, Y. Yang, S. Pandya, and C. Liu, “Design and Characterization of Artificial Haircell Sensor for Flow Sensing With Ultrahigh Velocity and Angular Sensitivity,” *J. Microelectromechanical Syst.*, vol. 16, no. 5, pp. 999–1014, 2007.
- [140] M. M. Sadeghi, R. L. Peterson, and K. Najafi, “Micro-hydraulic structure for high performance bio-mimetic air flow sensor arrays,” in *Electron Devices Meeting (IEDM), 2011 IEEE International*, 2011, pp. 29.4.1-29.4.4.
- [141] A. Alfadhel, B. Li, A. Zaher, O. Yassine, and J. Kosel, “A magnetic nanocomposite for biomimetic flow sensing,” *Lab. Chip*, vol. 14, no. 22, pp. 4362–4369, Oct. 2014.
- [142] J. Paek and J. Kim, “Microsphere-assisted fabrication of high aspect-ratio elastomeric micropillars and waveguides,” *Nat. Commun.*, vol. 5, p. 3324, Feb. 2014.
- [143] D. Sengupta *et al.*, “Characterization of single polyvinylidene fluoride (PVDF) nanofiber for flow sensing applications,” *AIP Adv.*, vol. 7, no. 10, p. 105205, Oct. 2017.
- [144] C. M. Bruinink *et al.*, “Advancements in Technology and Design of Biomimetic Flow-Sensor Arrays,” in *2009 IEEE 22nd International Conference on Micro Electro Mechanical Systems*, 2009, pp. 152–155.
- [145] A. M. Shkel and F.-G. Zeng, “An electronic prosthesis mimicking the dynamic vestibular function,” *Audiol. Neurotol.*, vol. 11, no. 2, pp. 113–122, 2006.
- [146] R. Hayden and C. C. D. Santana, “Paired linear accelerometers emulate gyros to reduce power consumption and size for an implantable multi-channel vestibular prosthesis,” in *Abs. Association for Research in Otolaryngology 30th Midwinter Meeting*, Denver, 2007, p. 342.

- [147] P. S. Challa, H. Töreyn, and P. T. Bhatti, “Differential measure of matched linear accelerometers as a sensing strategy for the development of a vestibular prosthesis,” in *2013 6th International IEEE/EMBS Conference on Neural Engineering (NER)*, 2013, pp. 1163–1166.
- [148] S. Dellea *et al.*, “A comprehensive study of NEMS-based piezoresistive gyroscopes for vestibular implant systems,” in *2017 IEEE International Symposium on Inertial Sensors and Systems (INERTIAL)*, 2017, pp. 1–4.
- [149] H. Gray, R. Howden, A. J. Jex-Blake, and W. F. Fedden, *Anatomy, Descriptive and Applied*. Longmans, Green, 1918.
- [150] H. H. Kornhuber, *Vestibular System Part 1: Basic Mechanisms*. Springer Science & Business Media, 2012.
- [151] E. N. Marieb and K. Hoehn, *Human Anatomy & Physiology*. Pearson Benjamin Cummings, 2007.
- [152] P. P. Mercier, A. C. Lysaght, S. Bandyopadhyay, A. P. Chandrakasan, and K. M. Stankovic, “Energy extraction from the biologic battery in the inner ear,” *Nat. Biotechnol.*, vol. 30, no. 12, pp. 1240–1243, Dec. 2012.
- [153] B. L. Day and R. C. Fitzpatrick, “The vestibular system,” *Curr. Biol.*, vol. 15, no. 15, pp. R583–R586, Aug. 2005.
- [154] G. M. Jones, “The Functional Significance of Semicircular Canal Size,” in *Vestibular System Part 1: Basic Mechanisms*, Springer, Berlin, Heidelberg, 1974, pp. 171–184.
- [155] R. W. Steer, “The influence of angular and linear acceleration and thermal stimulation on the human semicircular canal,” Thesis, Massachusetts Institute of Technology, 1967.
- [156] A. Yamauchi, R. D. Rabbitt, R. Boyle, and S. M. Highstein, “Relationship between Inner-Ear Fluid Pressure and Semicircular Canal Afferent Nerve Discharge,” *J. Assoc. Res. Otolaryngol.*, vol. 3, no. 1, pp. 26–44, Feb. 2002.
- [157] R. D. Rabbitt, K. D. Breneman, C. King, A. M. Yamauchi, R. Boyle, and S. M. Highstein, “Dynamic Displacement of Normal and Detached Semicircular Canal Cupula,” *J. Assoc. Res. Otolaryngol.*, vol. 10, no. 4, pp. 497–509, Dec. 2009.
- [158] K. D. Breneman, W. E. Brownell, and R. D. Rabbitt, “Hair Cell Bundles: Flexoelectric Motors of the Inner Ear,” *PLOS ONE*, vol. 4, no. 4, p. e5201, Apr. 2009.
- [159] S. M. Highstein, “Anatomy and Physiology of the Central and Peripheral Vestibular System: Overview,” in *The Vestibular System*, S. M. Highstein, R. R. Fay, and A. N. Popper, Eds. Springer New York, 2004, pp. 1–10.
- [160] R. A. Eatock and J. E. Songer, “Vestibular Hair Cells and Afferents: Two Channels for Head Motion Signals,” *Annu. Rev. Neurosci.*, vol. 34, no. 1, pp. 501–534, 2011.
- [161] D. Turner-Evans *et al.*, “Angular velocity integration in a fly heading circuit,” *eLife*, vol. 6, p. e23496, May 2017.

- [162] J. M. Goldberg and C. Fernandez, "Physiology of Peripheral Neurons Innervating Semicircular Canals of the Squirrel Monkey," *J. Neurophysiol.*, vol. 34, no. 4, pp. 676–684, Jul. 1971.
- [163] A. Steinacker, "Sensory Processing and Ionic Currents in Vestibular Hair Cells," in *The Vestibular System*, S. M. Highstein, R. R. Fay, and A. N. Popper, Eds. Springer New York, 2004, pp. 202–234.
- [164] A. Bronstein, *Oxford Textbook of Vertigo and Imbalance*. Oxford University Press, 2013.
- [165] H. Kingma and R. van de Berg, "Chapter 1 - Anatomy, physiology, and physics of the peripheral vestibular system," in *Handbook of Clinical Neurology*, vol. 137, J. M. Furman and T. Lempert, Eds. Elsevier, 2016, pp. 1–16.
- [166] W. Steinhausen, "Über Sichtbarmachung und Funktionsprüfung der Cupula terminalis in den Bogengangsanipullen des Labyrinthes," *Pflüg. Arch. Für Gesamte Physiol. Menschen Tiere*, vol. 217, no. 1, pp. 747–755, Dec. 1927.
- [167] G. Wiest, "The origins of vestibular science," *Ann. N. Y. Acad. Sci.*, vol. 1343, no. 1, pp. 1–9, 2015.
- [168] A. A. J. van Egmond, J. J. Groen, and L. B. W. Jongkees, "The mechanics of the semicircular canal," *J. Physiol.*, vol. 110, no. 1–2, pp. 1–17, 1949.
- [169] G. M. Jones, "Transfer Function of Labyrinthine Volleys Through the Vestibular Nuclei," in *Progress in Brain Research*, vol. 37, A. Brodal and O. Pompeiano, Eds. Elsevier, 1972, pp. 139–156.
- [170] O. Lowenstein and G. J. Compton, "A Comparative Study of the Responses of Isolated First-Order Semicircular Canal Afferents to Angular and Linear Acceleration, Analysed in the Time and Frequency Domains," *Proc. R. Soc. Lond. B Biol. Sci.*, vol. 202, no. 1148, pp. 313–338, Jul. 1978.
- [171] I. P. Howard, "The Vestibular System," in *Handbook of perception and human performance*, New York: Wiley, 1986.
- [172] A. M. Brichta and J. M. Goldberg, "The Papilla Neglecta of Turtles: A Detector of Head Rotations with Unique Sensory Coding Properties," *J. Neurosci.*, vol. 18, no. 11, pp. 4314–4324, Jun. 1998.
- [173] M. M. Iversen and R. D. Rabbitt, "Wave Mechanics of the Vestibular Semicircular Canals," *Biophys. J.*, vol. 113, no. 5, pp. 1133–1149, Sep. 2017.
- [174] R. David, A. Stoessel, A. Berthoz, F. Spoor, and D. Bennequin, "Assessing morphology and function of the semicircular duct system: introducing new *in-situ* visualization and software toolbox," *Sci. Rep.*, vol. 6, p. 32772, Sep. 2016.
- [175] D. J. Pender, "A toolbox of geometric elements for labyrinth model design and analysis," *The Laryngoscope*, vol. 122, no. 9, pp. 2051–2056, Sep. 2012.
- [176] M. A. Ifediba, S. M. Rajguru, T. E. Hullar, and R. D. Rabbitt, "The Role of 3-Canal Biomechanics in Angular Motion Transduction by the Human Vestibular Labyrinth," *Ann. Biomed. Eng.*, vol. 35, no. 7, pp. 1247–1263, Jul. 2007.
- [177] C. M. Oman and L. R. Young, "Physiological Range of Pressure Difference and Cupula Deflections in the Human Semicircular Canal: Theoretical

- Considerations,” in *Progress in Brain Research*, vol. 37, Supplement C vols., A. Brodal and O. Pompeiano, Eds. Elsevier, 1972, pp. 529–539.
- [178] I. S. Curthoys and C. M. Oman, “Dimensions of the Horizontal Semicircular Duct, Ampulla and Utricle in Rat and Guinea Pig,” *Acta Otolaryngol. (Stockh.)*, vol. 101, no. 1–2, pp. 1–10, Jan. 1986.
- [179] M. von Pfaundler, *The Diseases of children :a work for the practicing physician* /. Philadelphia :, 1914.
- [180] A. M. Yamauchi, “Cupular micromechanics and motion sensation in the toadfish vestibular semicircular canals,” Ph.D., The University of Utah, United States -- Utah, 2002.
- [181] D. W. Thompson, *On Growth and Form*. Cambridge University Press, 1992.
- [182] G. M. Jones and K. E. Spells, “A Theoretical and Comparative Study of the Functional Dependence of the Semicircular Canal upon Its Physical Dimensions,” *Proc. R. Soc. Lond. B Biol. Sci.*, vol. 157, no. 968, pp. 403–419, Mar. 1963.
- [183] T. M. Squires, “Optimizing the Vertebrate Vestibular Semicircular Canal: Could We Balance Any Better?,” *Phys. Rev. Lett.*, vol. 93, no. 19, p. 198106, Nov. 2004.
- [184] P. G. Cox and N. Jeffery, “Semicircular canals and agility: the influence of size and shape measures,” *J. Anat.*, vol. 216, no. 1, pp. 37–47, Jan. 2010.
- [185] J. A. Georgi, J. S. Sipla, and C. A. Forster, “Turning Semicircular Canal Function on Its Head: Dinosaurs and a Novel Vestibular Analysis,” *PLOS ONE*, vol. 8, no. 3, p. e58517, Mar. 2013.
- [186] F. Spoor, B. Wood, and F. Zonneveld, “Evidence for a link between human semicircular canal size and bipedal behaviour,” *J. Hum. Evol.*, vol. 30, no. 2, pp. 183–187, Feb. 1996.
- [187] H. Schutz, H. A. Jamniczky, B. Hallgrímsson, and T. Garland, “Shape-shift: Semicircular canal morphology responds to selective breeding for increased locomotor activity,” *Evolution*, vol. 68, no. 11, pp. 3184–3198, Nov. 2014.
- [188] M. D. Malinzak, R. F. Kay, and T. E. Hullar, “Locomotor head movements and semicircular canal morphology in primates,” *Proc. Natl. Acad. Sci.*, vol. 109, no. 44, pp. 17914–17919, Oct. 2012.
- [189] M. Kassemi, D. Deserranno, and J. G. Oas, “Effect of Gravity on the Caloric Stimulation of the Inner Ear,” *Ann. N. Y. Acad. Sci.*, vol. 1027, no. 1, pp. 360–370, Nov. 2004.
- [190] M. Kassemi, D. Deserranno, and J. G. Oas, “Fluid-structural Interactions in the Inner Ear,” *Comput Struct*, vol. 83, no. 2–3, pp. 181–189, Jan. 2005.
- [191] M. Kassemi, J. G. Oas, and D. Deserranno, “Fluid-structural dynamics of ground-based and microgravity caloric tests,” *J. Vestib. Res. Equilib. Orientat.*, vol. 15, no. 2, pp. 93–107, 2005.
- [192] J. M. Goldberg and C. Fernandez, “Physiology of peripheral neurons innervating semicircular canals of the squirrel monkey. I. Resting discharge and response to

- constant angular accelerations.,” *J. Neurophysiol.*, vol. 34, no. 4, pp. 635–660, Jul. 1971.
- [193] C. Fernandez and J. M. Goldberg, “Physiology of peripheral neurons innervating semicircular canals of the squirrel monkey. II. Response to sinusoidal stimulation and dynamics of peripheral vestibular system.,” *J. Neurophysiol.*, vol. 34, no. 4, pp. 661–675, Jul. 1971.
 - [194] H. Asadi, S. Mohamed, C. P. Lim, S. Nahavandi, and E. Nalivaiko, “Semicircular canal modeling in human perception,” *Rev. Neurosci.*, vol. 28, no. 5, pp. 537–549, 2017.
 - [195] M. Zidanic and W. E. Brownell, “Fine structure of the intracochlear potential field. I. The silent current,” *Biophys. J.*, vol. 57, no. 6, pp. 1253–1268, Jun. 1990.
 - [196] B. M. Johnstone, “Genesis of the Cochlear Endolymphatic Potential,” in *Current Topics in Bioenergetics*, vol. 2, D. R. Sanadi, Ed. Elsevier, 1967, pp. 335–352.
 - [197] G. H. Crampton, “Does Linear Acceleration Modify Cupular Deflection?,” *NASA Spec. Publ.*, vol. 115, p. 169, 1966.
 - [198] R. D. Rabbitt, R. Boyle, and S. M. Highstein, “Influence of Surgical Plugging on Horizontal Semicircular Canal Mechanics and Afferent Response Dynamics,” *J. Neurophysiol.*, vol. 82, no. 2, pp. 1033–1053, Aug. 1999.
 - [199] A. V. Kondrachuk and R. D. Boyle, “The Density Difference of Cupula and Endolymph Changes the Mechanics of Semicircular Canals,” *Microgravity Sci. Technol.*, vol. 23, no. 4, pp. 433–438, Nov. 2011.
 - [200] C. L. Kumaragamage, B. J. Lithgow, and Z. Moussavi, “Development of an ultra low noise, miniature signal conditioning device for vestibular evoked response recordings,” *Biomed. Eng. OnLine*, vol. 13, p. 6, Jan. 2014.
 - [201] W. Denk and W. W. Webb, “Thermal-noise-limited transduction observed in mechanosensory receptors of the inner ear,” *Phys. Rev. Lett.*, vol. 63, no. 2, pp. 207–210, Jul. 1989.
 - [202] W. Denk and W. W. Webb, “Forward and reverse transduction at the limit of sensitivity studied by correlating electrical and mechanical fluctuations in frog saccular hair cells,” *Hear. Res.*, vol. 60, no. 1, pp. 89–102, Jun. 1992.
 - [203] M. Muller, K. Heeck, and C. P. H. Elemans, “Semicircular Canals Circumvent Brownian Motion Overload of Mechanoreceptor Hair Cells,” *PLOS ONE*, vol. 11, no. 7, p. e0159427, Jul. 2016.
 - [204] M. Muller, “Semicircular Duct Dimensions and Sensitivity of the Vertebrate Vestibular System,” *J. Theor. Biol.*, vol. 167, no. 3, pp. 239–256, Apr. 1994.
 - [205] J. M. Benyus, *Biomimicry: Innovation Inspired by Nature*. Harper Collins, 2009.
 - [206] M. Fu, S. Cheng, M. Wang, L. Ming, and T. Wang, “Permeability modeling for porous transducer of liquid-circular angular accelerometer,” *Sens. Actuators Phys.*, 2017.
 - [207] Z. Fan, J. Chen, J. Zou, D. Bullen, C. Liu, and F. Delcomyn, “Design and fabrication of artificial lateral line flow sensors,” *J. Micromechanics Microengineering*, vol. 12, no. 5, p. 655, 2002.

- [208] F. Boselli, D. Obrist, and L. Kleiser, "Vortical flow in the utricle and the ampulla: a computational study on the fluid dynamics of the vestibular system," *Biomech. Model. Mechanobiol.*, vol. 12, no. 2, pp. 335–348, May 2012.
- [209] J. C. Berlin, E. C. Kirk, and T. B. Rowe, "Functional Implications of Ubiquitous Semicircular Canal Non-Orthogonality in Mammals," *PLOS ONE*, vol. 8, no. 11, p. e79585, Nov. 2013.
- [210] T. Q. Trung and N.-E. Lee, "Flexible and Stretchable Physical Sensor Integrated Platforms for Wearable Human-Activity Monitoring and Personal Healthcare," *Adv. Mater.*, vol. 28, no. 22, pp. 4338–4372, Jun. 2016.
- [211] T. Haslwanter, "Vestibular Simulation," 2013. [Online]. Available: https://en.wikibooks.org/wiki/Sensory_Systems/Computer_Models/Vestibular_Simulation. [Accessed: 21-Jun-2018].
- [212] B. Bara, K. Nandakumar, and J. H. Masliyah, "An experimental and numerical study of the Dean problem: flow development towards two-dimensional multiple solutions," *J. Fluid Mech.*, vol. 244, pp. 339–376, Nov. 1992.
- [213] H. Schlichting and K. Gersten, *Boundary-Layer Theory*, 9th ed. Springer-Verlag, 2017.
- [214] I. D. Piazza and M. Ciofalo, "Transition to turbulence in toroidal pipes," *J. Fluid Mech.*, vol. 687, pp. 72–117, Nov. 2011.
- [215] N. R. Tas, T. S. J. Lammerink, P. J. Leussink, J. W. Berenschot, H. E. de Bree, and M. C. Elwenspoek, "Toward thermal flow-sensing with pL/s resolution," in *Proceedings of SPIE In Micromachined Devices and Components VI*, 2000, vol. 4176, pp. 106–121.
- [216] K. H. Ahn and M. B. Ibrahim, "Laminar/turbulent oscillating flow in circular pipes," *Int. J. Heat Fluid Flow*, vol. 13, no. 4, pp. 340–346, Dec. 1992.
- [217] R. Hiratsuka, D. C. van Duyn, T. Otaredian, P. de Vries, and P. M. Sarro, "Design considerations for the thermal accelerometer," *Sens. Actuators Phys.*, vol. 32, no. 1–3, pp. 380–385, Apr. 1992.
- [218] T. S. J. Lammerink, N. R. Tas, M. Elwenspoek, and J. H. J. Fluitman, "Micro-liquid flow sensor," *Sens. Actuators Phys.*, vol. 37–38, pp. 45–50, Jun. 1993.
- [219] W. E. Langlois and M. O. Deville, "The Equations of Viscous Flow," in *Slow Viscous Flow*, Springer International Publishing, 2014, pp. 19–79.
- [220] A. Chupin and R. Stepanov, "Full perturbation solution for the flow in a rotating torus," *Phys. Rev. E*, vol. 77, no. 5, p. 057301, May 2008.
- [221] M. Elwenspoek, "Thermal flow micro sensors," in *Semiconductor Conference, 1999. CAS '99 Proceedings. 1999 International*, 1999, vol. 2, pp. 423–435 vol.2.
- [222] J. Courteaud, N. Crespy, P. Combette, B. Sorli, and A. Giani, "Studies and optimization of the frequency response of a micromachined thermal accelerometer," *Sens. Actuators Phys.*, vol. 147, no. 1, pp. 75–82, Sep. 2008.
- [223] A. Garraud, P. Combette, J. Courteaud, and A. Giani, "Effect of the Detector Width and Gas Pressure on the Frequency Response of a Micromachined Thermal Accelerometer," *Micromachines*, vol. 2, no. 2, pp. 167–178, May 2011.

- [224] R. Mukherjee, J. Basu, P. Mandal, and P. K. Guha, “A review of micromachined thermal accelerometers,” *J. Micromechanics Microengineering*, vol. 27, no. 12, p. 123002, 2017.
- [225] R. Amarasinghe, D. V. Dao, T. Toriyama, and S. Sugiyama, “Simulation, fabrication and characterization of a three-axis piezoresistive accelerometer,” *Smart Mater. Struct.*, vol. 15, no. 6, p. 1691, Dec. 2006.
- [226] A. Demuren and H. Grotjans, “Buoyancy-Driven Flows—Beyond the Boussinesq Approximation,” *Numer. Heat Transf. Part B Fundam.*, vol. 56, no. 1, pp. 1–22, Jun. 2009.
- [227] E. Buckingham, “On Physically Similar Systems; Illustrations of the Use of Dimensional Equations,” *Phys. Rev.*, vol. 4, no. 4, pp. 345–376, Oct. 1914.
- [228] J. Bahari, J. D. Jones, and A. M. Leung, “Sensitivity Improvement of Micromachined Convective Accelerometers,” *J. Microelectromechanical Syst.*, vol. 21, no. 3, pp. 646–655, 2012.
- [229] T. S. Zhao and P. Cheng, “The friction coefficient of a fully developed laminar reciprocating flow in a circular pipe,” *Int. J. Heat Fluid Flow*, vol. 17, no. 2, pp. 167–172, Apr. 1996.
- [230] A. Wu, “Thermal drift in convective micromachined accelerometers,” Thesis, School of Engineering Science - Simon Fraser University, 2007.
- [231] L. Lin and J. Jones, “A liquid-filled buoyancy-driven convective micromachined accelerometer,” *J. Microelectromechanical Syst.*, vol. 14, no. 5, pp. 1061–1069, 2005.
- [232] J. M. O. de Zárata, “Thermal nonequilibrium fluctuations in one-component fluids,” in *Hydrodynamic Fluctuations in Fluids and Fluid Mixtures*, J. V. Sengers, Ed. Amsterdam: Elsevier, 2006, p. v.
- [233] P. F. Hodnett, “Natural convection between horizontal heated concentric circular cylinders,” *Z. Für Angew. Math. Phys. ZAMP*, vol. 24, no. 4, pp. 507–516, 1973.
- [234] X. B. Luo, Z. X. Li, Z. Y. Guo, and Y. J. Yang, “Study on linearity of a micromachined convective accelerometer,” *Microelectron. Eng.*, vol. 65, no. 1–2, pp. 87–101, Jan. 2003.
- [235] W. E. Langlois and M. O. Deville, “Exact Solutions to the Equations of Viscous Flow,” in *Slow Viscous Flow*, Springer International Publishing, 2014, pp. 105–143.
- [236] R. Zhu, H. Ding, Y. Su, and Y. Yang, “Modeling and Experimental Study on Characterization of Micromachined Thermal Gas Inertial,” *Sensors*, vol. 10, no. 9, pp. 8304–8315, Sep. 2010.
- [237] A. Garraud, P. Combette, F. Pichot, J. Courteaud, B. Charlot, and A. Giani, “Frequency response analysis of an accelerometer based on thermal convection,” *J. Micromechanics Microengineering*, vol. 21, no. 3, p. 035017, Mar. 2011.
- [238] D. F. Reyes-Romero, A. S. Cubukcu, and G. A. Urban, “Measurement and simulation of the frequency response of a thermal flow sensor at different flow speeds,” *Sens. Actuators Phys.*, vol. 189, pp. 168–176, Jan. 2013.

- [239] A. Garraud, P. Combette, A. Deblonde, P. Loisel, and A. Giani, "Closed-loop micromachined accelerometer based on thermal convection," *IET Micro Nano Lett.*, vol. 7, no. 11, pp. 1092–1093, Nov. 2012.
- [240] A. Dribinsky, G. P. Pucci, Y. Cai, M. Varghese, G. J. O'Brien, and I. Memsic, "Temperature-gradient cancelation technique and device," US7862229, 22-Aug-2008.
- [241] H. Alrowais, O. Brand, and P. T. Bhatti, "Design, simulation and fabrication of thermal angular accelerometer," in *Hilton Head Workshop 2014: A Solid-State Sensors, Actuators and Microsystems Workshop*, 2014.
- [242] J.-M. Lin and C.-H. Lin, "Wireless Inertial Sensors Made on Flexible Substrates and Based on Thermal Convection and Near-Field-Communication Principles," *Sens. Mater.*, p. 609, 2016.
- [243] C. R. Tellier and A. J. Tosser, *Size Effects in Thin Films*. Elsevier, 2013.
- [244] F. Warkusz, "The size effect and the temperature coefficient of resistance in thin films," *J. Phys. Appl. Phys.*, vol. 11, no. 5, p. 689, Apr. 1978.
- [245] M. E. Wilson *et al.*, "Fabrication of circular microfluidic channels by combining mechanical micromilling and soft lithography," *Lab. Chip*, vol. 11, no. 8, pp. 1550–1555, Apr. 2011.
- [246] J. Monahan, A. A. Gewirth, and R. G. Nuzzo, "A Method for Filling Complex Polymeric Microfluidic Devices and Arrays," *Anal. Chem.*, vol. 73, no. 13, pp. 3193–3197, Jul. 2001.
- [247] B.-H. Jo, L. M. Van Lerberghe, K. M. Motsegood, and D. J. Beebe, "Three-dimensional micro-channel fabrication in polydimethylsiloxane (PDMS) elastomer," *J. Microelectromechanical Syst.*, vol. 9, no. 1, pp. 76–81, Mar. 2000.
- [248] A. Homsy *et al.*, "Solid on liquid deposition, a review of technological solutions," *Microelectron. Eng.*, vol. 141, pp. 267–279, Jun. 2015.
- [249] J. Charmet *et al.*, "Solid on liquid deposition," *Thin Solid Films*, vol. 518, no. 18, pp. 5061–5065, Jul. 2010.
- [250] B.-K. Nguyen, E. Iwase, K. Matsumoto, and I. Shimoyama, "Electrically driven varifocal micro lens fabricated by depositing parylene directly on liquid," in *IEEE 20th International Conference on Micro Electro Mechanical Systems, 2007. MEMS, 2007*, pp. 305–308.
- [251] A. Shapero, Y. Liu, and Y. C. Tai, "Parylene-on-oil packaging for implantable pressure sensors," in *2016 IEEE 29th International Conference on Micro Electro Mechanical Systems (MEMS)*, 2016, pp. 403–406.
- [252] C. A. Gutierrez and E. Meng, "Impedance-Based Force Transduction Within Fluid-Filled Parylene Microstructures," *J. Microelectromechanical Syst.*, vol. 20, no. 5, pp. 1098–1108, 2011.
- [253] C. A. Gutierrez and E. Meng, "Parylene-Based Electrochemical-MEMS Transducers," *J. Microelectromechanical Syst.*, vol. 19, no. 6, pp. 1352–1361, 2010.

- [254] C. A. Gutierrez and E. Meng, "Liquid Encapsulation in Parylene Microstructures Using Integrated Annular-Plate Stiction Valves," *Micromachines*, vol. 2, no. 3, pp. 356–368, 2011.
- [255] Y. Zhao, A. Leung, M. E. Rebeschini, G. P. Pucci, A. Dribinsky, and Y. Cai, "Method and circuitry for thermal accelerometer signal conditioning," US7305881B2, 11-Dec-2007.
- [256] A. A. Rekik, F. Azaïs, N. Dumas, F. Mailly, and P. Nouet, "A MEMS Convective Accelerometer Equipped with On-Chip Facilities for Sensitivity Electrical Calibration," in *Mixed-Signals, Sensors and Systems Test Workshop (IMS3TW), 2011 IEEE 17th International*, 2011, pp. 82–87.
- [257] A. A. Rekik, F. Azais, F. Mailly, P. Nouet, and M. Masmoudi, "Self-test and self-calibration of a MEMS convective accelerometer," in *2013 Symposium on Design, Test, Integration and Packaging of MEMS/MOEMS (DTIP)*, 2013, pp. 1–4.
- [258] D. M. Bachelder, R. E. Dao, H. H. Kries, and D. E. Morgan, "Convective accelerometer and inclinometer," WO1997040391 A1, 30-Oct-1997.
- [259] S. M. van Netten and M. J. McHenry, "The Biophysics of the Fish Lateral Line," in *The Lateral Line System*, Springer, New York, NY, 2013, pp. 99–119.
- [260] T. Shizhe, "Underwater artificial lateral line flow sensors," *Microsyst. Technol.*, vol. 20, no. 12, pp. 2123–2136, Dec. 2014.
- [261] D. Rowland, Y. Roongthumskul, J.-H. Lee, J. Cheon, and D. Bozovic, "Magnetic actuation of hair cells," *Appl. Phys. Lett.*, vol. 99, no. 19, p. 193701, Nov. 2011.
- [262] B. Andò *et al.*, "A bio-inspired device to detect equilibrium variations using IPMCs and ferrofluids," *Sens. Actuators Phys.*, vol. 144, no. 2, pp. 242–250, Jun. 2008.
- [263] F. Khademolhosseini and M. Chiao, "Fabrication and Patterning of Magnetic Polymer Micropillar Structures Using a Dry-Nanoparticle Embedding Technique," *J. Microelectromechanical Syst.*, vol. 22, no. 1, pp. 131–139, Feb. 2013.
- [264] P. Ribeiro *et al.*, "A Miniaturized Force Sensor Based on Hair-Like Flexible Magnetized Cylinders Deposited over a Giant Magnetoresistive Sensor," *IEEE Trans. Magn.*, vol. PP, no. 99, pp. 1–1, 2017.
- [265] Y. Wang, Y. Gao, H. Wyss, P. Anderson, and J. den Toonder, "Out of the cleanroom, self-assembled magnetic artificial cilia," *Lab. Chip*, vol. 13, no. 17, pp. 3360–3366, Jul. 2013.
- [266] J. le Digabel, N. Biais, J. Fresnais, J.-F. Berret, P. Hersen, and B. Ladoux, "Magnetic micropillars as a tool to govern substrate deformations," *Lab. Chip*, vol. 11, no. 15, pp. 2630–2636, 2011.
- [267] P. D. McGary, L. Tan, J. Zou, B. J. H. Stadler, P. R. Downey, and A. B. Flatau, "Magnetic nanowires for acoustic sensors (invited)," *J. Appl. Phys.*, vol. 99, no. 8, p. 08B310, Apr. 2006.

- [268] B. A. Evans, A. R. Shields, R. L. Carroll, S. Washburn, M. R. Falvo, and R. Superfine, "Magnetically Actuated Nanorod Arrays as Biomimetic Cilia," *Nano Lett.*, vol. 7, no. 5, pp. 1428–1434, May 2007.
- [269] F. Fahrni, M. W. J. Prins, and L. J. van IJzendoorn, "Micro-fluidic actuation using magnetic artificial cilia," *Lab. Chip*, vol. 9, no. 23, pp. 3413–3421, 2009.
- [270] F. Fahrni, M. W. J. Prins, and L. J. van IJzendoorn, "Magnetization and actuation of polymeric microstructures with magnetic nanoparticles for application in microfluidics," *J. Magn. Magn. Mater.*, vol. 321, no. 12, pp. 1843–1850, Jun. 2009.
- [271] M. A. Hein *et al.*, "Fabrication of BioInspired Inorganic Nanocilia Sensors," *IEEE Trans. Magn.*, vol. 49, no. 1, pp. 191–196, Jan. 2013.
- [272] F. Pirmoradi, L. Cheng, and M. Chiao, "A magnetic poly(dimethylesiloxane) composite membrane incorporated with uniformly dispersed, coated iron oxide nanoparticles," *J. Micromechanics Microengineering*, vol. 20, no. 1, p. 015032, 2010.
- [273] G. Nanni, S. Petroni, D. Fragouli, M. Amato, M. De Vittorio, and A. Athanassiou, "Microfabrication of magnetically actuated PDMS–Iron composite membranes," *Microelectron. Eng.*, vol. 98, no. Supplement C, pp. 607–609, Oct. 2012.
- [274] "TMR2901 - Magnetic Field Sensors - Sensors - MultiDimension Technology, The Leading Supplier of TMR Magnetic Sensors - MultiDimension Technology Co., Ltd." [Online]. Available: <http://www.dowaytech.com/en/1876.html>. [Accessed: 28-Jun-2018].
- [275] Y. Sharon, B. Khachatryan, and D. Cheskis, "Towards a low current Hall effect sensor," *Sens. Actuators Phys.*, vol. 279, pp. 278–283, Aug. 2018.
- [276] C. Fermon and M. Pannetier-Lecoeur, "Noise in GMR and TMR Sensors," in *Giant Magnetoresistance (GMR) Sensors*, Springer, Berlin, Heidelberg, 2013, pp. 47–70.
- [277] J. G. Deak, Z. Zhou, and W. Shen, "Tunneling magnetoresistance sensor with pT level 1/f magnetic noise," *AIP Adv.*, vol. 7, no. 5, p. 056676, Mar. 2017.
- [278] X. Li, L. Yin, W. Chen, X. Liu, and Q. Fu, "Study of a three-axis digital tunneling resistance-type magnetic sensor," *IEICE Electron. Express*, vol. 13, no. 13, pp. 20160319–20160319, 2016.
- [279] N. E. Ahmar, "da Vinci's Encephalogram: In search of significant brain signals," Thesis, 2005.
- [280] Y. Ouyang, J. He, J. Hu, G. Zhao, Z. Wang, and S. X. Wang, "Prediction and Optimization of Linearity of MTJ Magnetic Sensors Based on Single-Domain Model," *IEEE Trans. Magn.*, vol. 51, no. 11, pp. 1–4, Nov. 2015.
- [281] P. Ribeiro *et al.*, "Bio-inspired ciliary force sensor for robotic platforms," *IEEE Robot. Autom. Lett.*, vol. PP, no. 99, pp. 1–1, 2017.
- [282] A. Rüsçh and U. Thurm, "Cupula displacement, hair bundle deflection, and physiological responses in the transparent semicircular canal of young eel," *Pflüg. Arch.*, vol. 413, no. 5, pp. 533–545, Mar. 1989.

- [283] K. Moussi and J. Kosel, “3-D Printed Biocompatible Micro-Bellows Membranes,” *J. Microelectromechanical Syst.*, pp. 1–7, 2018.
- [284] S. Amara *et al.*, “High-Performance Flexible Magnetic Tunnel Junctions for Smart Miniaturized Instruments,” *ArXiv180401298 Cond-Mat Physicsphysics*, Apr. 2018.
- [285] Masae Nagase, Koichiro Kobayashi, Taeseong Woo, Yoshihiro Takiyama, Keita Yamazaki, and Masaki Sekino, “Measurement and shielding of extremely low-frequency urban magnetic noise,” *Int. J. Appl. Electromagn. Mech.*, vol. 52, no. 3/4, p. 1591, Nov. 2016.
- [286] Z. Q. Lei, G. J. Li, W. F. Egelhoff, P. T. Lai, and P. W. T. Pong, “Review of Noise Sources in Magnetic Tunnel Junction Sensors,” *IEEE Trans. Magn.*, vol. 47, no. 3, pp. 602–612, Mar. 2011.
- [287] H. Dong *et al.*, “Ultra-low field magnetic resonance imaging detection with gradient tensor compensation in urban unshielded environment,” *Appl. Phys. Lett.*, vol. 102, no. 10, p. 102602, Mar. 2013.
- [288] K. Yamazaki, M. Kotani, and Y. Uchikawa, “Consideration on Low Frequency Magnetic Field Noise from Electric Train for Design of Magnetic Shielded Room for Bio-Magnetics Measurement,” *IEEE Transl. J. Magn. Jpn.*, vol. 7, no. 7, pp. 519–524, Jul. 1992.